University of Southampton

Computer Simulation Studies of Liquid Crystals

by

Shaun Gary Whatling

A dissertation submitted in partial fulfilment of the requirements for the degree of Doctor of Philosophy at the University of Southampton.

Department of Chemistry

August 1997

UNIVERSITY OF SOUTHAMPTON

ABSTRACT

FACULTY OF SCIENCE

CHEMISTRY

Doctor of Philosophy

COMPUTER SIMULATION STUDIES OF LIQUID CRYSTALS

By Shaun Gary Whatling

The main aim of the work described in this Thesis is the identification of the essential features of various mesogenic molecules, necessary for the formation of liquid crystals with the aim of simulating the formation and behaviour of the liquid-crystalline mesophase.

The first two chapters introduce the various classes of liquid-crystalline mesophases and the techniques of computer simulation. This includes the calculation of various orientational, structural and dynamic properties used to classify the mesophase and a short review of the work done to date on the computer simulation of liquid crystals. This allows us to place our work in the appropriate context.

In Chapter 3, we use the Gay-Berne potential to represent the triphenylene moiety, and while is not liquid-crystalline itself, it is the basis for many thermotropic discotic mesogens. Via suitable parametrisation of our potential, we have performed molecular dynamics simulations studies which show that in addition to isotropic and crystal phases, discotic nematic and hexagonal columnar phases are also formed.

Chapter 4 uses the configurations generated from the simulation in the previous chapter to provide a basis for the calculation of X-ray diffraction patterns which allow us to gain further insight into the structure of the mesophase.

In Chapter 5, again via suitable parametrisation of our Gay-Berne potential model, we hoped to simulate the formation of a discotic smectic phase in which the symmetry axis of each discogen is normal to the layer, and while not entirely successful in this aim, it did bring to light some deficiencies in the potential which we have tried to address and correct.

Chapter 6 investigates the effect of the molecular anisotropy on the phase behaviour of the Gay-Berne potential, parametrised to represent a rod-shaped mesogen. We have formed nematic, smectic A and smectic B mesophases and by changing the shape anisotropy as well as the simulation density, we explore their effect on the nematic-isotropic transition temperature and the phase behaviour.

CONTENTS

Chapter 4: X-Ray diffraction of simulated mesophases

Chapter 5: The Gay-Berne discogen II

Chapter 6: The Gay-Berne mesogen

Acknowledgements

First and foremost, I would like to thank my supervisor Professor Geoffrey Luckhurst for his help, encouragement and patience over these past few years. I would also like to thank the Engineering and Physical Sciences Research Council and Merck Ltd, Poole for the award of a CASE studentship.

Secondly, I would like to thank the members of the Chemical Physics group, past and present, especially Andy Emerson, Guilio Galassi, Steve Roskilly, Martin Callaway and Shaun Jordan, who made computer modelling a bit more interesting.

Finally, to my family and friends, particularly Jason "Shut it!" Hughes, Chris "Mr C" Dunn, Saj "The Meister" Raza, Andy "Nipper" Neville, Mark "Hipster" Hyde, Maria "Db" Perrett and Lester "Lesty poos" Anderson, I send a big thank you for keeping me "un-mad" and "non-sober" over the years!

1. Liquid crystals

1.1 Introduction

The term *liquid crystal* describes one of the states of matter lying in between the crystalline solid and the isotropic liquid, another being the plastic crystal[1]. This intermediate state is known as the liquid crystal *mesophase* and at the macroscopic level exhibits the fluidity of a liquid, while having anisotropic properties such as birefringence, usually associated with a solid phase. Depending on the structure of the constituent molecule, a system may exhibit several different mesophases and transitions to these intermediate states can be brought about by varying the temperature and, if it is a binary system, the solvent concentration.

Lyotropic mesophases[1] are formed by systems composed of amphiphilic molecules, containing polar and non-polar parts, and a solvent, usually water. These amphiphiles aggregate into clusters known as micelles, and if the micelles are anisotropic in shape then they can arrange themselves into various mesophases.

Thermotropic mesophases[2] are usually composed of unassociated organic molecules and are obtained by heating and cooling pure mesogenic compounds. Several thousand organic and some inorganic compounds have shown liquid-crystalline mesophases, with the essential, but not sufficient, requirement for the formation of the liquid-crystalline phase being, that the constituent molecule must deviate from spherical symmetry. Thus the majority of thermotropic liquid crystals are composed of rod-shaped or disc-shaped molecules, though many new shapes of mesogen have been discovered, for example, phasmidic mesogens have three flexible, terminal substituents at each end of the molecule, while hemiphasmidic mesogens are a combination of both rod-shaped and disc-shaped moieties[3].

The main aim of this Thesis is to identify the features of mesogenic molecules essential for liquid crystal formation, and to then use them to see if we can model the formation and characteristics of the liquid-crystalline mesophase. First though, we shall describe the various types of liquid crystal phase, with particular emphasis on thermotropic liquid crystals formed by rod-shaped and disc-shaped molecules, the properties that define each phase and what happens at the transition from one phase to another.

1.2 Mesophases formed by rod-shaped molecules

The first liquid crystals were discovered in the 1880's[4], with their constituent molecules being rod-shaped, (see figure 1.1). The mesophases they form can be classified according to the long range molecular arrangement present within the phase and as such can be placed into three broad groups: *nematic*, *chiral nematic* and *smectic*. These mesophases are all distinguished from the isotropic phase by their long range orientational order with the constituent molecules tending to align themselves parallel to a common axis called the *director*. This is denoted by the unit vector **n**, with the states of the director, **n** or **–n** indistinguishable from each other. An important property we need to define is the order parameter S, introduced by Tsvetkov, which is used to give a quantitative measure of the degree of orientational order within a mesophase. Assuming the molecules have cylindrical symmetry, S is given as

$$S = \langle (3\cos^2\beta - 1)/2 \rangle, \tag{1.1}$$

where β is the angle between the main symmetry axis of a molecule and the director, with the angular brackets denoting a statistical average. Perfect parallel order, as in a crystal, leads to a value for S of 1, total disorder, as in an isotropic phase gives S of 0, while in liquid-crystalline mesophases, S takes intermediate values which are strongly dependent on the temperature.

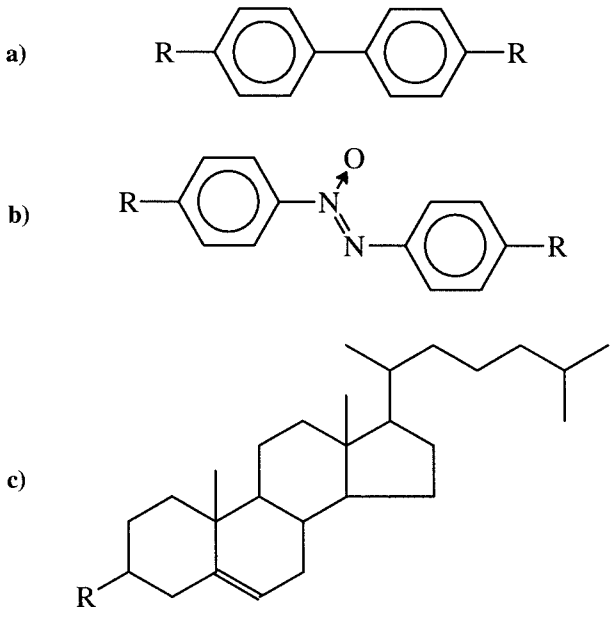

Figure 1.1: *Some examples of rod-shaped mesogenic cores: a) biphenyl, b) azoxybenzene and c) cholesterol.*

1.2.1 The nematic phase

The molecular arrangement within the nematic phase is the simplest of the three mesophase types, (see figure 1.2). The molecules are translationally disordered apart from some short range correlation but do possess long range orientational order. The nematic phase is uniaxial in its properties, in that there is a unique axis along which a property displays one value, which is different from any value measured along any perpendicular direction to this unique axis. A true uniaxial phase possesses $D_{\infty h}$ point group symmetry, but for a nematic phase only second rank tensor properties have been measured, so in theory it should have D_{nh} symmetry where $n \geq 3$, but it is normally assumed to have $D_{\infty h}$ symmetry. There is also the possibility of a biaxial nematic phase in which there are three distinct symmetry axes. This requires the constituent molecules to be biaxial and although a biaxial nematic phase in a lyotropic system has been discovered[5], a thermotropic biaxial N_B, remains elusive.

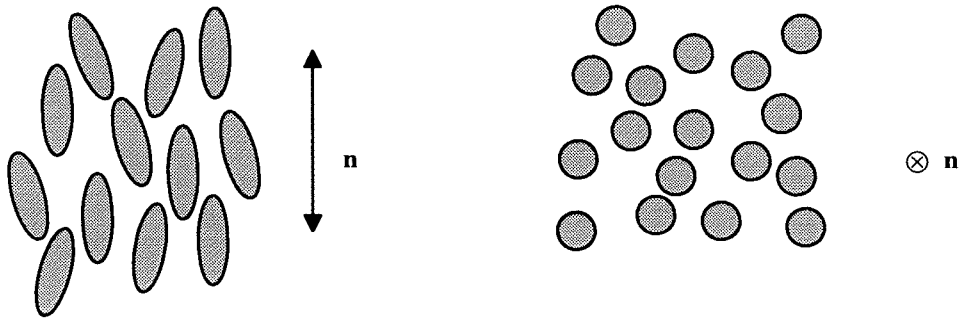

Figure 1.2: *A schematic of the molecular organisation in the nematic phase, both perpendicular and parallel to the director* **n**.

1.2.2 The chiral nematic phase

Though we have classified it in a group on its own, the chiral nematic phase is a special example of the nematic phase i.e. the nematic phase can be considered as a chiral nematic of infinite pitch. At any point throughout the sample the phase has local nematic ordering. On moving away from that point, in a direction perpendicular to the director, it can be seen that the sample has a helical structure, in which the director orientation rotates continuously in a helix along a preferred axis, (see figure 1.3). The pitch p, is defined as the distance for a 2π rotation of the director and because **n** and **-n** are equivalent, the periodicity of the structure is $p/2$.

This spiral arrangement of the molecules is responsible for the unique optical properties of the chiral nematic phase such as reflection of circularly polarised light and a rotatory power many times greater than that of ordinary optically active substances, with the mesophase having S_∞ point group symmetry. Some liquid crystals produce additional optically active phases between the chiral nematic phase and the isotropic liquid. Existing over a very narrow temperature range, ≈ 1 °C, these phases are known as *blue* phases and are generally produced by a chiral nematic with a very short pitch. Three distinct types have been identified: BPI having a body centred cubic lattice structure, BPII with a simple cubic lattice and BPIII, called the "*blue fog*", the structure of which has yet to be determined, and all of which are optically isotropic.

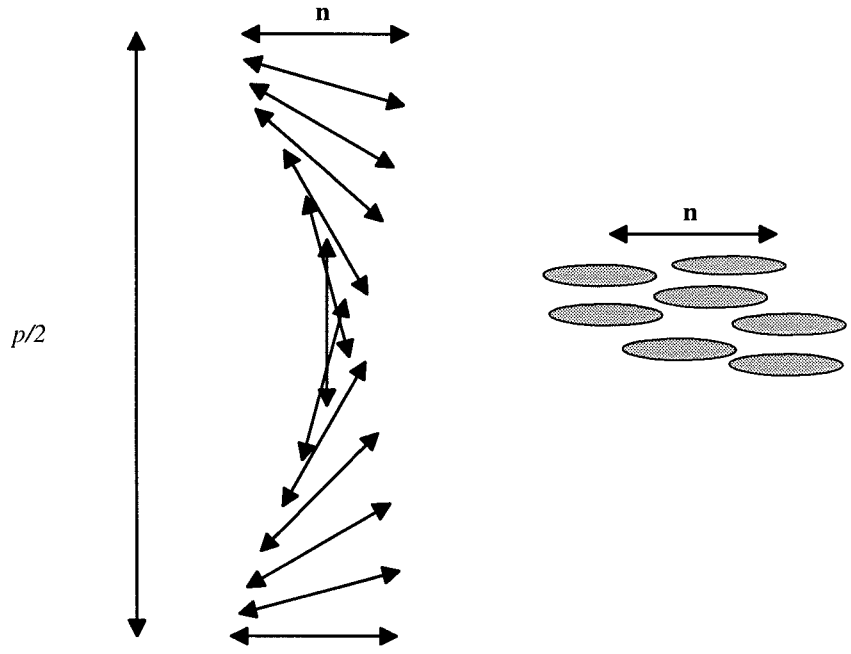

Figure 1.3: *A schematic of the director organisation in the chiral nematic phase.*

1.2.3 The smectic phase

There are at least 12 distinct smectic phases[6], S_A, S_B,..... S_K, S_J, differing in their long range order, which due to a higher degree of molecular long range translational ordering, generally appear at a lower temperature in a phase sequence than the nematic and chiral nematic. The smectic phases are layered structures and though they all have long range orientational order, they can be differentiated by the degrees of order within each mesophase.

An exception is the S_D or as it is now more commonly labelled, the D phase, which has a cubic lattice. The "one dimensional" smectic phases are the S_A and S_C phases where the order describes the layered structure. The smectic A phase is the most disordered of all the smectic phases with only short range positional order within or between layers, (see figure 1.4a). This structure results in the smectic A phase being uniaxial with $D_{\infty h}$ symmetry. The smectic C phase is the tilted version of the smectic A phase, (see figure 1.4b), in which the director within each layer is now tilted with respect to the layer normal. Though possessing very little positional order, the tilt of the director means that the smectic C phase is optically biaxial with C_{2h} symmetry. For strongly polar molecules exhibiting these "one dimensional" smectic phases, there are a variety of modifications of the smectic A and smectic C phases possible. These phases show additional ordering created by antiferroelectric effects[6] but they are not really relevant here and so shall not be discussed further.

The next class of smectic comprises the "two dimensional" phases, S_B, S_F and S_I. These phases have a layered structure, but also possess positional order within each layer and though correlation between layers is absent, there is long range bond orientational order, that is, there is a correlation between "bonds", vectors describing the axes joining adjacent molecules. This implies that there can be long range bond orientational order without long range positional order. The smectic B phase, (see figure 1.4c), has hexagonal packing within each layer, this resulting in the phase having local D_{6h} symmetry and being uniaxial. The smectic F and smectic I are tilted analogues of the smectic B thus are biaxial with C_{2h} point group symmetry.

The third class into which the smectic phases can be conveniently classified are the "three dimensional" orientationally disordered crystals. These include crystal B, E, G, H, J and K. Both the layered structure and positional order within each layer exist but now there is correlation between the positions of the molecules within different layers. Though these phases are crystal phases, the constituent molecules rotate about their long axes rather like a one dimensional plastic crystal, differentiating these phases from true crystals. The crystal B exhibits hexagonal packing within each layer and is uniaxial, (see figure 1.4d).

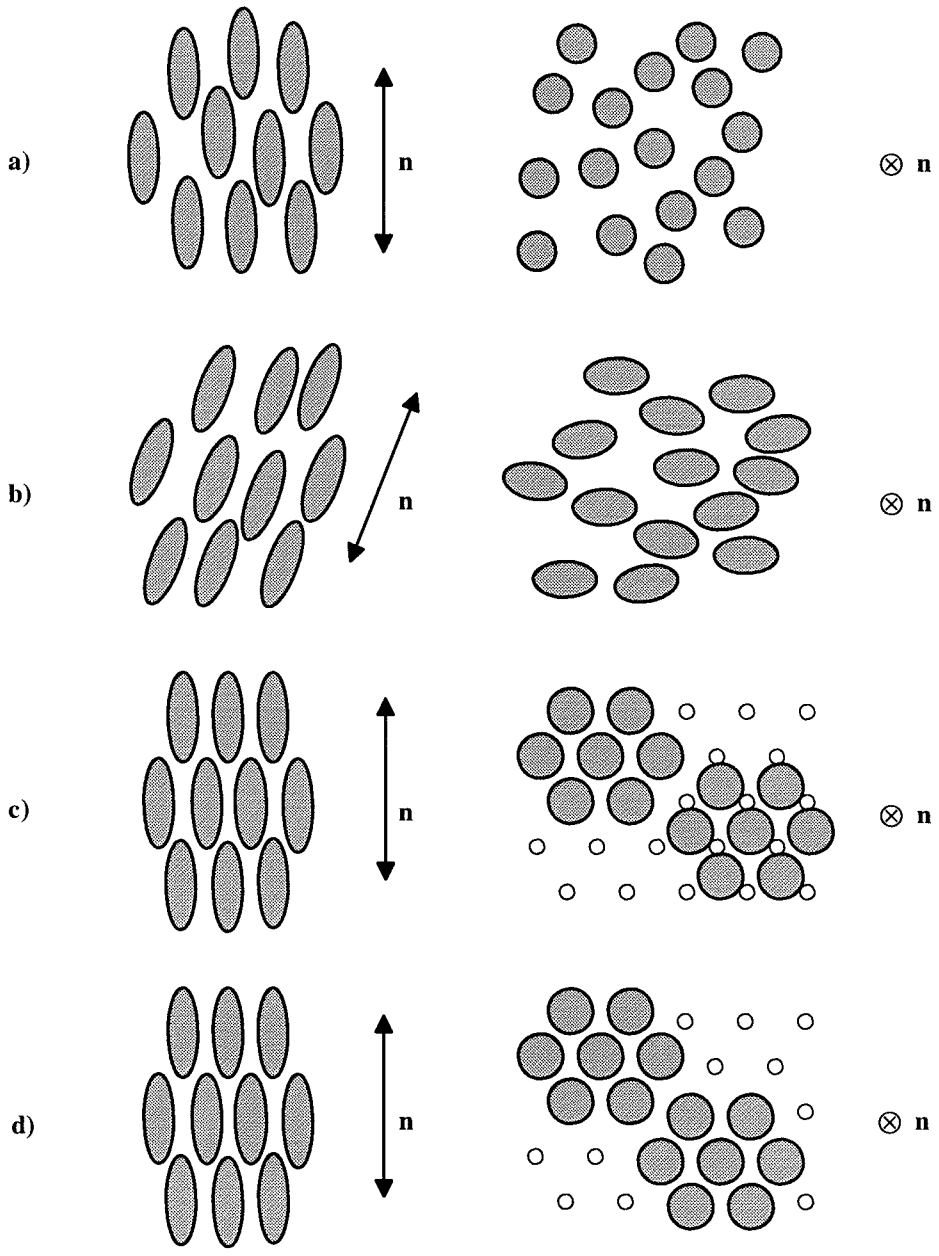

Figure 1.4: *A schematic of the molecular organisation in various smectic phases, both parallel and perpendicular to the director, a) smectic A, b) smectic C, c) smectic B and d) crystal B mesophases. The small circles in the latter two diagrams represent the sites of an imaginary lattice, used to illustrate the increased positional order within the crystal B mesophase.*

Crystal G and J are tilted versions of the crystal B thus have quasi-hexagonal packing with biaxial symmetry. The crystal E phase has a herringbone packing pattern within the layers while crystal H and K are the tilted analogues. There are also chiral analogues of various smectic phases namely, S_C*, S_F*, S_H*, S_I*, S_J* and S_K* where the twist axis is normal to the layers[6]. All tilted smectic phases possess C_{2h} symmetry but when they become chiral the

symmetry drops to C_2, with the symmetry axis being perpendicular to the tilt direction and to the layer normal. For the S_A* phase, the structure of the mesophase differs in that the helical axis is now parallel to the layers and consists of smectic A blocks separated by twist dislocations, giving rise to an alternative name, the "twist grain boundary" (TGA) phase.

1.3 Mesophases formed by disc-shaped molecules

In 1923, Vorländer[7] recognised that disc-shaped molecules should form mesophases but until twenty years ago, the vast majority of thermotropic mesogens were still composed of elongated, rod-shaped molecules. Then in 1977 the first discotic liquid crystals were synthesised by Chandrasekhar *et al.*[8], the general shape of the molecules having a flat aromatic core with four, six or eight lateral alkyl chain substituents. Figure 1.5 shows the basic molecular structure of a variety of disc-shaped compounds which form discotic liquid-crystalline mesophases. Unlike rod-shaped molecules where they can play a small part, and sometimes are not needed at all, in mesophase formation, these lateral alkyl chains seem to be crucial for the formation of the discotic liquid-crystalline phase.

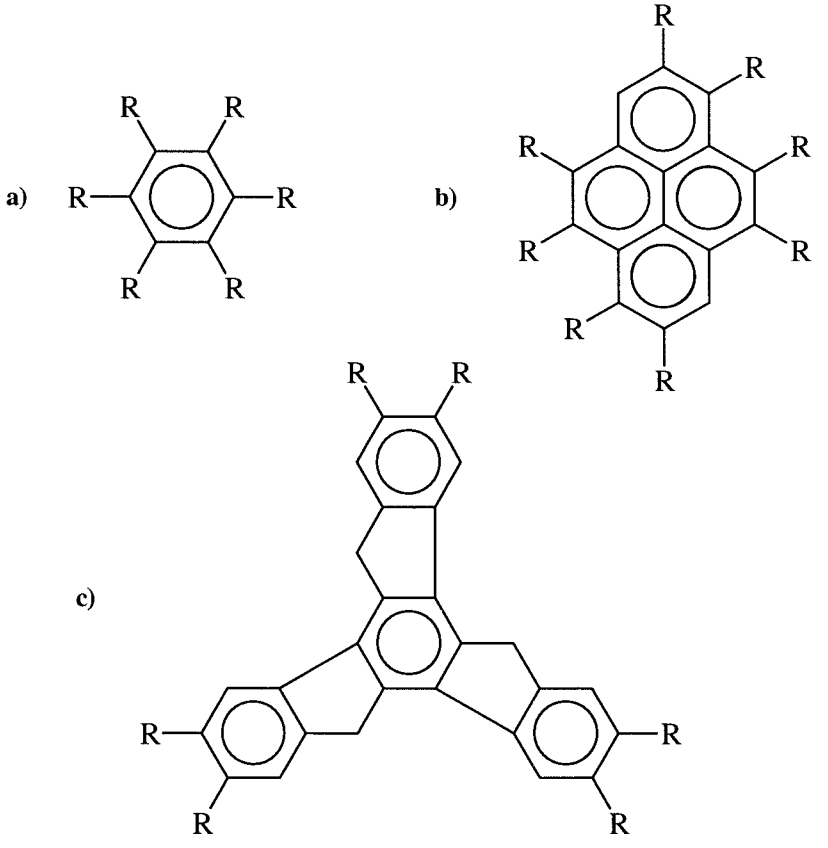

Figure 1.5: *Some examples of disc-shaped mesogenic cores: a) benzene, b) truxene and c) pyrene.*

The molecules align with their symmetry axes parallel, as in mesophases formed from rod-shaped molecules, and this leads to three main phase types, *discotic nematic*, *columnar* and *discotic smectic*. To avoid any confusion, for discotic mesogens, the symmetry axis is normal to the plane of the disc, so in contrast to the nematic phase in §1.2.1, these phases are generally optically negative, although this also depends on the molecular structure as well as the molecular organisation within the phase.

1.3.1 The discotic nematic phase

As with the nematic phase composed of rod-shaped molecules, the molecular arrangement within the discotic nematic phase is the simplest of the mesophase types, (see figure 1.6), and the first examples of this mesophase were discovered by Tinh *et al.*[9], in the hexa-substituted ethers of triphenylene. The molecules are translationally disordered apart from the usual short range correlation but do possess long range orientational order. In a sense the term discotic is not needed because the phase is just like any other nematic phase, it is just the constituent molecules which are different, though we shall persist with the terminology in order to differentiate between mesophases formed by rod-shaped molecules.

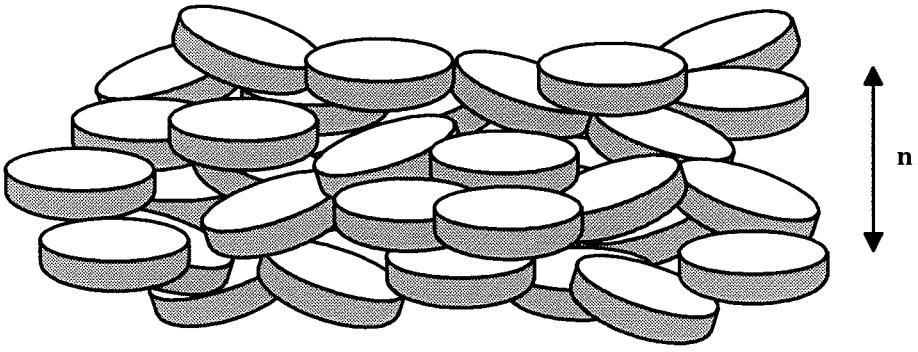

Figure 1.6: *A schematic of the molecular organisation in the discotic nematic phase.*

The *discotic columnar nematic* phase is a recently discovered phase[10,11] which was found to be exhibited by a binary mixture of compounds that formed a charge-transfer complex. On their own both components are not liquid-crystalline but on mixing, a complex is formed composed of the two compounds stacking in short columns in such a way as to maximise the number of unlike contacts. These columns then behave as rod-shaped mesogens, forming a nematic phase with long range orientational order but only short

range translational order, (see figure 1.7). However there is considerable doubt as to whether this is a new phase when the difference between it and the discotic nematic phase seems to be one of local packing.

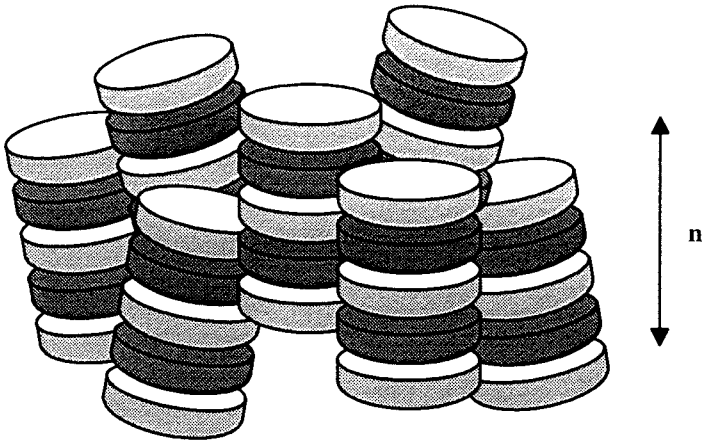

Figure 1.7: *A schematic of the molecular organisation in the discotic columnar nematic phase.*

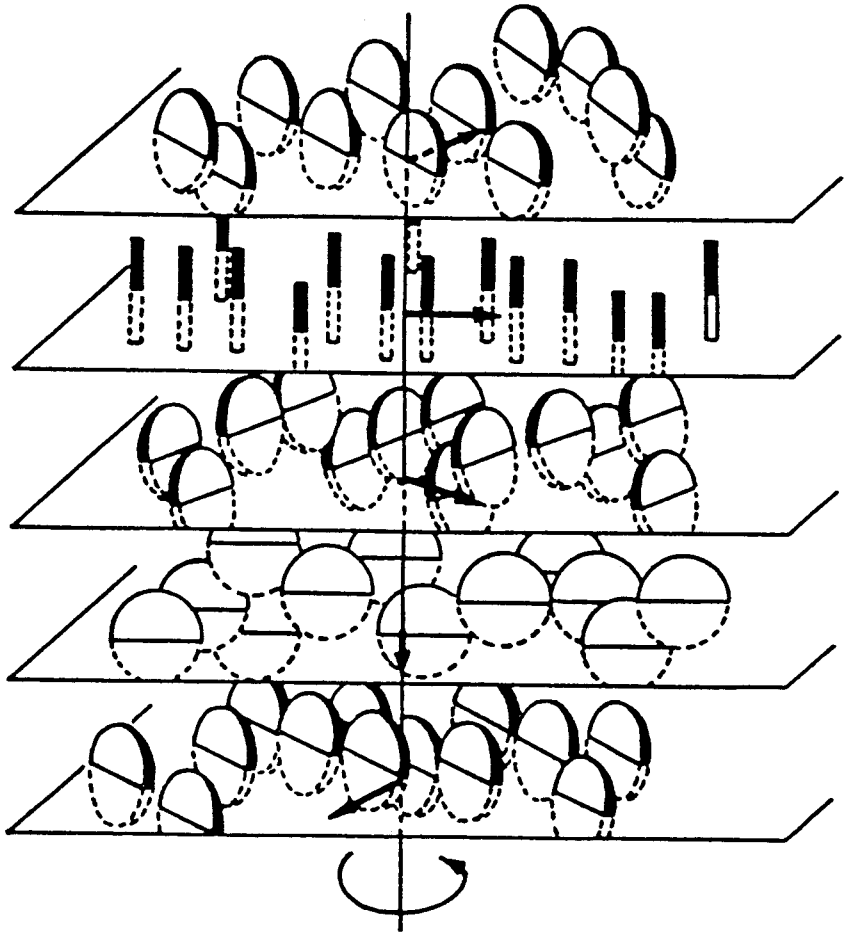

Figure 1.8: *A schematic of the molecular organisation in the chiral discotic nematic phase.*

1.3.2 The chiral discotic nematic phase

Analogous to the chiral nematic phase formed by chiral rod-shaped mesogens, there also exists a *chiral discotic nematic* phase, (see figure 1.8), and as expected for a chiral phase, these mesophases are highly coloured. The first compounds to exhibit the twisted discotic nematic phase were the enantiomeric esters of hexa-substituted benzene, triphenylene and truxene[12], where the chiral centre is located in the substituted chain.

1.3.3 The columnar phase

These were the first discotic phases to be discovered[8] and are characterised by columns of stacked molecules that have two dimensional long range translational order and three dimensional long range bond orientational order. The molecules within each column can be ordered, D_o, with respect to neighbouring molecules in the column, or disordered, D_d, producing liquid-like columns, and can be orthogonal or tilted with respect to the column axis. The columns themselves can either be parallel or tilted relative to the director, while the packing varies from a hexagonal net to a variety of rectangular lattices, (see figure 1.9). It is interesting to note that X-ray diffraction studies have shown that in most columnar phases, it is the molecular cores that are highly ordered with the terminal, flexible chains being conformationally disordered[13].

1.3.4 The discotic smectic phase

The class of molecules known as the metallomesogens[14] have been shown to form a wide range of mesophases, from the nematic, smectic and chiral nematic phases exhibited by rod-shaped mesogens to the discotic nematic and columnar phases previously discussed. But one of the most intriguing discoveries came in the form of a new class of mesophase formed by disc-shaped metallomesogens, (see figure 1.10), the discotic smectic phases. These phases are characterised by sheets of molecules in which there is no translational ordering and that the symmetry axis of each molecules can be perpendicular[15], (see figure 1.11a) or possess a tilt, similar to the smectic C, with respect to the layer normal[16]. A *discotic columnar smectic* phase has also discovered[17] in which the molecules within each layer form columns, similar to the smectic B phase, (see figure 1.11b). Another possibility exists in which the discs in the layers have their symmetry axis perpendicular to the layers[18] and it is this mesophase we shall explore in Chapter 5.

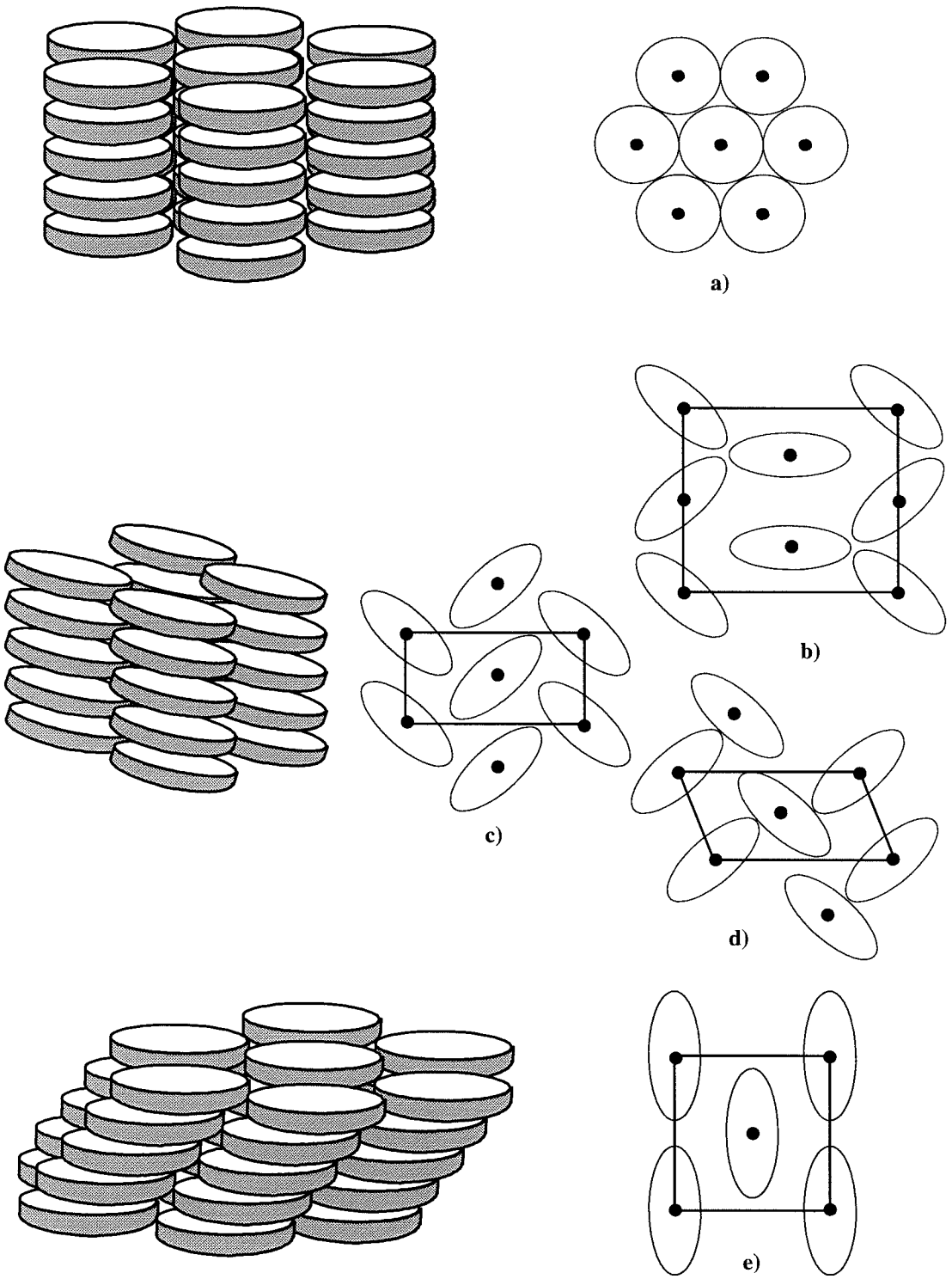

Figure 1.9: *A schematic of the packing within the various columnar phases. Structures of the orthogonal columnar phases, a) hexagonal (P6 2/m 2/m), b) rectangular ($P2_1/a$), c) oblique (P_1), d) rectangular (P_2/a) and tilted columnar phase e) rectangular face-centred (C2/m).*

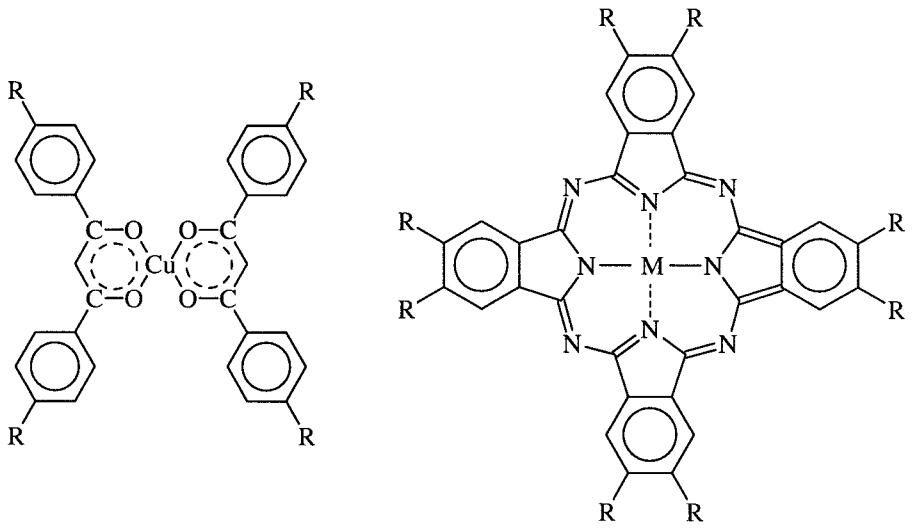

Figure 1.10: *An example of the disc-shaped metallomesogens, a) the bis-(4-n-decylbenzoyl)methanato copper (II) series of compounds, and b) the octa- substituted metallo-phthalocyanine series of compounds.*

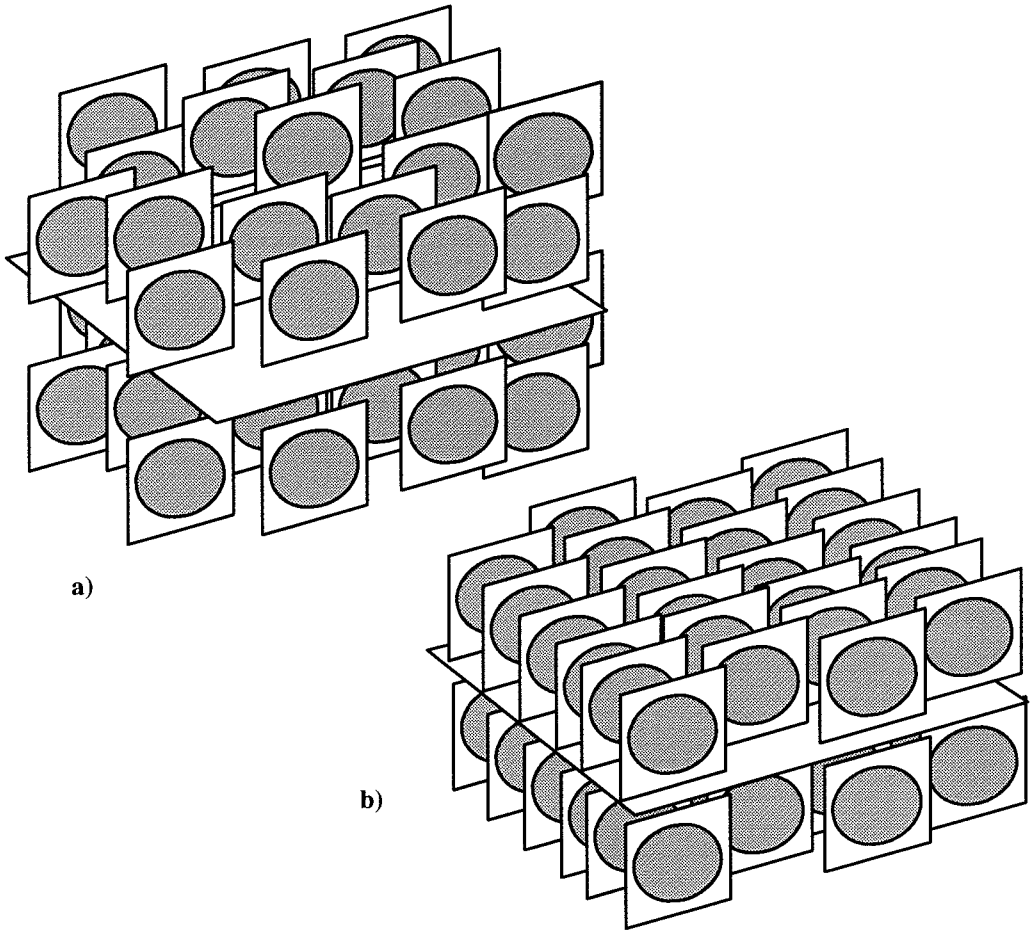

Figure 1.11: *A schematic of the molecular organisation within a) the discotic smectic phase and b) the discotic columnar smectic phase.*

1.4 Phase transitions between liquid-crystalline mesophases

1.4.1 Polymorphism

An important point to note is that each liquid-crystalline compound is not constrained to exhibit just one type of mesophase. In fact, many compounds exhibit a wide range of mesophases. But far from occurring in a haphazard order, we can usually predict the sequence in which the phases will appear, from the fact that raising the temperature results in progressive destruction of the long range molecular order. Thus generally, the sequence proceeds from the smectic phases at lower temperatures with a high degree of molecular ordering due to their layered structure, through the nematic or chiral nematic phases, to the isotropic fluid. There is also a predetermined order[19] within the smectic phase with increasing temperature. Starting from the disordered crystals, crystal B, E, G, H, J, K and D, which have three dimensional orientational and translational order to the two dimensionally ordered mesophases, smectic B, smectic F and smectic I. The smectic phases appearing at the highest temperatures are the one dimensional phases, smectic A and smectic C. As usual there are exceptions to these rules, and it concerns the phenomenon known as *re-entrance*. Usually occurring in strongly polar compounds, it involves the formation of a nematic or smectic phase in between a smectic and another smectic/crystal phase on cooling from the isotropic phase, e.g. S_B - $N_{Re\text{-}entrant}$ - S_A - N - I.

Discotic liquid crystals also exhibit a rich polymorphism. On heating from the crystal the columnar phases appear first with their highly ordered columns, then the discotic nematic phases onto the isotropic liquid. As with the smectic phases, there are a variety of phase transitions between the columnar polymorphs. Examples include ordered hexagonal columnar to disordered hexagonal columnar where the order refers to the stacking of the molecules within a column, and hexagonal columnar to rectangular columnar. This latter phase transition consists of a small distortion in the lattice combined with an orientational order-disorder transition of the molecular cores, in that the tilts in neighbouring columns are no longer rotationally correlated[20]. As with rod-shaped mesogens, there also exists the possibility of re-entrant columnar and discotic nematic phases. The first example of re-entrant phases in discotic mesophases was found in a truxene derivative[21], (see figure 1.12).

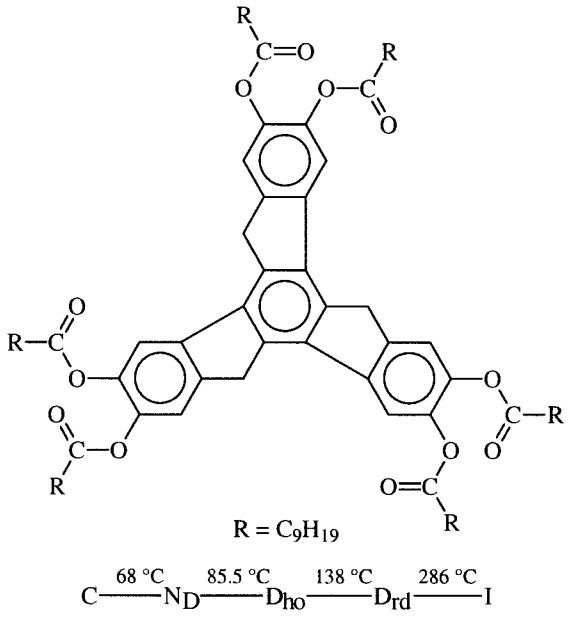

Figure 1.12: *A typical disc-shaped mesogen exhibiting a variety of mesophases that include a columnar and a re-entrant discotic nematic phase.*

1.4.2 Phase transitions

Most of these phase transitions are enantiotropic in that they take place reversibly on heating and cooling, though conversion to the solid phases is usually accompanied by some supercooling. There are also monotropic phase transitions, that is they are only observed on cooling a system from the isotropic liquid, as they occur below the melting point. We have discussed the types of mesophase that can be formed by liquid-crystalline compounds and the order in which the phases appear, but what happens at a phase transition and are there differences between the transitions?

At the microscopic level, the positional and orientational ordering changes as the molecules respond to change in external stimuli such as temperature or pressure, while changes also occur in the macroscopic properties of the system, such as the density, refractive index and long range orientational order. But these changes are not the same at each transition, and so the phase transitions are classified into various types characterised by the thermodynamic properties of the system. We shall now discuss the Ehrenfest classification using the thermodynamic free energy and its derivatives.

The quantities[22] used to classify a phase transition for a liquid-crystalline system of N particles at constant volume are the Helmholtz free energy A, and its first and second derivatives, that is, the entropy S and heat capacity C_V, defined respectively by

$$S = -(\partial A/\partial T)_V, \tag{1.2}$$

$$C_V = -T(\partial^2 A/\partial T^2)_V \tag{1.3}$$

In the original classification by Ehrenfest, a phase transition is classified as being n^{th} order if the first $(n-1)$ derivatives of the free energy functions are continuous across the phase transition, while the n^{th} derivative shows a discontinuity. Thus for a *first order* transition there is a finite discontinuous change in S but an infinite discontinuous change in C_V. Following this, for a *second order* transition, the entropy is continuous and the second derivative of the free energy, the heat capacity is discontinuous. The phase transitions of liquids crystals and other compounds can thus be classified as first order if there is a change in entropy, and second order or higher if no change in the entropy occurs. We should note that at constant pressure which applies for most experimental studies, we should use the Gibbs free energy G, instead of the Helmholtz free energy.

For rod-shaped mesogens[23], the nematic - isotropic and chiral nematic - isotropic transitions are weakly first order reflecting the low difference in molecular order between the various phases, with ΔS generally being in the range 1 - 5 J K^{-1} mol^{-1}, this value being smaller for disc-shaped mesogens. This is compared with a value of 5 - 15 J K^{-1} mol^{-1} or higher for strong first order transitions such as the smectic C - isotropic and smectic B - smectic A transitions. An example of a second order transition is the smectic C - smectic A phase transition in which only the tilt of the director changes, with ΔS in the range of 1 - 2 J K^{-1} mol^{-1}. Similar trends can be observed in systems of discotic liquid crystals[24], with the columnar - isotropic being an example of a strong first order transition. The columnar - discotic nematic transition is weakly first order, while a second order transition can occur between different columnar mesophases.

1.5 Summary of the remaining chapters

In this Chapter we have given a basic text book introduction to the area of liquid crystals, laying out the various mesophases that can be formed and describing the properties of these

phases that are of interest to us in this Thesis. The next chapter, Chapter 2, is similar in that there we describe the techniques of computer simulation and how they can be applied to the area of liquid crystals, while also reviewing previous simulations of the liquid-crystalline mesophase. We also give definitions of the various order parameters and distribution functions that we use to investigate the phases. The remaining chapters will seek to show how we can use these computer simulations of model liquid crystals, to gain a better understanding of the physics of real liquid crystals. Specifically, we shall concentrate on the model used for the molecular interactions, the Gay-Berne potential.

Chapter 3 describes our simulations of discotic liquid crystals based on the Gay-Berne potential model and illustrates some interesting aspects of phase behaviour. Chapter 4 shows how we can use the various results from the preceding chapter to calculate X-ray diffraction patterns, allowing us to gain a better understanding of the structure of the mesophases and to make contact with experiment. Chapter 5 describes some additional simulations of discotic liquid crystals using the Gay-Berne potential, while also discussing some deficiencies that have arisen in the potential model used and Chapter 6 explores a system of Gay-Berne rods of varying length-to-breadth ratios and the effect of this on their phase behaviour.

1.6 References

[1] S.Friberg. (ed.) *Lyotropic Liquid Crystals.* ACS (1976).

[2] G.W.Gray. (ed.) *Thermotropic Liquid Crystals.* Wiley (1987)

[3] D.Demus. *Liq.Cryst.* (1989) **5** 75.

[4] F.Reinitzer. *Monatsch.Chem.* (1888) **9** 421. [English translation. *Liq.Cryst.* (1989) **5** 7.]

[5] L.J.Yu and A.Saupe. *Phys.Rev.Lett.* (1980) **45** 1000.

[6] S.Chandrasekhar. *Liquid Crystals. 2nd Ed.* Cambridge (1992).

[7] D.Vorländer. *Z.Phys.Chem.* (1923) **105** 211.

[8] S.Chandrasekhar, B.K.Sadashiva and K.A.Suresh. *Pramana.* (1977) **9** 471.

[9] Nguyen Huu Tinh, C.Destrade and H.Gasparoux. *Phys.Lett.* (1979) **72A** 251.

[10] K.Praefcke, D.Singer, B.Kohne, M.Ebert, A.Liebmann and J.H.Wendorff. *Liq.Cryst.* (1991) **10** 147.

[11] H.Bengs, O.Karthaus, H.Ringsdorff, C.Baehr, M.Ebert and J.H.Wendorff. *Liq.Cryst.* (1991) **10** 161.

[12] C.Destrade, Nguyen Huu Tinh, J.Malthète and J.Jacques. *Phys.Lett.* (1980) **79A** 189.

[13] S.Chandrasekhar, B.Sadashiva, K.A.Suresh, N.Madhusudana, S.Kumar, R.Shashidar and G.Venkatesh. *J.Phys.Paris.* (1979) **40** C3 120.

[14] A.M.Giroud-Godquin and P.M.Maitlis. *Angew.Chem.Int.Ed.Engl.* (1991) **30** 375.

[15] A.M.Giroud-Godquin and J.Billard. *Mol.Cryst.Liq.Cryst.* (1981) **66** 147.

[16] K.Ohta, H.Muroki, A.Takagi, K.I.Hatada, H.Ema, I.Yamamoto and K.Matsuzaki. *Mol.Cryst.Liq.Cryst.* (1986) **140** 131.

[17] A.C.Ribeiro, A.F.Martins and A.M.Giroud-Godquin. *Mol.Cryst.Liq.Cryst.Lett.* (1988) **5** 133.

[18] N.Boden, S.A.Corne and K.W.Jolley. *J.Phys.Chem.* (1987) **91** 4092.

[19] A.J.Leadbetter in *Thermotropic Liquid Crystals.* (G.W.Gray (ed.)), Wiley (1987).

[20] C.R.Safinya, K.S.Liang, W.A.Varady, N.A.Clark and G.Anderson. *Phys.Rev.Lett.* (1984) **53** 1172.

[21] C.Destrade, J.Malthète, Nguyen Huu Tinh and H.Gasparoux. *Phys.Lett.* (1980) **78A** 82.

[22] P.W.Atkins. *Physical Chemistry. 3rd Ed.* Oxford University Press (1986).

[23] G.H.Brown, J.W.Doane and V.D.Neff. *C.R.C: A Review of the Structure and Physical Properties of Liquid Crystals.* Butterworths (1971).

[24] A.Beguin, J.Billard, F.Bonamy, J.M.Bustine, P.Curelier, J.C.Dubois and P.Le Barny. *Mol.Cryst.Liq.Cryst.* (1984) **115** 1.

2. Techniques in computer simulation

2.1 Introduction

2.1.1 Why use computer simulation?

Before we discuss in detail the techniques of computer simulation, we should mention what we mean by computer simulation and our motivation in using it to study liquid crystals. The liquid-crystalline state, having characteristics of both the solid and liquid phases i.e. a combination of long range and short range order, is fairly complicated. Despite this, a great deal is known about the macroscopic properties of liquid crystals such as the structure of their mesophases and the transitions between them. Indeed, quite a lot is also known about the microscopic properties of liquid crystals and how subtle changes in molecular detail can have a profound effect on the macroscopic behaviour. There are also many theories, such as the molecular field and continuum theories[1], describing the liquid crystal mesophases, yet many features still remain to be discovered and understood. This is where computer simulations can help us.

By using the techniques of *Monte Carlo*[2] simulation in which we use random numbers to generate a sequence of molecular configurations in phase space, and *molecular dynamics*[3], where the newtonian equations of motion are solved for a limited number of particles, we can introduce our model of a liquid crystal. If we then run the simulation and observe the behaviour of the system, we can test the validity or otherwise of the initial model by comparing the results of the simulation with those obtained from real experiments. We can then refine and improve our models of how liquid crystals behave, in addition we can test various analytical theories and see how they might be improved.

Computer simulation also has several other advantages that make it attractive to use in studying liquid crystals. We can control the majority of conditions with great accuracy and observe behaviour under various extremes of temperature, pressure and external fields, that could not be readily achieved by the usual experimental methods. It also allows us to calculate structural and dynamic properties, such as the distribution and correlation functions, not easily obtainable in the laboratory, giving us additional information on the behaviour and structure of liquid crystals.

2.1.2 Intermolecular forces

We have previously indicated how we can use computer simulations by introducing our model of the intermolecular interactions. Well for liquid crystals, in fact for all systems, this is achieved by defining an intermolecular potential, an equation that describes the interaction between constituent molecules of the system as a function of the coordinates describing their positions. These interactions or forces between molecules can be conveniently divided into the attractive and repulsive components[14], and occur in all molecules, not just those which form liquid crystals.

The attractive forces between molecules are generally represented by the van der Waals or dispersion interactions between molecules and they usually vary as a function of distance as $1/r^6$. These forces act over several molecular lengths and hence are known as long range attractive forces. We can also build into our intermolecular potential more explicit attractive forces such as dipole-dipole, quadrupole and charge-charge interactions which are longer ranged.

The repulsive interactions between molecules occur when the molecules are squeezed close together causing electronic repulsions, these repulsions increase sharply, the closer the molecules approach each other. Producing a functional form for these repulsive interactions from first principles is extremely complicated, but again we can define the repulsive forces between molecules as a function of distance and this usually takes the form of $1/r^{12}$. These forces act as the molecules approach close together and hence are known as short range repulsive forces. We have just given an overview of the forces acting between molecules but we need a way of incorporating them into the simulation. This is achieved by the use of the *pair potential.*

2.1.3 Pair potentials

For a system of N molecules, the potential energy may be divided into terms depending on the coordinates of individual molecules, pairs of molecules, triplets etc. and as such can be written as

$$U = \sum_i U(\mathbf{r}_i) + \sum_i \sum_{j>i} U_2(\mathbf{r}_i, \mathbf{r}_j) + \sum_i \sum_{j>i} \sum_{k>j>i} U_3(\mathbf{r}_i, \mathbf{r}_j, \mathbf{r}_k) + \ldots \qquad (2.1)$$

though in the case of liquid crystals we must build in anisotropic forces as well. Care must also be taken to sum over all distinct pairs i and j without counting any pair twice. The first term represents the effect of an external field, while the remainder define the intermolecular interactions. The second term $U_2(\mathbf{r}_i, \mathbf{r}_j)$, the pair potential, is the most important; it represents the interaction between two molecules and contributes the most to the total energy. Higher terms also contribute but as they are very computationally expensive to calculate, they are often neglected. As we normally use only the pair term in a simulation this might not seem to be an accurate reflection of the various interactions, so we overcome this in part by defining the pair term as an *effective* pair potential in that it represents all the many body interactions, albeit in an approximate manner. This does mean that the effective pair potential will depend on the temperature and density of the system, where as the real pair potential does not. We have previously discussed representing repulsive and attractive forces in various functional forms, and as such, can be used on their own as pair potentials. One such potential is the hard sphere potential, where

$$U_{\mathrm{HS}} = 0 \quad (r \geq \sigma), \tag{2.2a}$$

$$U_{\mathrm{HS}} = \infty \quad (r < \sigma). \tag{2.2b}$$

Here, r is the separation between the interacting molecules and σ is a range parameter known as the contact diameter, the distance at which two particles touch. Another approximation used is the soft sphere potential defined as:

$$U_{\mathrm{SS}} = \varepsilon(\sigma/r)^{\nu}, \tag{2.3}$$

where ν is a parameter, often chosen to be an integer and as ν is increased, the potential becomes "harder", tending to the shape of the hard sphere potential. An extension of the hard sphere potential that contains attractive forces is the square well potential defined as

$$\infty \quad (r < \sigma_1), \tag{2.4a}$$

$$U_{\mathrm{SW}} = -\varepsilon \quad (\sigma_1 \leq r < \sigma_2), \tag{2.4b}$$

$$0 \quad (\sigma_2 \leq r), \tag{2.4c}$$

while one of the most commonly used pair potentials that incorporates attractive forces is the Lennard-Jones 12-6 potential and takes the form:

$$U(r) = 4\varepsilon[(\sigma/r)^{12} - (\sigma/r)^{6}], \tag{2.5}$$

with the repulsive part represented by the $(\sigma/r)^{12}$ term and the attractive part by the $(\sigma/r)^{6}$ term. At separations less than the molecular diameter σ, the potential is repulsive with a steep wall, becoming increasingly steeper the closer the molecules approach. As the molecules move further away from each other, the attractive forces dominate. At very large separations though, the molecules do not interact between each other thus the energy and hence the potential tends to zero. To make these potentials model the behaviour of liquid crystals, an orientational dependence needs to be built in and we shall describe how this is achieved and the variety of potentials that are actually used to simulate liquid crystals in §2.5.

2.1.4 Ensembles

The aim of a computer simulation is to calculate the thermodynamic, structural and dynamic properties of a system, the macroscopic behaviour, from the microscopic behaviour via the pair potential. This conversion is achieved by statistical mechanics[15] and the use of *ensembles*. A basic postulate of statistical mechanics is that the time average of a mechanical property in a system is equal to an average over an imaginary array of replicas of the system so instead of following one system over time, we can take an average picture of a collection of systems, the so-called ensemble. As the original system is defined by fixed thermodynamic parameters, we can fix certain properties of the ensemble, allowing us to perform computer simulations under varying conditions. There are a variety of ensembles[16] that are currently used.

The *microcanonical* or constant *NVE* ensemble, is most commonly used in molecular dynamics simulations (see §2.3). The total energy E, and volume V, of the system are fixed but the temperature and pressure vary. This means, especially in our system of Gay-Berne particles, a step is needed in which we scale the velocity of each particle so as to keep the temperature at the desired value. The *canonical* or constant *NVT* ensemble is mainly used in Monte Carlo simulation, where the temperature of the system is fixed. As with the microcanonical system, the pressure is free to fluctuate but as most experimental data is obtained at constant pressure, these two ensembles are generally considered unsuitable for some simulations.

Thus the *isothermal-isobaric* or constant *NPT* ensemble becomes particularly useful as we can now vary both the size and shape of the simulation box. This has the advantage in that you should not be able to observe two phases coexisting, an important feature when studying a series of phase transitions. In the *grand canonical* or constant $V\mu T$ ensemble, the chemical potential μ, is fixed, while the number of particles can fluctuate. Its great advantage is that the free energy of the system can be easily calculated, with its main use being the study of monolayer adsorption near a surface. In our discussion of ensembles, we should perhaps mention the *Gibbs* Monte Carlo technique[7] which is used to simulate fluid phase equilibria. It has two simulation boxes which consist of two coexisting phases in which the chemical potential is equal but the volume and number of particles can change.

2.1.5 Small systems

There is one major obstacle to be overcome with computer simulation and that is the problem of the system size. The number of molecules with which simulations are carried out, typically ranging from a hundred to several thousand, are well short of the numbers present in real systems. This limitation is due to the finite speed and limited storage and memory capacity of even today's computers. As we are interested in the bulk properties of liquid crystals, a legitimate question[8] is, can we compare the properties of the few hundred particles in a computer simulation with real systems composed of 10^{23} particles? Well, fortunately, the bulk properties of a system can be obtained from relatively few molecules provided the range of the intermolecular potential is relatively short and periodic boundary conditions are used to eliminate the effects of any free surfaces.

As an example of periodic boundary conditions, let us take a square simulation box in two dimensions which is surrounded by exact replicas of itself, (see figure 2.1). Each replica box is in turn surrounded by similar images to form an infinite lattice containing no surfaces. During the simulation, when a particle moves in the original box, all the images of the particle necessarily move in their corresponding boxes. If a particle leaves the original box, an image of it appears on the opposite side of the box, from a neighbouring box and this is illustrated by the particle *D,* thus a constant density is maintained in the simulation box.

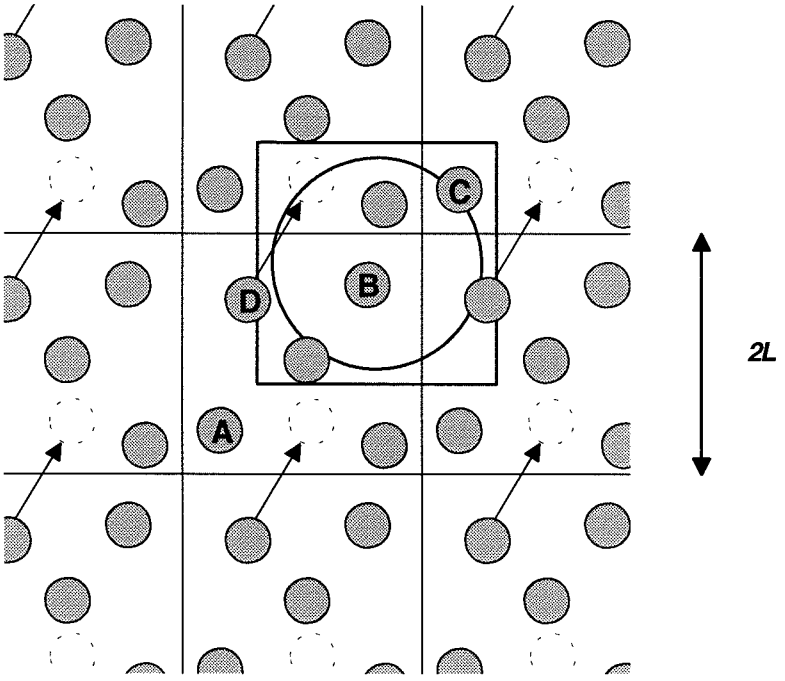

Figure 2.1: *A two dimensional periodic system with minimum image convention (square) and potential cut-off (circle).*

This method of periodic boundary conditions is not perfect for it inherently imposes a periodicity of half the box size, L, on the system but it is successful in allowing us to simulate systems using a small number of particles by removing the free surface. The minimum image convention needs to be used when employing periodic boundary conditions. This constrains each particle in the original box, to interact with every other particle or its periodic image only once, that is, a single particle interacts with the closest image of the other N–1 particles. This is equivalent to constructing a box of the same dimensions around one particle, and allowing it to interact only with the particles in the new box. Thus for particle B, instead of interacting with particle A in its own box, it will interact with the closest periodic image of A, that is particle C.

Also, as the largest contribution to the potential energy comes from neighbours close to the particle of interest, we apply a spherical cut-off, r_c. This means that if a particle is more than a pre-set distance away from the particle of interest, such as particle A, the pair potential for the two particles is set equal to zero. Though the number of such contributions increases with the separation, it is pointless to calculate essentially zero contributions to

$U(r)$ and so the cut-off is applied in order to minimise the time a simulation takes. This will mean that the calculated potential energy will be incorrect, thus r_c should be large enough to minimise any errors, though by applying long range corrections[6] we can estimate this lost energy of interaction. A particular problem encountered in molecular dynamics is that we need to stop the potential from being discontinuous at the cut-off point as this avoids problems in calculating the derivatives of the force. What we do is to "ramp" the potential from $0.95r_c$ to $1.0r_c$, so that the potential is truncated at a $U(r)$ of 0[9], (see figure 2.2).

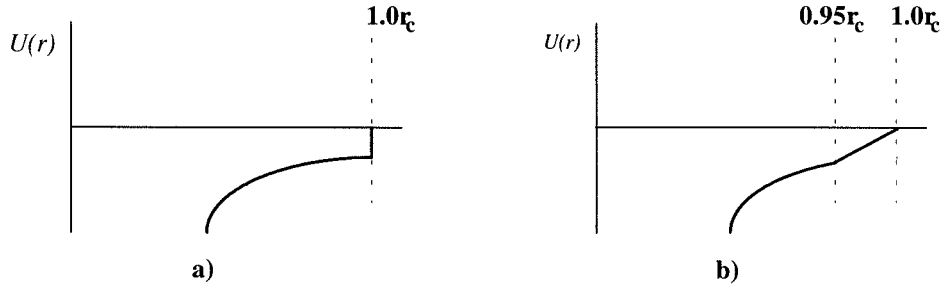

Figure 2.2: *a) A straight potential cut-off applied to an intermolecular potential. b) By "ramping" the potential from 0.95 r_c to 1.0 r_c, we can avoid any discontinuity in the potential.*

But this still leaves us with the question, can we compare a small, infinitely, periodic system with a macroscopic one? This depends of the range of the intermolecular potential used and the type of phenomenon under investigation. If the potential is short ranged then a box of several molecular lengths should be long enough so that the system does not "sense" the symmetry imposed by periodic boundary conditions. If the potential is long ranged such as a charge-charge interaction, then there will be a substantial interaction between a particle and its own periodic images, thus in this case other techniques for handling long ranged forces are implemented[6].

2.2 Monte Carlo simulations

The Monte Carlo technique gained its name from the use of random numbers, and was devised in 1953 by Metropolis *et al.*[2] to evaluate statistical averages. If we have a system of known potential energy

$$U_N = \frac{1}{2} \sum_{i \neq j} U(\mathbf{r}_i, \Omega_i, \mathbf{r}_j, \Omega_j), \tag{2.6}$$

where $\mathbf{r}_i$ represents the position and Ω_i the orientation of a molecule i, then we can calculate any time independent property A for a certain configuration j, as an average $\langle A \rangle$. This can be written for the NVT ensemble as

$$\langle A \rangle = \frac{\int A exp(\beta U_N) \mathrm{d}\{(\mathbf{r}, \Omega)^N\}}{\int exp(\beta U_N) \mathrm{d}\{(\mathbf{r}, \Omega)\}}, \tag{2.7a}$$

which is approximated by

$$\langle A \rangle \approx \frac{\sum A exp(\beta U_N)}{\sum exp(\beta U_N)}, \tag{2.7b}$$

with the value of A for this configuration being $A^{(j)}$. If we repeat this process M times, then the average $\langle A \rangle$ in equation (2.7b) would now be

$$\langle A \rangle = \frac{1}{M} \sum_{j=1}^{M} A^{(j)}(i\Delta m), \tag{2.8}$$

with M being large enough to reduce any significant statistical errors in $\langle A \rangle$. Providing the system is ergodic, we can replace the average in equation (2.8) with an ensemble average,

$$\langle A \rangle_{\mathrm{ens}} = \frac{1}{M} \sum_{j=1}^{M} A(\Gamma_j) \rho_{\mathrm{ens}}(\Gamma_j), \tag{2.9}$$

where our collection of systems of points in phase space are distributed with a probability $\rho_{\mathrm{ens}}(\Gamma)$, with the property A of the system having a value Γ at that instance. Thus the aim of a Monte Carlo simulation is to generate a trajectory in phase space which samples from a chosen statistical ensemble defined by a set of fixed parameters. One vital part of the Monte Carlo technique that we should briefly mention is importance sampling[9] in which we concentrate on performing the simulation in regions of phase space that make important contributions to the integral in equation (2.7a). Sampling from this non-uniform distribution, allows us to simulate more quickly and efficiently. The main steps in a Monte Carlo simulation include:

i) The initial configuration: The first step is to set up a starting configuration with N particles contained in a cubic box or similar boundary conditions. In theory we could start from any state as the ergodic hypothesis means that any state can be reached from any other, given infinite time. But as we need to reach an equilibrium state within a finite time,

we need choose a reasonable starting configuration. For example, it is generally considered difficult to generate a crystal from an isotropic fluid via one state point, so in practice a number of intermediate state points are simulated, each run using the final configuration of the previous run as its starting point. Usually in the initial run of a simulation, especially if a new system is being studied, the position of each particle is associated with a lattice. Historically an α-*f.c.c.* lattice has been used for liquid crystal simulations, the initial orientations, being chosen either at random, or selected from a gaussian distribution.

Especially with simulations of liquid crystals, there is the problem of *hysteresis*, that is, the system remembers the order from a previous simulation i.e. the starting configuration. This will impose various degrees of order that would otherwise not be present in the system, this being particularly true when starting from a lattice configuration. This would be a big problem in liquid crystal simulations where we are trying to form liquid-crystalline phases spontaneously. So we try to minimise this effect by heating the starting crystal structure into the isotropic fluid, so hopefully destroying all residual order within the system. This process can be monitored to see if it is successful by calculating properties of the system such as the translational order parameter[6]. Once we are confident that all order has been removed, we would be ready to proceed with the simulation by cooling the system. Once an initial configuration has been generated, be it either a lattice or from a previous simulation, the energy U_{old} of the configuration is calculated:

$$U_{old} = \sum_{j=1}^{N} U\left(r_{ij}^{old}\right). \tag{2.10}$$

ii) Moving the molecules: Once the initial configuration has been set up and the energy calculated, the particles are then ready to be moved one at a time. The first particle, either picked at random or sequentially, is given a uniform, random, translational displacement according to the equation

$$r_x^{new} = r_x^{old} + (2\xi - 1)\delta r_{\max}. \tag{2.11}$$

This is repeated along each of its coordinate axes with $\delta r_{\max}$ being the maximum displacement that a particle is allowed and ξ a random number. If $\delta r_{\max}$ is too large then most of the attempted moves are rejected and the phase space is explored very slowly. If $\delta r_{\max}$ is too small then most moves are accepted but the particles never move any

significant distance. The maximum displacement is usually adjusted during the simulation so that half the moves are accepted and half the moves are rejected. The rotational motion of the particles is handled in a similar fashion to the translational motion. The orientation of the particles u, can be described in terms of the Euler angles, and the new component is calculated by selecting a laboratory axis at random, in this case the x axis, and rotating the particle about an angle ϕ so that:

$$u_x^{new} = u_x^{old} + (2\xi - 1)\delta\phi_{max}, \tag{2.12}$$

where $\delta\phi_{max}$ is the maximum displacement of the Euler angle and ξ is a random number.

iii) Calculating the change in energy: Once the first particle has been moved, the change in energy δU between the old and new configurations is calculated by comparing the energy of the first particle, i, with all other particles before and after the move, so that

$$\delta U = U_{new} - U_{old} = \left(\sum_{j=1}^{N} U(\mathbf{r}_{ij}^{new}) - \sum_{j=1}^{N} U(\mathbf{r}_{ij}^{old}) \right). \tag{2.13}$$

iv) Accepting or rejecting the move: Once the particle move has been attempted and the change in energy δU calculated, it must be decided whether to accept or reject the move as being significant to the system. If the move is downhill in energy, $\delta U \leq 0$, then the move and the new configuration are accepted and the new energy of the configuration becomes $U_{old} + \delta U$. If the move is uphill in energy, $\delta U > 0$, then the value $\exp(-\beta\delta U)$ is compared with a random number ξ, uniformly distributed between 0 and 1. If the random number is less than $\exp(-\beta\delta U)$ then the move is accepted. If a move is rejected the particle is returned to its original position and the old configuration retained and counted again in the averaging. This strategy is performed to allow the simulation to explore other regions of phase space with possible potential minima, instead of locating and residing within the first potential well found.

v) Equilibration: Once the process of selecting and moving a particle, calculating the change in energy δU and accepting or rejecting the move, has been performed N times, one Monte Carlo cycle has been completed. The simulation is then run for many thousands of cycles until properties such as the order parameter and energy are constant within the

desired limits. Once the system is regarded as being in equilibrium, the various properties of interest can then be calculated. As we have performed only molecular dynamics simulations in this thesis, we shall not go into any further detail about Monte Carlo techniques[10], but instead concentrate on molecular dynamics.

2.3 Molecular dynamics simulations

It was first recognised that Newton's equations of motion could be solved numerically for many interacting particles by Alder and Wainwright in 1957[11]. The system is treated by setting up the newtonian equations of motion, which are coupled with the interaction potential between the particles via the forces and torques. This set of equations is then solved numerically to give the positions, orientations and velocities of all particles as a function of time. We have shown that in Monte Carlo simulations we calculate thermodynamic observables by taking an ensemble average, but in a molecular dynamics simulation, the system evolves in a real time sense and so we obtain physical properties by taking a time average. Even so, we do employ the use of ensembles as a means of defining the thermodynamic state of the system we are to study. If a property A at a particular point Γ, in phase space has a value $A(\Gamma)$ and the system evolves in time t, the macroscopic property $\langle A \rangle$ can be thought of as a time average given by

$$\langle A \rangle = \langle A(\Gamma(t)) \rangle_{\text{time}} = \lim_{t \to \infty} \frac{1}{t} \int_0^t A(\Gamma(t))\, \mathrm{d}t. \tag{2.14}$$

This equation can be rewritten to average over a long finite time t consisting of a number n of time steps of length $\delta t = t/n$ so that

$$\langle A \rangle = \langle A \rangle_{\text{time}} = \frac{1}{n} \sum_{n=1}^{n} A(\Gamma(n)). \tag{2.15}$$

i) The initial configuration: The same criteria used to generate an initial configuration for a Monte Carlo simulation are used in a molecular dynamics simulation but an extra process is needed to define the initial translational and rotational velocities of the particles. They may all be assigned a value of zero or selected from a Maxwell-Boltzmann distribution which matches the initial starting temperature. Additionally, the total translational momentum, which is conserved throughout the simulation, and the angular momentum are set to zero to stop the box from moving in space.

ii) Calculating the force: Once the starting configuration has been set up, the forces and torques are calculated, using a double loop over all distinct pairs of molecules with the minimum image convention and a spherical cut-off being employed. To do this we need a potential function with which to define the interaction between the constituent particles. The intermolecular potential can have a multitude of forms, common ones being the hard sphere potential and the Lennard-Jones 12-6 potential, (see §2.1.3). For liquid crystal simulations, an orientational dependence is built into the potential, the forms of which are discussed in section §2.5. In this Thesis, we will use continuous potentials, so we shall discuss how the system is treated with this type of interaction in mind, as different methods are used when handling discontinuous potentials as for example with hard particles[112].

iii) Moving the molecules: Once the forces and torques have been calculated using the appropriate potential, the molecules can be advanced forward one time step by integrating the newtonian equations of motion. The most fundamental form of these is the lagrangian equation of motion,

$$\frac{\mathrm{d}}{\mathrm{dt}}(\partial L/\partial \dot{\mathrm{q}}_k) - (\partial L/\partial \mathrm{q}_k) = 0, \tag{2.16}$$

where q_k represents the coordinates of the particles and L the difference between the kinetic and potential energies. If we express q_k in terms of cartesian coordinates, U the potential energy, in terms of the sum of the pair interaction energies and K the kinetic energy, as the sum of the momenta, then we obtain from equation (2.16),

$$m\mathbf{a}_i = \mathbf{F}, \tag{2.17}$$

where $\mathbf{F} = -\partial U/\partial \mathbf{r}_i$ is the total force acting on the particle of mass m, with centre of mass $\mathbf{r}_i$ and acceleration $\mathbf{a}_i$. An equivalent set of equations can also be constructed for the rotational motion and assuming axial symmetry, can be written as

$$I\dot{\omega}_i = \mathbf{T}, \tag{2.18}$$

where $\mathbf{T}$ is the torque, I is the moment of inertia and $\dot{\omega}$ the angular acceleration of each particle. For a rigid body, the torque is the sum of the forces acting on each site in the particle, but we use the Gay-Berne potential, a single site potential, in this Thesis. Thus we can define the torque as equivalent to a force acting on a point at unit distance from the centre of mass, in a direction perpendicular to the symmetry axis[113]. This force is the

derivative of the potential at these coordinates, where the centre of mass is taken as the origin, and is given by,

$$\mathbf{E} = \begin{pmatrix} (\partial U/\partial \hat{u}_x) \\ (\partial U/\partial \hat{u}_y) \\ (\partial U/\partial \hat{u}_z) \end{pmatrix}, \tag{2.19}$$

where $\hat{u}_i$ represents the orientation of the particle. The torque is now defined as

$$\mathbf{T} = \hat{\mathbf{u}} \times \mathbf{E}. \tag{2.20}$$

Once these equations of motion have been set up, the integration method used to solve them must be chosen. The object of any integration procedure is to determine the phase point Γ_{n+1} representing the state of the system at time $t_{n+1} = t_n + \Delta t$. The state point Γ_{n+1} is calculated by means of a power series in Δt and for continuous potentials, we can use a variety of finite difference methods. The procedure for choosing the integration algorithm can be found in any general reference[6,9,14] and, amongst other factors, will depend on the type of system being simulated and the computer resources available. The algorithm used in our simulations, being present in the original program, is that developed by Verlet[15]. The Verlet method is computationally cheap in that only one evaluation of the forces is performed, but it does have some disadvantages in that the calculation of the velocities is prone to errors and it is not self-starting in that we need to generate the first few points in phase space before the main routine takes over. The Verlet algorithm is based on a Taylor series expansion of the positions at time $t + \delta t$ and $t - \delta t$, where δt is the time step, such that for an atomic system:

$$\mathbf{r}(t+\delta t) = \mathbf{r}(t) + \mathbf{v}(t)\delta t + \tfrac{1}{2}\delta t^2 \mathbf{a}(t).....,\tag{2.21}$$

$$\mathbf{r}(t-\delta t) = \mathbf{r}(t) - \mathbf{v}(t)\delta t + \tfrac{1}{2}\delta t^2 \mathbf{a}(t).....,\tag{2.22}$$

where **r** are the coordinates, **v** is the velocity and **a** the acceleration. Addition of these two equations produces the algorithm for the translational coordinates,

$$\mathbf{r}(t+\delta t) = 2\mathbf{r}(t) - \mathbf{r}(t-\delta t) + \delta t^2 \mathbf{a}(t). \tag{2.23}$$

The algorithm for the rotational coordinates is slightly non-standard but is a Verlet-type algorithm as used by Luckhurst *et al.*[13] in their molecular dynamics simulations of Gay-Berne mesogens.

Equation (2.23) can be written for the angular coordinates so that,

$$\mathbf{u}(t+\delta t)= 2\hat{\mathbf{u}}(t) - \hat{\mathbf{u}}(t+\delta t)+ \delta t^2\dot{\omega}(t), \tag{2.24}$$

where $\mathbf{u}$ is the vector defining the orientation of a particle and $\dot{\omega}$ is the angular acceleration. But to constrain the vector $\mathbf{u}(t + \delta t)$ to have unit length, a corrective force $\mathbf{f}(t)$ is applied, parallel to the symmetry axis of the particle, so at time t

$$\mathbf{f}(t) = \lambda\hat{\mathbf{u}}(t), \tag{2.25}$$

where λ is a scalar quantity. So the corrected orientation at time $t + \delta t$ is

$$\hat{\mathbf{u}}(t+\delta t) = \mathbf{u}(t+\delta t) + \lambda\hat{\mathbf{u}}(t), \tag{2.26}$$

where

$$\lambda = -\hat{\mathbf{u}}(t+\delta t).\hat{\mathbf{u}}(t) \pm \{[\mathbf{u}(t+\delta t).\hat{\mathbf{u}}(t)]^2 - [\mathbf{u}(t+\delta t).\mathbf{u}(t+\delta t)] + 1\}^{1/2}. \tag{2.27}$$

The positive root is taken to minimise the corrective force. Similar to the maximum displacement δr_{max}, in the Monte Carlo method, the time step δt, controls how well the phase space of the system is explored. Too small a time step and the particles never move any significant distance. Too large a time step and the solutions to the equations of motion become unstable i.e. the energy is not conserved. The procedure to obtain the optimum δt is discussed in reference[6]. The velocities do not appear directly in the equations but can be calculated from

$$\mathbf{v}(t+\delta t) = \frac{1}{2\delta t}[\mathbf{r}(t+\delta t) - \mathbf{r}(t-\delta t)], \tag{2.28}$$

with a similar analogue for the rotational velocities:

$$\dot{\mathbf{u}}(t+\delta t) = \frac{1}{2\delta t}[\hat{\mathbf{u}}(t+\delta t) - \hat{\mathbf{u}}(t-\delta t)]. \tag{2.29}$$

iv) Equilibration: The main problem, especially with liquid-crystalline systems, is that near a phase transition, large fluctuations in the thermodynamic and structural properties can occur, so considerable periods of time are needed for the system to reach an equilibration state. Before a new state point is reached in the simulation, the system is run at a certain temperature until it has lost all memory of its starting configuration. This is called the equilibration period. This part of the simulation is especially important in a molecular dynamics simulation as the temperature is not a constant of motion and so will drift from its initial value. When this happens the integration must be periodically halted, usually

every time step, though in our simulations we wait until the temperature has reached a certain tolerance level. Then the translational and rotational velocities can be multiplied by a scaling factor $(T/T')^{½}$ to restore the temperature to its desired value. The components of this scaling factor are T, the desired temperature and T', the actual value as calculated from the sum of the translational and orientational kinetic energies of the particles. Once the system has reached equilibrium at a certain configuration, that is the temperature drift is replaced by a fluctuation about a desired value T, temperature scaling of the velocities is ceased and the production period begins in which the various properties of interest are calculated.

2.4 Calculation of thermodynamic, structural and dynamic properties

Once a system has been equilibrated at a certain state point, the production period begins, where in a molecular dynamics simulation, the temperature scaling has been turned off, and the thermodynamic, structural and dynamic properties of interest are calculated. For the essential properties, such as the temperature, internal energy and orientational order parameters, it is usual to calculate them during the course of the simulation, at each time step and then average them according to the procedure described in equation (2.15). Other properties such as time correlation functions are more usually calculated after the simulation has finished, from a tape file that contains the positions, orientations and velocities, both translational and orientational, of the particles stored at, say, every 5 or 10 time steps.

2.4.1 Thermodynamic properties

Temperature: In a molecular dynamics simulation, temperature is not a constant of the motion, and so it has to be calculated from the translational and rotational components, obtained from the equipartition principle,

$$\frac{1}{2}\left\langle \sum m_i |\mathbf{v}_i|^2 \right\rangle = \frac{1}{2} N k_B N_T T_T \tag{2.30}$$

and

$$\frac{1}{2}\left\langle \sum I_i |\boldsymbol{\omega}_i|^2 \right\rangle = \frac{1}{2} N k_B N_R T_R, \tag{2.31}$$

where N_T and N_R are the number of translational and rotational degrees of freedom respectively. In our simulations $N_T = 3$, corresponding to three dimensional movement while $N_R = 2$ as we assume each particle to be uniaxial in symmetry. The average temperature T can then be calculated from,

$$T = \frac{N_T T_T + N_R T_R}{N_T + N_R}. \tag{2.32}$$

Internal energy: The average total potential energy per particle $\langle U \rangle$ is calculated from the sum of just the pairwise interactions such that,

$$\langle U \rangle = \frac{1}{N} \sum_{1 \le i \le j \le N} U(\mathbf{r}_i, \Omega_i, \mathbf{r}_j, \Omega_j), \tag{2.33}$$

where $U(\mathbf{r}_i, \Omega_i, \mathbf{r}_j, \Omega_j)$, the effective pair potential, is summed over all time steps.

Heat capacity: At constant volume, the heat capacity C_V is defined as

$$C_V = (\partial U/\partial T)_V. \tag{2.34}$$

Calculation of this could involve using a cubic spline fit to values of $\langle U \rangle$, the average internal energy, over a range of temperatures, and performing a numerical differentiation with respect to the temperature. An alternative way to calculate the heat capacity is from fluctuations in the potential or kinetic components of the energy. Thus,

$$\langle \delta K^2 \rangle_{NVE} = (N_F/2) N k_B^2 T^2 (1 - 3N k_B / 2C_V), \tag{2.35}$$

where K is the total kinetic energy, N_F the number of degrees of freedom, which takes the value of 5 for our system and

$$\langle \delta K^2 \rangle_{NVE} = \langle K^2 \rangle - \langle K \rangle^2. \tag{2.36}$$

However, as this property is calculated from fluctuations, we would expect it to be affected by larger errors than values for the heat capacity calculated from equation (2.34) especially near phase transitions. Against this, the heat capacity can be obtained from this method using a single simulation state points whereas for $\partial U/\partial T$, at least three simulation state points are needed.

2.4.2 Orientational properties

Orientational order parameters: The calculation of these properties are particularly important in the simulations, as it gives us a quantitative measure of the orientational order in the system, which is the essential feature of liquid crystals. For a uniaxial phase in which the director is known, the second rank order parameter $\langle P_2 \rangle$ at any one time step is,

$$\langle P_2 \rangle = \frac{1}{N} \sum_{i=1}^{N} (3\cos^2\beta_i - 1)/2, \tag{2.37}$$

where β is the angle between the symmetry axis of the particle and the director **n**. However in our simulations, the director orientation is not known, so the order parameter is obtained by maximising the expression

$$\langle P_2 \rangle = \frac{1}{N} \sum_{i=1}^{N} P_2(\hat{\mathbf{u}}_i.\hat{\mathbf{n}}), \tag{2.38}$$

with respect to the unit vector $\hat{\mathbf{n}}$ which renders $\langle P_2 \rangle$ a maximum. $\hat{\mathbf{u}}$ defines the orientation of the i^{th} particle in the laboratory frame. Equation (2.38) can be rewritten as

$$\langle P_2 \rangle = \frac{3}{2} \langle \hat{\mathbf{n}}.\mathbf{Q}.\hat{\mathbf{n}} \rangle, \tag{2.39}$$

where the tensor **Q** is

$$\mathbf{Q} = \frac{1}{N} \sum_{i=1}^{N} \{ \hat{\mathbf{u}}_i \hat{\mathbf{u}}_i - \frac{\mathbf{I}}{3} \}. \tag{2.40}$$

After diagonalising **Q** and averaging the elements after each time step, the eigenvalues of the ordering matrix are, in decreasing size, λ_+, λ_0 and λ_-, with the order parameter being obtained from the largest positive eigenvalue, λ_+, so that

$$\langle P_2 \rangle = (3/2)\lambda_+, \tag{2.41}$$

and the corresponding eigenvector being the director orientation. If **n** is parallel to the z axis of the simulation box, **Q** in its diagonalised form is

$$\begin{pmatrix} -(1/3)\langle P_2 \rangle + \varepsilon & & \\ & -(1/3)\langle P_2 \rangle - \varepsilon & \\ & & (2/3)\langle P_2 \rangle \end{pmatrix}, \tag{2.42}$$

where ε is a measure of the phase biaxiality. Thus in a uniaxial phase, ε is zero, but the small system size in the simulation means it deviates from zero. The use of λ_+ gives a good

estimate of $\langle P_2 \rangle$ in the nematic phase, but leads to an order parameter of $1/\sqrt{N}$ in the isotropic phase, instead of zero, as we are always averaging a positive quantity. Eppenga and Frenkel[116] recommend that in certain applications it may be preferable to use the middle eigenvalue λ_0. In the nematic phase, $\lambda_0 \approx \lambda_- = -1/2\lambda_+$, resulting from **Q** being traceless, thus the order parameter is equal to $-2\lambda_0$. In the nematic phase this would make very little difference, however in the isotropic phase, $\langle P_2 \rangle$ would be closer to zero, as we are averaging λ_0 which can change from positive to negative, having an associated error of $1/N$. An alternative route to the order parameter is the pair orientational correlation coefficient $G_2(r)$, the use of which will be discussed later.

We can also calculate the fourth rank orientational order parameter $\langle P_4 \rangle$, a quantity which is difficult to measure using experimental methods, though the use of polarised Raman scattering has provided a route to obtaining some experimental values[117]. $\langle P_4 \rangle$ is the average of the fourth rank Legendre polynomial and is defined as

$$\langle P_4 \rangle = \frac{1}{8}\langle 35\cos^4\beta - 30\cos^2\beta + 3 \rangle. \tag{2.43}$$

This calculation is possible in our simulation as we have already calculated the director orientation and hence can quite easily find β, the angle between the symmetry axis of each particle and the director.

Singlet orientational distribution function: The orientational order of an ensemble of molecules can be specified by the distribution function $P(\mathbf{r}, \Omega)$ which gives the probability of finding a molecule at a particular position **r** with a particular orientation Ω. For the nematic phase,

$$P(\mathbf{r}, \Omega) = \rho f(\Omega), \tag{2.44}$$

where ρ is the number density and $f(\Omega)$ is the orientational distribution function with Ω being the set of angles α, β and γ, the molecule makes with the laboratory frame. In a uniaxial phase such as the nematic phase the distribution depends on just β, so the particles have their long axes at an angle between β and $\beta + d\cos\beta$, with respect to the director. We can expand $f(\beta)$ in terms of Legendre polynomials, and because $\mathbf{n} \equiv -\mathbf{n}$, it follows that $f(\pi$

$-\beta) = f(\beta)$ as $\cos(\pi - \beta) = \cos(\beta)$, thus this implies that only even terms can occur, so $f(\beta)$ becomes,

$$f(\beta) = \sum_{L=0\ \&\ \text{even}}^{\infty} \frac{1}{2}(2L+1) f_L P_L(\cos\beta). \tag{2.45}$$

We can evaluate the expansion coefficients f_L, from the orthogonality of the Legendre polynomials, so that the first three coefficients are

$$f_0 \equiv \langle P_0(\cos\beta)\rangle = 1, \tag{2.46}$$

$$f_2 \equiv \langle P_2(\cos\beta)\rangle = \langle 3\cos^2\beta - 1\rangle/2, \tag{2.47}$$

$$f_4 \equiv \langle P_4(\cos\beta)\rangle = \langle 35\cos^4\beta - 30\cos^2\beta + 31\rangle/8, \tag{2.48}$$

where f_2 can be recognised as the order parameter introduced in equation (1.1) and as that calculated in the simulation, and f_4 the fourth rank order parameter $\langle P_4\rangle$ as defined in equation (2.43). Substituting equations (2.46) - (2.48) into (2.45) gives $f(\beta)$ as

$$f(\beta) = \frac{1}{2}(1 + 5\langle P_2(\cos\beta)\rangle^2 + 9\langle P_4(\cos\beta)\rangle^2 .....). \tag{2.49}$$

To obtain the singlet orientational distribution function in the simulation, we calculate the angle between the symmetry axis of the particle and the director. We then sort the angles into histograms bins over the range $\cos\beta = 0$ - 1, normalising with the number of particles present in each bin and the number of configurations used.

2.4.3 Structural properties

The radial distribution function: The radial distribution function $g(r)$, is a widely used quantity with which to investigate the translational order within a system; it can be defined as

$$g(r) = \frac{N(N-1)}{\rho^2 Z_N} \int \exp(-\beta U(\mathbf{r}_1, \mathbf{r}_2 ..... \mathbf{r}_N)) d\mathbf{r}_3 .... d\mathbf{r}_N, \tag{2.50}$$

where ρ is the number density and Z_N is the configurational partition function. It gives the probability of finding a particle at a distance r from the origin of another particle, relative to the probability in an ideal gas. At large separations, the positions of any two particles will be largely uncorrelated, so the probability will tend to the density ρ of the fluid, but as $g(r)$ is normalised by ρ, $g(r)$ will tend to the value of one. For particles with a hard

repulsive core there is a zero probability of finding another particle closer than a minimum distance σ, the molecular diameter, so $g(r)$ takes the value of 0 at separations less than σ. The position of the peaks can be used to identify shells of neighbouring particles and the area under each peak is the number of neighbouring particles, thus helping to determine the structure of the phase under investigation. The radial distribution function in the simulation is calculated by constructing a histogram $n_{simulation}$, of all the minimum image particle separations, where each bin has a width δr and extends from $r - \delta r/2$ to $r + \delta r/2$. To obtain $g(r)$, each interval in the histogram is then divided by the number of particles in an ideal gas at the same density n_{ideal}, which is given by:

$$n_{ideal} = \frac{4\pi\rho}{3}\left[\left(r+\frac{\delta r}{2}\right)^3 - \left(r-\frac{\delta r}{2}\right)^3\right], \tag{2.51a}$$

$$= \frac{4\pi\rho}{3}\left[3r^2\delta r + \frac{\delta r^3}{4}\right]. \tag{2.51b}$$

As δr is small, the term involving δr^3 is usually neglected. The $g(r)$ at a certain separation can now be given by

$$g(r) = \frac{n_{simulation}}{n_{ideal}}. \tag{2.52}$$

The orientational pair correlation coefficient: The pair distribution function $g(r, \Omega)$ is dependent on the orientation as well as the separation between two particles and is easy to determine via the simulation but difficult to represent graphically though it can be expanded in terms of Legendre polynomials. Thus for one set orientation Ω, it can be defined as

$$g(r,\Omega) = \frac{1}{g(r)} \sum (2L + 1/64\pi^4) G_L(r) P_L(\cos\beta), \tag{2.53}$$

where β is now the angle between the symmetry axis of the two particles and not between one particle and the director, while $g(r)$ is the radial distribution function defined in the previous section. The coefficients $G_L(r)$, are averages of the Legendre functions,

$$G_L(r) = \langle P_L(\cos\beta(r))\rangle. \tag{2.54}$$

$G_0(r)$ is the radial distribution function, and $G_2(r)$ is the second rank orientational pair correlation coefficient.

These can be easily calculated during the course of the simulation for each time step by,

$$G_2(r) = \frac{1}{N} \sum_{i=1}^{N} \sum_{i \neq j} P_2(\cos \beta_{ij}(r)). \tag{2.55}$$

At large separations, i.e. the limit $r \rightarrow \infty$, angular correlations between particles are lost and so,

$$G_2(r) = \langle P_2(\cos \beta) \rangle^2. \tag{2.56}$$

Thus the limiting value of $G_2(r)$ provides an alternative method for the calculation of the order parameter $\langle P_2 \rangle$. For small separations, $G_2(r)$ takes a value of approximately one, even in the isotropic phase. This behaviour can be explained as follows: as the separation between the particles approaches the smallest dimension of a particle, the particles must be essentially parallel to each other, i.e. the orientational vectors are parallel, and hence $\langle P_2 \rangle$ of 1. The pair correlation coefficient $G_2(r)$ is calculated in a similar fashion to the radial distribution function in that a histogram of minimum image separations is constructed, that also depends on the relative orientations of the particles as well. Each bin is then divided by the corresponding bin from the $g(r)$ histogram giving the plot of $G_2(r)$.

The longitudinal and transverse pair correlation functions: The functions $g_{||}(r_{||})$ and $g_{\perp}(r_{\perp})$ are calculated in a similar way to the radial distribution function $g(r)$, in that a histogram of all interparticle separations is calculated then normalised by a suitable volume element. These correlation functions provide additional information by allowing us to probe in greater detail the structure of the mesophase, revealing such detail as the onset of columnar ordering. In the simulation we transform the simulation box into the director frame, with the director now placed along the z axis of the transformed simulation box. Histograms of the interparticle separations of the specific components, r_z for $g_{||}(r_{||})$, and r_x and r_y along the orthogonal xy plane for $g_{\perp}(r_{\perp})$, are then calculated.

The density distribution function: The density distribution functions, $\rho_{||}(r_{||})$ and $\rho_{\perp}(r_{\perp})$, measure the density of particles in directions parallel and perpendicular to the director. $\rho_i(r_i)$ is calculated by first transforming the particle coordinates such that the director is oriented along a reference direction, for example the z axis. A histogram is then complied of all the z coordinates and then normalised by dividing each histogram bin by the number

of particles and the number of configurations analysed. Though this function does suffer from the problem of the director origin fluctuating during the simulation, resulting in the smearing out of any peaks in the distribution curve.

2.4.4 Dynamic properties

The velocity autocorrelation function: Perhaps the most informative way of analysing the dynamic properties of liquids is via time autocorrelation functions[18] which describe the relationship between a property at a certain time and its value at a later time. From the area of these functions we can calculate the macroscopic transport coefficients such as the diffusion coefficient D[6]. In general, for ergodic systems, a time correlation function of a property A is defined by,

$$C_{AA}(\tau) = \lim_{\tau_{max}\to\infty} \frac{1}{\tau_{max}} \int_0^{\tau_{max}} (A_{\tau_0})(A_{t_0+\tau}) d\tau. \tag{2.57}$$

The property we have chosen to illustrate these ideas is the translational velocity of the particles $\mathbf{v}$, and thus the velocity autocorrelation function C_{VV}, at a time τ is given by,

$$C_{VV}(\tau) = \langle \mathbf{v}(\tau).\mathbf{v}(0) \rangle, \tag{2.58}$$

At long time intervals where there is little or no correlation between velocities, the C_{VV} decays to zero, while at the initial stages of the simulation, the velocities are highly correlated. In the simulation, we calculate the dynamic properties from a tape file that contains the positions, orientations and velocities for the whole state point. The velocities are stored at time intervals δt, with each step labelled as τ i.e. $t = \tau\delta t$. We have τ_{max} time origins and calculate the averages of C_{VV} at time $\tau_0\delta t$ and then at a time $\tau\delta t$ later. In our simulations, we use 200 time steps with time origins every 5 steps and calculate the C_{VV} for the system as a whole or transform into the director frame and calculate the C_{VV} parallel and perpendicular to the director. The normalised C_{VV} is defined as

$$C_{VV}(\tau) = \frac{\langle \mathbf{v}(\tau).\mathbf{v}(0) \rangle}{\langle \mathbf{v}(0).\mathbf{v}(0) \rangle}. \tag{2.59}$$

The mean squared displacement: This dynamic property measures the square of the distance a particle travels relative to its initial position. It is important though to use the coordinates that represent the actual movement in space, rather than those resulting from

the application of periodic boundary conditions. The mean squared displacement $m(t)$ is extremely useful in indicating the translational movement of the particles and hence to what extent a system is "liquid-like" or "solid-like"; it is defined by

$$m(t) = \left\langle |\mathbf{r}_i(t) - \mathbf{r}_i(0)|^2 \right\rangle. \tag{2.60}$$

In the simulation this is calculated as

$$m(t) = \frac{1}{N} \sum_{i=1}^{N} |(\mathbf{r}_i(t) - \mathbf{r}_i(0))|^2 \quad t = (\mathrm{m} - \mathrm{n})\delta t. \tag{2.61}$$

We can also resolve the mean squared displacement parallel and perpendicular to the director yielding extra information about the phase behaviour and dynamics. At sufficiently long times, the mean squared displacement becomes linear, the diffusion coefficient D can then be obtained from the Einstein relationship[6],

$$D = \lim_{t \to \infty} \frac{1}{6t} m(t). \tag{2.62}$$

An alternative method of obtaining the diffusion coefficient is from the integration of the velocity autocorrelation function C_{VV}, such that

$$D = \frac{1}{3} \int_0^{\infty} \langle \mathbf{v}(t).\mathbf{v}(0) \rangle \mathrm{d}t \,. \tag{2.63}$$

2.4.5 Calculating and estimating errors

As with all experiments, real or numerical, the results obtained by computer simulations are subject to errors. Systematic errors are of the most concern and include system size, the use of random numbers and poor equilibration. Statistical errors occur when calculating equilibrium averages of the various properties of interest, $\langle A \rangle$. We calculate these averages in our molecular dynamics simulations by the general formula,

$$\langle A \rangle_{\mathrm{run}} = \frac{1}{\tau_{\mathrm{run}}} \sum_{\tau=1}^{\tau_{\mathrm{run}}} A(\tau). \tag{2.64}$$

If we divide the simulation into sub-chains and in each chain α, calculate the average $\langle A \rangle_{\alpha}$ together with $\langle A \rangle$ over the whole chain, the statistical error of $\langle A \rangle$ is estimated as the standard deviation from the average

$$\sigma(A) = \left[\frac{1}{M_\alpha(M_\alpha - 1)} \sum_{\alpha=1}^{M_\alpha} (\langle A \rangle_\alpha - \langle A \rangle)^2 \right]^{\frac{1}{2}}, \tag{2.65}$$

where M_α is the number of sub-averages. An alternative method is to calculate the standard statistical variance,

$$\sigma^2(\langle A \rangle_{run}) = \sigma^2(A)/\tau_{run}, \tag{2.66}$$

where

$$\sigma^2(A) = \langle \delta A^2 \rangle_{run} = \frac{1}{\tau_{run}} \sum_{\tau=1}^{\tau_{run}} (A(\tau) - \langle A \rangle_{run})^2. \tag{2.67}$$

The estimated error is then given by

$$\sigma(\langle A \rangle_{run}). \tag{2.68}$$

2.4.6 Scaled variables

In computer simulations it is common to calculate static and dynamic properties in dimensionless, scaled variables, normally indicated by an *. The most common scaled variables used are

Internal energy per particle	U^*	$= U/N\varepsilon$,
Temperature	T^*	$= k_B T/\varepsilon$,
Density	ρ^*	$= N\sigma_0^3/V$,
Time	t^*	$= (\varepsilon/m\sigma_0^2)^{1/2} t$,
Distance	r^*	$= r/\sigma_0$.

In this section we have outlined some of the techniques available to the computer simulator, and in the final part of our introduction, we review how these techniques have been applied previously to the simulation of the liquid-crystalline mesophases.

2.5 Molecular models of liquid crystals

2.5.1 Introduction

The liquid-crystalline state, having characteristics of both the solid and liquid phases is very complex, thus modelling this phase is quite a challenge to the computer simulator. This is compounded by the intricate nature of most mesogens at the molecular level, as even the simplest of mesogenic molecules have at least nineteen atoms, thus constructing a realistic atom-atom potential for a liquid crystal molecule will involve a large, complicated

superposition of interacting force sites. As liquid crystals sometimes undergo weak phase transitions and possess long range order, large system sizes are desirable, so most realistic simulations are long and expensive to perform. However, these problems can be overcome and the simulations of liquid crystals have used increasingly detailed and realistic models as the power of computers has increased.

For the purpose of discussing the simulations of rod-shaped and disc-shaped mesogens we shall neglect the various lattice models, the most widely studied being the *Lebwohl-Lasher* model[19-22] where the particles are restricted to the sites of a simple cubic lattice, and concentrate on models that allow full translational and orientational degrees of freedom. These various models can be classified into three general types of increasing complexity, a) hard, non-spherical models, b) soft, non-spherical models and c) atom-atom models. The first two do not attempt to model the behaviour of actual liquid crystal compounds, but try to identify the essential features which are responsible for mesophase formation. It is worth reviewing the range of simulations that have been performed on liquid-crystalline systems, but this is not meant to be an exhaustive survey, rather it highlights the major results and places our work in context.

2.5.2 Hard, non-spherical models

These models were developed based on the view that the structure of simple liquids is governed by short range repulsive forces[23]. In broad terms, the liquid state is dominated by the harsh electronic repulsions between molecules and this can be represented at one extreme by the infinitely steep hard sphere potential, (see §2.1.3). Indeed the freezing of an atomic liquid incorporating only these repulsive forces was successfully modelled as early as 1957[11]. The problem we encounter is that, in these simulations, the particles are represented as spheres, but as we know from experiment, molecules must deviate from spherical symmetry to form a liquid-crystalline mesophase, so this raises several questions[24]. First, what shape of particle is needed to represent the liquid crystal molecules? secondly, can these repulsive forces or *excluded volume effects* be used alone to model liquid crystals? and thirdly, if hard repulsive forces can be used to cause a phase transition, can it be assumed that these are responsible for the transitions in real liquid crystals?

In answer to the first question, it has emerged that for non-atomistic potentials, several basic anisotropic shapes can be used to model liquid crystals, with the majority of the pioneering work being performed by Frenkel and co-workers. The obvious feature that these models have in common, are that they are all anisotropic in shape, but as we shall see, they must still possess a certain minimum length-to-breadth ratio to exhibit liquid-crystalline mesophases. These shapes include prolate ellipsoids and spherocylinders used to model rod-shaped mesogens, and oblate ellipsoids and cut spheres used to represent disc-shaped mesogenic molecules. It must be remembered that these are only rigid, idealised shapes and do not include characteristics of real liquid crystal molecules such as flexible chains and specific attractive interactions, though increasingly, researchers are extending the complexity of their simulations to include such common features.

The second question, as to whether repulsive forces can produce orientationally ordered phases, has been answered by the theory of Onsager[25]. The second law of thermodynamics states that an isolated system tends to maximise its entropy and hence its disorder, so it seemed surprising that Onsager used this tendency to maximise entropy as an ordering force. He showed that, at a sufficiently high density and constant volume, a system of infinitely thin spherocylinders with length L and diameter D, could spontaneously order, from an isotropic fluid, to form an orientationally ordered nematic phase. Although the entropy associated with the orientational degrees of freedom decreases, this is offset by the increase in the translational entropy of the system. This is because the excluded volume of two rods in a nematic phase is smaller than in the isotropic fluid[26]. This theory was borne out by the early computer simulations[27,28] of rod-shaped mesogens in the 1970's though it was only until the 1980's that we saw the first simulation of a nematic - isotropic transition in a system of disc-shaped mesogens[29]. We shall now look more closely at the results obtained from the simulations using these anisotropic shapes.

Spheroids: The first type of hard particle to be extensively studied were the spheroids which could be divided into two classes, ellipsoids of revolution $a \neq b = c$ and biaxial ellipsoids $a \neq b \neq c$, where a, b and c are the three semi-axes of the ellipsoid. The first really successful simulations were of the hard ellipsoids of revolution[30,31], the shape of which is characterised by the aspect ratio a/b, where the major axis of the ellipsoid has length $2a$

and the minor axis length $2b$. This system was extensively studied over the years allowing a phase diagram to be constructed, (see figure 2.3). This shows the existence of isotropic, nematic and solid phases for both prolate and oblate hard ellipsoids, where the regions of nematic stability and two phase coexistence, the black lines, were established by free energy calculations. The diagram also raises several interesting points. First, there is a high degree of symmetry between oblate and prolate ellipsoids under the operation $e \Leftrightarrow 1/e$ on the length-to-breadth ratio a/b. Secondly, the phase diagram also shows that a minimum non-sphericity is needed to form a stable nematic phase, a/b being roughly < 0.4 for discs and > 2.5 for rods, though the precise values have been challenged[32], the authors claiming that the a/b ratio needs to be greater than 3 to exhibit a nematic phase. It should be noted that for all a/b ratios, the nematic phase was formed by spontaneous ordering from the compression of the isotropic phase.

Another point of interest is why does the system of hard ellipsoids not produce any smectic or columnar phases[26]? Consider the case for smectic mesophases, they have a large degree of orientational order and to a first approximation can be represented by a system of perfectly aligned non-spherical molecules. A system of hard ellipsoids parallel to an arbitrary direction, say the director **n**, can be mapped onto hard spheres by scaling the system with the factor b/a along the director. Since hard spheres do not form smectics, a system of parallel ellipsoids should not be able too either. So unless orientational degrees of freedom can stabilise a smectic phase, which intuitively seems unlikely, it can be concluded that a system of freely rotating, hard ellipsoids can only produce a nematic phase. This fact is of particular relevance to us, as hard ellipsoids resemble the shape of the particles used in the simulations in this thesis.

Recent simulations have shown a biaxial nematic phase can be formed by a hard ellipsoid with three distinct semi-axes[33], that is $a \neq b \neq c$. The mesophase was found using the parameters $c/a = 10$, $b/a \approx \sqrt{10}$ and $1 \leq b/a \leq 10$. While of importance in itself, it would be interesting to study the effect of molecular biaxiality on the strength of the nematic - isotropic transition. Theory[34,35] predicts that the transition weakens with increasing biaxiality and this would help to explain the difference between the weak transition seen in experiment and the stronger ones predicted by theory.

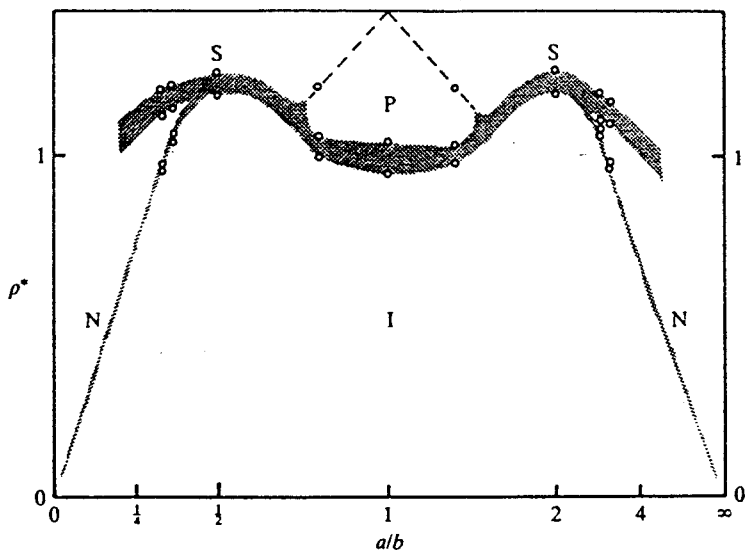

Figure 2.3: *Schematic of the phase diagram for hard ellipsoids of revolution[31]. The x axis represents the aspect ratio under the operation* e ⇔ 1/e, *while the y axis reflects the packing density.*

Spherocylinders: To explore further the possibility of smectic ordering in a system of hard particles, a subtle change of shape to a spherocylinder was performed. Spherocylinders are represented as a cylindrical rod of length L and diameter D with hemi-spherical caps each of diameter D, thus the length-to-breadth ratio is $(L+D)/D$. After the initial work by Vieillard-Baron[27], a full study was carried out on a system of parallel spherocylinders[36,37] i.e. the particles only possessed translational freedom. At high densities, the system formed a close packed crystal, and as the particles were confined to be perfectly aligned, the low density fluid phase was always a nematic phase. Systems of L/D ratios, 0.25. 0.5, 1, 2 and 3 were studied using the Monte Carlo technique with smectic ordering occurring when $L/D >$ 0.5. There was no bond orientational order present in the phase and so it was deduced that it was a smectic A phase. The transition from the smectic A phase to the nematic showed strong pretransitional fluctuations but there was no observable change in density, thus it was tentatively assigned as a second order transition.

Further work[38] produced a columnar phase for $L/D > 5$ with a system size of 270 particles, (see figure 2.4a). This columnar phase was investigated further for $L/D > 5$ with a system consisting of 1080 particles[39] to produce a different phase diagram, (see figure 2.4b), in which the columnar phase was replaced by a AAA stacking hexagonal crystalline phase.

The columnar phase observed with the lower system size was believed to be a consequence of the fact that the small system size allowed unphysical diffusion of the columns, with the range of stability dependent on the system size. These results indicate another important reason in using simple models, in that it allows us to investigate fully the effect of system size, boundary conditions etc. on the phase behaviour of the system, before we proceed with more detailed and realistic models.

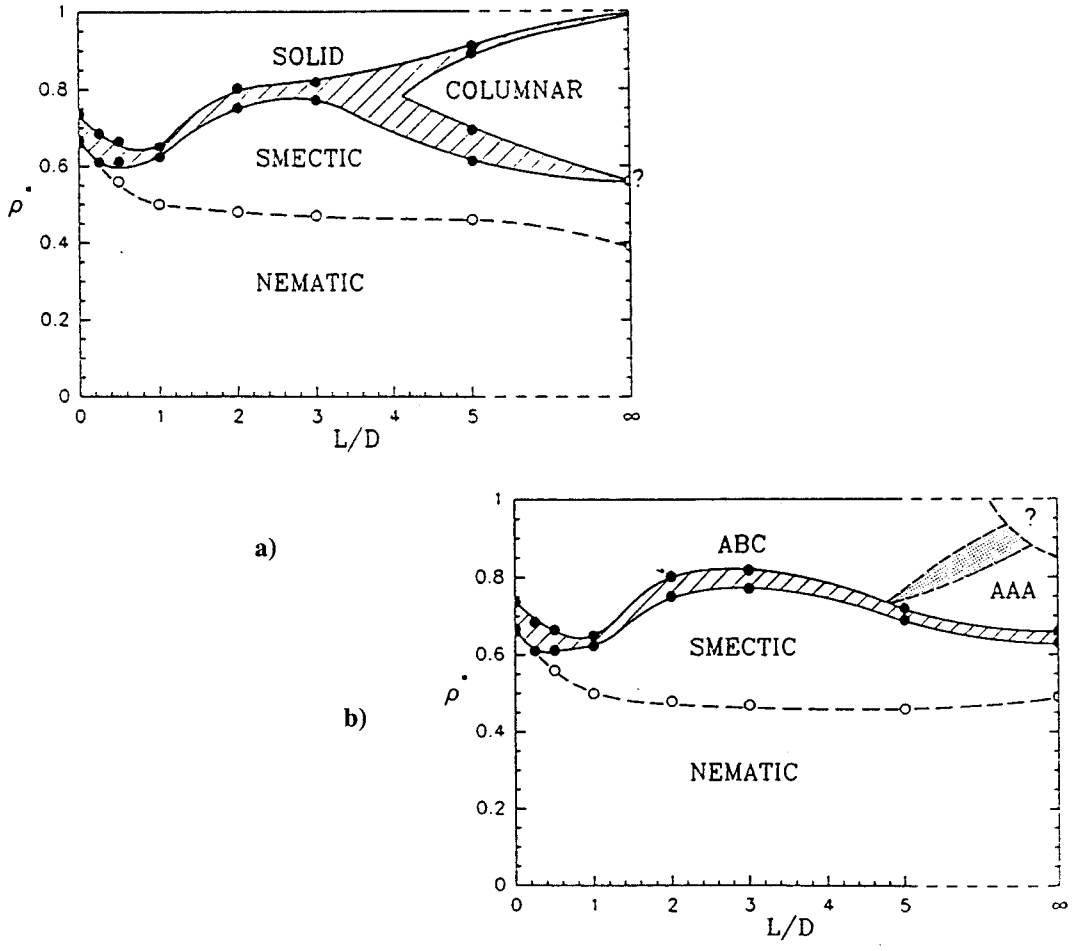

Figure 2.4: *Phase diagrams for hard parallel spherocylinders where the number of particles in simulation are a) N = 270 and b) N = 1080.*

Even though these systems of spherocylinders were constrained to lie parallel to each other, it showed how a change in shape of the particle can dramatically alter the phase behaviour. The next step was to study the same system but with full translational and orientational degrees of freedom allowed. Intuitively this would change the phase behaviour in two possible ways. First, there would be an isotropic fluid at low densities instead of a perfectly aligned nematic phase, while the orientational degrees of freedom

could quite possibly destroy the smectic ordering. For a *L/D* ratio of 5[40,41], a *f.c.c.* crystal was expanded to an isotropic fluid. On compression, nematic and smectic A phases were produced. A tentative phase diagram, (see figure 2.5), for *L/D* ratios between 0 (hard sphere case) and 5, was produced[42] showing the formation of liquid-crystalline mesophases for *L/D* > 3.5. It is interesting that compared to parallel spherocylinders, the orientational degrees of freedom do indeed destroy the liquid-crystalline phases for a wide range of *L/D* ratios. It is also worth noting that just the shape of a particle i.e. the hard repulsive forces, can produce a thermodynamically stable smectic that was generally thought to be exclusive to models that incorporate attractive forces, though theories can now predict the hard core smectic phases[43].

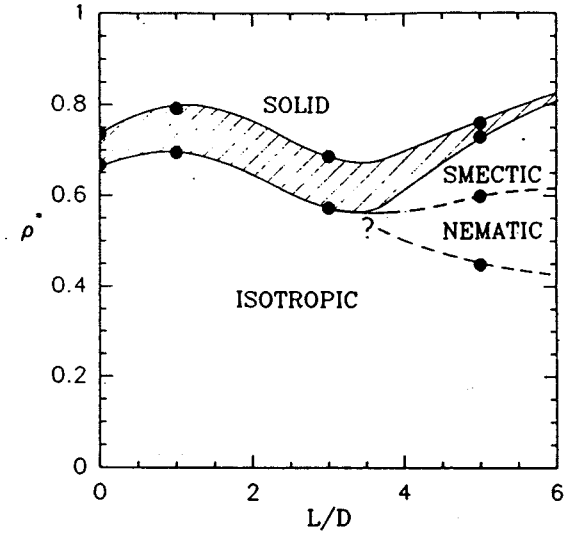

Figure 2.5: *Schematic phase diagram for hard spherocylinders.*

Cut spheres: We have seen that while prolate ellipsoids only form a nematic phase, a spherocylinder will produce a smectic phase, in addition to a nematic, thus it seems reasonable to see if an oblate counterpart of the spherocylinder could produce a columnar phase. The actual geometric shape that fitted this description was the *spheroplatelet* but this proved difficult to use because of numerical considerations in calculating the overlap so the shape that was decided on was of a *cut sphere*[26].

It consists of a sphere of diameter *D* with the top and bottom removed, these flat parts are separated by a thickness *L*. This has the advantages that it is numerically easier to cope

with and in the limit $L/D = 1$, reduces to a hard sphere. Compressing the isotropic fluid, for a system of cut spheres with L/D of 0.1, causes the spontaneous formation of nematic and columnar phases, though the columns in the latter where somewhat buckled. Expansion of the crystal phase produced a defect free columnar phase with hexagonal packing of the columns. Further simulations[44] were carried out with the aspect ratios of 0.2 and 0.3. At L/D of 0.2, the system exhibited isotropic, columnar and solid phases, but no stable nematic phase in contrast to L/D of 0.1, instead a cubatic phase was found. This consisted of columnar stacks of 4 or 5 particles packing against each other, frequently at 90° angles and though there is short range translational order, the columns themselves are orientationally disordered.

As the L/D ratio was increased to 0.3, all liquid-crystalline behaviour disappeared, the isotropic liquid crystallising directly to the solid phase; the full phase diagram is shown in figure 2.6. After taking into account the example of hard parallel spherocylinders, where the finite system size induced spurious columnar ordering, a range of simulations with differing numbers of particles was performed to test the stability of the columnar phase. It was found that the crystal - columnar phase transition appeared to be continuous, the columnar - nematic strongly first order and the nematic - isotropic weakly first order.

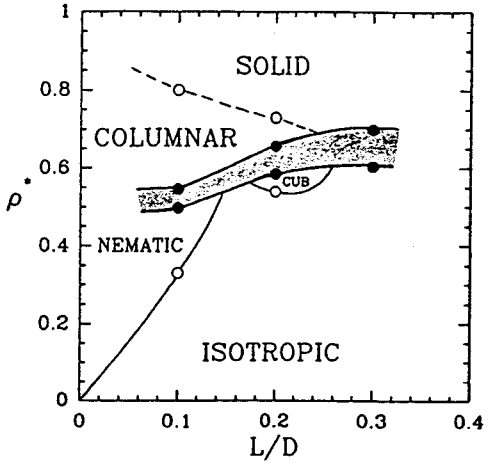

Figure 2.6: *Schematic phase diagram for hard cut spheres.*

It has been shown that the hard model potentials with only short range repulsive forces can produce liquid-crystalline mesophases, though the nature of these phases is dependent on

the shape of the molecule used. The question as to whether repulsive forces are also responsible for transitions in real liquid crystals is much harder to answer. It is true that for a molecule to form a liquid-crystalline mesophase it must deviate from spherical symmetry, and that hard models with a non-spherical core have shown some of the characteristics of the nematic - isotropic phase transition as well as other mesophase behaviour. It is also true that a system that contains only attractive forces will collapse, but it is thought that the inclusion of attractive forces is necessary for the stability of all mesophases.

2.5.3 Soft, non-spherical models

The hard model, though successful in describing certain liquid crystal mesophases, only involves the repulsive forces between molecules, thus the soft model of liquid crystals tries to take into account the attractive as well as the repulsive forces between molecules. The main advantage over the hard repulsive model, is that raising the temperature and not just the density can cause transitions from disordered phases into liquid-crystalline phases i.e. hard models do not exhibit thermotropic phase transitions. When studying liquid crystals, the intermolecular potential must be dependent not on just the separation between molecules but on their orientation, so these models are essentially anisotropic versions of the Lennard-Jones potential:

$$U(r) = 4\varepsilon[(\sigma/r)^{12} - (\sigma/r)^{6}], \tag{2.69}$$

where σ and ε are the length and energy parameters, respectively. At large molecular separations, attractive forces dominate, while at small separations the repulsive forces take over. By the addition of attractive forces and by splitting up the potential into repulsive and attractive components, we can investigate the relative contributions each makes to the stability of the liquid-crystalline mesophase[23]. For instance, it has been shown that, for the Gay-Berne system at least, the attractive forces play a crucial role in the formation and stability of the more ordered phases[45].

The Gay-Berne potential: The Gay-Berne potential falls into the category of a soft non-spherical model, in that it takes into account the role of attractive forces as well as repulsive forces in the formation of liquid crystal mesophases. The ground work was laid by Corner as far back as 1948, when he suggested that linear non-spherical molecules

could be modelled by placing a number of Lennard-Jones force centres, equidistant along the symmetry axis. However this gave a complicated interaction between many force sites, so Corner[46] overcame this by proposing a single site potential where the multi-site potential was fitted numerically to a single 12-6 Lennard-Jones potential, obtaining range and energy parameters which were orientation dependent. The potential had the interaction between two particles as a function of the distance between their centres and was scaled by a range parameter $\sigma(\Omega)$ giving the form of the potential as,

$$U_{\text{Corner}} = \varepsilon(\Omega) f(r/\sigma(\Omega)). \tag{2.70}$$

Both the strength $\varepsilon(\Omega)$ and range $\sigma(\Omega)$ parameters were dependent upon the orientations Ω of the molecules and of the intermolecular vector $\mathbf{r}$. Berne and Pechukas[47] then developed forms for the strength and range parameters using the gaussian overlap model. The gaussian function of a three dimensional vector $\mathbf{x}$ is defined by

$$G(\mathbf{x}) = \exp(-\mathbf{x}.\gamma^{-1}.\mathbf{x}), \tag{2.71}$$

where

$$\gamma = (\sigma_{\parallel}^2 - \sigma_{\perp}^2)\hat{\mathbf{u}}\hat{\mathbf{u}} + \sigma_{\perp}^2\mathbf{I}, \tag{2.72}$$

$\hat{\mathbf{u}}$ is the unit vector of the orientation of the particle and $\mathbf{I}$ is the unit matrix with the surface of constant G producing an ellipsoid of revolution about the symmetry axis.

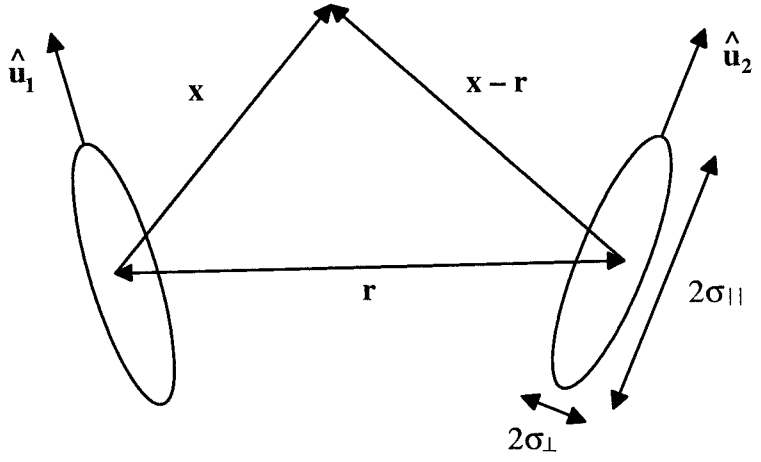

Figure 2.7: *Geometry of two ellipsoids used in the gaussian overlap model.*

They then calculated the overlap between two ellipsoids of revolution using the geometry of figure 2.7, obtaining

$$G(\hat{\mathbf{u}}_1, \hat{\mathbf{u}}_2, \mathbf{r}) \approx |\gamma_1|^{-\frac{1}{2}} |\gamma_2|^{-\frac{1}{2}} \int d\mathbf{x} \exp(-\mathbf{x}.\gamma_1^{-1}.\mathbf{x} - (\mathbf{x}-\mathbf{r}).\gamma_2^{-1}.(\mathbf{x}-\mathbf{r})), \tag{2.73}$$

where $|\gamma_i|$ is the determinant of the range matrix γ_i and

$$\gamma_i = (\sigma_{i||}^2 - \sigma_{i\perp}^2)\hat{\mathbf{u}}_i\hat{\mathbf{u}}_i + \sigma_{i\perp}^2\mathbf{I}. \tag{2.74}$$

Equation (2.73) can be expressed in the simplified form

$$G(\hat{\mathbf{u}}_1, \hat{\mathbf{u}}_2, \mathbf{r}) = \varepsilon(\hat{\mathbf{u}}_1, \hat{\mathbf{u}}_2)\exp[-\mathbf{r}^2/\sigma^2(\hat{\mathbf{u}}_1, \hat{\mathbf{u}}_2, \hat{\mathbf{r}})], \tag{2.75}$$

where $\varepsilon(\hat{\mathbf{u}}_1, \hat{\mathbf{u}}_2)$ and $\sigma(\hat{\mathbf{u}}_1, \hat{\mathbf{u}}_2, \hat{\mathbf{r}})$ are assumed to be the orientation dependent strength and range parameters which are of prime interest to us. These parameters are calculated by finding the eigenvectors and eigenvalues of $(\gamma_1 + \gamma_2)$ and in the case that both interacting ellipsoids have the same dimensions, we find

$$\varepsilon(\hat{\mathbf{u}}_1, \hat{\mathbf{u}}_2) = \varepsilon_0[1 - \chi^2(\hat{\mathbf{u}}_1, \hat{\mathbf{u}}_2)^2]^{-\frac{1}{2}}, \tag{2.76}$$

and

$$\sigma(\hat{\mathbf{u}}_1, \hat{\mathbf{u}}_2, \hat{\mathbf{r}}) = \sigma_0\left\{1 - \frac{\chi}{2}\left[\frac{(\hat{\mathbf{u}}_1.\hat{\mathbf{r}} + \hat{\mathbf{u}}_2.\hat{\mathbf{r}})^2}{1 + \chi(\hat{\mathbf{u}}_1.\hat{\mathbf{u}}_2)} + \frac{(\hat{\mathbf{u}}_1.\hat{\mathbf{r}} - \hat{\mathbf{u}}_2.\hat{\mathbf{r}})^2}{1 - \chi(\hat{\mathbf{u}}_1.\hat{\mathbf{u}}_2)}\right]\right\}^{-\frac{1}{2}}. \tag{2.77}$$

The parameter χ is defined by

$$\chi = \frac{\sigma_{||}^2 - \sigma_{\perp}^2}{\sigma_{||}^2 + \sigma_{\perp}^2}. \tag{2.78}$$

This overlap model, the BPK model, was first used to simulate liquid crystals by Berne and Kushick[48], and Decoster *et al.*[49], using the forms for σ and ε generated by Berne and Pechukas, in a Lennard-Jones 12-6 potential,

$$U_{\mathrm{BPK}}(\hat{\mathbf{u}}_1, \hat{\mathbf{u}}_2, \mathbf{r}) = 4\varepsilon(\hat{\mathbf{u}}_1, \hat{\mathbf{u}}_2)\left[\left(\frac{\sigma(\hat{\mathbf{u}}_1, \hat{\mathbf{u}}_2, \hat{\mathbf{r}})}{r}\right)^{12} - \left(\frac{\sigma(\hat{\mathbf{u}}_1, \hat{\mathbf{u}}_2, \hat{\mathbf{r}})}{r}\right)^{6}\right]. \tag{2.79}$$

However, it was realised by Gay and Berne[50] that the potential possessed a number of unrealistic features. First, as the well depth, (see equation (2.76)), depends on the relative orientation of the particles and not on the orientation with respect to the intermolecular vector, the well depth for various orientations are identical, when they should be different, (see figure 2.8). Further, the width of the attractive well varies with orientation of the particles with respect to the intermolecular vector, thus the potential becomes softer for different orientations, though the distance dependence should be independent of the orientation[51].

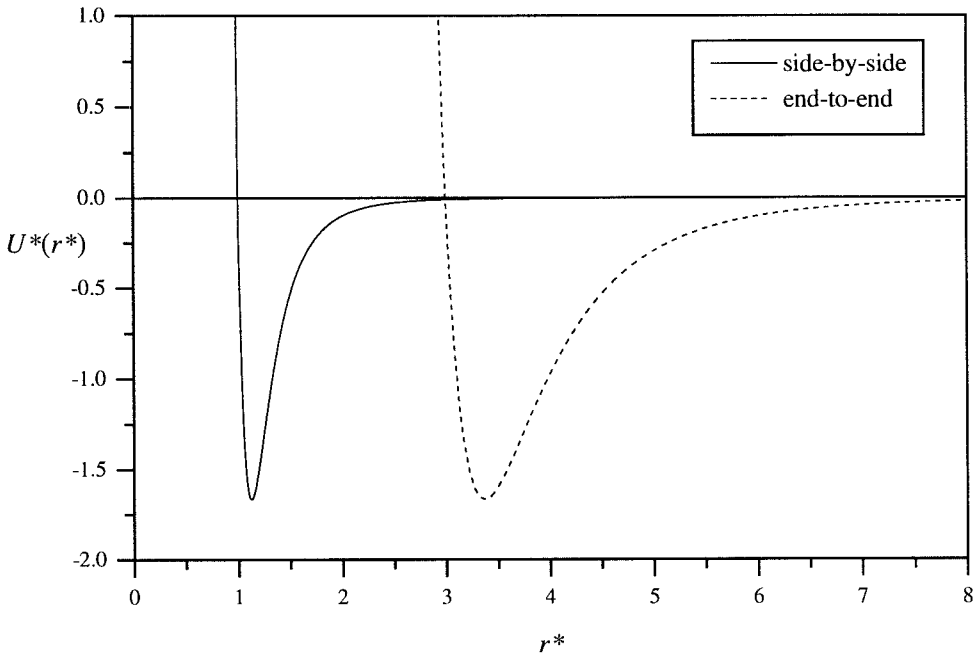

Figure 2.8: *The distance dependence for the BPK intermolecular potential for two orientations, illustrating how the well width varies with the orientation of the particles, with* σ_s/σ_e *of* 3.0.

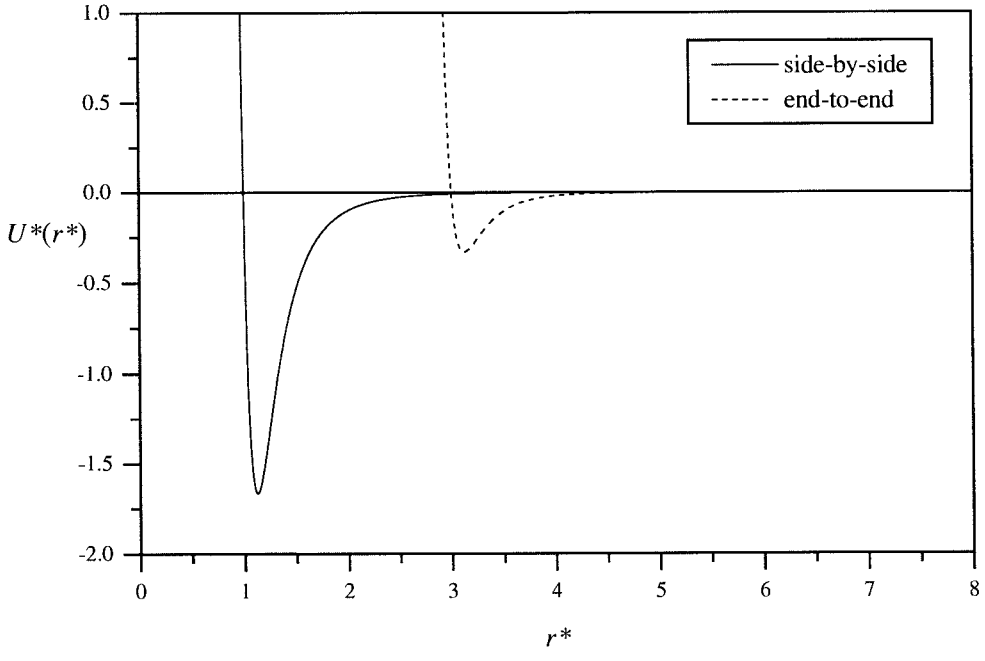

Figure 2.9: *The distance dependence for the Gay-Berne intermolecular potential for two orientations, showing how the deficiency with the well widths has been corrected, with* σ_s/σ_e *of* 3.0.

In order to rectify these problems in the BPK model, a number of modifications were tried by Walmsley[52], and by Tsykalo and Bagmet[53], but by far the most important and successful modification was the further development of the overlap model by Gay and Berne[50]. They first changed the potential by using a shifted form, analogous to that proposed by Kihara[54] rather than the scaled versions used previously, thus the potential now took the form,

$$U(\hat{\mathbf{u}}_1,\hat{\mathbf{u}}_2,\mathbf{r}) = 4\varepsilon(\hat{\mathbf{u}}_1,\hat{\mathbf{u}}_2,\hat{\mathbf{r}})\left[\left(\frac{1}{r-\sigma(\hat{\mathbf{u}}_1,\hat{\mathbf{u}}_2,\hat{\mathbf{r}})+1}\right)^{12}-\left(\frac{1}{r-\sigma(\hat{\mathbf{u}}_1,\hat{\mathbf{u}}_2,\hat{\mathbf{r}})+1}\right)^{6}\right]. \quad (2.80)$$

This now meant that the well width was independent of the molecular orientations i.e. the form of the potential was now the same for any orientation, (see figure 2.9). The range parameter is the same as in the BPK potential, but the strength parameter was redefined,

$$\varepsilon(\hat{\mathbf{u}}_1,\hat{\mathbf{u}}_2,\hat{\mathbf{r}}) = \varepsilon_0\varepsilon^{\nu}(\hat{\mathbf{u}}_1,\hat{\mathbf{u}}_2)\varepsilon_1^{\mu}(\hat{\mathbf{u}}_1,\hat{\mathbf{u}}_2,\hat{\mathbf{r}}), \quad (2.81)$$

similar to that used by Walmsley, and by Tsykalo and Bagmet, and with the exponential parameters as μ of 1 and ν of 2, took the form,

$$\varepsilon_1(\hat{\mathbf{u}}_1,\hat{\mathbf{u}}_2,\hat{\mathbf{r}}) = 1-\frac{\chi'}{2}\left[\frac{(\hat{\mathbf{u}}_1.\hat{\mathbf{r}}+\hat{\mathbf{u}}_2.\hat{\mathbf{r}})^2}{1+\chi'(\hat{\mathbf{u}}_1.\hat{\mathbf{u}}_2)}+\frac{(\hat{\mathbf{u}}_1.\hat{\mathbf{r}}-\hat{\mathbf{u}}_2.\hat{\mathbf{r}})^2}{1-\chi'(\hat{\mathbf{u}}_1.\hat{\mathbf{u}}_2)}\right], \quad (2.82)$$

where

$$\chi' = \frac{1-(\varepsilon_e/\varepsilon_s)^{\frac{1}{\mu}}}{1+(\varepsilon_e/\varepsilon_s)^{\frac{1}{\mu}}}. \quad (2.83)$$

Here, $\varepsilon_e/\varepsilon_s$ is the ratio of the well depth for the end-to-end and side-by-side configurations. The values of μ of 1, ν of 2 and $\varepsilon_e/\varepsilon_s$ of 0.2 were obtained by fitting the potential to a linear array of four Lennard-Jones centres placed $2\sigma_0/3$ apart, chosen as they have been used to model diatomics. The fitting to this array of Lennard-Jones sites, was by comparison of the maximum well depths and separation at the maximum well depths for a range of five configurations between the two particles. The first simulations using the dimensionally correct Gay-Berne potential, (equation (2.84)), were by Adams *et al.*[55] who successfully simulated a nematic - isotropic transition in a system of rod-shaped mesogens.

$$U(\hat{\mathbf{u}}_1,\hat{\mathbf{u}}_2,\mathbf{r}) = 4\varepsilon(\hat{\mathbf{u}}_1,\hat{\mathbf{u}}_2,\hat{\mathbf{r}})\left[\left(\frac{\sigma_0}{r-\sigma(\hat{\mathbf{u}}_1,\hat{\mathbf{u}}_2,\mathbf{r})+\sigma_0}\right)^{12}-\left(\frac{\sigma_0}{r-\sigma(\hat{\mathbf{u}}_1,\hat{\mathbf{u}}_2,\mathbf{r})+\sigma_0}\right)^{6}\right]. \quad (2.84)$$

Luckhurst *et al.*[13] used the same potential form, but with μ of 2 and ν of 1, leading to the formation of smectic A and smectic B, in addition to the usual isotropic, nematic, and crystal phases. A more detailed study of the Gay-Berne fluid composed of prolate particles was performed by de Miguel *et al.*[45,56] and using the Monte Carlo method they showed the existence of a tilted smectic B phase as well as producing a full phase diagram[57]. Further simulations on prolate particles with σ_e/σ_s of 3.0 were performed by Berardi *et al.*[58], who using the parameters μ of 1 and ν of 3, demonstrated how the orientational and structural properties of the system can change depending on the parametrisation. The structure of the smectic B phase has also been investigated by Hashim *et al.*[59], revealing it to contain rippled layers.

Up to now, the parameters employed in the Gay-Berne potential have been obtained by comparison with a line of four Lennard-Jones centres and as such, might not be representative of those for mesogenic molecules. To obtain more typical values for the parameters, σ_e/σ_s and $\varepsilon_e/\varepsilon_s$, Luckhurst and Simmonds[60] compared the Gay-Berne potential with a site-site potential for the rod-shaped mesogen *p*-terphenyl, obtaining values for σ_e/σ_s of 4.4 and $\varepsilon_e/\varepsilon_s$ of 1/39.6, compared with the original Gay-Berne[50] values of σ_e/σ_s of 3.0 and $\varepsilon_e/\varepsilon_s$ of 1/5. Using these new parameters they successfully simulated nematic and smectic A phases. In order to model chiral systems, Memmer *et al.*[61] added a chiral term U_c to the Gay-Berne potential. The potential now took the form

$$U(\hat{\mathbf{u}}_1,\hat{\mathbf{u}}_2,\mathbf{r}) = aU_a(\hat{\mathbf{u}}_1,\hat{\mathbf{u}}_2,\mathbf{r}) + cU_c(\hat{\mathbf{u}}_1,\hat{\mathbf{u}}_2,\mathbf{r}), \tag{2.85}$$

where

$$U_c(\hat{\mathbf{u}}_1,\hat{\mathbf{u}}_2,\mathbf{r}) = 4\varepsilon(\hat{\mathbf{u}}_1,\hat{\mathbf{u}}_2,\hat{\mathbf{r}})\left(\frac{\sigma_0}{r-\sigma(\hat{\mathbf{u}}_1,\hat{\mathbf{u}}_2,\hat{\mathbf{r}})+\sigma_0}\right)^7 [(\hat{\mathbf{u}}_1\times\hat{\mathbf{u}}_2).\mathbf{r}](\hat{\mathbf{u}}_1.\hat{\mathbf{u}}_2), \tag{2.86}$$

and U_a is the normal Gay-Berne potential as in equation (2.84). Simulating along an isotherm, they produced isotropic, cholesteric and BPII phases, while additional simulations cooling the system along an isochiral, *c* being 0.8, managed to produce a helical smectic A* phase, the so-called twist grain boundary phase. But the simulation of these chiral systems raised the question of what type of boundary conditions to use? In their initial work, Memmer *et al.* used ordinary cubic boundary conditions, so they addressed this by using the twisted boundary conditions as used by Allen and Masters[62],

and as a result, the potential energy of the system[63] was reduced and the pitch increased when compared with the results of their earlier work[61].

All of the simulations up to now have used parametrisation for rod-shaped mesogens, mainly achieved by using the value of σ_e/σ_s of 3.0. The first simulations of disc-shaped mesogens were performed by Emerson *et al.*[64] who used a value for σ_f/σ_e of 0.345 in producing discotic nematic and columnar phases, the detailed results of which will be discussed in later chapters. Apart from using the Gay-Berne potential to calculate the properties of liquid-crystalline mesophases, it has been used as a solvent in studying the conformations of flexible molecules[65] and in the calculation of the dependence on density of the orientational order via the parameter Γ[66], which will again be discussed in a later chapter. There has also been investigations into modelling systems other than liquid crystals with the Gay-Berne potential and these have tended to concentrate on molecules such as benzene[67,68] and napthalene[69,70].

At this point we should mention the shape of the Gay-Berne particle[60,71]. Up to now, we have described the Gay-Berne particle as being ellipsoidal in shape but this only holds true when two particles are in a parallel arrangement. Though these are prevalent in liquid crystals phases, there are other situations, such as when two particles are in the tee arrangement, that the zero potential energy contour deviates from an ellipsoid, and in this case is spherical.

Hybrid GBLR potential: The other main soft potential that has been used for the simulation of liquid crystals is that based on the potential first developed by Luckhurst and Romano[72] to study the classical nematic phase. The particles interact via a scalar Lennard-Jones potential U_o but with an additional anisotropic term U_a. The potential has the form:

$$U = \underbrace{4\varepsilon[(\sigma/r)^{12} - (\sigma/r)^6]}_{U_0} + \underbrace{[-4\lambda\varepsilon(\sigma/r)^6 P_2(\cos\beta)]}_{U_a}, \qquad (2.87)$$

and with λ of 0.15, the simulations show a weak first order nematic - isotropic transition. Though all of the models we have discussed here are single site potentials, there lies the possibility of joining force centres together in an array of complex geometries to model

more accurately the interactions within real mesogens. This approach suffers from the same problem of the complex models to be discussed later, in that the system becomes computationally very expensive. To overcome this problem, De Luca *et al.*[73] have developed a potential that takes a $1/10^{th}$ of the computational time of the Gay-Berne potential, while still retaining some of its more important features. They took the Luckhurst-Romano potential, (see equation (2.87)), and scaled the total potential by an energy term with the same functional form as that in the Gay-Berne potential[50],

$$\varepsilon'(\hat{\mathbf{u}}_1, \hat{\mathbf{u}}_2, \hat{\mathbf{r}}) = 1 - \frac{\chi'}{2}\left\{\frac{(\hat{\mathbf{u}}_1.\hat{\mathbf{r}} + \hat{\mathbf{u}}_2.\hat{\mathbf{r}})^2}{1 + \chi'(\hat{\mathbf{u}}_1.\hat{\mathbf{u}}_2)} + \frac{(\hat{\mathbf{u}}_1.\hat{\mathbf{r}} - \hat{\mathbf{u}}_2.\hat{\mathbf{r}})^2}{1 - \chi'(\hat{\mathbf{u}}_1.\hat{\mathbf{u}}_2)}\right\}, \tag{2.88}$$

where

$$\chi' = \frac{(1 - \varepsilon_e/\varepsilon_s)^{\frac{1}{\mu}}}{(1 + \varepsilon_e/\varepsilon_s)^{\frac{1}{\mu}}}, \tag{2.89}$$

such that the potential now became,

$$U = \varepsilon'(\hat{\mathbf{u}}_1, \hat{\mathbf{u}}_2, \hat{\mathbf{r}})(U_0 + U_a). \tag{2.90}$$

This allowed the potential to differentiate not only between orientations with their orientational vectors parallel and perpendicular, as only the Luckhurst-Romano potential could, but between face-to-face, edge-to-edge, cross and tee orientations. By then allowing the well depth ratio to take a form suitable for disc-shaped molecules, i.e. the face-to-face orientation is favoured over all others, the formation of a discotic nematic and columnar-like phase, consisting of short stacks of particles, were observed.

2.5.4 Atom-atom models

The increase in computing power over the years, and the desire to produce more realistic models has led to the simulation of liquid crystals using atom-atom models. Whereas the previous potentials have represented mesogenic molecules as a variety of solid geometric shapes with just one interacting force centre, these realistic potentials include the atomic detail, by having force centres at each atomic site. The molecular charge distribution, obtained by *ab initio* calculations, is then incorporated by the addition of a Coulomb term to the potential. Once this molecular framework is established, we can introduce some measure of flexibility by adding extra potentials for bond stretching, bending and torsion, though this increase in the complexity of the model potential is only allowed by reducing

the size of the system to approximately 100 particles. There have been many studies on rod-shaped mesogens with a variety of approaches being taken. A number of bulk studies have been undertaken[74,75,76,77,78] on mesogens such as *trans*-4-(*trans*-4-*n*-pentylcyclohexyl) cyclohexylcarbonitrile (CCH5), 4-ethoxy benzylidene-4'-*n*-butyaniline (EBBA) and 4-n-pentyl-4'-cyanobiphenyl (5CB), while other work has concentrated on pairs of molecules[79]. Systems such as thin films[80] and molecules adsorbed onto a variety of surfaces[81] have also been investigated.

Discotic systems suffer, in that the number of atoms in even the smallest mesogens are so much greater than in a simple rod-shaped mesogen such as 5CB, so to date there has only been one study on a real discotic mesogen. Ono and Kondo[82] undertook a study of hexakis(pentyloxy)triphenylene (THE5) in an attempt to investigate the behaviour of the diffusion coefficients. The system was assumed to be in the D_{ho} phase as the particles were arranged into 9 columns each containing 6 molecules. Each molecule had a coulomb potential, with charges obtained from *ab initio* calculations, placed at each site but with united atoms representing the alkyl chain. Then performing molecular dynamics simulations in the *NVT* ensemble, they found the diffusion coefficient to be greater perpendicular to the director as expected[83]. They measured the order parameter $\langle P_2 \rangle$ to be ≈ 0.95 for the aromatic core, a result verified by N.M.R studies[84].

2.6 References

[1] S.Chandrasekhar. *Liquid Crystals. 2nd. Ed.* Cambridge (1993).

[2] N.Metropolis, A.W.Rosenbluth, M.Rosenbluth, A.H.Teller and E.Teller. *J.Chem.Phys.* (1953) **21** 1087.

[3] B.J.Alder and T.E.Wainwright. *J.Chem.Phys.* (1959) **31** 459.

[4] P.W.Atkins. *Physical Chemistry. 3rd Ed.* Oxford University Press (1986).

[5] D.Chandler. *Introduction to Statistical Mechanics.* Oxford (1987).

[6] M.P.Allen and D.J.Tildesley. *Computer Simulation of Liquids.* Claredon (1987).

[7] A.Z.Panagiotopoulos. *Molec.Phys.* (1987) **61** 813.

[8] C.Zannoni in *The Molecular Physics of Liquid Crystals.* (G.R.Luckhurst and G.W.Gray eds.) Academic Press (1979).

[9] J.Kushick and B.J.Berne. *Statistical Mechanics:Part B.* (B.J.Berne ed.) Plenum (1977).

[10] K.Binder (ed.) *Monte Carlo Methods in Statistical Physics.* Springer-Verlag (1979).

[11] B.J.Alder and T.E.Wainwright. *J.Chem.Phys.* (1957) **27** 1208.

[12] J.J.Erpenbeck and W.W.Wood in *Statistical Mechanics:Part B.* (B.J.Berne ed.) Plenum (1977).

[13] G.R.Luckhurst, R.A.Stephens and R.W.Phippen. *Liq.Cryst.* (1990) **8** 451.

[14] D.Fincham and D.M.Heyes. *Adv.Chem.Phys.* (1985) **53** 493.

[15] L.Verlet. *Phys.Rev.* (1967) **159** 98.

[16] R.Eppenga and D.Frenkel. *Molec.Phys.* (1984) **52** 1303.

[17] K.Miyano. *J.Chem.Phys.* (1978) **69** 4807.

[18] B.J.Berne and G.D.Harp. *Adv.Chem.Phys.* (1970) **17** 63.

[19] G.R.Luckhurst and P.Simpson. *Molec.Phys.* (1982) **47** 251.

[20] G.Lasher. *Phys.Rev.A.* (1972) **5** 1350.

[21] P.A.Lebwohl and G.Lasher. *Phys.Rev.A.* (1972) **6** 426.

[22] U.Fabbri and C.Zannoni. *Molec.Phys.* (1986) **58** 763.

[23] D.J.Weekes, D.Chandler and H.C.Anderson. *J.Chem.Phys.* (1971) **54** 5237.

[24] D.Frenkel. *Molec.Phys.* (1987) **60** 1.

[25] L.Onsager. *Ann.N.Y.Acad.Sci.* (1949) **51** 627.

[26] D.Frenkel. *Liq.Cryst.* (1989) **5** 929.

[27] J.E.Vieillard-Baron. *Molec.Phys.* (1974) **28** 809.

[28] J.E.Vieillard-Baron. *J.Chem.Phys.* (1972) **56** 4729.

[29] D.Frenkel and R.Eppenga. *Phys.Rev.Lett.* (1982) **49** 1089.

[30] D.Frenkel, B.M.Mulder and J.P.MacTague. *Phys.Rev.Lett.* (1984) **52** 287.

[31] D.Frenkel and B.M.Mulder. *Molec.Phys.* (1985) **55** 1171.

[32] G.J.Zarragoicoechea, D.Levesque and J.J.Weis. *Molec.Phys.* (1992) **75** 989.

[33] M.P.Allen. *Liq.Cryst.* (1990) **8** 499.

[34] B.M.Mulder. *Liq.Cryst.* (1986) **1** 539.

[35] R.Holyst and A.Poniewierski. *Molec.Phys.* (1990) **69** 193.

[36] D.Frenkel. *J.Phys.Chem.* (1987) **91** 4912.

[37] A.Stroobants, H.N.W.Lekkerkerker and D.Frenkel. *Phys.Rev.Lett.* (1986) **57** 1452.

[38] A.Stroobants, H.N.W.Lekkerkerker and D.Frenkel. *Phys.Rev.A.* (1987) **36** 2929.

[39] J.A.C.Veerman. and D.Frenkel. *Phys.Rev.A.* (1991) **43** 4334.

[41] D.Frenkel, H.N.W.Lekkerkerker and A.Stroobants. *Nature.* (1988) **332** 822.

[42] J.A.C.Veerman and D.Frenkel. *Phys.Rev.A.* (1990) **41** 3237.

[43] M.P.Allen. *Phil.Trans.R.Soc.Lond.* (1993) **A344** 323.

[44] J.A.C.Veerman and D.Frenkel. *Phys.Rev.A.* (1992) **45** 5632.

[45] E.de Miguel, L.F.Rull, M.K.Chalam and K.E.Gubbins. *Molec.Phys.* (1991) **74** 405.

[46] J.Corner. *Proc.R.Soc.Lond.* (1948) **A192** 275.

[47] B.J.Berne and P.Pechukas. *J.Chem.Phys.* (1972) **56** 4213.

[48] J.Kushick and B.J.Berne. *J.Chem.Phys.* (1976) **64** 1362.

[49] D.Decoster, E.Constant and M.Constant. *Mol.Cryst.Liq.Cryst.* (1983) **97** 263.

[50] J.G.Gay and B.J.Berne. *J.Chem.Phys.* (1981) **74** 3316.

[51] A.J.Stone in *The Molecular Physics of Liquid Crystals.* (G.R.Luckhurst and G.W.Gray eds.) Academic (1979).

[52] S.H.Walmsley. *Chem.Phys.Lett.* (1977) **49** 390.

[53] A.L.Tsykalo and A.D.Bagmet. *Mol.Cryst.Liq.Cryst.* (1978) **46** 111.

[54] T.Kihara. *J.Phys.Soc.Jap.* (1951) **6** 289.

[55] D.J.Adams, G.R.Luckhurst and R.W.Phippen. *Molec.Phys.* (1987) **61** 1575.

[56] E.de Miguel, L.F.Rull, M.K.Chalam, K.E.Gubbins and F.Van Swol. *Molec.Phys.* (1991) **72** 593.

[57] M.K.Chalam, K.E.Gubbins, E.de Miguel and L.F.Rull. *Mol.Sim.* (1991) **7** 357.

[58] R.Berardi, A.P.J.Emerson and C.Zannoni. *J.Chem.Soc.Faraday.Trans.* (1993) **89** 4069.

[59] R.Hashim, G.R.Luckhurst and S.Romano. *J.Chem.Soc.Faraday.Trans.* (1995) **91** 2141.

[60] G.R.Luckhurst and P.S.J.Simmonds. *Molec.Phys.* (1993) **80** 233.

[61] R.Memmer, H.G.Kuball and A.Schönhofer. *Liq.Cryst.* (1993) **15** 345.

[62] M.P.Allen and A.J.Masters. *Molec.Phys.* (1993) **79** 277.

[63] R.Memmer, H.G.Kuball and A.Schönhofer. *Ber.Bunsenges.Phys.Chem.* (1993) **97** 1193.

[64] A.P.J.Emerson, G.R.Luckhurst and S.G.Whatling. *Molec.Phys.* (1994) **82** 113.

[65] J.Alejandre, J.W.Emsley, D.J.Tildesley and P.Carlson. *J.Chem.Phys.* (1994) **101** 7027.

[66] J.W.Emsley, G.R.Luckhurst, W.E.Palke and D.J.Tildesley. *Liq.Cryst.* (1992) **11** 519.

[67] V.N.Kabadi and W.A.Steele. *Ber.Bunsenges.Phys.Chem.* (1985) **89** 2.

[67] V.N.Kabadi and W.A.Steele. *Ber.Bunsenges.Phys.Chem.* (1985) **89** 2.

[68] V.N.Kabadi. *Ber.Bunsenges.Phys.Chem.* (1986) **90** 327.

[69] W.B.Sediawan, S.Gupta and E.McLaughlin. *Molec.Phys.* (1987) **62** 141.

[70] W.B.Sediawan, S.Gupta and E.McLaughlin. *J.Chem.Phys.* (1989) **90** 1888.

[71] A.P.J.Emerson. *Ph.D.* University of Southampton (1991).

[72] G.R.Luckhurst and S.Romano. *Proc.R.Soc.Lond.* (1980) **A373** 111.

[73] M.D.De Luca, M.P.Neal and C.M.Care. *Liq.Cryst.* (1994) **16** 257.

[74] A.V.Komolkin, Yu V.Molchanov and P.P.Yakutseni. *Liq.Cryst.* (1989) **6** 39.

[75] S.J.Picken, W.F.Van Gunsteren, P.Th.Van Duijnen and W.H.De Jeu. *Liq.Cryst.* (1989) **6** 357.

[76] A.V.Komolkin, A.Laaksonen and A.Maliniak. *J.Chem.Phys.* (1994) **101** 4103.

[77] M.R.Wilson and M.P.Allen. *Mol.Cryst.Liq.Cryst.* (1991) **198** 465.

[78] M.P.Allen and M.R.Wilson. *Liq.Cryst.* (1992) **12** 157.

[79] M.R.Wilson and D.A.Dunmur. *Liq.Cryst.* (1989) **5** 987.

[80] M.A.Glaser, N.A.Clark, R.Malzbender and D.M.Walba. *J.Phys.Condes.Matter.* (1994) **6** A261.

[81] M.J.Callaway. *Ph.D. Thesis,* University of Southampton (1996).

[82] I.Ono and S.Kondo. *Bull.Chem.Soc.Jap.* (1992) **65** 1057.

[83] R.Y.Dong, D.Goldfarb, M.E.Moseley, Z.Luz and H.Zimmermann. *J.Phys.Chem.* (1984) **88** 3148.

[84] D.Goldfarb, Z.Luz and H.Zimmermann. *J.Phys.Paris.* (1981) **42** 1303.

3. The Gay-Berne discogen I

3.1 Introduction

We have seen in the previous chapter, (see §2.5), that for model mesogens, a sufficient condition for the system to form a nematic phase is for the constituent particles to deviate from spherical symmetry. However, whether the mesophase is observed or not depends on the freezing point. It is recognised as result of computer simulations studies that a subtle change in shape is all that is needed for the system to exhibit the more ordered mesophases, such as the smectic phase for rod-shaped particles and columnar phase for disc-shaped particles. These simulations have used hard particle models in which each molecule interacts via repulsive forces alone. Obviously this oversimplifies the behaviour of real mesogens, as it neglects the other intermolecular forces, and so the next stage would be to incorporate attractive forces into the model. This would allow us to investigate the thermal behaviour of the model mesogen as well as seeing whether these forces might be able to stabilise mesophases not observed with hard particle models.

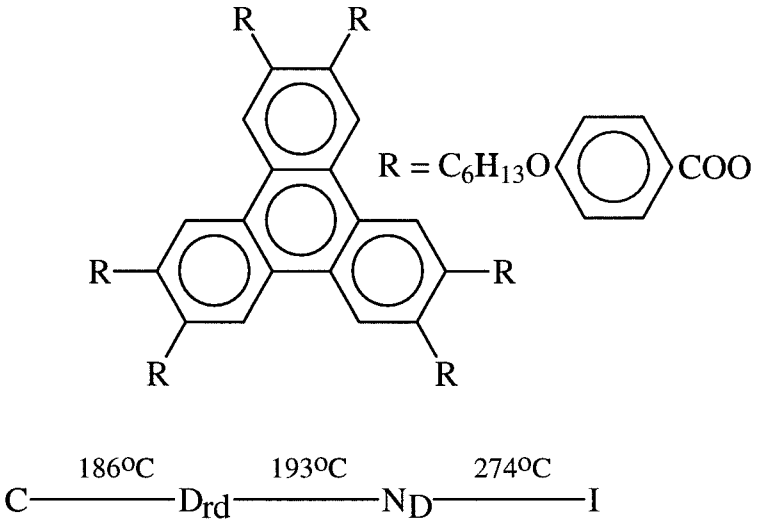

Figure 3.1: *A typical disc-shaped mesogen based on triphenylene, which forms the starting point for our model Gay-Berne discogen.*

In Chapter 2 we discussed the various types of models that can be used to simulate the bulk properties of liquid crystals, paying special attention to the Gay-Berne potential as this is a particularly successful model for the liquid-crystalline mesophase, while still retaining computational and conceptual simplicity.

For these reasons, we chose to use this potential in our studies of liquid crystals. The Gay-Berne potential can be thought of as representing each interacting particle as an ellipsoid, and though the definition of the shape is not straightforward, (see §2.5), it has been used to model rod-shaped mesogens by using prolate ellipsoids. This has proved successful in terms of simulating a range of mesophases including nematic, smectic A and smectic B[11]. This illustrates that the addition of attractive forces can stabilise the translationally ordered phases, previously absent in the corresponding system of hard ellipsoids. The next logical step is to model a discotic liquid crystal, (see figure 3.1), and this is one of the great attractions of the Gay-Berne potential in that it is very simple to change the shape of the interacting ellipsoids from prolate to oblate or disc-shaped.

The initial work on these systems was carried out by Emerson[12] who performed molecular dynamics simulations of the Gay-Berne discogen at the scaled densities ρ^* of 2.7 and 3.0 ($\rho^* \equiv N\sigma_0^3/V$). The results were similar in that isotropic, discotic nematic, columnar and crystal phases were produced for both densities, again proving the value of this potential in that it can provide a range of mesophases. The only difference between the two densities were the transition temperatures, which were lower at the lower density ρ^* of 2.7. This is to be expected, because at higher densities the particles are closer together so the intermolecular forces experienced by each particle are stronger, with the increased attractive forces stabilising the ordered phases so causing the transition temperatures to rise.

Of greater interest to us is the structure of the columnar phase, in which the columns are arranged in a square lattice, (see figure 3.2). The particles within each column are not tilted as might be expected with the normal square or rectangular phase[13], but lie with their symmetry axes parallel to the column axis. This results from the fact that the particles within each column are staggered with respect to particles in the neighbouring columns, thus allowing the columns to penetrate each other. Such an interdigitated structure is analogous to that observed in some smectic phases. The extent of interdigitation was quantified by the transverse pair correlation function $g_\perp(r_\perp^*)$ which gave the distance between particles as 0.9, instead of 1.0 or greater, expected for non inter-penetrating columns, (see figure 3.3).

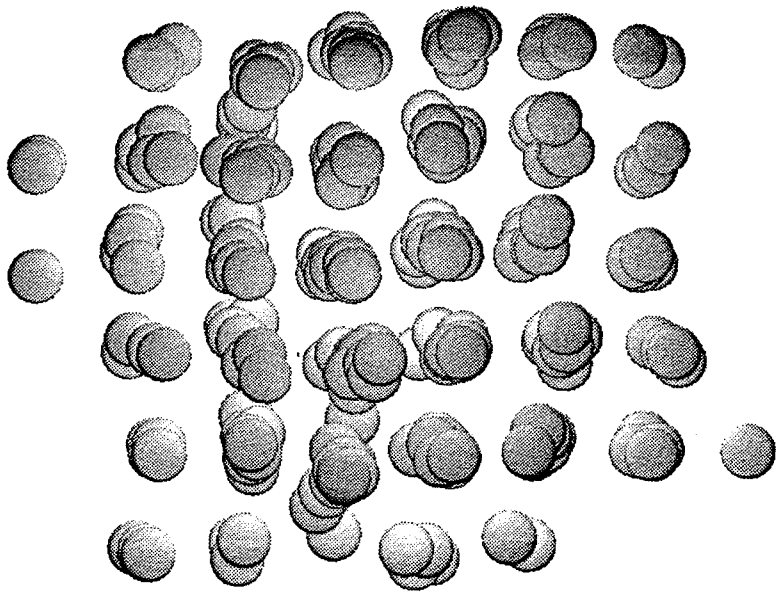

Figure 3.2: *View parallel to the director for the columnar phase at* ρ^* *of 2.7 with the ellipsoids shown at half the correct size for ease of visualisation, illustrating the square packing structure of the columns.*

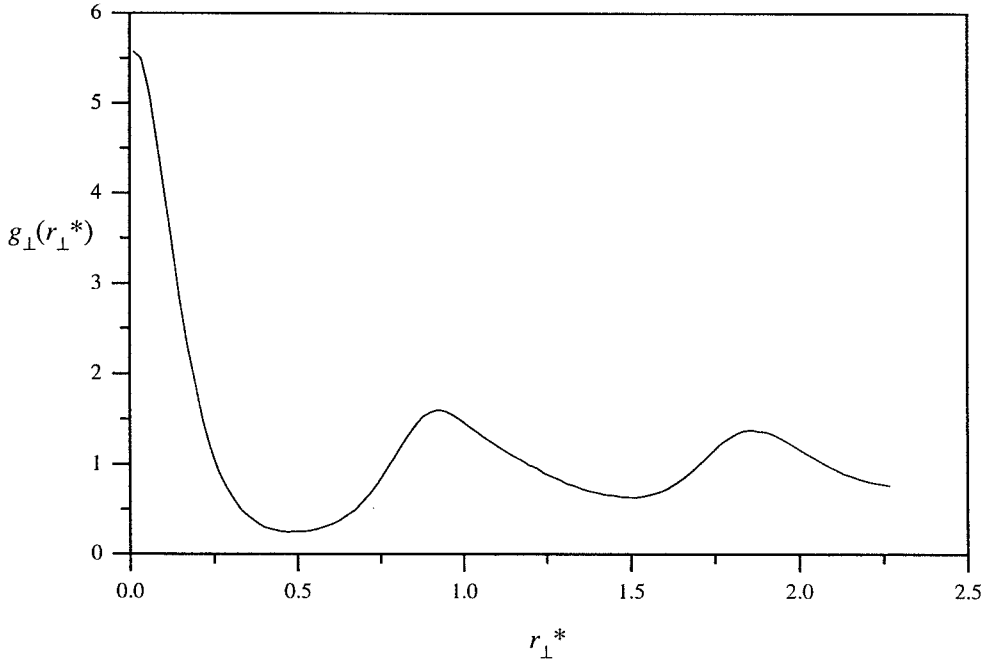

Figure 3.3: *The transverse pair correlation function* $g_\perp(r_\perp^*)$ *for the square columnar phase at the density* ρ^* *of 2.7. The peak at* $r_\perp^*$ *of 0.9 indicates that the columns penetrate each other as the particle diameter is defined as* $1.0\sigma_0$.

Though the structure might be seen as an artefact produced by the constant volume and size of the box shape, a square columnar phase has been observed experimentally in a lyotropic system[4] in which the constituent micelles, lie horizontally within each column. The staggered arrangement and the square lattice within the columnar phase were the same for both densities ρ^* of 2.7 and 3.0. This led us to ask why a hexagonal phase was not observed as this would certainly allow the most efficient packing of the columns within the phase?

It seemed reasonable therefore to perform further simulations at other densities in the expectation of, a) observing hexagonal packing between columns, and b) to see if the columnar phase exists at all at lower densities. These experiments can be thought of as being analogous to various pressure studies performed on a variety of systems. From similar experiments on real rod-shaped mesogens[3], we know that, at constant temperature, as the pressure is decreased any smectic phase present will slowly disappear, with, in most cases, all mesogenic behaviour ceasing at extremely low pressures, though the stability of the phase depends on ΔS and ΔV at the transition via the Clapeyron equation. This behaviour could conceivably be applied to disc-shaped mesogens, with the columnar phases being present at higher pressures, then gradually vanishing as the pressure is reduced.

The starting point for the choice of the simulation density is the phase diagram determined by Frenkel[5] for hard ellipsoids, (see figure 2.3). It would be more useful to redraw the phase diagram by defining the density as a number density, as used in this Thesis, in units $N\sigma_0^3/V$, where N is the number of particles and V the volume of the simulation box, and the aspect ratio a/b, (defined in §2.5), in a simple linear scale, (see figure 3.4). The enclosed area of the graph represents the regions of two phase coexistence, while it is interesting to note that the nematic - isotropic density is essentially independent of the a/b ratio. The original densities ρ^* of 2.7 and 3.0 were chosen as they lay either side of the nematic - isotropic transition boundary as defined by the phase diagram for hard ellipsoids. A density greater than ρ^* of 3.0 could have been chosen, and although this lay in the nematic region of the phase diagram, there is a danger that the density could be too high, leading to the system being locked in an ordered phase at all temperatures.

Conversely, choosing too low a density might mean that no liquid crystal phase would be formed, the particles being too far apart to experience sufficient anisotropic, attractive forces from other particles to hold them in an ordered state. Thus to maximise the probability of forming liquid-crystalline phases as well as exploring the Gay-Berne discogen phase diagram further, a scaled density ρ* of 2.5 was chosen which lay just outside of the nematic region of densities for hard oblate ellipsoids. We must remember that the hard ellipsoid phase diagram is only used as a rough guide in helping us choose the correct density, since the shape and nature of the intermolecular forces of the Gay-Berne particle does not represent a true hard, ellipsoid.

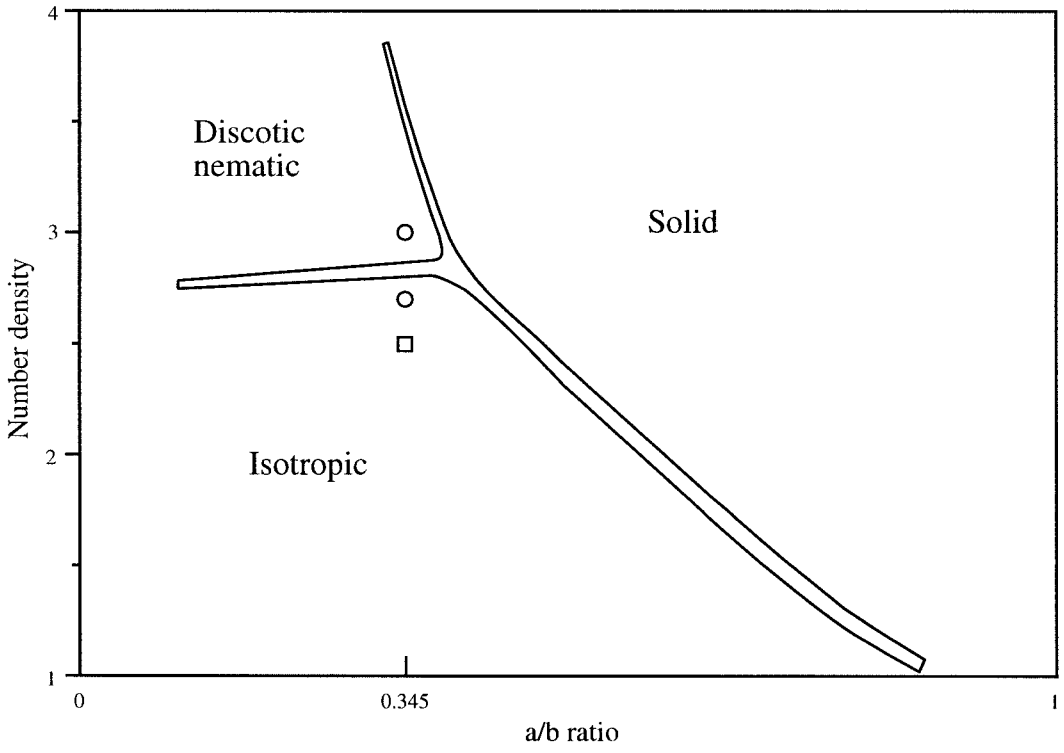

Figure 3.4: *A schematic of the phase diagram for hard ellipsoids[51] redrawn with different axes scales from the original reference. Previous densities used[121] are marked by* ○, *with the density used in this Thesis indicated by* □.

3.2 Parametrisation of the Gay-Berne potential

The development of the Gay-Berne potential, and the variety of parameters used to model rod-shaped mesogens are described in Chapter 2. The Gay-Berne potential has the form

$$U(\hat{\mathbf{u}}_1, \hat{\mathbf{u}}_2, \mathbf{r}) = 4\varepsilon(\hat{\mathbf{u}}_1, \hat{\mathbf{u}}_2, \hat{\mathbf{r}})\left[\left(\frac{\sigma_0}{r - \sigma(\hat{\mathbf{u}}_1, \hat{\mathbf{u}}_2, \hat{\mathbf{r}}) + \sigma_0}\right)^{12} - \left(\frac{\sigma_0}{r - \sigma(\hat{\mathbf{u}}_1, \hat{\mathbf{u}}_2, \hat{\mathbf{r}}) + \sigma_0}\right)^{6}\right], \quad (3.1)$$

where $\hat{\mathbf{u}}_1$ and $\hat{\mathbf{u}}_2$ are the unit vectors for the orientations of the symmetry axes of the two particles and $\mathbf{r}$ denotes the intermolecular vector. In the original development of the potential, the four adjustable parameters, $\varepsilon_f/\varepsilon_e$, σ_f/σ_e, μ and ν, were used to model a best fit for a row of four Lennard-Jones centres[6], each centre being $2/3\sigma_0$ apart. For oblate particles, a best fit to a ring or plate of Lennard-Jones centres could be used, but the aim was also to keep some conformity and simplicity to the model. Though rather than arbitrarily choosing the value of these parameters, there has been some attempt to mimic a real disc-shaped mesogen, so the parameters first used to represent the Gay-Berne discogen were based on triphenylene, and although not liquid-crystalline itself, it is the basis for many discotic mesogens, (see figure 3.1).

The range parameter σ_f/σ_e is the ratio of the separation when the two particles are in a face-to-face (σ_f) or an edge-to-edge (σ_e) arrangement, and in reality controls the shape anisotropy of the particles, thus for the disc-shaped particles of triphenylene, σ_f/σ_e takes the value of 0.345. The energy parameter $\varepsilon_f/\varepsilon_e$ is just the ratio of the well depths for the face-to-face and edge-to-edge arrangements and for our study, the value of 5.0 was used. The variety of values for the parameters, μ and ν are discussed in Chapter 2. Previous simulations of Gay-Berne discogens used the values, μ of 1 and ν of 2, which were chosen because they stabilise the face-to-face and edge-to-edge arrangements relative to the cross and tee arrangements, thus enhancing the formation of translationally ordered phases. For our choice of parameters in this work, it must be remembered that we wanted to investigate the effect of the density of the system, thus it would be sensible to use these same parameters as Emerson to be consistent with previous simulations, thus we kept the values, μ of 1 and ν of 2. The form of the potential energy with respect to the intermolecular separation for the different arrangements of the Gay-Berne discogen is shown in figure 3.5.

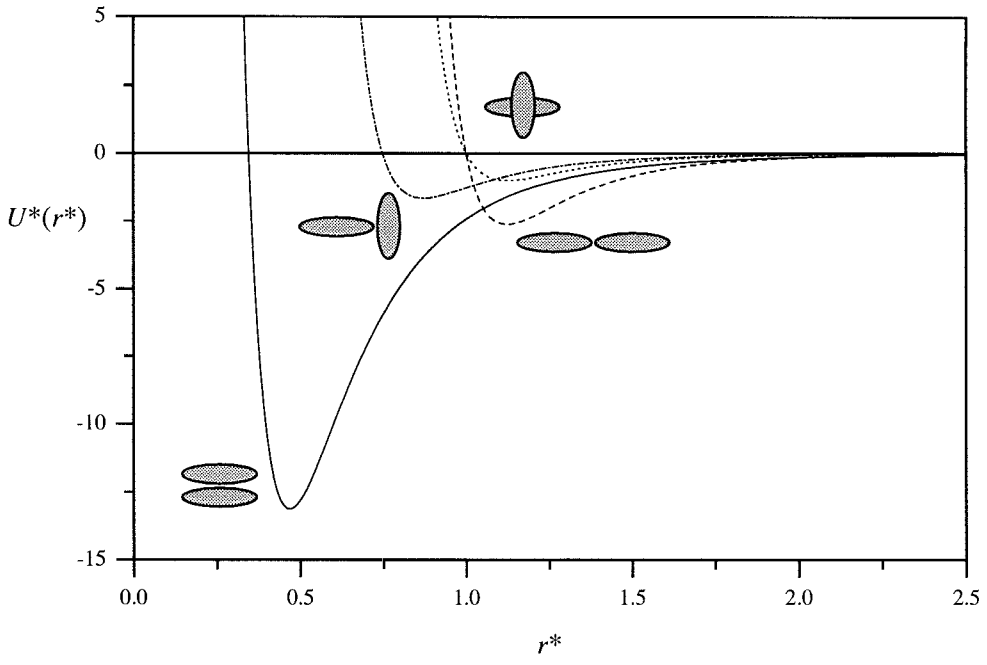

Figure 3.5: *The Gay-Berne potential parametrised for disc-shaped mesogens with* σ_i/σ_e *of 0.345,* $\varepsilon_i/\varepsilon_e$ *of 5.0,* μ *of 1 and* ν *of 2. U*(r*) is the scaled potential energy at a particular scaled separation r*.*

3.3 The molecular dynamics simulation

The simulation was performed in the constant *NVE* or microcanonical ensemble, with 256 particles in a cubic box with periodic boundary conditions. A minimum image summation and a spherical cut-off of $2.0\sigma_0$ were also employed, the latter value chosen as at this point, the potential energy for the model is essentially zero, (see figure 3.5). The scaled density ρ^* of 2.5 was used, this being chosen according to the arguments given in §3.1. The simulation was started from an α-*f.c.c.* lattice with all 256 particles parallel. A scaled time step δt^* of 0.005 was used, with the simulations being performed on an IBM 3090-VF mainframe, with each time step needing 1.5s of c.p.u. time. The phases were identified by graphic visualisation of configurational snapshots and the calculation of various structural distribution functions. Since it was not possible to melt a lattice with a scaled density ρ^* of 2.5, the simulation was started from a lattice with a lower density of 1.8, which was equilibrated at the scaled temperature T^* of 4.0, for 10,000 time steps.

The density was then increased via the intermediate densities of 2.1 and 2.4 scaled units until the desired density, ρ^* of 2.5, had been reached. Equilibration stages of 10,000 time steps were performed after each density rise with the orientational order parameter $\langle P_2 \rangle$ and radial distribution function monitored to ensure that the system had melted. This left the simulation at a temperature T^* of 4.0 and a density ρ^* of 2.5, for which the order parameter $\langle P_2 \rangle$ was 0.897. This indicated that the system was in a highly orientationally ordered state, but from the $g(r^*)$ and graphic snapshots it was clear that the system was in a nematic phase. The temperature was then raised by 1.0 to 2.0 scaled units, with equilibration stages of 10,000 time steps and production stages of 8,000 time steps until T^* had reached 14.0. From previous studies, this temperature should be high enough to form an isotropic liquid; this proved to be the case with $\langle P_2 \rangle$ having fallen to a value of approximately 0.1, the value not being zero due to the associated systematic error in the eigenvalue of the **Q** tensor (see §2.4).

The scaled time step δt^* could have been adjusted at each state point to give acceptable temperature and energy conservation, but was not necessary as the values were generally to within a few parts in 10^4. From the state point ρ^* of 2.5 and T^* of 14.0, the temperature was lowered in steps of 0.5 to 1.0 scaled units until a temperature T^* of 0.5 was achieved. By now the order parameter $\langle P_2 \rangle$ had reached a value of 0.995, consistent with a very highly orientationally ordered phase, probably a crystalline phase. For each state point, the system underwent an equilibrium stage consisting of between 10,000 and 60,000 time steps, until the temperature and order parameter had reached constant values. A production stage was then performed in which the temperature scaling was turned off and the simulation run until the values of the properties, T^* and $\langle P_2 \rangle$ had reached equilibrium. The values of the important properties obtained from the cooling run are given in table 3.1.

Set T^*	Actual T^*	$N_E/10^3$	$N_P/10^3$	$\langle U^* \rangle$	$\langle P_2 \rangle$
14	13.41 ± 0.21	30	10	−6.56 ± 0.54	0.106 ± 0.051
13	12.88 ± 0.19	30	15	−7.21 ± 0.41	0.094 ± 0.013
12	12.05 ± 0.24	30	10	−8.07 ± 0.61	0.102 ± 0.019
11	11.05 ± 0.14	30	25	−9.21 ± 0.53	0.121 ± 0.025
10	10.77 ± 0.12	30	20	−9.69 ± 0.59	0.151 ± 0.021
9	9.09 ± 0.14	60	10	−16.12 ± 0.56	0.556 ± 0.025
8	8.11 ± 0.09	20	10	−19.86 ± 0.46	0.682 ± 0.014
7	7.17 ± 0.07	20	10	−23.94 ± 0.47	0.797 ± 0.011
6	5.94 ± 0.08	15	10	−27.51 ± 0.54	0.859 ± 0.012
5	5.04 ± 0.05	15	10	−30.02 ± 0.32	0.901 ± 0.015
4	4.04 ± 0.06	15	10	−32.73 ± 0.35	0.931 ± 0.015
3	3.03 ± 0.04	15	10	−35.44 ± 0.41	0.952 ± 0.011
2	2.01 ± 0.02	20	10	−41.51± 0.17	0.981 ± 0.007
1	0.98 ± 0.03	10	10	−44.32 ± 0.09	0.991 ± 0.003
0.5	0.55 ± 0.01	10	10	−45.44 ± 0.08	0.995 ± 0.002

Table 3.1: *Values of T^*, $\langle U^* \rangle$ and $\langle P_2 \rangle$ for the simulation at ρ^* of 2.5, where N_E and N_P are the number of time steps performed during the equilibrium and production stages.*

3.4 Results and discussion

3.4.1 Orientational properties

Second and fourth rank order parameters: The variation of the second rank order parameter $\langle P_2 \rangle$ with temperature T^* for the cooling run of the simulation is shown in figure 3.6. As the temperature was lowered from T^* of 13.41 to 10.77, $\langle P_2 \rangle$ remained relatively constant at around a value of 0.1, suggesting that the phase is isotropic. This value of $\langle P_2 \rangle$ was not exactly zero because the system was probably fluctuating between the isotropic and nematic phases, although there is also an inherent statistical uncertainty in the value of $\langle P_2 \rangle$, when calculated from the **Q** tensor, of the order of $1/\sqrt{N}$ i.e. 0.0625. When the system was cooled from T^* of 9.09 to 0.55, the order parameter rose until it attained a value close to unity, the gradual increase in the order parameter suggesting that we had formed intermediate orientationally ordered phases. As with previous simulations[121], the change in $\langle P_2 \rangle$ from the disordered phase (above T^* of 9.09) to an ordered phase (T^* of 9.09 and below) was relatively sharp indicating a possible first order transition.

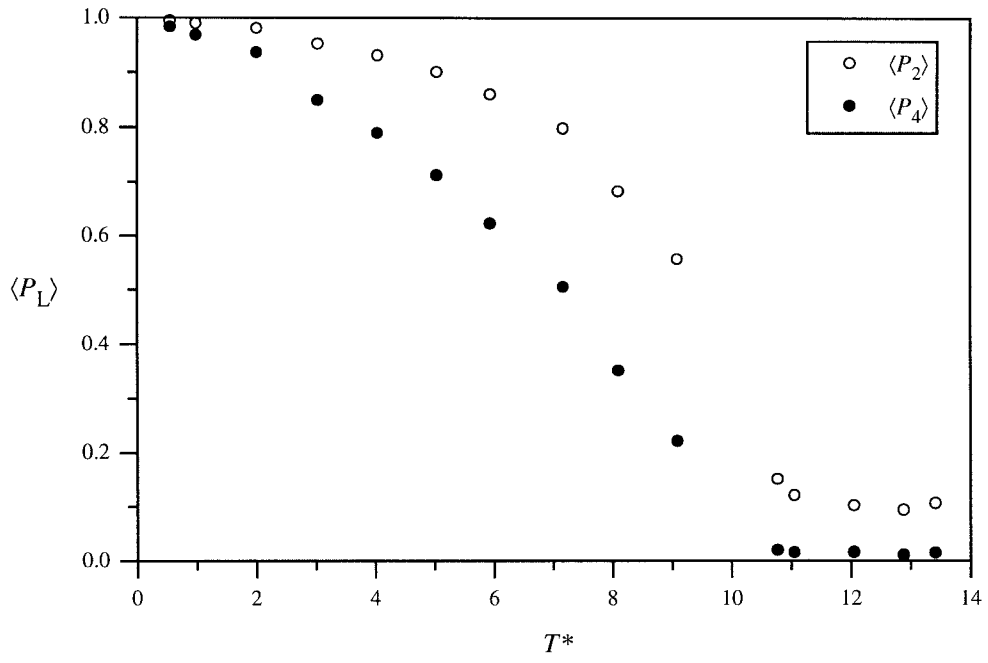

Figure 3.6: *Variation of the order parameters $\langle P_2 \rangle$ and $\langle P_4 \rangle$ with scaled temperature T*.*

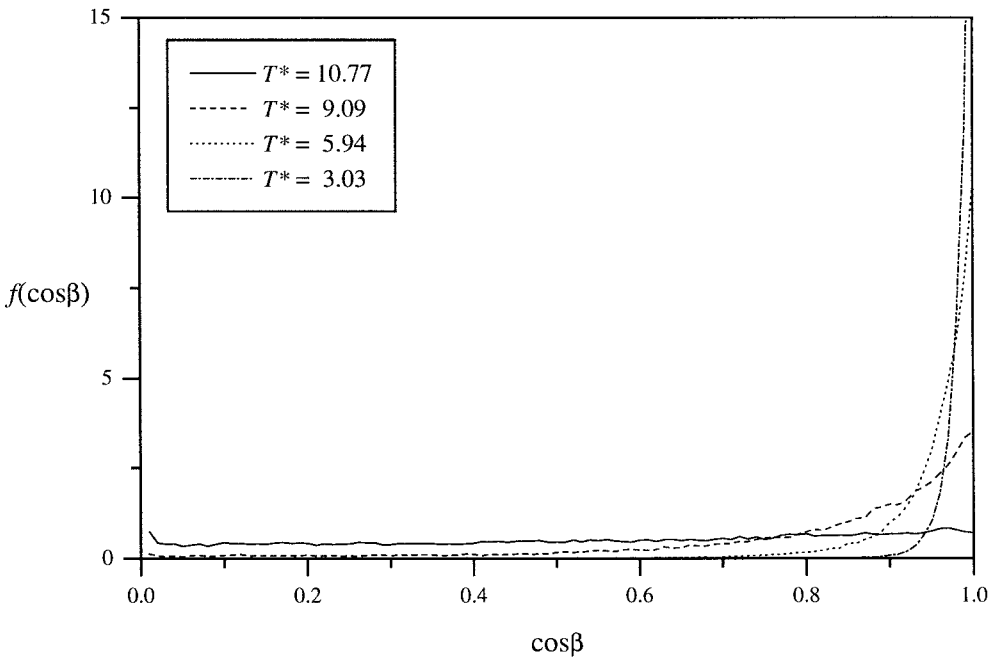

Figure 3.7: *The plot of $f(\cos\beta)$ for the system at the scaled temperatures T* indicated.*

The variation of the fourth rank order parameter $\langle P_4 \rangle$ with the scaled temperature T^* for the cooling run is also shown in figure 3.6. The shape of the curve mimics that obtained for $\langle P_2 \rangle$, though the values are lower as expected. There is also a rise in $\langle P_4 \rangle$ at the phase transition, between T^* of 10.77 and 9.09, as for the second rank order parameter, though it is not quite so pronounced.

Singlet orientational distribution function: The singlet orientational distribution function $f(\cos\beta)$ for both the isotropic and discotic nematic phases are shown in figure 3.7. For the isotropic phase, T^* of 10.77, we can see that the probability is essentially the same for all orientations, showing the randomness of the system. For the discotic nematic phase, at T^* of 9.09, the plot of $f(\cos\beta)$ peaks at $\cos\beta$ equal to one, as expected, indicating that there is a preferred direction of orientation. The plot decays as the value of β increases towards an orientation perpendicular to the director, telling us that very few particles lie with their symmetry axes along this direction. As the temperature is lowered, the peak at $\cos\beta$ of 1 grows, reflecting the increased ordering of the particles with their symmetry axes parallel to the director. A comparison of the orientational properties compared with the predictions of the Maier-Saupe theory will be presented in §3.4.5.

3.4.2 Thermodynamic properties

Internal energy: The plot of the scaled internal energy per particle $\langle U^* \rangle$ ($\equiv \langle U \rangle / N\varepsilon_0$) against scaled temperature T^* is shown in figure 3.8. This graph indicates two changes in the slope of the internal energy; the first change in $\langle U^* \rangle$ between the temperatures 10.77 and 9.09, agrees with the change in the second rank order parameter $\langle P_2 \rangle$, in that the system has undergone a phase transition from a disordered to an ordered state, more than likely the nematic - isotropic phase transition. The second discontinuity in the plot of $\langle U^* \rangle$ occurs between the lower scaled temperatures, T^* of 3.03 and 2.01. This indicates another phase transition, this time between two orientationally ordered phases. However at this stage we do not have enough information to speculate on what mesophases these may be.

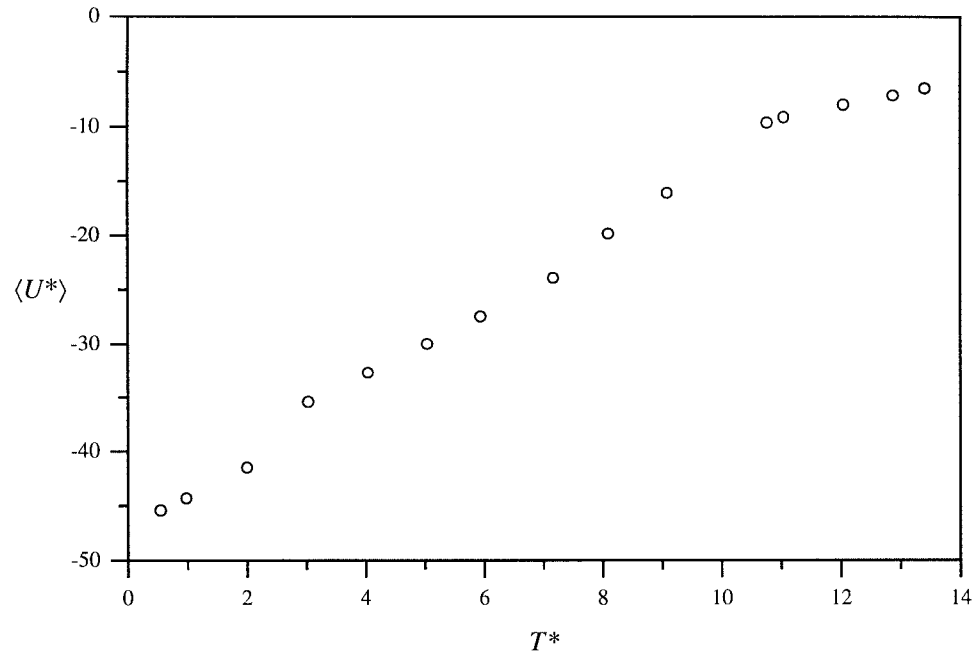

Figure 3.8: *Variation of the internal energy ⟨U*⟩ with the scaled temperature T*.*

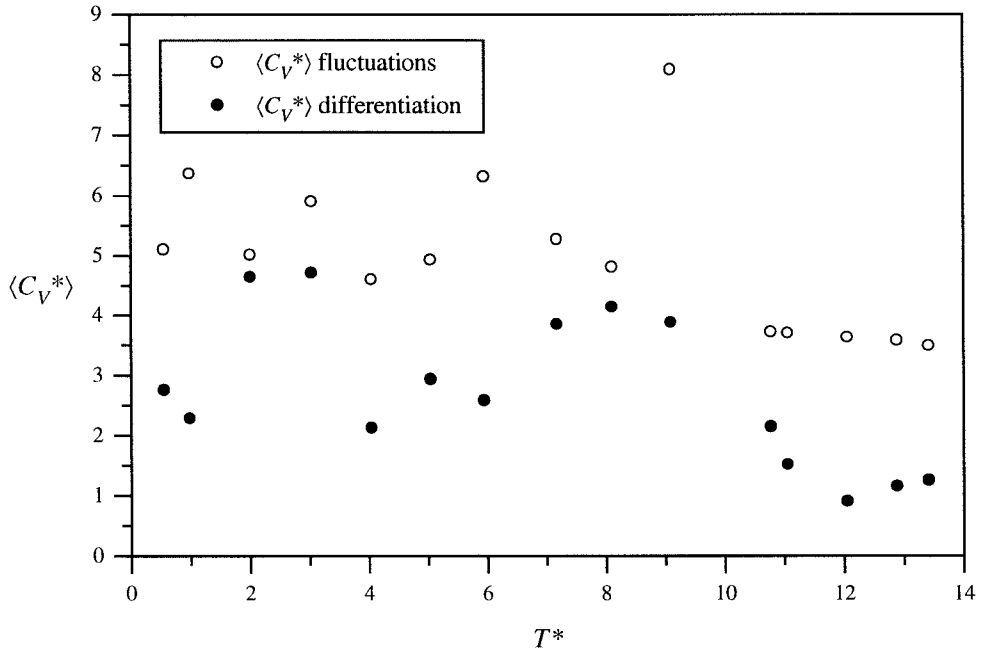

Figure 3.9: *Variation of the heat capacity ⟨C_V*⟩ with the scaled temperature T*.*

Heat capacity: The plot of the scaled heat capacity $\langle C_V^* \rangle$ ($\equiv \langle C_V \rangle / N k_B$) against temperature is shown in figure 3.9. This shows the heat capacity as calculated from both the fluctuations in the kinetic energy and the differentiation of the internal energy $\langle U^* \rangle$. The graph from the fluctuation method yields no real information about the system, though there seems to be a large peak corresponding to the nematic - isotropic transition at around T^* of 9.09 but this is only one value which may well be in error. The heat capacity from the cubic spline differentiation of the internal energy only reveals the discontinuities already present in the plot of $\langle U^* \rangle$, and as such gives us no new insight into the behaviour of the system.

3.4.3 Structural Properties

Graphic visualisation and g(r):* Of the various properties calculated during the course of the simulation, the two with the most readily accessible information are the radial distribution function $g(r^*)$, (see §2.4) and computer graphic visualisation. The latter technique consists of taking a single configuration from the production run, and displaying the image using the Silicon Graphics GL graphics library. This method represents each particle as a solid three dimensional ellipsoidal body, giving a realistic view of the system. But there is a fundamental difference between the technique and the $g(r^*)$ as it shows just one configuration at one point in phase space, while the $g(r^*)$ is averaged over many configurations of the simulation.

The radial distribution function $g(r^*)$, plotted against the scaled temperature for the simulation is shown in figure 3.10. The first phase to be identified is that at T^* of 10.77 and above, previously assigned as the isotropic fluid, due to the low orientational order present. We can see that the plot of $g(r^*)$ shows no long range translational order and only a small amount of short range order though even this appears to be more consistent with a gas phase than an isotropic fluid, a point we shall discuss later. The small peak at r^* of 0.8 seems to indicate that the particles, rather than existing in an edge-to-edge arrangement, as would be given by a peak at $1.0\sigma_0$, seem to prefer to lie in a slightly overlapping arrangement. The configurational snapshot, (see figure 3.12), reveals no major orientational or translational order, so we can safely assign this phase as the isotropic fluid.

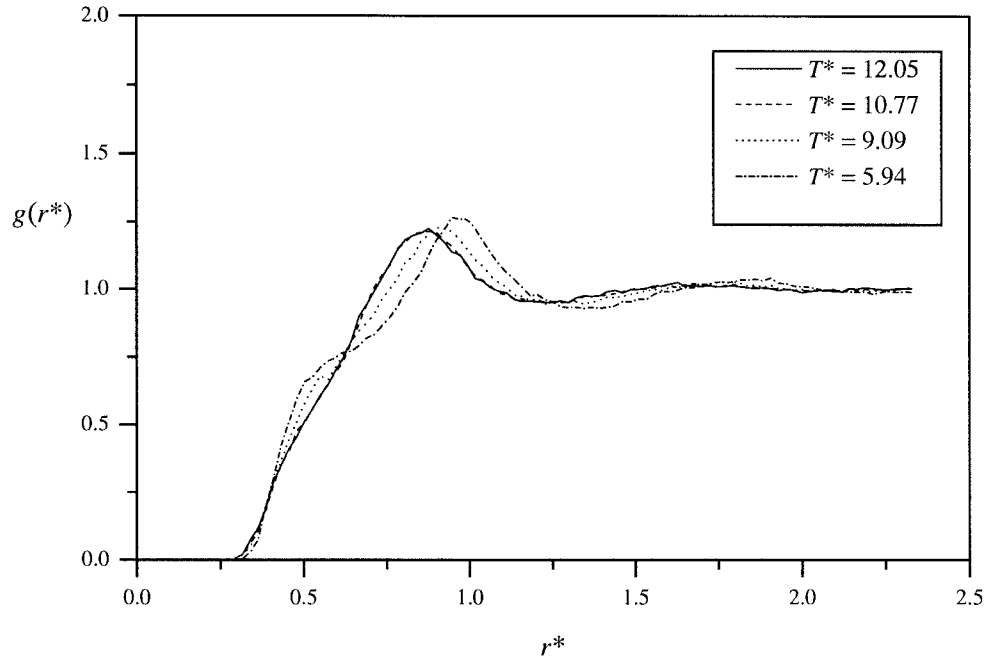

Figure 3.10: *The radial distribution function g(r*) at the scaled temperatures T* indicated.*

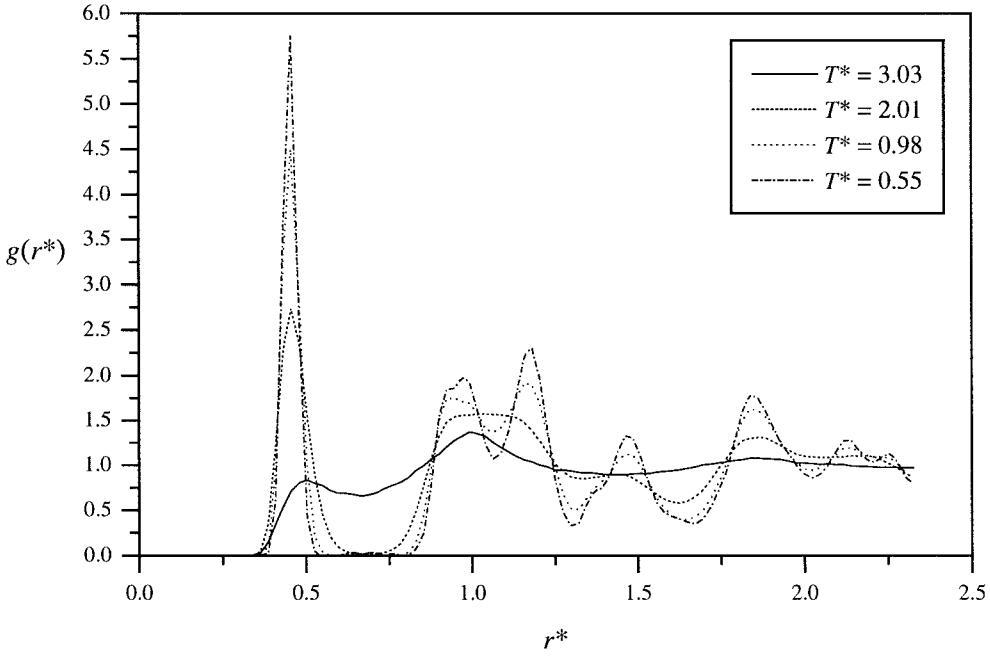

Figure 3.11: *The radial distribution function g(r*) at the scaled temperatures T* indicated.*

The next phase to be investigated is that possessing orientational order, occurring between the temperatures T^* of 9.09 and 3.03, the boundaries indicated by the plot of the scaled internal energy $\langle U^* \rangle$, (see figure 3.8). At the higher temperature of 9.09, it is noticeable that although the phase has a high orientational order, the plot of the $g(r^*)$ is essentially the same as that of the isotropic fluid, showing once again the lack of long range translational order. There is a slight peak at r^* of 0.9, showing the preference for a slightly overlapping edge-to-edge arrangement. Considering these factors, namely long range orientational order but short range translational order, we identify this phase as the discotic nematic phase. This is illustrated by the configurational snapshots, taken a) parallel and b) perpendicular to the director and shown in figure 3.13.

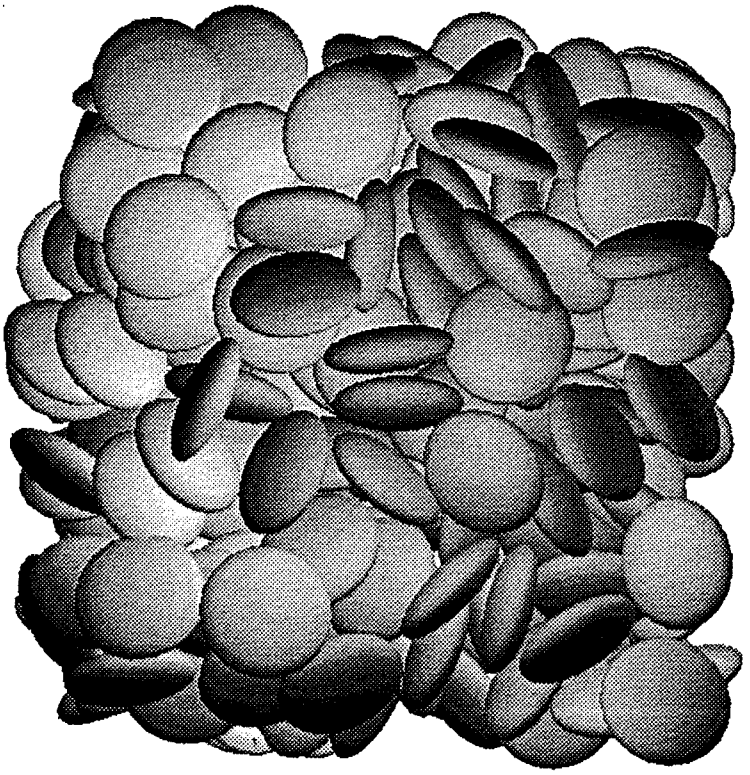

Figure 3.12: *The configurational snapshot for the isotropic phase at the scaled temperature T* of 10.77.*

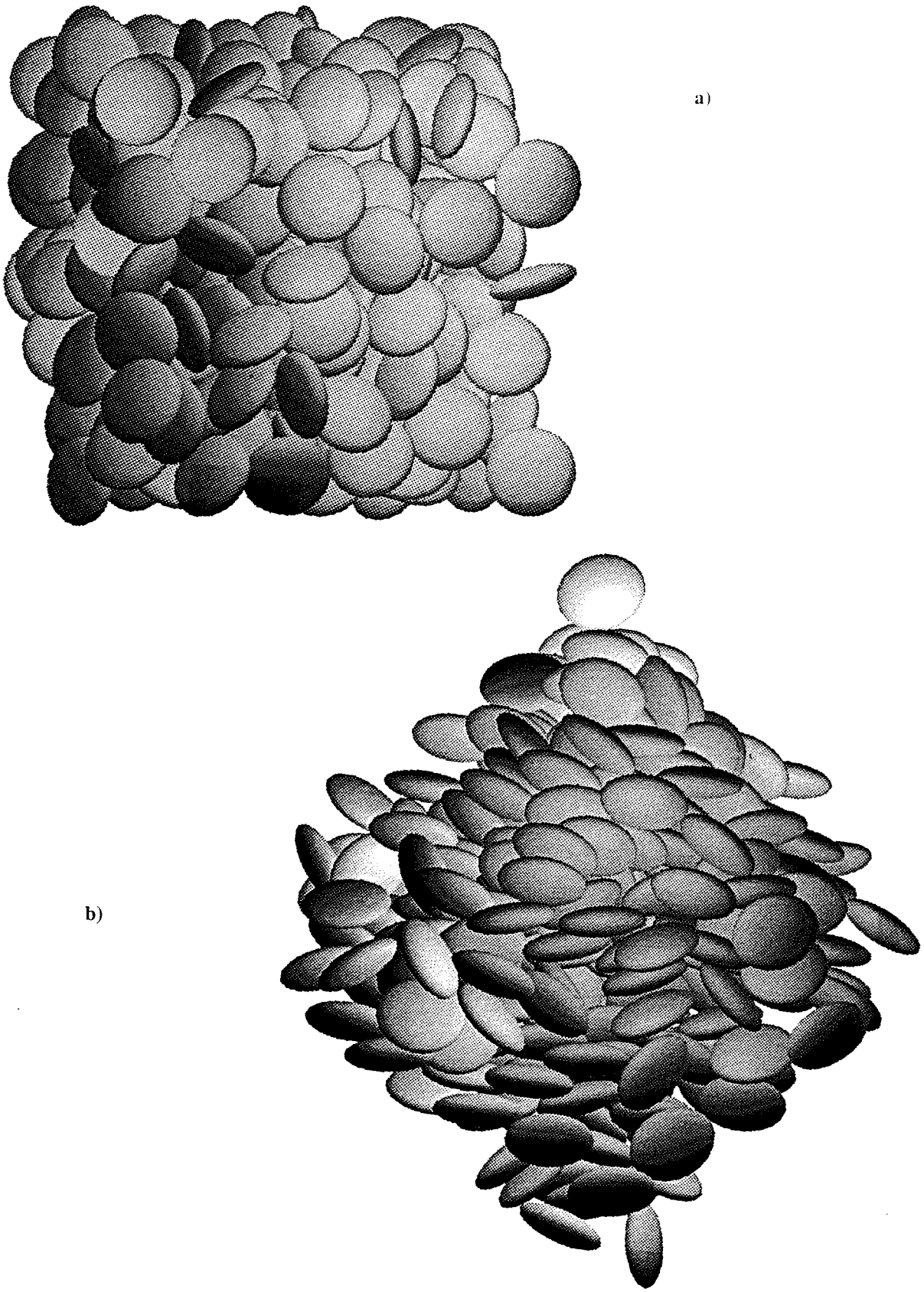

Figure 3.13: *The configurational snapshots taken a) parallel and b) perpendicular to the director for the discotic nematic phase at the scaled temperature T* of 9.09.*

Inspection of the plot of the radial distribution function and the configurational snapshots for T^* of 3.03, the low temperature limit of the discotic nematic phase, revealed two interesting features. First, a peak at $r^* \approx 0.5$, which is present at higher temperatures and probably represents the face-to-face arrangement, has become more prominent though its maximum value was still lower than one i.e. the value for the gas phase. This suggests that even though the face-to-face arrangement is still not favoured compared to the edge-to-edge, the increase in the peak height reflects an increase in face-to-face ordering.

It might seem that this behaviour, as indicated by the plots of $g(r^*)$, is somewhat strange but it is consistent with results obtained from theoretical and molecular dynamics studies[7,8] of hard, oblate ellipsoids and from the previous simulations of the Gay-Berne discogen[2]. The explanation for the low value of the peak at r^* of 0.4 comes from the definition of the radial distribution function[9]. It measures the number of particles in a spherical shell of a certain width from the origin, scaled with the number of particles in an ideal gas. Because of the excluded volume of the discogen, the number of particles that lie within a spherical shell of radius σ_e is necessarily less than that appearing in the scaling factor.

The second feature of note is the peak found at r^* of 0.9 when T^* of 9.09, which has now moved to r^* of 1.0 at the lower temperature, showing that the particles in the edge-to-edge arrangement, previously overlapping, have now moved into a real edge-to-edge arrangement. Again this shows, that despite the phase still being a discotic nematic, there is possible pretransitional, translational ordering occurring before the onset of a columnar phase. The configurational snapshots do indeed show the phase as a discotic nematic. The view of the image parallel to the director, (see figure 3.14a), shows a random distribution of particles, while the view perpendicular to the director, (see figure 3.14b), illustrates the presence of high orientational order but with short range translational order.

We have now identified two different phases, an isotropic fluid at temperatures T^* of 10.77 and above, and the liquid-crystalline discotic nematic phase between T^* of 9.09 and 3.03. It now remains to characterise the highly orientationally ordered phase or phases at temperatures lower than T^* of 3.03.

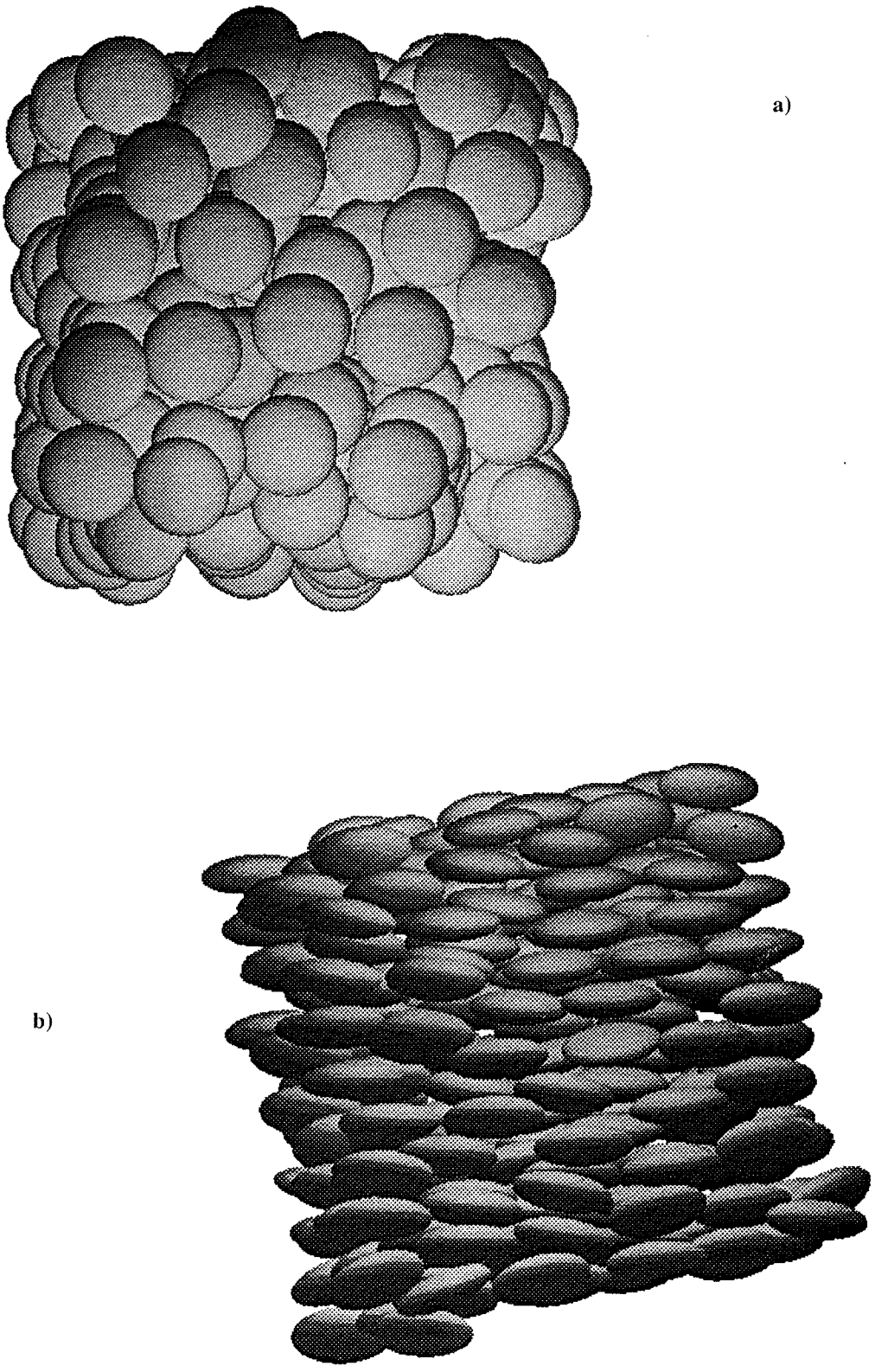

Figure 3.14: *The configurational snapshots taken a) parallel and b) perpendicular to the director for the discotic nematic phase at the scaled temperature T^* of 3.03.*

The first feature of interest is the peak at r^* of 0.46, which corresponds to the particles approaching each other in a face-to-face arrangement. Though present in the nematic phase, it was not of sufficient intensity to be considered as a structural feature, but as the height of this peak is above one, this suggests that columnar order has been formed, but as the thickness of a disc is $0.345\sigma_0$, the particles are not close packed within each column.

The peaks around $1.0\sigma_0$ seem to indicate an edge-to-edge arrangement though no definite assignments can be made at this stage because we do not know the symmetry of the phase. We can distinguish between two possible ordered phases by comparing the maximum values of $g(r^*)$. For the temperatures T^* of 0.98 and 0.55, at r^* of 0.46, the maximum value of $g(r^*) \approx 6$ and as the height of the peaks represents the number of nearest neighbours, and assuming hexagonal or rectangular symmetry, which is not unreasonable, we could assign the phases at these temperatures as crystals.

For the temperature T^* of 2.01 though the value of $g(r^*)$ is high, at around 3, we can deduce that though it is highly ordered, it is not a crystalline phase. So what is it? Looking at the configurational snapshots, (see figure 3.15b), it is obvious that the system has formed a columnar phase, with particles in neighbouring columns being interleaved with respect to each other. This is not remarkable in itself as exactly the same structure was observed in earlier work[2], via $g_{||}(r_{||}^*)$, which gave the distance between particles in a face-to-face arrangement as $0.22\sigma_0$, half the actual difference as revealed by the $g(r^*)$. On closer examination however, looking down the director, (see figure 3.15a), we can see that the columns have arranged themselves into a hexagonal net. This is in contrast to the square net produced at the higher densities ρ^* of 2.7 and 3.0.

Having proposed a D_h symmetry for the columnar phase and seen that the particles within the columns are ordered and staggered with respect to particles in neighbouring columns, we can now assign the peaks in the radial distribution function with greater certainty, (see figures 3.10 and 3.11). The peak at $r^* \approx 0.5$ represents the particles stacking face-to-face to form columns.

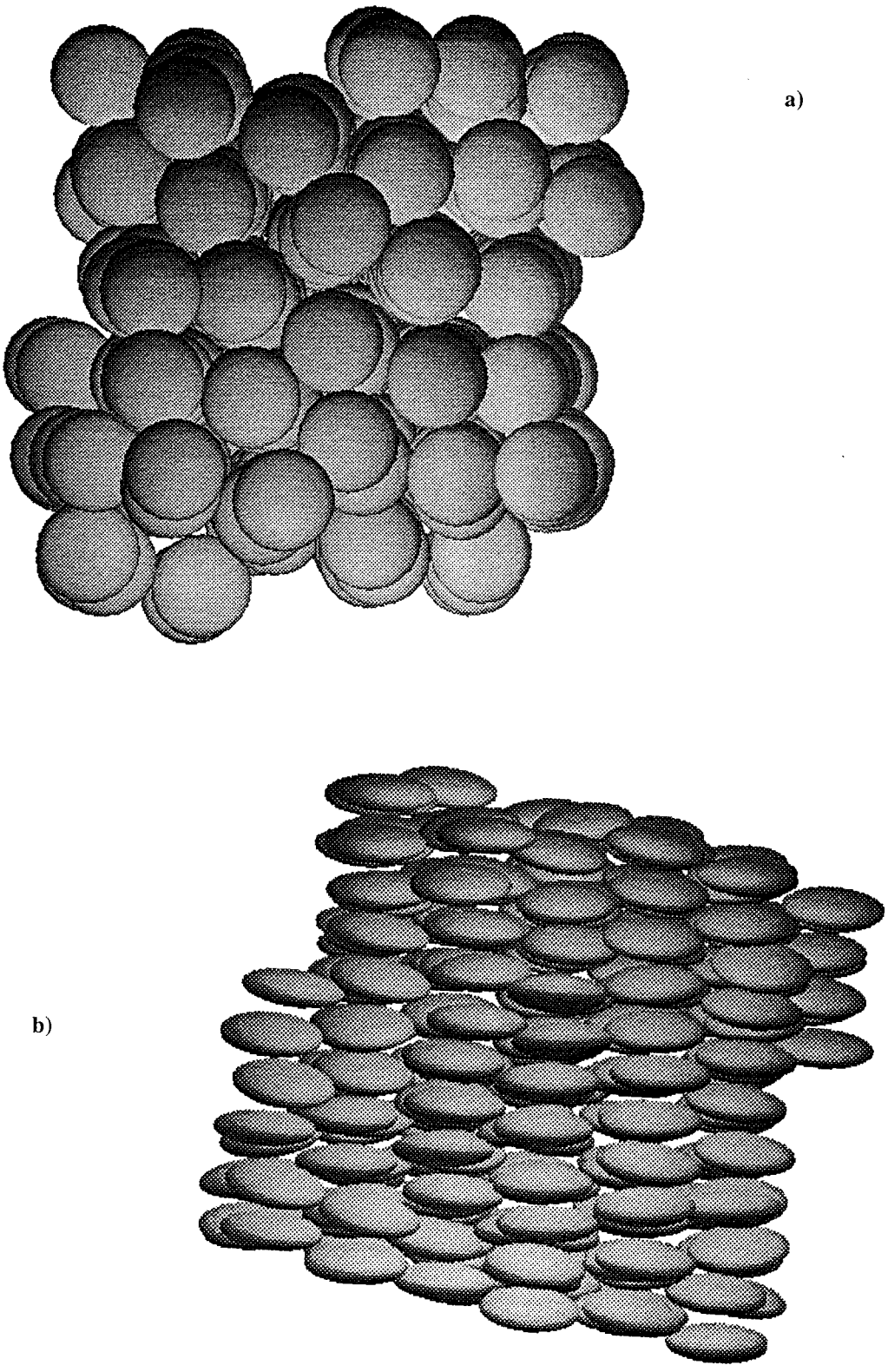

Figure 3.15: *The configurational snapshots taken a) parallel and b) perpendicular to the director for the columnar phase at the scaled temperature T* of 2.01.*

The peak at around $0.9\sigma_0$ is from particles within the same column but an extra $0.46\sigma_0$ on, while the peak at r^* of 1.1 is the distance between particles in neighbouring columns, which is slightly greater than 1 because they are not in the same plane but staggered. The peaks at scaled distances greater than r^* of 1.5 come from a complicated superposition of particles in various arrangements with the main contributions being from the next shell of columns packing in a hexagonal fashion, r^* of 1.8 and 2.1, and from particles along a column. But why are the particles within a columnar interdigitated rather than lying in plane with particles in neighbouring columns? and why are the particles evenly spaced within each column rather than in an random arrangement? These questions can be answered by looking at the plots of the energy of interaction between two particles with their symmetry axes parallel i.e. in a face-to-face and edge-to-edge arrangements, (see figure 3.5). Within a column, the particles are about $0.46\sigma_0$ apart, inferred from the $g(r^*)$, thus it seems that the minimum separation depends on the minimum energy distance, this being $\approx 0.5\sigma_0$. But why are the particles within a columnar interdigitated rather than lying in plane with particles in neighbouring columns? We have seen in both the isotropic and discotic nematic phases, that the particles prefer to pack in a slightly off edge-to-edge arrangement. From the packing behaviour, we expect two hard ellipsoids to slip over each other rather than lie in the same plane, and from figure 3.5, we can see that in a slightly overlapping edge-to-edge arrangement, there is still a considerable attractive part of the potential which will help stabilise this arrangement. But we must not overlook the effect, the fixed size and shape of the simulation box might have on the packing of the columns.

The orientational correlation function: The graph of $G_2(r^*)$ for various scaled temperatures is shown in figure 3.16, the range of the graph being determined by the maximum size of the simulation box i.e. $2.34\sigma_0$. For the isotropic fluid, T^* of 10.77, there is essentially no long range orientational order as the limiting value of $G_2(r^*)$ decays rapidly to zero. In the nematic phase, T^* of 9.09, the plot of $G_2(r^*)$ has a non-zero limiting value, equivalent to $\langle P_2 \rangle^2$, (see table 3.2) showing the persistence of long range orientational order. This leads to a value of 0.552 for the order parameter which is in good agreement with $\langle P_2 \rangle$ of 0.556, obtained from the **Q** tensor. The plots for $G_2(r^*)$ at the other values of T^* all show increasing long range orientational order as the system is cooled.

The high values at separations less than $0.5\sigma_0$, indicate that the particles at these separation are in a face-to-face arrangement, having their orientation vectors parallel, hence their value of $G_2(r^*)$ of 1, though this does not mean that the face-to-face arrangement is necessarily favoured. Also noticeable for the higher temperatures, is a slight peak at around r^* of 1. This illustrates, that for particles at this distance apart, in an edge-to-edge arrangement, there is a greater degree of short range orientational order.

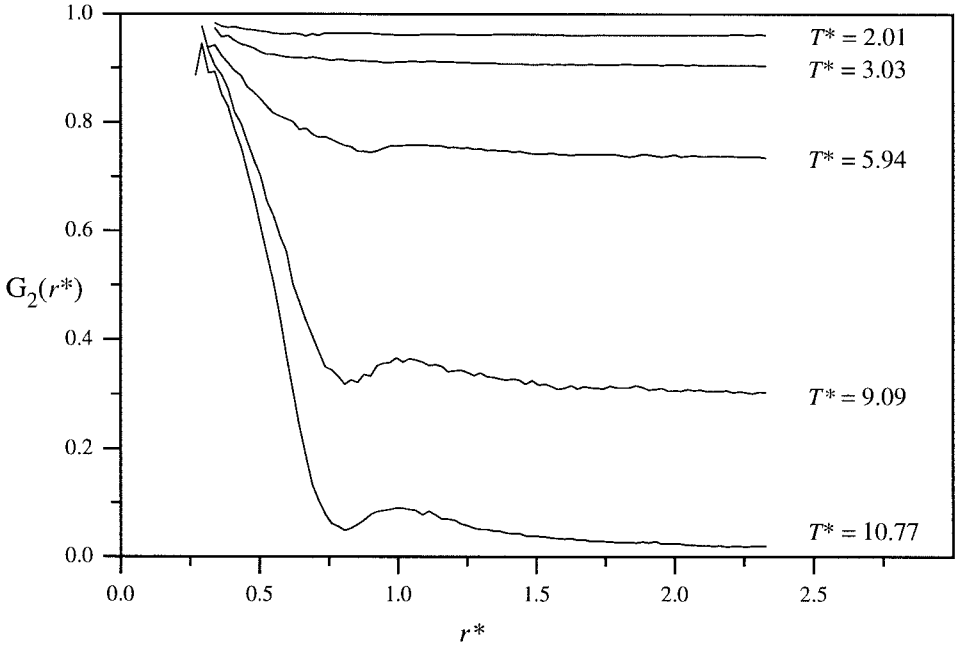

Figure 3.16: *The pair orientational correlation function $G_2(r^*)$ for the scaled temperatures T^* indicated.*

T^*	$\langle P_2 \rangle$ *from* $\mathbf{Q}$ *tensor*	$\langle P_2 \rangle$ *from* $G_2(r^*)$
10.77 ± 0.12	0.151 ± 0.021	0.138
9.09 ± 0.14	0.556 ± 0.025	0.552
5.94 ± 0.08	0.859 ± 0.012	0.857
3.03 ± 0.04	0.952 ± 0.011	0.951
2.01 ± 0.02	0.981 ± 0.007	0.982
0.55 ± 0.01	0.995 ± 0.002	0.995

Table 3.2: *Values of $\langle P_2 \rangle$ calculated from the $\mathbf{Q}$ tensor and the limiting values of $G_2(r^*)$.*

Longitudinal and transverse pair correlation functions: These distribution functions are essentially the radial distribution function along a direction either parallel or perpendicular to the director. Figures 3.17 and 3.18 show the $g_{||}(r_{||}^*)$ for temperatures between T^* of 12.05 and 0.55. We can see that for the isotropic phase, T^* of 12.05 and 10.77, and the nematic phase, between T^* of 9.09 and 3.03, there is little indication of any short range or long range translational order along the director, though there is a very small, broad peak centred at about $0.5\sigma_0$ within the nematic phase. This does increase slightly in intensity as the temperature is lowered and represents a build up of short range translational order in the form of the face-to-face arrangement. For the columnar phase we expect the plot of $g_{||}(r_{||}^*)$ to be very different. It shows a series of highly defined peaks which should correlate to the inter-particle distances within the columns. The distance between the peaks is about $0.22\sigma_0$ which is half the value given by the radial distribution function $g(r^*)$ for the face-to-face distance, thus what the $g_{||}(r_{||}^*)$ is actually showing is the vertical distance between one particle and its next nearest neighbour in an adjacent column.

We can now investigate the translational structure perpendicular to the director by looking at the transverse pair correlation function $g_{\perp}(r_{\perp}^*)$, (see figures 3.19 and figure 3.20). For the isotropic phase at T^* of 10.77 and the nematic phase at T^* of 9.09, we see little structure except for a small peak at around $0.9\sigma_0$ indicating some correlation between particles in an overlapping edge-to-edge arrangement. The absence of any particles in the face-to-face arrangement is shown by the plot of $g_{\perp}(r_{\perp}^*)$ taking a value below 1 at r^* of 0.0.

At T^* of 3.03, the lowest temperature of the discotic nematic range, the graph of $g_{\perp}(r_{\perp}^*)$ shows that the peak, originally at $0.9\sigma_0$ has now moved to $1.0\sigma_0$ indicating the preference for the edge-to-edge arrangement. There is also an additional peak at r^* of 0.0. This is picking up particles directly above each other, in the process of forming columns i.e. in the face-to-face arrangement. Again this is an indicator of the pretransitional ordering present within the discotic nematic phase at this temperature. In the columnar phase, T^* of 2.01, the arrangement between the columns becomes more apparent.

The peaks at r^* of 0.0 and 1.0 indicate a columnar structure, the particles within the same column being represented at r^* of 0.0 with neighbouring columns being $1.0\sigma_0$ apart, and not interpenetrating as in the square columnar phase. The peak at r^* of 1.8 originates from the next shell of columns in a hexagonal arrangement.

Density distribution functions: The density distribution functions $\rho_{||}(r_{||}^*)$ and $\rho_{\perp}(r_{\perp}^*)$ for the discotic nematic and columnar phases, again show the onset of long range translational order at the lower temperature. The density distribution function $\rho_{||}(r_{||}^*)$ illustrates nicely the onset of long range translational order in the system along the director, (see figure 3.21 and figure 3.22). For the nematic phase, the plot is linear but for the columnar phase, T^* of 2.01, the plot is dramatically different, with the peak position, being a measure of the distance between particles within each column. This is given, from the plot of $\rho_{||}(r_{||}^*)$ as 0.21 but again this does not agree with the value of 0.5 for the face-to-face arrangement as given by the $g(r^*)$. As with the $g_{||}(r_{||}^*)$, what this distribution function is revealing is the distance between neighbouring particles in adjacent columns, backing up the conclusion that the neighbouring columns are interdigitated.

Figures 3.23 and 3.24 shows the distribution of the particles perpendicular to the director, $\rho_{\perp}(r_{\perp}^*)$. For the discotic nematic phase, T^* of 3.03, we can see some small amount of order within the simulation box, while for the columnar phase at T^* of 2.01, the plot of the $\rho_{\perp}(r_{\perp}^*)$ indicates the formation of the columns across the box, each one being roughly $1.0\sigma_0$ apart. It is unfortunate that the plane of $r_{\perp}^*$ is not unique in that we cannot distinguish between the two orthogonal planes x and y, perpendicular to the director, as this would yield greater information about the structure of the phase under investigation. A similar restriction occurs when we calculate both the $g_{\perp}(r_{\perp}^*)$ and the X-ray diffraction patterns in the next chapter.

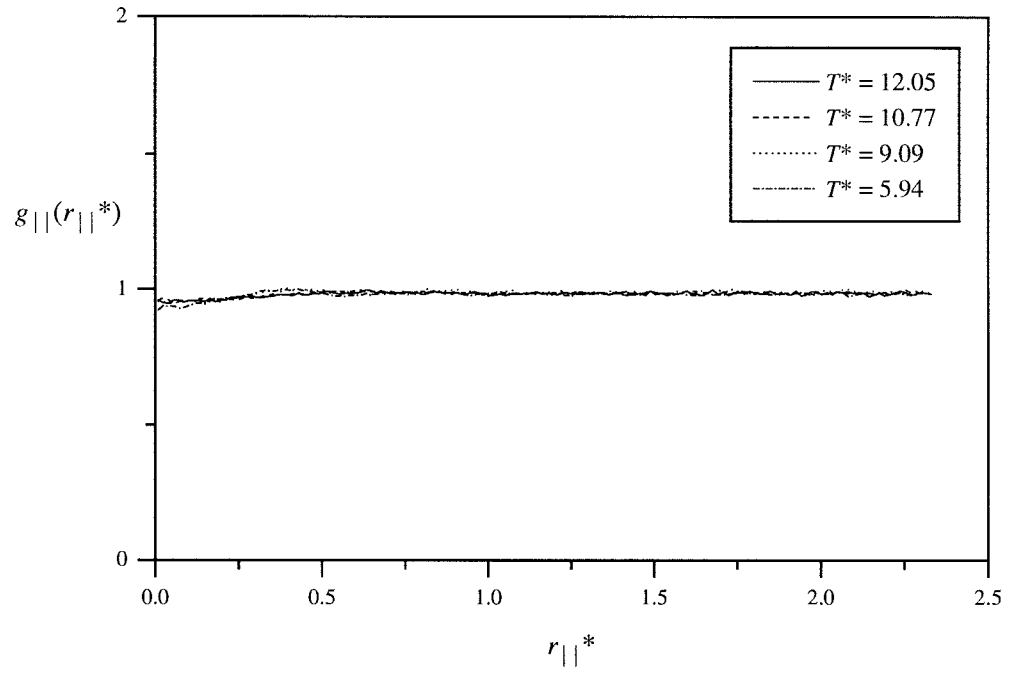

Figure 3.17: *The longitudinal pair correlation function $g_{||}(r_{||}^*)$ at the scaled temperatures T* indicated.*

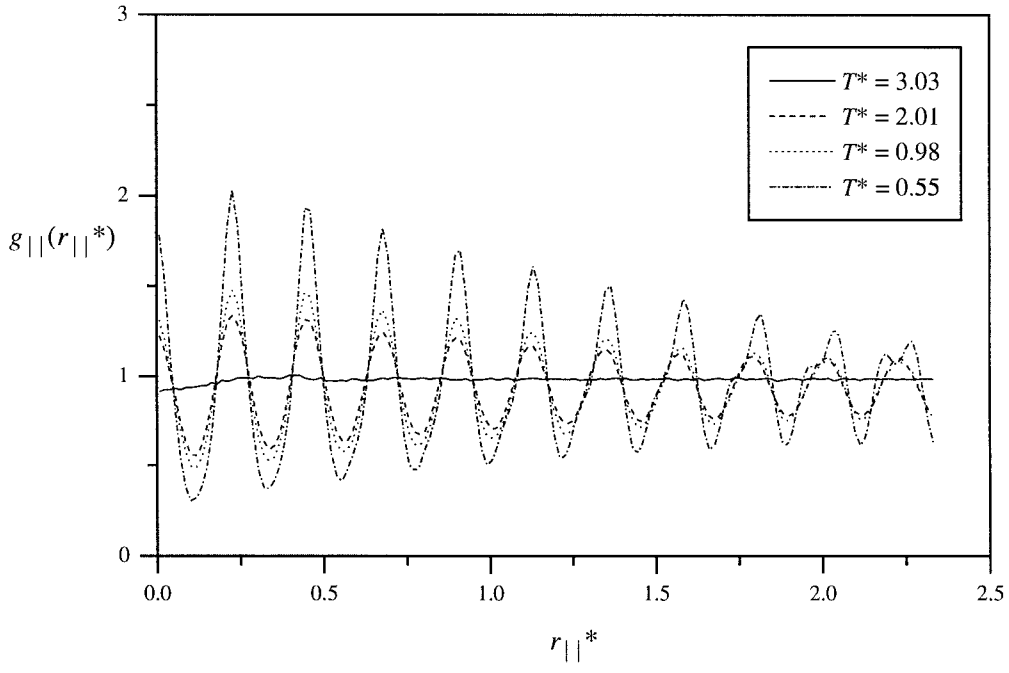

Figure 3.18 *The longitudinal pair correlation function $g_{||}(r_{||}^*)$ at the scaled temperatures T* indicated.*

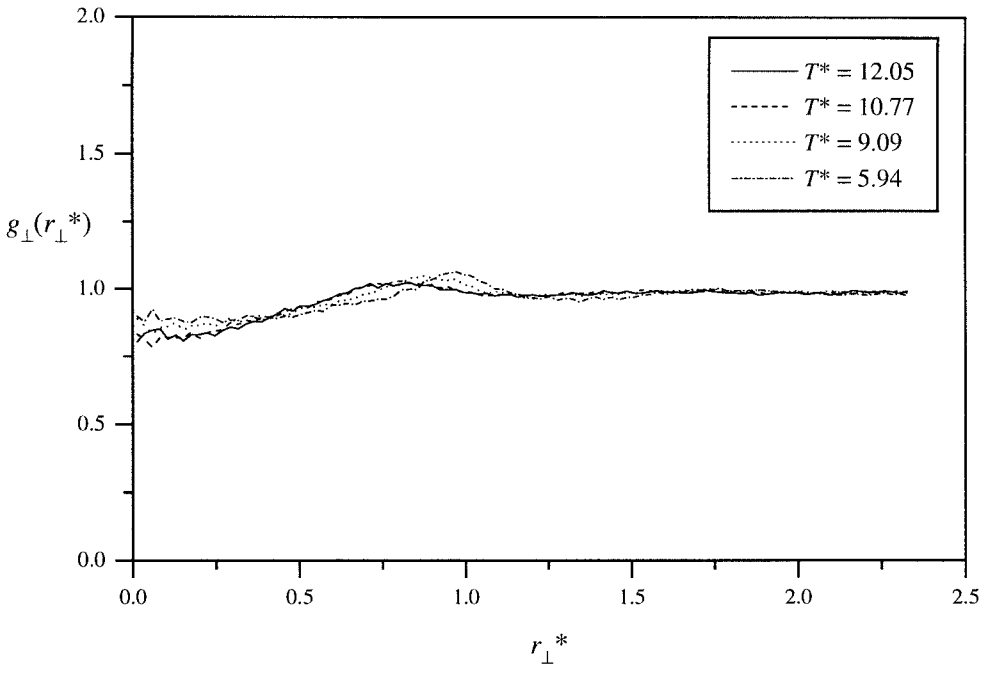

Figure 3.19: *The transverse pair correlation function $g_\perp(r_\perp^*)$ at the scaled temperatures T* indicated.*

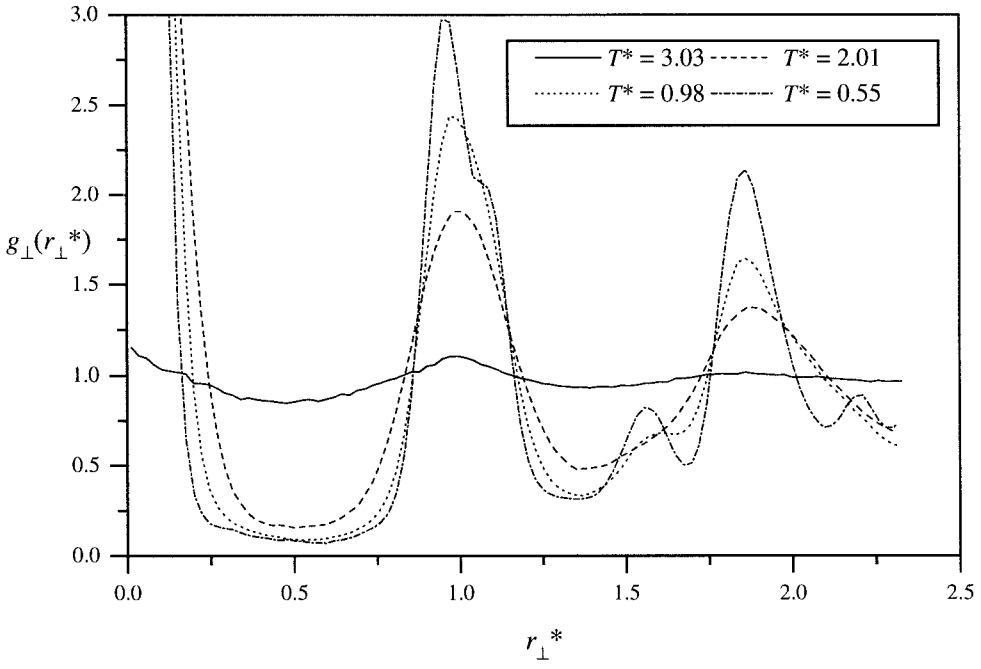

Figure 3.20: *The transverse pair correlation function $g_\perp(r_\perp^*)$ at the scaled temperatures T* indicated.*

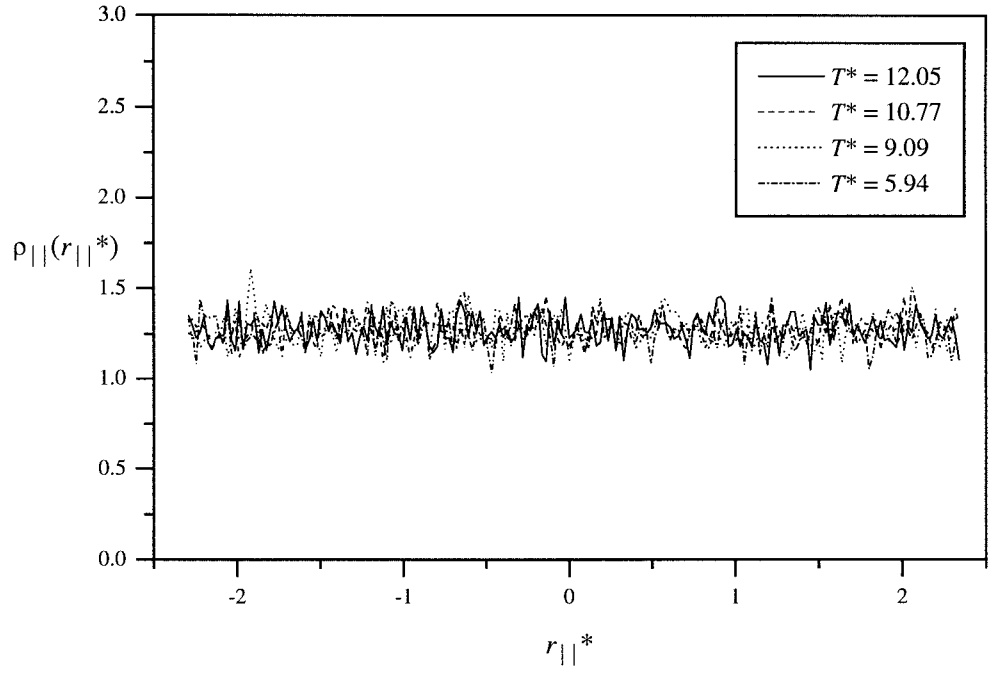

Figure 3.21: *The density distribution function* $\rho_{||}(r_{||}^*)$ *at the scaled temperatures T* indicated.*

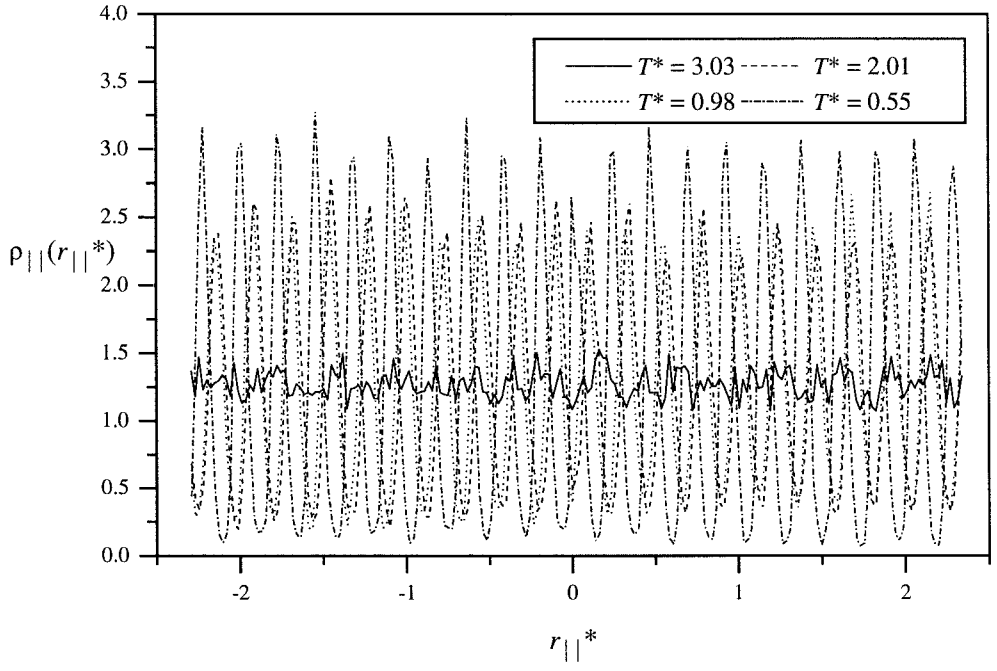

Figure 3.22: *The density distribution function* $\rho_{||}(r_{||}^*)$ *at the scaled temperatures T* indicated.*

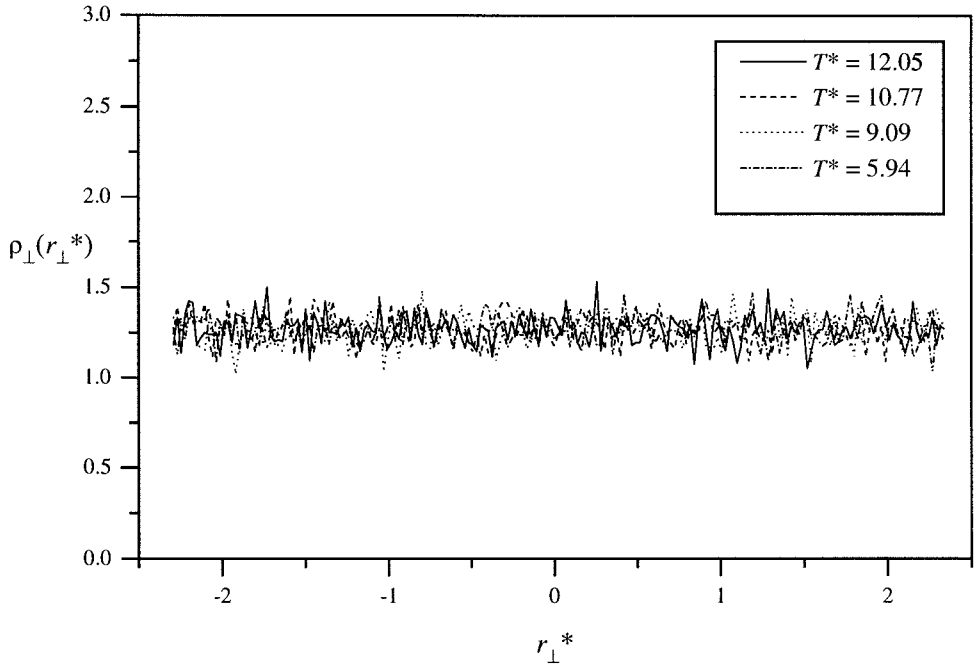

Figure 3.23: *The density distribution function* $\rho_\perp(r_\perp^*)$ *at the scaled temperatures T* indicated.*

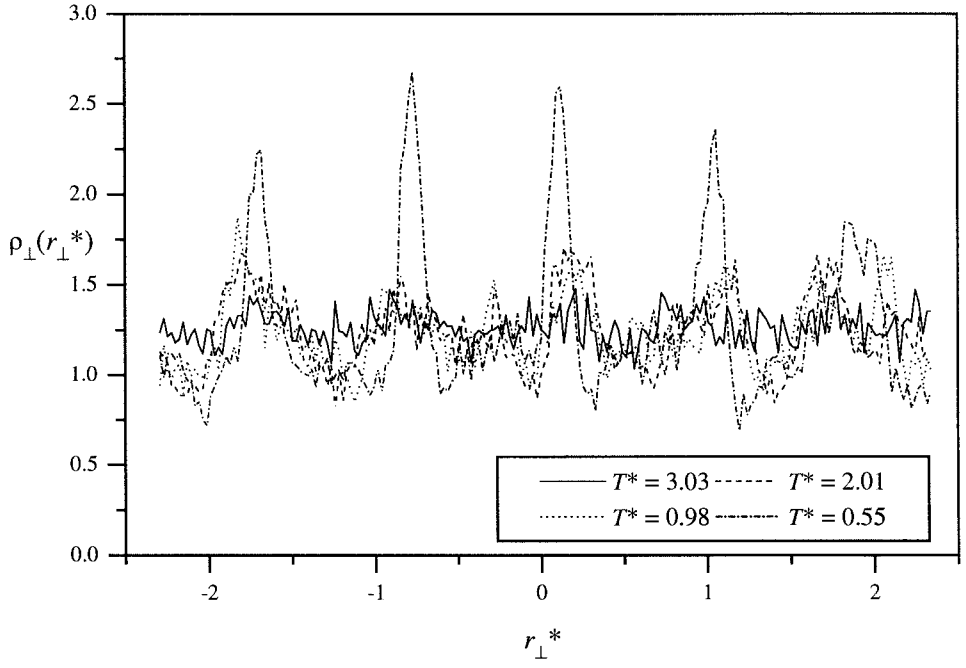

Figure 3.24: *The density distribution function* $\rho_\perp(r_\perp^*)$ *at the scaled temperatures T* indicated.*

3.4.4 Dynamic properties

One of the advantages of using the molecular dynamics technique over Monte Carlo is that we can calculate the dynamic as well as the static properties of a system; this can be especially useful in characterising highly ordered phases such as the columnar and solid phases. The two dynamic or time dependent properties that we have calculated are the mean squared displacement and the velocity autocorrelation function. But before we investigate these properties, we should discuss the mass and the moment of inertia which are used to scale other quantities in these simulations such as the time. As we have seen, (see §2.4), the motion of the simulation particles can be separated into two components, translational and rotational motion. The translational movement of the particles is dependent on their mass which is given a value of 1, while the rotational motion is governed by the moment of inertia tensor I. But when the trajectories of the particles are calculated by solving the equations of motion, a value of 4 is given for the moment of inertia I^* to ensure that the optimum translational and rotational time steps are approximately the same. This value is not the same as that calculated from the equation,

$$I^* = \frac{1 + (\sigma_e/\sigma_s)^2}{20}, \tag{3.2}$$

for an ellipsoid with mass of 1. Using this equation leads to a value for I^* of 0.05 for our Gay-Berne ellipsoid. Thus to be perfectly rigorous, any quantitative dynamic measurement obtained from the simulation will be incorrect, but the use of these correlation functions in a purely qualitative manner in determining and analysing the various mesophases is undiminished. It is with this in mind, that we will now discuss the results for the time dependent properties.

The mean squared displacement: By measuring the distance moved by a particle with time, a plot of the scaled mean squared displacement $m^*(t^*)$ can show how fluid a system is, particles being able to move more freely in a liquid phase than in a solid while the motion is also qualitatively different between the two phases. The total mean squared displacement for a variety of scaled temperatures is shown in figures 3.25 and 3.26. These were calculated using the method described in §2.4, with the tape file, consisting of particle position, orientation and velocity, extending to 10,000 time steps i.e. 200 data points.

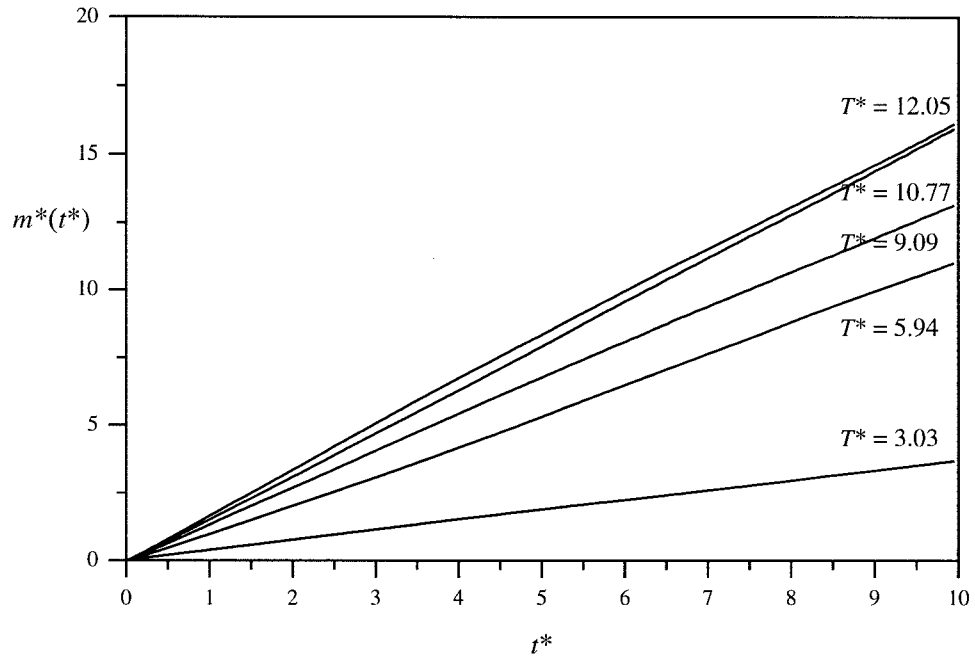

Figure 3.25: *The mean squared displacement $m^*(t^*)$ at the scaled temperatures T^* indicated.*

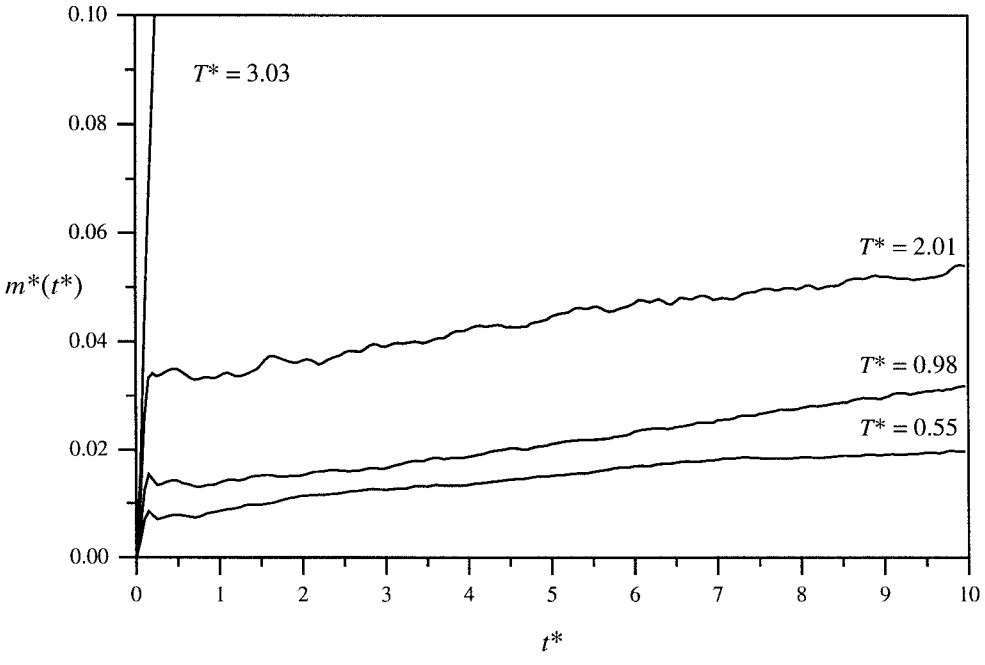

Figure 3.26: *The mean squared displacement $m^*(t^*)$ at the scaled temperatures T^* indicated.*

It is interesting to see that in the discotic nematic phase at T^* of 9.09 the particles are less mobile than in the isotropic phase, T^* of 10.77. This is in contrast to the results at the higher density of ρ^* of 3.0, in which particles in the discotic nematic phase had more translational freedom than particles in the isotropic phase. As the temperature is lowered to T^* of 3.03, the slope of the $m^*(t^*)$ plots decrease indicating the increasing viscosity of the phases, though the plots are linear with time, highlighting the liquid-like behaviour of the discotic nematic mesophase. Figure 3.26 shows the mean squared displacement for scaled temperatures lower than T^* of 3.03. The different form of the $m^*(t^*)$ for these translationally ordered phases, compared to the discotic nematic phase, can be explained by the high degree of rattling motion within the former, resulting in the steep feature at the origin i.e. librational motion about a mean position.

The mean squared displacement can also be resolved into two components, parallel and perpendicular to the director. Figure 3.27 shows both the parallel $m_{||}^*(t^*)$ and perpendicular $m_{\perp}^*(t^*)$ components for the simulation at a selection of scaled temperatures. Both plots of the $m^*(t^*)$ within the isotropic phase are very jagged due to the orientation of the director rapidly changing as the mean squared displacement is being calculated. Within the nematic phase, T^* of 9.09, the particles have more translational freedom in a direction perpendicular rather than parallel to the director. This is to be expected as the disc-shaped particles are able to slip over each other relatively easy in this direction. But again these plots deviate from linearity with a distinct plateau at long times. This raises the question as to are we following the behaviour for long enough times to be in the diffusional limit. As the temperature is lowered, the behaviour of the system remains the same, in that the particles have greater translational freedom perpendicular to the director, as shown by the lowest temperature, T^* of 3.03, (see figure 3.27d), of the discotic nematic phase, though the actual extent of the motion is less than at the higher temperatures.

The phase transition between the discotic nematic and columnar/crystal phases is shown by the major change in the mean squared displacement at T^* of 2.01, (see figure 3.27e). It is interesting to see that the particles find it easier to move side-to-side within rather than along a column. For the crystal phase we can see that the particle motion has essentially ceased, (see figure 3.27f).

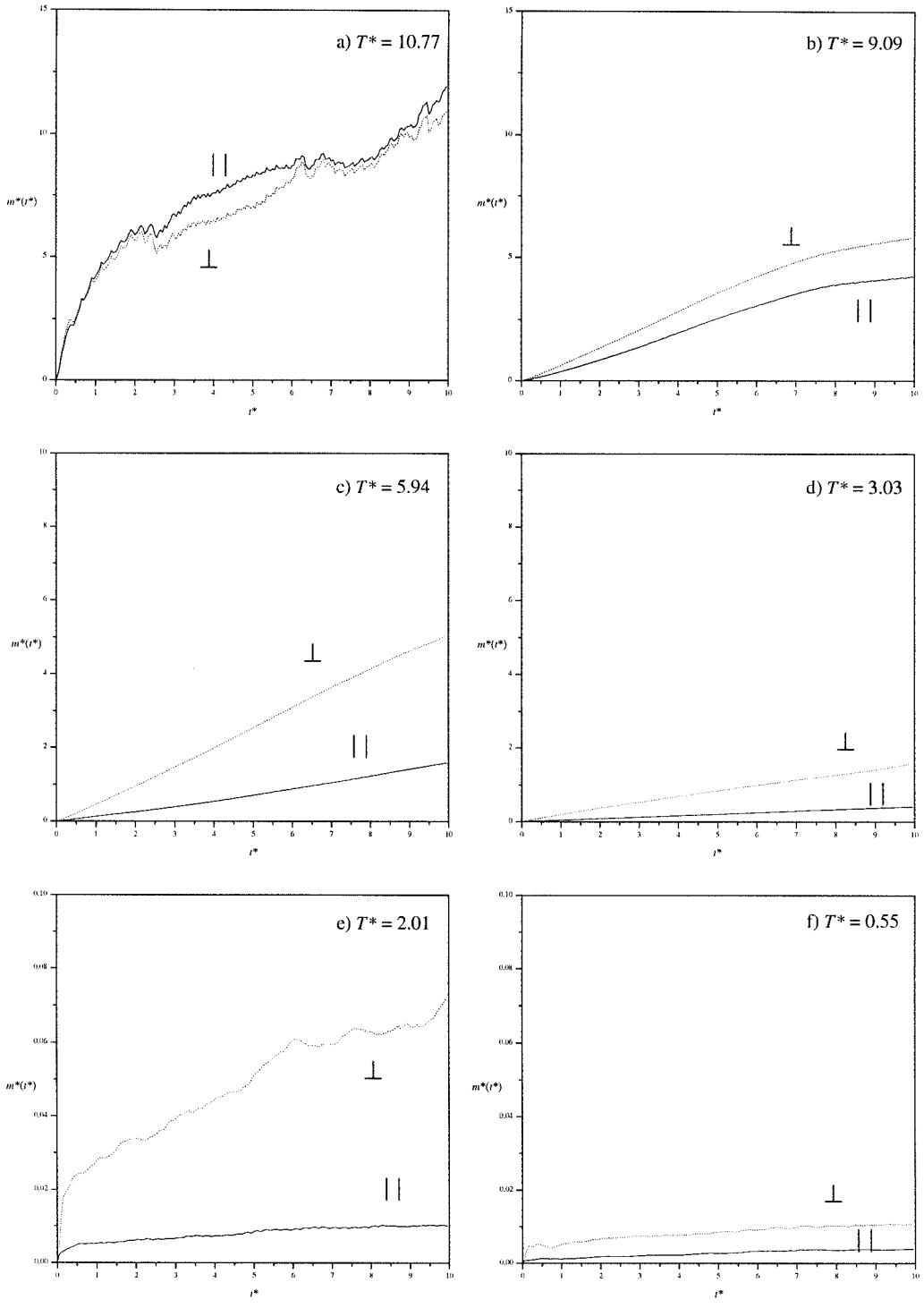

Figure 3.27: *The mean squared displacement resolved parallel, $m_{||}$*(t*), and perpendicular, $m_{\perp}$*(t*), to the director, at the scaled temperatures T* indicated.*

The diffusion coefficient D can be obtained from the plot of the mean squared displacement via the Einstein relationship, (see equation (2.62)). It can also be calculated from integration of the velocity autocorrelation function, (see equation (2.63)). We give the results from these calculations in table 3.3. For the scaled total diffusion coefficient D^*, we can see that it decreases as the translational order within the system increases. The same situation applies to the components of the diffusion tensor parallel and perpendicular to the director. From the ratio of these components, $D^*_{||}/D^*_{\perp}$, for the nematic phase, T^* between 9.09 and 3.03, the difference between the motion in these directions increases as the ordering builds up. It becomes easier for the particles to move perpendicular to the director i.e. for the ellipsoidal particles to slip over each other. Unfortunately, the values obtained from integration of the $C_{VV}(t^*)$, do not correlate with those obtained from the $m^*(t^*)$. This is probably due to errors associated with the truncation of the plots of $C_{VV}(t^*)$, which as observed in figure 3.29, do not decay exactly to zero after t^* of 0.25, the limit of our calculation due to limitations in computer storage.

There can also be another problem when calculating the diffusion coefficient by these differing methods. The velocity autocorrelation function decays to zero relatively quickly, sometimes over the first 250 - 500 time steps of a simulation, while the diffusion coefficient from the mean squared displacement is obtained when the slope of the function is linear which can be many thousands of time steps in to a simulation. In theory, if the system is in equilibrium, this should not make any difference, though in practice it seems that the statistics are better at longer time scales.

T^*	*Phase*	D^* *from* $m^*(t^*)$	D^* *from* $C_{VVtot}(t^*)$	$D^*_{\|\|}$	$D^*_{\perp}$	$D^*_{\|\|}/D^*_{\perp}$
10.77	I	1.612	0.023	-	-	-
9.09	N	1.318	0.025	0.432	0.579	0.78
5.94	N	1.123	0.027	0.162	0.51	0.32
3.03	N	0.367	0.023	0.04	0.154	0.26
2.01	D_h	0.002	0.005	0.003	0.005	0.6

Table 3.3: *The values of the scaled diffusion coefficients for the system at the scaled temperatures T^* indicated.*

The velocity autocorrelation function: Figures 3.28 and 3.29 show the plots of the total velocity autocorrelation function $C_{VV}(t^*)$ as a function of scaled time t^* for a variety of scaled temperatures throughout the simulation. At t^* of 0, $C_{VV}(t^*)$ has the value of one, by definition of $C_{VV}(t^*)$ as a normalised quantity, indicating that the velocities are the same. Then as the simulation proceeds, the value of $C_{VV}(t^*)$ drops gradually as the velocities from the current time step $\mathbf{v}(t^*)$ become less correlated with the initial velocity $\mathbf{v}(0)$. Eventually the graph decays to a value approaching zero as the velocities from the two time steps under comparison become uncorrelated. In contrast to the mean squared displacement, which can be measured over large time scales, t^* of 10, the $C_{VV}(t^*)$ is calculated over just the first 250 time steps of the simulation, t^* of 0.25. This is an order of magnitude less indicating that velocity correlations are lost over a relatively short time scale.

Looking at the plot for the total $C_{VV}(t^*)$, (see figures 3.28 and 3.29), in greater detail, we can see that, for the isotropic and nematic phases, the correlation of the velocities decays rapidly after t^* of 0.05 and approaches zero within t^* of 0.10. The behaviour at T^* of 3.03 is slightly different however, perhaps reflecting the pretransitional ordering within the phase. The plot does not decay to zero until t^* of 0.175, having become negative in sign. This reflects the particles undergoing collisions with each other which reverses the direction of the original motion. The behaviour in the columnar phase, T^* of 2.01, is dramatically different, with a large negative region, indicating the increased rattling motion within each column, this effect being observed in the plot of $m^*(t^*)$.

As with most correlation functions, the velocity autocorrelation function for the translational motion can be resolved parallel and perpendicular to the director, giving additional information about the dynamics within the phase. In the isotropic phase, the motion in both directions is very similar, with the $C_{VV}(t^*)$ decaying to zero after about t^* of 0.07, (see figure 3.30a). The plot of the $C_{VV}(t^*)$ for the discotic nematic phase at T^* of 9.09 shows, as expected, that the movement of the particles parallel to the director is more hindered than in a direction perpendicular to the director. This can be deduced from the plot as the $C_{VV}(t^*)$ decays quicker and the sign of the $C_{VV}(t^*)$ in the parallel direction is negative indicating a reversal of the velocity, resulting from a particle collision.

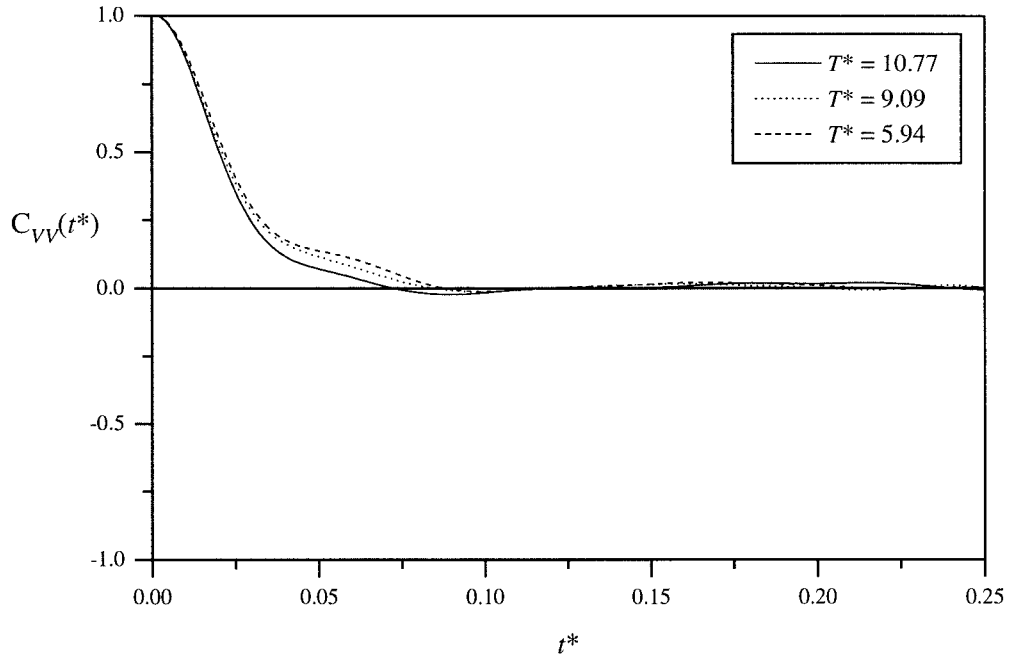

Figure 3.28: *The velocity autocorrelation function $C_{VV}(t^*)$ at the scaled temperatures T^* indicated.*

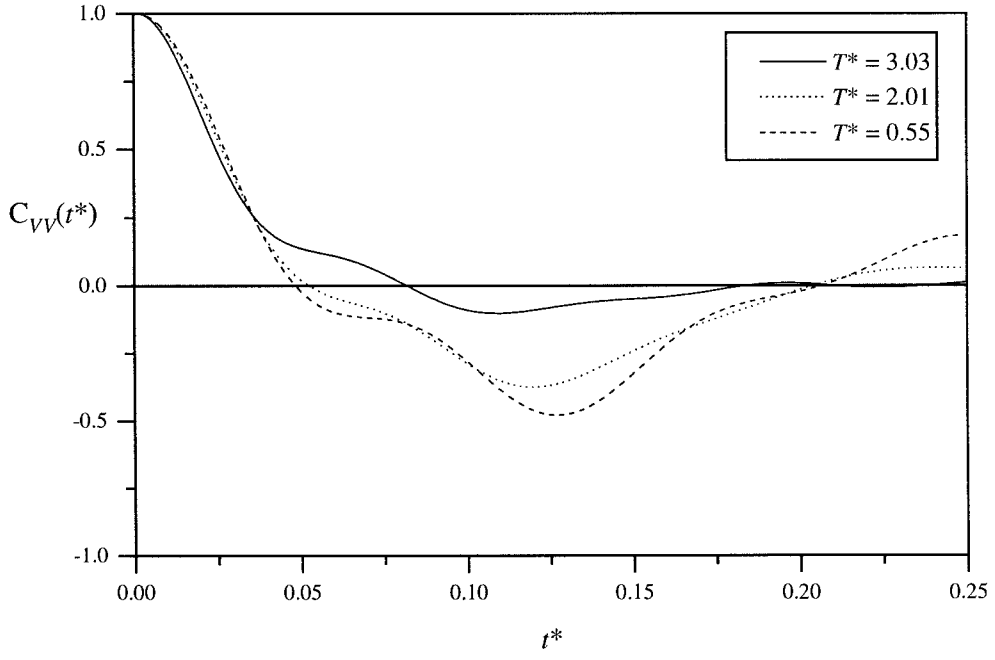

Figure 3.29: *The velocity autocorrelation function $C_{VV}(t^*)$ at the scaled temperatures T^* indicated.*

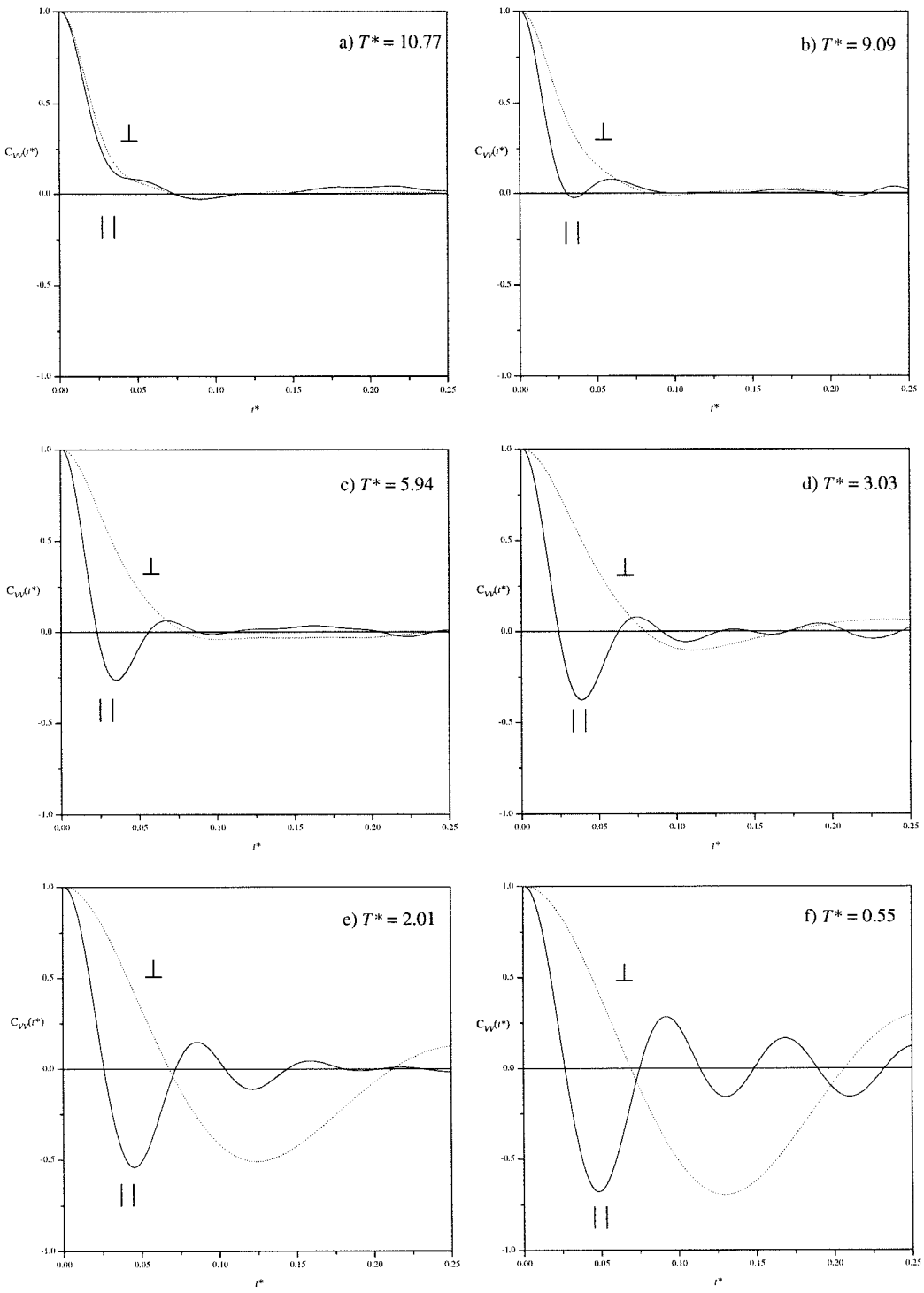

Figure 3.30: *The velocity autocorrelation function resolved parallel, $C_{VV||}(t^*)$, and perpendicular, $C_{VV\perp}(t^*)$, to the director, at the scaled temperatures T* indicated.*

At the lower temperature T^* of 3.03, for the discotic nematic phase, the shape of the $C_{VV}(t^*)$ is the same as at T^* of 9.09 but the features are more pronounced, for example, $C_{VV||}(t^*)$ falls to a very low value and even $C_{VV\perp}(t^*)$ undergoes a sign reversal, in contrast to the system at T^* of 9.09. This shows the greater structure and hence slower movement of the particles at the lower temperature, resulting from a more significant cage effect. Inspection of the plot for $C_{VV}(t^*)$ for the columnar phase at T^* of 2.01, shows that movement in both directions is strongly hindered, especially in the parallel direction where the many oscillations in the plot indicate a rattling motion caused by particle collisions. It is also interesting to note that the particle movement perpendicular to the director decays to zero very slowly, only after about t^* of 0.2 indicating considerable residual movement perpendicular to the director.

3.4.5 Location of the phase transitions

We have just discussed in depth the behaviour of the Gay-Berne discogen via the calculation of various structural and dynamic properties and have shown that on cooling from the isotropic fluid, discotic nematic, hexagonal columnar and crystal phases are formed. But it still remains to determine more precisely, or at least a more accurately the discotic nematic - isotropic transition temperature and the range of the hexagonal columnar phase.

Discotic nematic to isotropic transition: We have carried out additional simulations to locate the discotic nematic - isotropic transition with a greater accuracy. We know from the initial simulation that the transition lies between the scaled temperatures T^* of 10.77 and 9.09. So starting from the isotropic phase at T^* of 10.77, we reduced the temperature in steps of 0.1 to 0.2 scaled temperature units, with equilibration runs of between 30,00 and 60,000 time steps being performed at each state point. Production runs of between of 10,000 and 25,000 time steps were then performed. Looking at the temperature dependence of the order parameter $\langle P_2 \rangle$, (see figure 3.31), we can see that the values exhibited by the system in the isotropic phase are non-zero, so deciding where the phase transition can be difficult. For real systems of rod-shaped molecules, it is generally thought that the order parameter has a value of ≈ 0.35 at the transition, and as the transition between discs seems to be weaker, we could deduce that the transition might be between T^* of 9.84 and 9.73.

Set T^*	Actual T^*	$N_E/10^3$	$N_P/10^3$	$\langle U^* \rangle$	$\langle P_2 \rangle$
10	10.77 ± 0.21	30	10	−9.69 ± 0.54	0.151 ± 0.051
9.9	9.91 ± 0.19	30	15	−10.84 ± 0.41	0.178 ± 0.013
9.8	9.84 ± 0.24	30	10	−11.63 ± 0.61	0.274 ± 0.019
9.7	9.73 ± 0.14	30	25	−12.41 ± 0.53	0.339 ± 0.025
9.6	9.61 ± 0.22	30	20	−12.11 ± 0.59	0.285 ± 0.021
9.5	9.52 ± 0.14	60	10	−12.39 ± 0.56	0.315 ± 0.025
9.4	9.36 ± 0.11	60	20	−15.85 ± 0.28	0.517 ± 0.018
9.2	9.21 ± 0.29	60	10	−15.99 ± 0.25	0.538 ± 0.022
9	9.09 ± 0.44	60	10	−16.12 ± 0.55	0.556 ± 0.025

Table 3.4: *Values of T^*, $\langle U^* \rangle$ and $\langle P_2 \rangle$ for the simulation of the nematic - isotropic transition at ρ^* of 2.5, where N_E and N_P are the number of time steps performed during the equilibrium and production stages.*

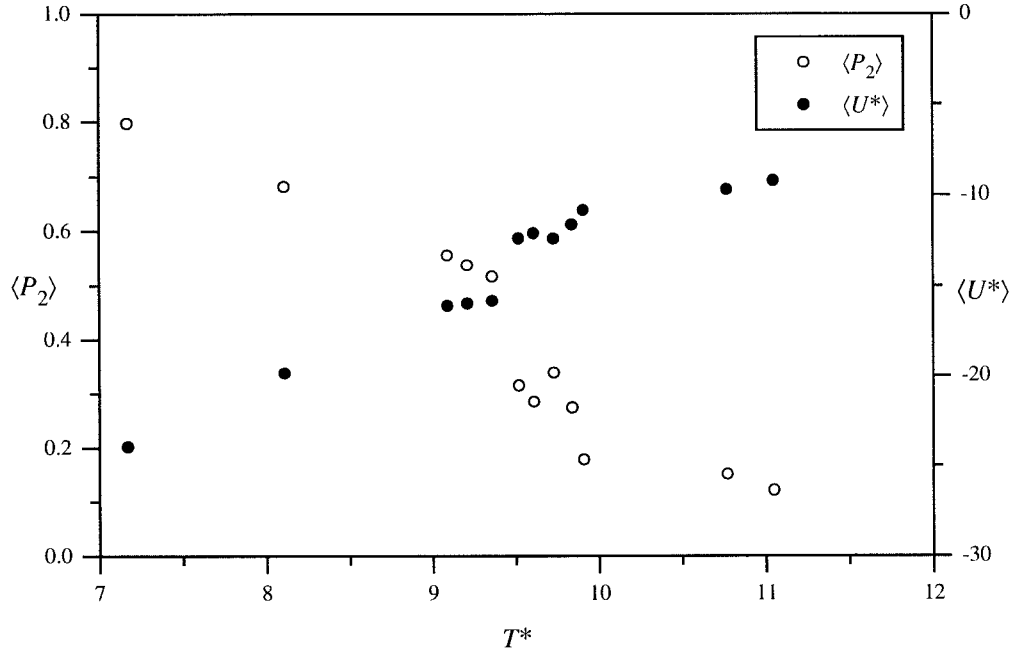

Figure 3.31: *Location of the discotic nematic - isotropic transition as shown by $\langle P_2 \rangle$ and $\langle U^* \rangle$.*

But it is good practice to look at many different properties of the system before making any firm conclusions about the phase behaviour. If we now add the plot of the internal energy per particle $\langle U^* \rangle$, we can make a slightly different interpretation of the order parameter. Any discontinuity in the plot of $\langle U^* \rangle$ usually demonstrates a first order phase transition, though at constant volume the transition is more continuous as there will be a biphasic region, and from this we can see that the discotic nematic - isotropic phase transition occurs between T^* of 9.52 and 9.36.

Discotic nematic to columnar transition: To locate this phase transition we followed a similar procedure to that for the discotic nematic - isotropic transition. Starting from the discotic nematic phase at T^* of 3.03, we slowly decreased the temperature in steps of 0.1 scaled units, with equilibrium runs ranging from between 15,000 to 100,00 time steps and production runs from 10,000 to 40,000 time steps. The actual location of the transition temperature for the columnar - discotic nematic transition is relatively easy. Inspection of a plot of the longitudinal distribution function $g_{||}(r_{||}^*)$, (see figure 3.32), reveals the onset of translational order along the director indicating that the transition occurs between T^* of 2.73 and 2.61.

Once we had located the columnar - discotic nematic transition we decided to continue and find the range of the columnar phase and if possible, locate a crystal - columnar phase transition. The temperature was further reduced in 0.1 steps until T^* of 1.5. Looking at plots of $\langle P_2 \rangle$, $\langle P_4 \rangle$, $\langle U^* \rangle$ and $\langle C_V^* \rangle$ revealed no discontinuity or indication of a phase transition. The only distribution/correlation function that showed a possibility of any phase transition was the total mean squared displacement, (see figure 3.33). For comparison, we have also included the plot for the discotic nematic phase T^* of 2.73. This shows that in the nematic phase, the particles undergo considerable translational diffusion as the plot deviates from a horizontal plateau and is linear with time. The next three temperatures T^* of 2.61, 2.49 and 2.37 show a markedly different form of the $m^*(t^*)$. Initially there is a steep part, then there is a change in slope, but it still increases with time showing that the particles within the system are still moving, albeit through small distances when compared with the nematic phase. So, more than likely, we can identify this phase as a columnar phase.

Set T^*	Actual T^*	$N_E/10^3$	$N_P/10^3$	$\langle U^* \rangle$	$\langle P_2 \rangle$
3	3.03 ± 0.12	15	10	−35.44 ± 0.10	0.952 ± 0.009
2.9	2.88 ± 0.10	20	20	−35.98 ± 0.11	0.956 ± 0.011
2.8	2.81 ± 0.11	30	30	−36.19 ± 0.13	0.957 ± 0.010
2.7	2.73 ± 0.09	30	20	−36.70 ± 0.12	0.960 ± 0.011
2.6	2.61 ± 0.06	55	30	−39.24 ± 0.10	0.968 ± 0.007
2.5	2.49 ± 0.08	30	30	−39.73 ± 0.09	0.972 ± 0.011
2.4	2.37 ± 0.08	100	25	−40.17 ± 0.08	0.974 ± 0.009
2.3	2.28 ± 0.06	30	40	−40.48 ± 0.09	0.975 ± 0.010
2.2	2.19 ± 0.07	50	30	−40.73 ± 0.10	0.976 ± 0.011
2.1	2.01 ± 0.06	70	30	−41.31 ± 0.11	0.979 ± 0.010
2	1.98 ± 0.05	30	20	−41.37 ± 0.08	0.980 ± 0.011
1.9	1.90 ± 0.03	50	30	−41.60 ± 0.09	0.980 ± 0.008
1.8	1.81 ± 0.02	35	10	−41.85 ± 0.10	0.981 ± 0.006
1.7	1.70 ± 0.01	30	20	−42.18 ± 0.09	0.983 ± 0.003
1.6	1.58 ± 0.02	30	20	−42.49 ± 0.08	0.984 ± 0.003
1.5	1.52 ± 0.01	25	10	−42.68 ± 0.08	0.986 ± 0.003

Table 3.5: *Values of T^*, $\langle U^* \rangle$ and $\langle P_2 \rangle$ for the simulation of the crystal - columnar - discotic nematic transition at ρ^* of 2.5, where N_E and N_P are the number of time steps performed during the equilibrium and production stages.*

The plots below T^* of 2.37 have a similar shape to those of the columnar phase, but after the initial step, the graph becomes horizontal with time, essentially showing that the particles have stopped moving. This is obviously analogous to a crystal phase, so on this basis the crystal - columnar transition could be said to occur between T^* of 2.37 and 2.28. If this analysis of the data is correct, it is interesting to note the extremely small temperature range of the columnar phase, just 0.3 scaled temperature units compared with the discotic nematic phase of 6.8 scaled temperature units, in all just 4% of the entire mesophase range. This is not entirely out of the ordinary as hexa-6-alkoxybenzoate of triphenylene, (see figure 3.1) exhibits a rectangular columnar phase of 7 °C compared with 81 °C for the discotic nematic phase[110], which is about 8% of the entire mesophase range.

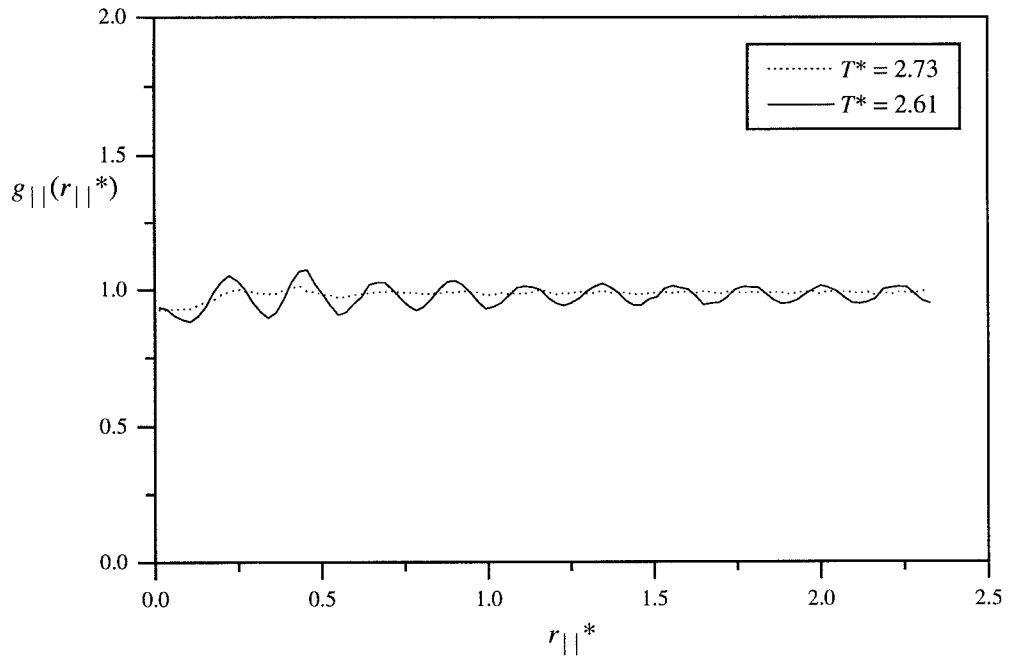

Figure 3.32: *Location of the hexagonal columnar - discotic nematic transition as shown by the* $g_{||}(r_{||}^*)$.

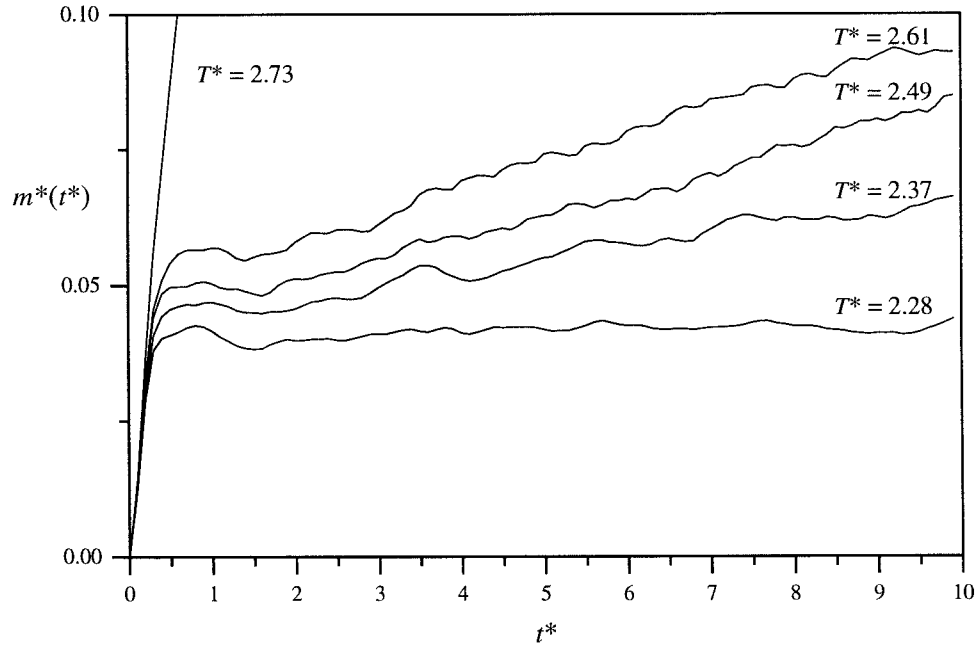

Figure 3.33: *Location of the crystal - columnar transition as shown by the* $m^*(t^*)$.

3.4.6 Comparisons with the Maier-Saupe theory.

One of the most popular theories used in describing the behaviour of nematic liquid crystals is the Maier-Saupe theory developed in the late 1950's[11,12] and based on the molecular field approximation. It has been used extensively to understand the behaviour of the nematic mesophase and the predications have been found to be in good agreement with many of the properties of the nematic - isotropic transition in real systems. It does, however, neglect certain important features of liquid crystals such as biaxiality and flexibility. We shall only give a very brief outline of the Maier-Saupe theory and the properties of interest to us, but for a deeper understanding, the reader is directed to the previous references[13].

In the original work, Maier and Saupe made some general assumptions about how liquid crystal mesogens interact. The first was that the dominant contribution to the stability of the nematic phase came from the anisotropic dispersion forces between molecules (see §2.1.2) and secondly, that the nematic phase is made up of cylindrically symmetrical particles. The central equation in the theory is the potential of mean torque experienced by a molecule in the field generated by its anisotropic interactions with the other molecules in the system. This is written as

$$U(\beta) = -\varepsilon\langle P_2\rangle P_2(\cos\beta), \tag{3.3}$$

where $P_2(\cos\beta)$ is the second Legendre polynomial, $\langle P_2\rangle$ is its ensemble average, the second rank orientational order parameter and ε is a function of molecular structure and density. This now leads us to the question, what can we do with $U(\beta)$? Well, we can calculate the second and fourth rank orientational order parameters as a function of temperature using the assumption that the singlet orientational distribution function can be truncated at the second rank term,

$$f(\cos\beta) = Z^{-1}\exp\{aP_2(\cos\beta)\}, \tag{3.4}$$

where the normalisation factor Z is defined as

$$Z = \int_0^{\pi} \exp\{aP_2(\cos\beta)\}\sin\beta \, d\beta, \tag{3.5}$$

where

$$a = \frac{\varepsilon}{kT}\langle P_2\rangle. \tag{3.6}$$

This leads to the self consistency equation

$$\langle P_2 \rangle = Z^{-1} \int_0^{\pi} P_2(\cos\beta)\exp\{aP_2(\cos\beta)\}\sin\beta \, d\beta. \tag{3.7}$$

By then plotting the values of the order parameter against T^*/T_{NI}^*, (see figure 3.34), we can see that the Maier-Saupe theory predicts a nematic - isotropic transition with the value of the order parameter being 0.429 at the transition. By now plotting our simulation results for $\langle P_2 \rangle$ and $\langle P_4 \rangle$ onto the graph obtained from the Maier-Saupe theory, we can see how our results from the simulation compare with the theory. Very close to the transition, there is reasonable agreement between theory and experiment in the nematic phase, though there is some deviation as the temperature is increased into the columnar phase. This is also illustrated to some extent by plotting $\langle P_4 \rangle$ *vs.* $\langle P_2 \rangle$ for both simulation data and values obtained from the Maier-Saupe theory, (see figure 3.35), where there seems to be reasonable agreement between both sets of data, confirming the quality of the fit of the second rank form of the distribution. We can also compare the singlet orientational distribution function $f(\cos\beta)$, given by

$$f(\cos\beta) = \frac{\exp\{aP_2(\cos\beta)\}}{\int \exp\{aP_2(\cos\beta)\}\sin\beta d\beta}. \tag{3.8}$$

To predict the form for the scaled temperature in our simulation, we first need to calculate the coefficient a, given by equation (3.6). In the Maier-Saupe theory, ε is predicted to be proportional to the nematic - isotropic transition temperature by,

$$\varepsilon = 4.539 T_{NI}^*. \tag{3.9}$$

From our simulations, (see §3.4.4), $T^*_{NI} \approx 9.45$. This means that a is now, in scaled units, from equation (3.8),

$$a = 42.89\frac{\langle P_2 \rangle}{T^*}, \tag{3.10}$$

and by using the appropriate values of $\langle P_2 \rangle$ and T^* from our simulations, we are able to predict the singlet orientational distribution function $f(\cos\beta)$. From figure 3.36, we can see, that for the scaled temperatures of 9.09 and 3.03, the agreement of the simulation data and that from the Maier-Saupe predication is reasonably good, underlining the predication that the coefficient a is related to the second rank orientational order parameter $\langle P_2 \rangle$.

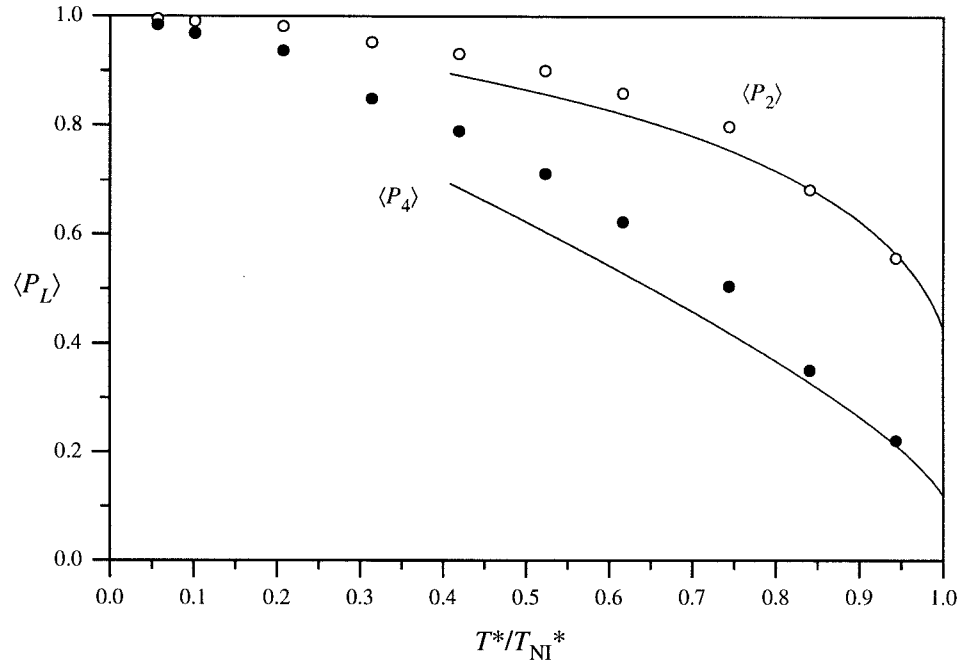

Figure 3.34: *Plot of $\langle P_2 \rangle$ and $\langle P_4 \rangle$ from our simulations (circles) and those predicted by the Maier-Saupe theory (solid lines) against the scaled transition temperature T^*/T_{NI}^*.*

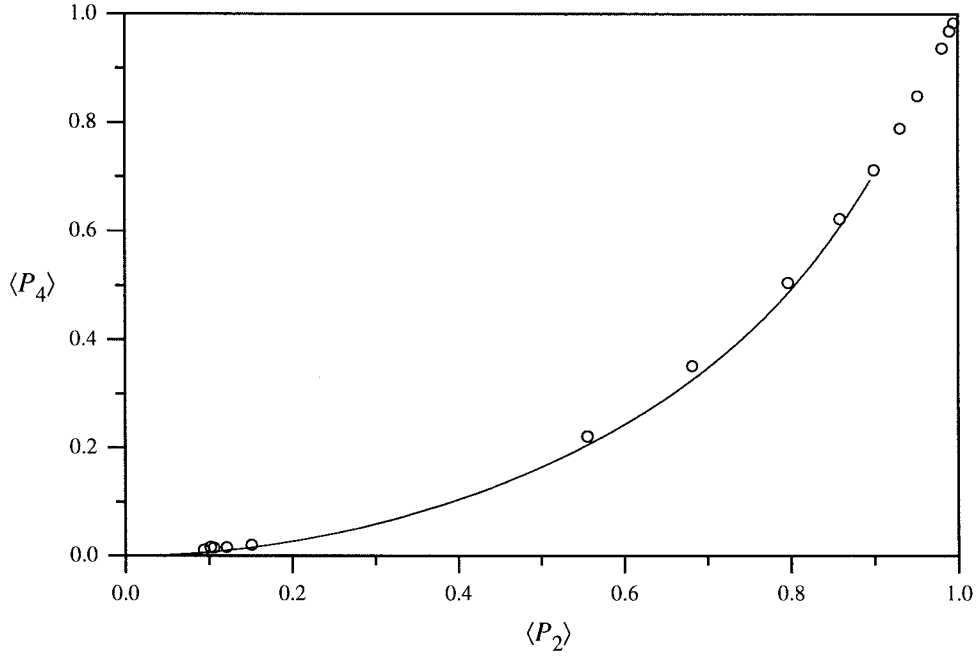

Figure 3.35: *Plot of the order parameters $\langle P_4 \rangle$ vs. $\langle P_2 \rangle$ from our simulations (circles) against that predicted by the Maier-Saupe theory (solid line).*

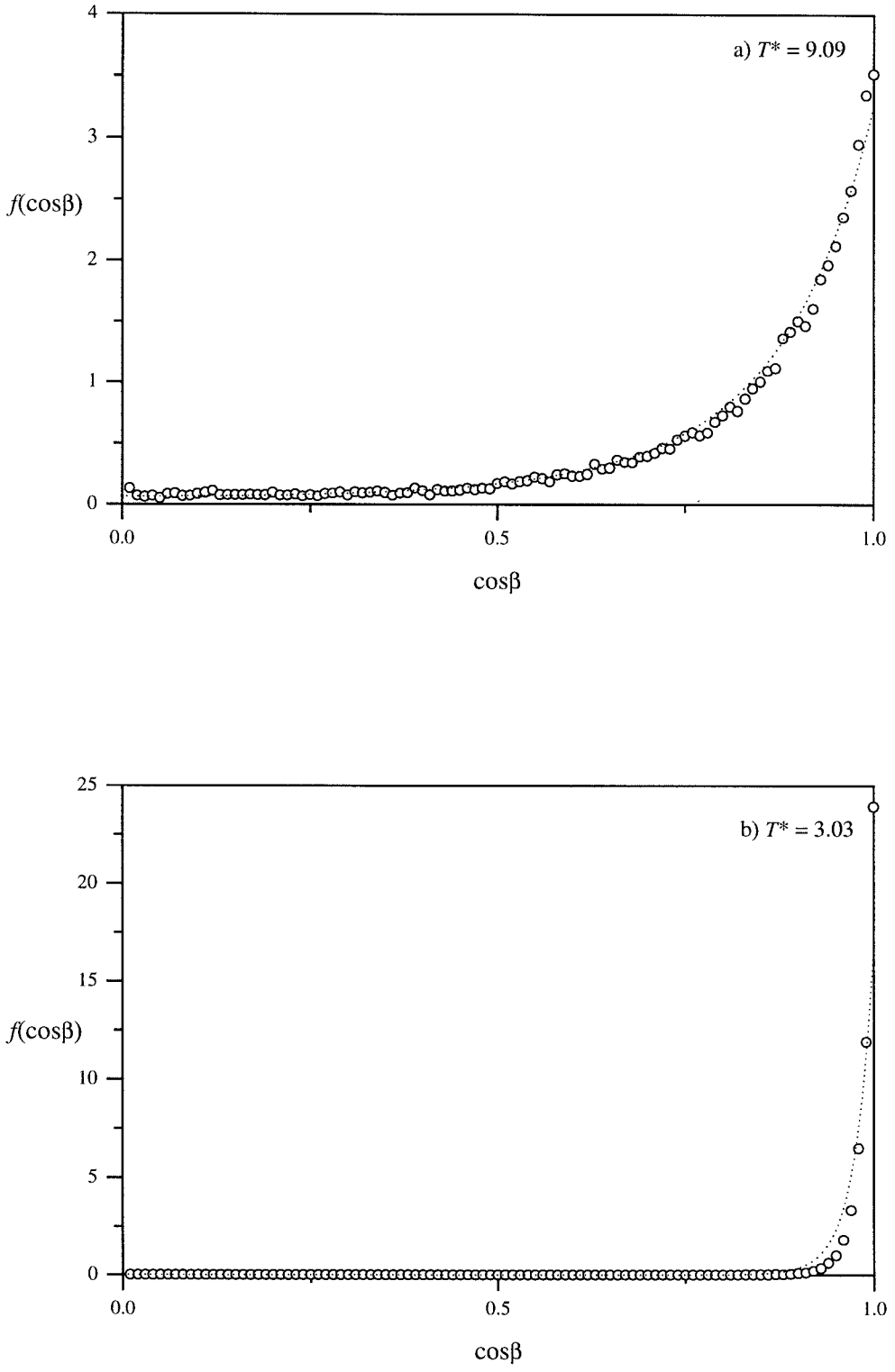

Figure 3.36: *Plot of the singlet orientational distribution function f(cosβ) from our simulations (circles) against that predicted by the Maier-Saupe theory (dotted lines) for the scaled temperatures of a) T* of 9.09 and b) T* of 3.03.*

Order parameter for the intermolecular vector: One of the other assumptions that Maier and Saupe made, was that the intermolecular vector between two particles is spherically distributed in the nematic phase, that is all values are equally probable. We can test this distribution of the intermolecular vector with respect to the director for our simulations, by calculating the order parameter $\langle P_2^+(r^*)\rangle$ for the intermolecular vector as a function of the scaled separation r^* ($\equiv r/\sigma_0$) between a pair of particles.

We calculate $\langle P_2^+(r^*)\rangle$ by constructing two histograms every 50 time steps, from a series of 10,000 time steps stored on a tape file. The x axis is just the interparticle distance r^* with a bin width Δr^* of 0.05. The y axis was just the sum of $P_2(\cos\beta_r)$ for pairs of molecules with separation between r^* and $r^* + \Delta r^*$. The second histogram contained the number of particles between r^* and $r^* + \Delta r^*$, and was used to normalise the $P_2(\cos\beta_r)$ histograms. The results of these calculations are shown in figure 3.37. The large non-zero values found for the order parameter clearly demonstrate that the intermolecular vector is not distributed with a spherical symmetry at short range as assumed by the Maier-Saupe theory. This result is not unexpected as a similar conclusion was reached by Emerson *et al.*[114] for a system of rod-shaped Gay-Berne mesogens exhibiting a nematic phase.

The results for $\langle P_2^+(r^*)\rangle$ can be explained as follows. There is a large, positive peak at $r^* \approx 0.4$ corresponding to pairs of particles in a face-to-face arrangement, though from the plot of the radial distribution function we know that there are not many of these. The peak is positive, because for this arrangement, the intermolecular vector is parallel to the director. The next peak is a minimum at $r^* \approx 1.0$, approximating to particles in the edge-to-edge arrangement. But for this arrangement, the intermolecular vector is now orthogonal to the director resulting in the negative value for order parameter. Beyond these peaks the distribution of the intermolecular vector decays to zero, corresponding to a spherical distribution of the intermolecular vector.

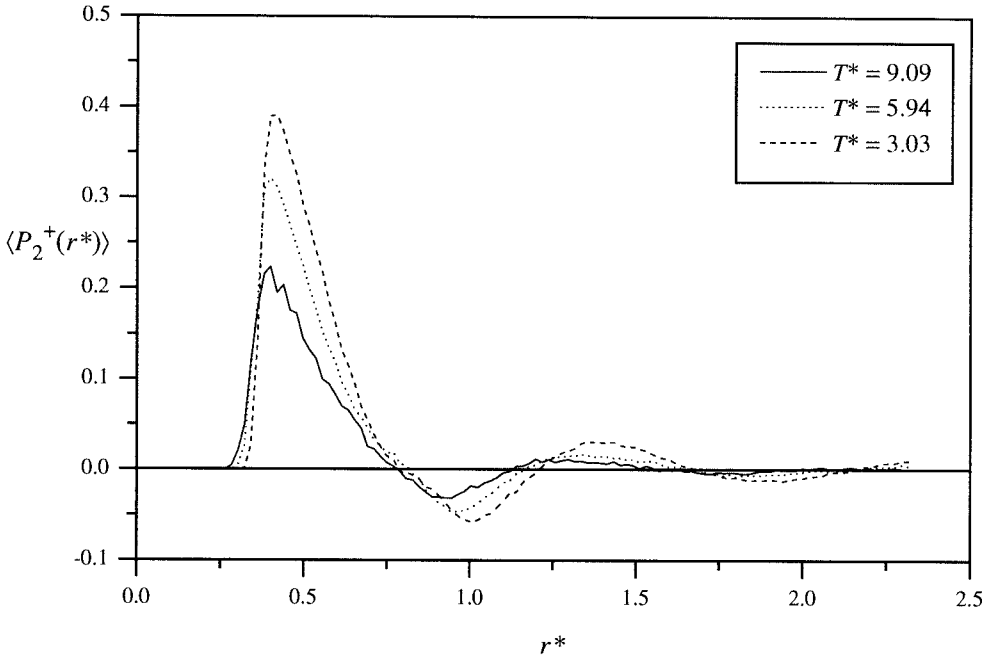

Figure 3.37: $\langle P_2^+(r^*)\rangle$ *for the intermolecular vector, at the scaled temperatures* T^* *indicated.*

3.5 Conclusions

Liquid crystals can be investigated using a variety of potential models, ranging from the simple lattice model to a full atom-atom potential. We have chosen to use the Gay-Berne potential which in terms of complexity lies in between these two extremes. Each particle has full translational and orientational degrees of freedom but only represents each mesogenic molecule as a single force centre having an ellipsoidal core but with anisotropic attractive forces built in.

By a weak parametrisation of the shape anisotropy and the energy of interaction between particles to resemble a disc-shaped mesogen we have successfully simulated isotropic, discotic nematic and columnar phases. We have investigated further the orientational, structural and dynamic behaviour of these mesophases by the calculation of various distribution and time correlation functions such as the radial distribution function $g(r^*)$ and the mean squared displacement $m^*(t^*)$. We have found a discotic nematic - isotropic phase transition and a columnar - discotic nematic phase transition.

The columnar phase exists over a very small temperature range. We have demonstrated that the symmetry of the columnar phase is hexagonal at lower densities but forms a rectangular phase at higher densities[12]. In most thermotropic rectangular phases, either the columns or the molecules within each columnar are tilted, but for the Gay-Berne rectangular phase, the neighbouring columns are interdigitated allowing the particles and the column axes to remain orthogonal to the director.

Unlike most real discotic systems, the range of the discotic nematic phase is quite large and considering the strength of the face-to-face interaction, we would expect a more defined columnar phase. But these observations can be rationalised if we consider the nature of our model compared to real discogens. First we have neglected the role of flexible alkyl chains, that while playing a vital role in disrupting the strong interaction between molecular cores, would also increase the effective radius of the particle, making it easier to form a columnar phase. In a sense, instead of our model being a generic model for a whole range of disc-shaped mesogens, it could be regarded as having the general features of discogens but due its fixed size and shape, resembles only a specific mesogen, as one compound is only one member of a homologous series.

Further Work

Although we have been reasonably successful in achieving our aim of simulating and understanding somewhat better the behaviour of the various mesophases formed, there are problems that still need to be addressed. The major problem that afflicts all computer simulations of complex liquids, is the limited number of particles with which we perform our simulations. This has two consequences when applied to our work. The first is the effect on the nature and the position of the various transitions between different phases. It has been noted, that small system sizes can affect the order of the nematic - isotropic transition[15] and in some cases could force a phase transition on the system. If the model of the nematic - isotropic transition, proposed by Luckhurst and Zannoni[16] is considered, they state that in the isotropic phase, there are small clusters of orientationally ordered molecules and that the transition to the nematic phase is just the extension of orientational order between these clusters.

So the problem we face, is what if these clusters present in the isotropic phase are of equivalent size to the numbers used in our simulation? The next logical step is the increase in the number of particles used in the simulation[17].

The next problem relates to the essentially artificial nature of our simulation, in that we have a fixed size and shape box in which we place our molecules. This would especially manifest itself in the translationally ordered phases such as the columnar phases. We have seen that the columns can pack into a hexagonal lattice, though that does not pose any problem as that is what we would expect. But what about the square columnar phase, where, due to the higher densities, the columns are forced to penetrate each other to accommodate the columns. What would be the effect on allowing the box size and shape to relax, to attain an equilibrium position? This would have to be investigated by performing constant pressure simulations.

We have just discussed work that could be performed on the present systems, but we could also extend this work to encompass the search for other mesophases, such as the addition of dipoles and quadrupoles, with the possibility of forming tilted phases. We could also investigate particles with additional flexible chains or chiral centres. But we must not forget, that we need to examine the techniques we use, in particular the effect system size, different ensemble and boundary conditions would have.

3.6 References

[1] G.R.Luckhurst, R.A.Stephens and R.W.Phippen. *Liq.Cryst.* (1990) **8** 451.

[2] A.P.J.Emerson, S.G.Whatling and G.R.Luckhurst. *Liq.Cryst.* (1994) **82** 113.

[3] S.Chandresekhar. *Liquid Crystals. 2nd Ed.* Cambridge (1992).

[4] P.J.B.Edwards. *Ph.D. Thesis*, University of Leeds, (1993).

[5] D.Frenkel and B.M.Mulder. *Molec.Phys.* (1985) **55** 1171.

[6] J.G.Gay and B.J.Berne. *J.Chem.Phys.* (1981) **74** 3316.

[7] A.Perera and G.N.Patey. *J.Chem.Phys.* (1989) **91** 3045.

[8] J.Talbot, A.Perera and G.N.Patey. *Molec.Phys.* (1990) **70** 285.

[9] M.P.Allen and D.J.Tildesley. *Computer Simulation of Liquids.* Claredon Press (1987).

[10] D.Demus and H.Zaschke. *Flüssige Kristalle in Tabellen II.* VEB (1984).

[11] W.Maier and A.Saupe. *Z.Naturforsch.* (1958) **13a** 564.

[12] W.Maier and A.Saupe. *Z.Naturforsch.* (1959) **14a** 882.

[13] For a modern treatment see G.R.Luckhurst. *The Molecular Physics of Liquid Crystals.* (G.R.Luckhurst and G.W.Gray. eds.) Academic Press (1979).

[14] A.P.J.Emerson, R.Hashim and G.R.Luckhurst. *Molec.Phys.* (1992) **76** 241.

[15] G.R.Luckhurst and P.Simpson. *Molec.Phys.* (1982) **47** 251.

[16] G.R.Luckhurst and C.Zannoni. *Nature.* (1977) **267** 412.

[17] M.A.Bates and G.R.Luckhurst. *J.Chem.Phys.* (1996) **104** 6696.

4. X-Ray diffraction from Gay-Berne mesophases.

4.1 Introduction

X-Ray diffraction is generally used to investigate the structure of matter at the molecular level with probably the most common application being the determination of the positions of atoms in crystals. However, the technique is far more versatile than this. For example, biologists use X-ray diffraction to determine the arrangement of molecules in complicated systems such as viruses and cell membranes. The technique is also used as a common analytical method for identifying the structural and chemical composition of mixtures. We can also use X-ray diffraction for the characterisation of the various liquid-crystalline mesophases, especially for translationally ordered phases where it is an essential method for distinguishing between the various smectic and columnar phases.

But apart from a purely qualitative use, we can also gain some quantitative measurements of the orientational order in a mesophase from the technique and we shall discuss these matters in greater depth at the appropriate time. We begin with a brief discussion of X-ray diffraction, followed by some explanation of how we extract the essential information from a real diffraction experiment. We shall then talk about how we apply the technique to liquid crystals, discuss the aims of our simulation experiments, the models we shall use and finally the results of our initial studies on the system of Gay-Berne discogens discussed in Chapter 3.

4.1.1 X-Ray and neutron beams

X-Rays are produced[1] by bombarding a metal with high energy electrons. When these electrons hit the metal they decelerate, producing radiation with a range of wavelengths. Superimposed on this continuum radiation are a few sharp, high intensity peaks. These arise from the interaction of the incoming electrons with electrons in the inner shells of the metal atoms. The collision expels one electron and an electron of higher energy drops into the vacancy left, emitting the excess energy as an X-ray photon; a typical target metal being copper which produces X-rays at 0.154 nm. We can also use neutron beams, generated from within a nuclear reactor, to determine the structure of a system and as they produce similar diffraction phenomena as X-rays, they will arise further in our discussion.

4.1.2 The diffraction process

We have just described the variety of energy beams that can be used for diffraction experiments but what can they be used for? As the wavelengths of these beams are approximately 0.1 nm, which is comparable to the atomic spacing in crystals, Von Laue suggested that they might be diffracted by crystals and hence give some idea about the structure of the material. Thus the idea of X-ray diffraction was born, with the first pattern recorded in 1913[12]. Diffraction is produced by the interference of waves that are scattered from an object. When the amplitudes are in phase the waves augment each other and the intensity increases and vice versa, thus out of phase waves destructively interfere with each other. It can thus be distinguished from scattering phenomena, of which it is a subset, where the scattered rays do not necessarily interfere. Before we deal with the actual diffraction experiment, we should say what happens when X-rays interact with matter. The scattering of X-ray beams from matter occurs by two processes:

(i) *Incoherent or Compton* scattering is a billiard ball effect. Incident X-rays can be considered as photons. When an X-ray photon hits an electron, the electron is knocked aside and the X-ray photon is scattered through an angle 2θ. Energy from the X-ray photon has been used to move the electron, thus the wavelength of the scattered X-ray photon is different from that of the incident X-ray photon. There is no phase relationship between the scattering events and so one cannot assign positions to the scattering pattern, thus this is known as incoherent scattering. Its only effect is to give rise to an overall background scattering.

(ii) *Coherent or Thomson* scattering occurs when, as the X-ray hits an electron, the electromagnetic field of the X-ray causes the electron to oscillate with the same frequency as the X-ray. This change in frequency forms the source of a secondary scattered ray which has the same wavelength as the X-ray but differs in phase by π radians. All the scattered waves have the same phase relationship to the incident beam, hence the scattering is coherent.

Both X-ray and neutron diffraction are similar in that they are an indirect method of finding the structure, in that a direct image cannot be formed. As X-rays and neutrons cannot be focused, the scattered beam is intercepted by a detecting system such as photographic film or electronic counter. This means that the phase relationship is lost but through the use of Fourier synthesis[3], the recombination of the scattered rays can be simulated. Optical microscopy on the other hand gives an enlarged image with a continuous flow of radiation that can be recombined by a lens system to maintain the phase relationship.

4.1.3 The diffraction experiment

To develop the theory of X-ray diffraction we start with the most fundamental equation that usually describes scattering from a crystal. Consider a series of parallel lattice planes of a crystal, (see figure 4.1).

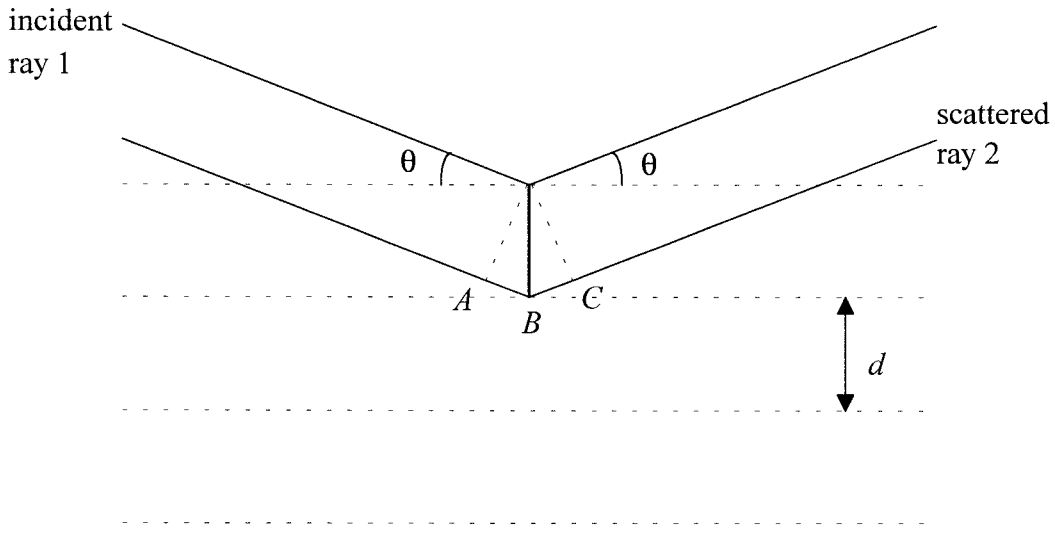

Figure 4.1: *Schematic diagram of Bragg scattering from a series of crystal planes.*

If the separation between planes of atoms is d, then the path difference between the incident radiation, ray 1, and the scattered radiation, ray 2, $AB + BC$ can be written as

$$AB + BC = 2d\sin\theta. \tag{4.1}$$

For most scattering, the angle θ will not result in an integral wavelength difference and so will be out of phase and the intensity will decrease. But at some angles, $AB + BC$ will be an exact integral multiple n, of the wavelength λ, of the incident X-ray, so that,

$$AB + BC = n\lambda. \tag{4.2}$$

For this case, the amplitudes will be in phase and constructive interference will occur. Combining equations (4.1) and (4.2) leads to

$$2dsin\theta = n\lambda. \tag{4.3}$$

This is known as Bragg's law which is used to predict the position in space of diffracted rays. The problem with this, is that it only applies to diffraction from crystals i.e. structures with long range positional order, so we need to extend this theory to encompass diffraction from fluid phases. Figure 4.2 illustrates a basic diffraction experiment by considering parallel beams of monochromatic X-rays of wavelength λ impinging on a body of electron density that contains two scattering centres *O* and *P*, i.e. we have an electron density $\rho(\mathbf{r})$ at position **r** from the centre *O*.

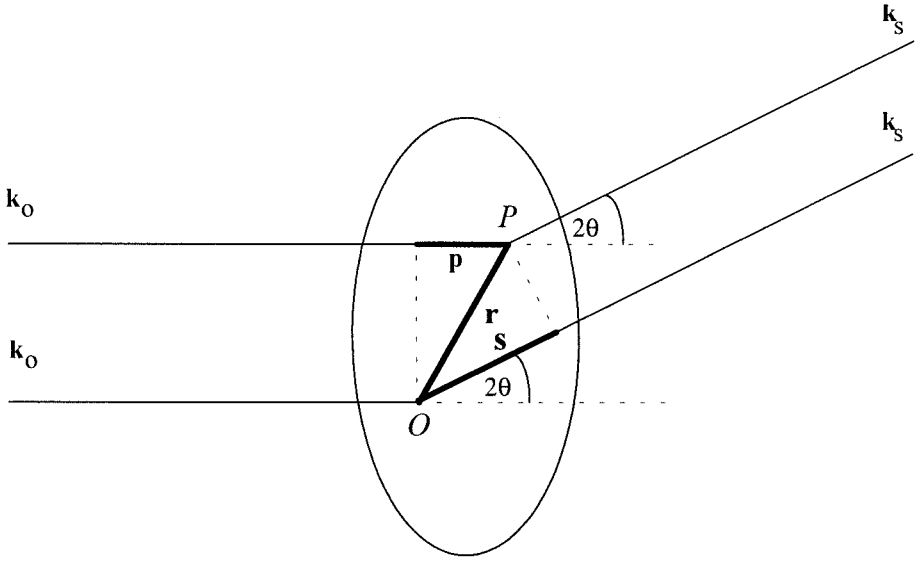

Figure 4.2: *Scattering from a body of electron density.*

In figure 4.2, $\mathbf{k}_O$ is the wavevector for the incident X-ray beam with wavelength λ and $\mathbf{k}_S$, that for the scattered radiation. There will be a path difference between the X-rays scattered from *O* and *P* both of which are scattered through an angle 2θ. By analogy with the Bragg experiment, this path difference is

$$\mathbf{s} - \mathbf{p} = n\lambda. \tag{4.4}$$

This can be rewritten as

$$\mathbf{r}.\mathbf{k}_S - \mathbf{r}.\mathbf{k}_O = n\lambda, \tag{4.5}$$

with **r** being the vector describing the position of *P*, and hence a phase difference of

$$\mathbf{r}.(\mathbf{k}_S - \mathbf{k}_O) = \frac{n\lambda}{2\pi}. \tag{4.6}$$

A vector **Q**, (see figure 4.3), is used to define the scattering vector $\mathbf{k}_S - \mathbf{k}_O$, where

$$\mathbf{Q} = (2\pi/\lambda)(\mathbf{k}_S - \mathbf{k}_O), \tag{4.7}$$

and so the phase difference can now be defined as

$$\mathbf{Q}.\mathbf{r}. \tag{4.8}$$

The vector **Q**, far from being a convenient notation, is also used to describe a position in diffraction or reciprocal space, in the same way as **r** does in real space, with its magnitude defined by

$$|\mathbf{Q}| = 4\pi \sin\theta/\lambda. \tag{4.9}$$

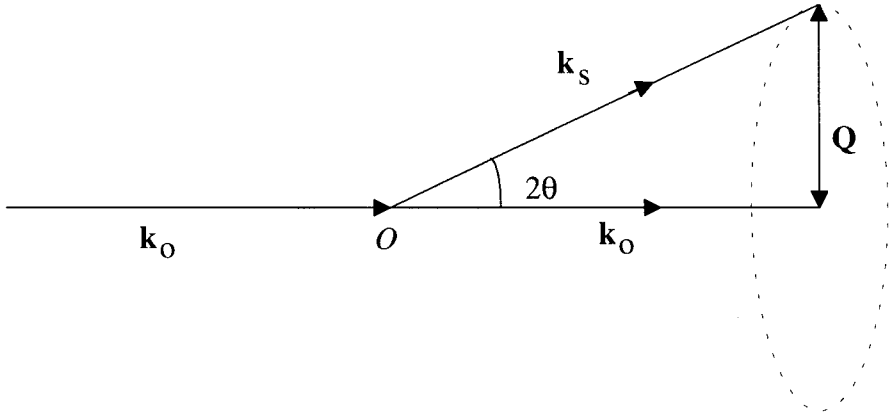

Figure 4.3: *Definition of the vector **Q** used to measure positions in diffracted space.*

The scattering by a small unit volume d**v** at position **r** relative to *O* has an amplitude proportional to the electron density $\rho(\mathbf{r})$ and a phase of **Q.r**. Thus the scattering at a distance **r** from the origin is

$$\rho(\mathbf{r}) \exp(i\mathbf{Q}.\mathbf{r})d\mathbf{r}. \tag{4.10}$$

Thus the total wave scattered by the entire volume V is given as

$$F(\mathbf{Q}) = \int \rho(\mathbf{r}) \exp(i\mathbf{Q}.\mathbf{r})d\mathbf{r}, \tag{4.11}$$

where $F(\mathbf{Q})$ is known as the form factor which describes the effective scattering or amplitude of the sample[4].

We now know the amplitude of the diffracted X-ray, it just remains to calculate the intensity $I(\mathbf{Q})$ and this is related to the scattering amplitude or form factor by

$$\begin{aligned} I(\mathbf{Q}) &= F(\mathbf{Q})F^*(\mathbf{Q}), \\ &= \int\int \rho(\mathbf{r}_1)\rho(\mathbf{r}_2)\exp[i\mathbf{Q}.(\mathbf{r}_1-\mathbf{r}_2)]d\mathbf{r}_1 d\mathbf{r}_2, \end{aligned} \tag{4.12}$$

where $F^*(\mathbf{Q})$ is the complex conjugate of $F(\mathbf{Q})$. If integration of $F(\mathbf{Q})$ is over all space, then $F(\mathbf{Q})$ is the Fourier transform of $\rho(\mathbf{r})$, thus the diffraction of scattered X-rays can be explained using the properties of the Fourier transform[3]. But equation (4.12) encompasses all scattering from the body of electron density $\rho(\mathbf{r})$, so we need to extend the theory to extract the forms for the scattering we are interested in. If we now consider N fixed, discrete scattering sites within a sample of electron density,

$$\rho(\mathbf{r}) = \frac{1}{V}\sum_{i=1}^{N} a_i\delta(\mathbf{r}-\mathbf{r}_i), \tag{4.13}$$

where a_i is a generalised atomic scattering factor, applicable to either X-ray or neutron radiation, and is dependent on the property of the atom under investigation. Substituting (4.13) into equation (4.11) the form factor now becomes

$$\begin{aligned} F(\mathbf{Q}) &= \sum_{i=1}^{N}\int a_i\exp(i\mathbf{Q}.\mathbf{r})\delta(\mathbf{r}-\mathbf{r}_i)d\mathbf{r}, \\ &= \sum_{i=1}^{N} a_i\exp(i\mathbf{Q}.\mathbf{r}_i). \end{aligned} \tag{4.14}$$

Thus the intensity of the diffracted radiation, be it X-ray or neutron, is given as

$$I(\mathbf{Q}) = \sum_{i}^{N}\sum_{j}^{N}\langle a_i a_j\exp(i\mathbf{Q}.\mathbf{r}_{ij})\rangle, \tag{4.15}$$

where the brackets represent an ensemble average and the vector for scattering from site i to site j is $\mathbf{r}_{ij} = \mathbf{r}_i - \mathbf{r}_j$ and includes both $\mathbf{r}_{ji} = -\mathbf{r}_{ij}$ and $\mathbf{r}_{ij} = 0$. We still need to separate this expression for the total intensity given by equation (4.15) into coherent and incoherent, self and interference and intra- and intermolecular terms. In general,

$$\langle a_i a_j\rangle = \langle a_i\rangle\langle a_j\rangle + \delta_{ij}(\langle a_i^2\rangle - \langle a_i\rangle\langle a_j\rangle). \tag{4.16}$$

Substituting equation (4.16) into (4.15) allows the expression to be separated into self, where $i = j$, and interference terms, where $i \neq j$, giving,

$$I(\mathbf{Q}) = \sum_i \langle a_i^2 \rangle + \sum_{i \neq i} \sum \langle a_i a_j \exp(\mathrm{i}\mathbf{Q}.\mathbf{r}_{ij}) \rangle, \tag{4.17}$$

$$= I^{self}(\mathbf{Q}) + I^{inter}(\mathbf{Q}).$$

It is more usual to divide equation (4.17) into incoherent and coherent terms so that,

$$I(\mathbf{Q}) = \sum (\langle a_i^2 \rangle - \langle a_i \rangle^2) + \sum_i \sum_j \langle a_i a_j \exp(\mathrm{i}\mathbf{Q}.\mathbf{r}_{ij}) \rangle, \tag{4.18}$$

$$= I^{incoh}(\mathbf{Q}) + I^{coh}(\mathbf{Q}),$$

where terms for $i = j$ have been removed from the self scattering term and added to the interference scattering term. The incoherent scattering is the major contributor to the background and so is of no interest to us, but the coherent scattering is, and is given by

$$I^{coh}(\mathbf{Q}) = \sum_i \sum_j \langle a_i a_j \exp(\mathrm{i}\mathbf{Q}.\mathbf{r}_{ij}) \rangle. \tag{4.19}$$

This can be subdivided into terms depending on whether the two scattering sites i and j are in the same molecule or not. First, we need to define the quantities

$$\mathbf{r}_i = \mathbf{R}_m + \mathbf{r}_i^m \quad \text{and} \quad \mathbf{r}_j = \mathbf{R}_n + \mathbf{r}_j^n, \tag{4.20}$$

where the vector $\mathbf{r}_i$ of the i^{th} site is the sum of the vector to the origin of the m^{th} molecule fixed frame, $\mathbf{R}_m$, plus the vector from the origin to the i^{th} site in this frame, $\mathbf{r}_i^m$. Thus

$$\mathbf{r}_{ij} = \mathbf{r}_i - \mathbf{r}_j = (\mathbf{R}_m - \mathbf{R}_n) + (\mathbf{r}_i^m - \mathbf{r}_j^n). \tag{4.21}$$

Putting equation (4.21) into the expression for the total coherent scattering (4.19) gives

$$I^{coh}(\mathbf{Q}) = \sum_m^{N_m} \sum_n^{N_m} \sum_i^{N_n} \sum_j^{N_n} \langle a_i a_j \exp\left[\mathrm{i}\mathbf{Q}.\{(\mathbf{R}_m - \mathbf{R}_n) + (\mathbf{r}_i^m - \mathbf{r}_j^n)\}\right] \rangle, \tag{4.22}$$

where the summations are performed over the N_m molecules each containing N_a nuclei i.e. the total number of sites $N = N_m N_a$.

Separating terms for $m = n$ and $m \neq n$, produces

$$I^{coh}(\mathbf{Q}) = \sum_{m \neq n} \sum_{n} \sum_{i} \sum_{j} \langle a_i a_j \exp\left[i\mathbf{Q}.\{(\mathbf{R}_m - \mathbf{R}_n) + (\mathbf{r}_i^m - \mathbf{r}_j^n)\}\right]\rangle + N_m \sum_{i} \sum_{j} \langle a_i a_j \exp\left[i\mathbf{Q}.(\mathbf{r}_i^m - \mathbf{r}_j^n)\right]\rangle. \quad (4.23)$$

$$= \underset{\substack{intermolecular \\ term}}{I^{coh}(\mathbf{Q})} + \underset{\substack{intramolecular \\ term}}{N_m I^{coh}(\mathbf{Q})}.$$

When we set out on this analysis, we stated that this would be a general derivation for fluids, thus for neutron scattering, a_i is the nuclear scattering length, while for X-rays, we can replace a_i with the atomic scattering amplitude which, for the spherical atom approximation, is given by

$$a_i = f_i(\mathbf{Q}) = \int \rho(\mathbf{r}) \frac{\sin(\mathbf{Q}.\mathbf{r})}{\mathbf{Q}.\mathbf{r}} d\mathbf{r}. \quad (4.24)$$

We have just outlined how, from the measured intensity, we can divide the scattering into various parts, that arising from individual molecules and interference scattering from a collection of molecules, but what we need to do now is to outline briefly how X-ray diffraction is applied to the specific problems encountered with liquid-crystalline mesophases.

4.2 X-Ray diffraction from real liquid-crystalline mesophases

X-Ray diffraction studies on real liquid-crystalline mesophases can be divided into two categories[5], those that employ unoriented or "powder" samples and those where the sample under investigation is oriented by the use of an external force. A powder sample consists of many director domains giving all possible orientations of the particles, thus all possible diffraction peaks can be seen. This manifests itself as a pattern consisting of concentric circles, (see figure 4.4a). These patterns are often used for the initial characterisation of mesophases and can give details of molecular packing such as layer and correlation lengths. Diffraction patterns from oriented samples, (see figure 4.4b), provide much more information. They allow us to achieve more detailed conclusions on the packing and structure within the mesophase, both parallel and perpendicular to the director, information unobtainable from unoriented samples. The results obtained from these oriented patterns can also be used quantitatively, it is claimed, to determine aspects such as the singlet orientational distribution function $f(\cos\beta)$[6].

4.2.1 Effect of ordering on diffraction patterns

We begin by discussing the effect, of the type of ordering found in liquid-crystalline mesophases, on the diffraction pattern. But what do we mean by the type of ordering? Well, we have both short range and long range, as well as translational and orientational ordering.

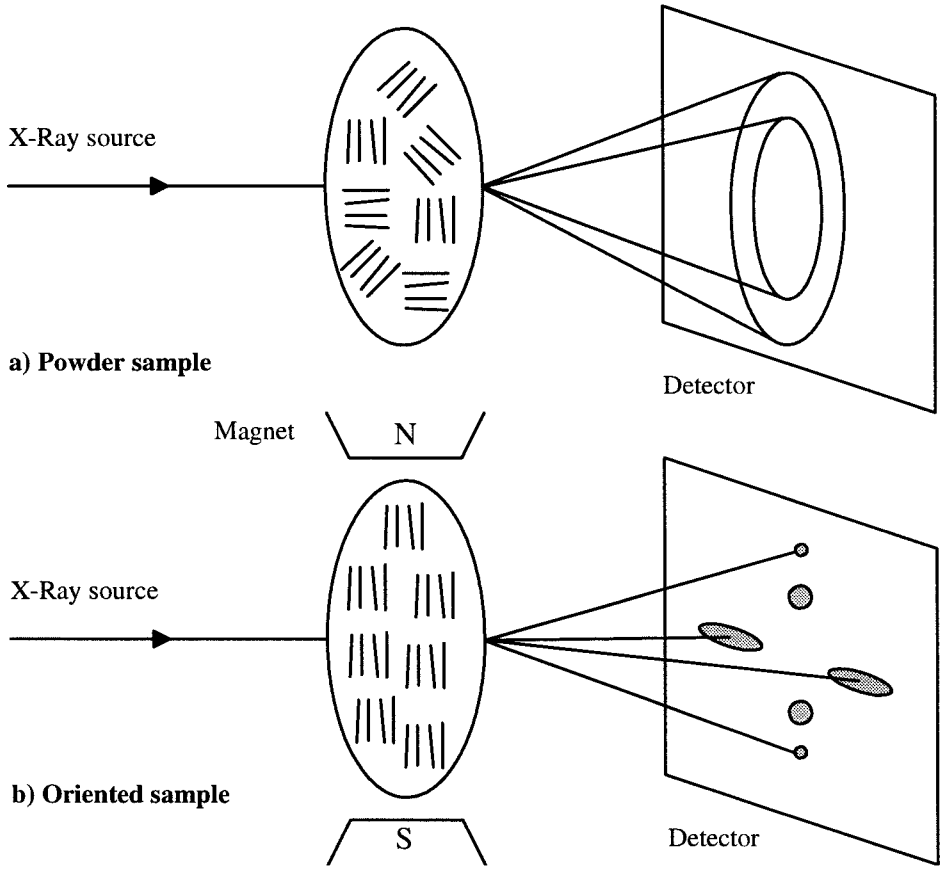

Figure 4.4: *Production of a) powder and b) oriented X-ray diffraction patterns.*

If we consider the scattering from a perfect crystal, we obtain a series of infinitely sharp Bragg peaks, (see figure 4.5a), resulting from the infinite range translational order. Quasi-long range ordering, of the type found in the highly ordered smectic and columnar phases, is temperature dependent, with the correlation between particles decaying algebraically with distance, the effect being to smear out the Bragg peak, (see figure 4.5b). If there is only short range translational order, decaying exponentially over the sample, as present in the nematic phase, the peak now broadens out quite substantially, with a width proportional to the positional correlation length, ξ_P, (see figure 4.5c).

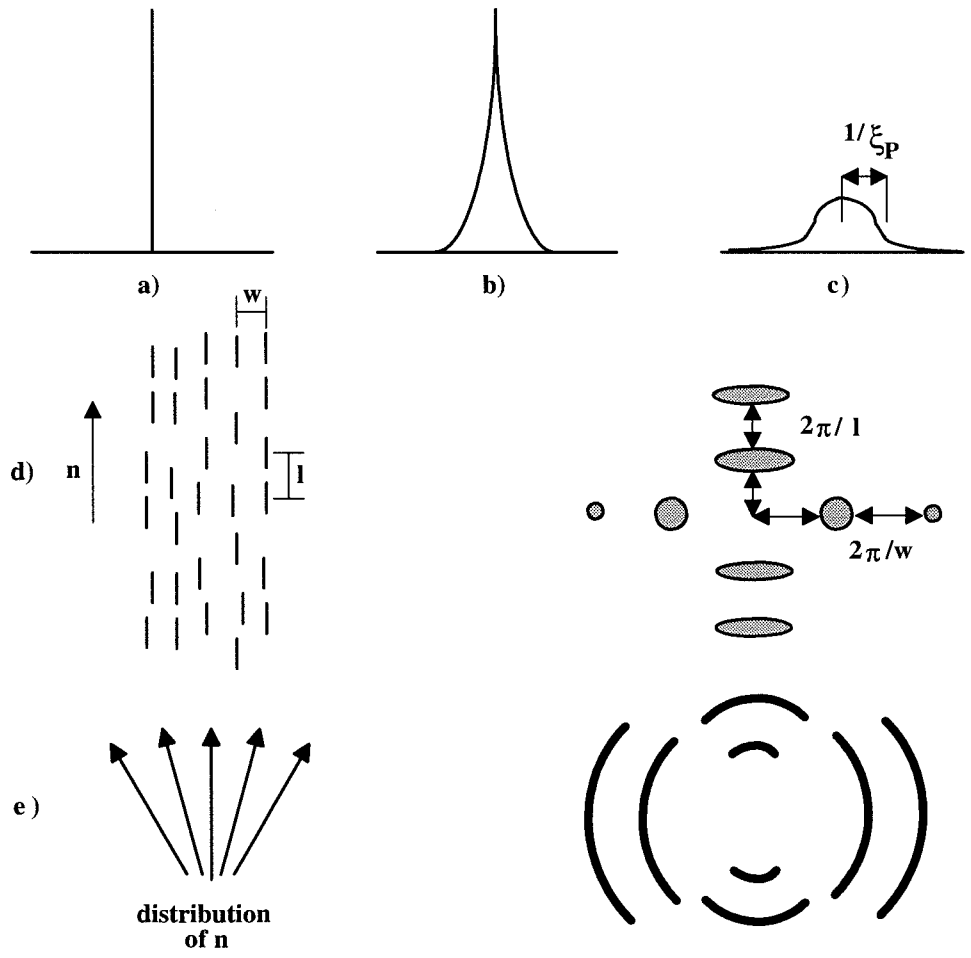

Figure 4.5: *The effect of a) infinite range, b) quasi-long range and c) short range translational order on a diffraction peak, and d) and e) the effect of orientational disordering on a simple diffraction pattern*[5].

The effect of orientational order can also have a similar effect on the appearance of the diffraction pattern. If we consider a series of evenly spaced chains of particles, that are translationally disordered within each chain, (see figure 4.5d), we can see that the diffraction pattern[5] has both meridional, representing the average end-to-end length, and equatorial peaks arising from the side-by-side correlations. The effect of an orientational distribution of these monodomains of local directors, on the patterns can now be clearly observed, as the peaks are smeared out into diffuse arcs, (see figure 4.5e).

4.3 X-Ray diffraction from model liquid-crystalline mesophases

4.3.1 Motivation

We have just described how X-ray diffraction can be a powerful technique for the determination of both molecular structure and macroscopic order, i.e. characterisation between various liquid-crystalline mesophases. So there is no reason why we should not apply the same techniques to study mesophases generated from the results of computer simulation. There are two main aims as to why we should generate X-ray diffraction patterns. The first is to probe in greater detail the structure of our simulated phases and allow differentiation between them. In this respect, the diffraction patterns complement graphic snapshots and distribution functions which are normally used to determine structure. Secondly, they provide us with a further test on the validity of our model used.

To expand on the latter reason, in Chapter 3 we used a generic model of a disc-shaped mesogen to see if we could identify some of the essential features responsible for the formation of discotic nematic and columnar mesophases. We did indeed show that our model, the Gay-Berne model, has the necessary characteristics of both anisotropic shape and attractive forces, to be able to form these two phases. To see if these models were representative, if only in a qualitative sense, of real mesophases we also calculated various orientational and structural properties, such as the singlet orientational distribution function $f(\cos\beta)$ and the radial distribution function $g(r^*)$, which are not available directly from experiment. But when assessing the quantitative accuracy of a model potential in representing the real mesophase, it is necessary to compare as many of these orientational and structural properties as possible. Thus by calculating X-ray diffraction patterns and comparing them with those obtained from real systems, we obtain an additional test to see if we have modelled the liquid-crystalline mesophase correctly.

4.3.2 The spherical scattering model

The Gay-Berne potential represents each interacting particle essentially as an ellipsoid of revolution with a length-to-breadth ratio σ_e/σ_s. Initial simulations of rod-shaped mesogens, with σ_e/σ_s of 3.0 produced isotropic, nematic, smectic A, smectic B and crystal phases[7]. It was with configurations taken from these simulations that the first attempts at calculating the X-ray diffraction pattern were performed. Hamley's initial model[8] was to place a series

of spherical or point scattering centres along the major axis of each ellipsoid. As the Gay-Berne potential was originally parametrised as a row of four interacting Lennard-Jones centres[9], a tetratomic particle with the same overall length was used, but this resulted in the problem of the intramolecular terms producing bands of intense scattering over all values of $\mathbf{Q}^*$, (see figure 4.6a). These could mask other, more interesting features of the diffraction pattern such as the intermolecular diffraction features.

His solution was to increase the number of spherical atoms, placed along the symmetry axis of each particle to sixteen. As we can see from figure 4.6b, the only band of scattering is now at $\mathbf{Q}^* \cong 0$, and though it is very intense, it would obscure less of the pattern at medium to high $\mathbf{Q}^*$ values, allowing the intermolecular scattering to dominate. By using this linear hexadecatomic particle, various diffraction patterns of the isotropic, nematic, smectic A and smectic B phases were calculated and, in general, reproduced, at least qualitatively, those exhibited by their real counterparts. The intramolecular diffraction patterns were quite smooth with a low signal-to-noise ratio. In a direction parallel to the director, the plots were generally isotropic as expected for these uniaxial phases, while in the plane perpendicular to the director, the anisotropy of the patterns increased with increasing $\langle P_2 \rangle$. Both of these results were encouraging as they gave confidence in the calculation of the structure factor.

For the intermolecular diffraction patterns, the wide angle arcs of the nematic phase were modelled quite successfully, while in the smectic A phase, sharp peaks were observed which were consistent with the layer spacing obtained from the density distribution function $\rho_{||}(r_{||}^*)$. Parallel to the director, the six-fold symmetry of the smectic B phase was revealed by six sharp, Bragg peaks, but due to the small system size, it was not possible to distinguish between a hexatic or crystal B phase from the diffraction pattern. Though calculations from further simulations, using constant *NPT* Monte Carlo, have suggested a hexatic B[10]. It is worth noting that these were actually neutron diffraction patterns as the scattering from each particle was $\mathbf{Q}^*$ independent, i.e. the nuclear scattering length was set to unity. This is in contrast to our studies, in which we calculate the X-ray diffraction pattern, where the scattering is $\mathbf{Q}^*$ dependent.

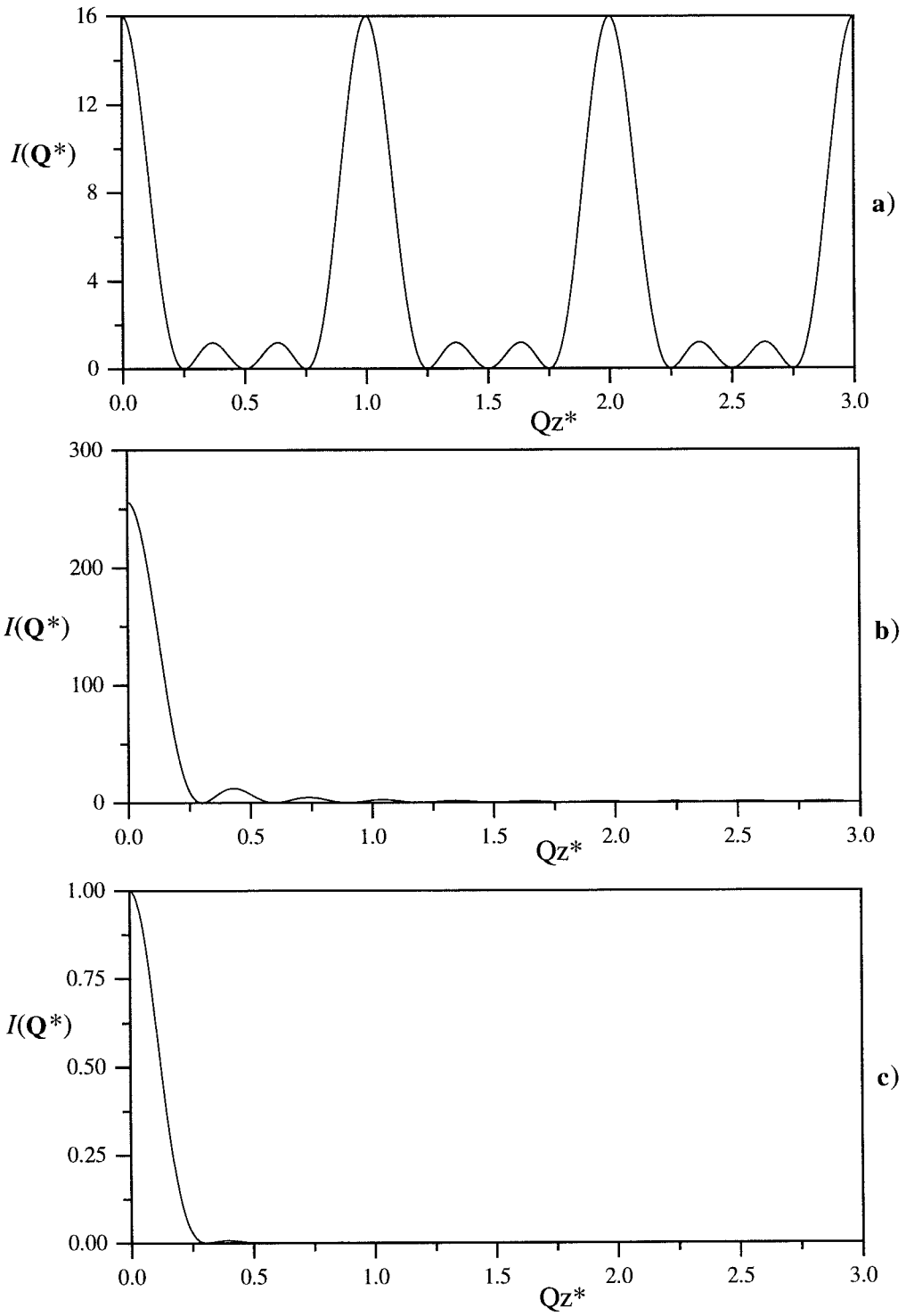

Figure 4.6: *Diffracted intensity in the plane perpendicular to the major symmetry axis for a single a) linear tetratomic, b) linear hexadecatomic and c) ellipsoid of revolution, each having a length of* $3\sigma_0$.

Many of these intermolecular plots were noisy, but they could in principal have been improved by averaging the calculation over more configurational snapshots. However this procedure is still imperfect as there is no easy way of lining up the phase symmetry axes from one configuration to the next, a problem we encountered when calculating distribution functions such as the $g_{\perp}(r_{\perp}^*)$ and $\rho_{\perp}(r_{\perp}^*)$. But the main drawback of using these spherical scattering centres is the inability to extend this model to oblate particles. It is possible to construct a disc of spheres but this would be time consuming because so many spheres would be needed, so the ideal solution, for the purposes of calculating the X-ray diffraction patterns, is to put a three dimensional ellipsoid of revolution at each particle position. Though this does not accurately mimic the actual shape of the Gay-Berne mesogen, (see §2.5.3) it allows the model to be extended from disc-shaped to rod-shaped particles just by the variation of one parameter, the length-to-breadth ratio σ_e/σ_s, while also giving a better signal-to-noise ratio.

4.3.3 The ellipsoidal scattering model

To illustrate the advantage of using an ellipsoid instead of a set of spherical particles we should look at the scattering from a single ellipsoid having the σ_e/σ_s ratio of a rod-shaped ellipsoid as used in the simulations of Luckhurst *et al.*[7]. Figure 4.6c shows that when the X-ray beam impinges on the ellipsoid perpendicular to the main symmetry axis, the scattering is generally uniform over the whole **Q*** range of interest, which is controlled by the size of the diffracting particle, and comparing it to that of the 4 and 16 atom system, we can see that it is less intense. This should make the diffraction patterns smoother, as we are mainly concerned with diffraction arising from interference between different particles rather than the single particle and, thus in theory, should allow an easier calculation of $f(\cos\beta)$ from the intensity of the wide angle arcs in the nematic phase[6]. For our model of the structure factor, we start from the expression for the total coherent intensity, (see equation (4.19)), which can be written as

$$I^{coh}(\mathbf{Q}) = F_T(\mathbf{Q})F_T^*(\mathbf{Q}) = \sum_i^N \sum_j^N \langle a_i a_j \exp(i\mathbf{Q}.\mathbf{r}_{ij})\rangle, \qquad (4.25)$$

where for neutron diffraction experiments, $a_i = a_j = 1$.

But for X-ray diffraction from solid, geometrical particles we need to replace a_i with the atomic scattering factor $f(\mathbf{Q})$, which for a sphere[11] is

$$f(\mathbf{Q}) = \frac{3(\sin \mathbf{u} - \mathbf{u}\cos \mathbf{u})}{\mathbf{u}^3}, \tag{4.26}$$

where $\mathbf{u} = \mathbf{Q}x$, and x is the radius of the sphere. We can modify this equation for an ellipsoid of revolution, having semi-axes x and y, (defined as σ_s and σ_e in the Gay-Berne potential) simply by writing $\mathbf{u}$ as

$$\mathbf{u} = \mathbf{Q}x(\cos^2\beta + \frac{y^2}{x^2}\sin^2\beta)^{\frac{1}{2}}, \tag{4.27}$$

where β is the angle between the symmetry axis of the ellipsoid and the direction of the scattering vector $\mathbf{Q}$, (see figure 4.7).

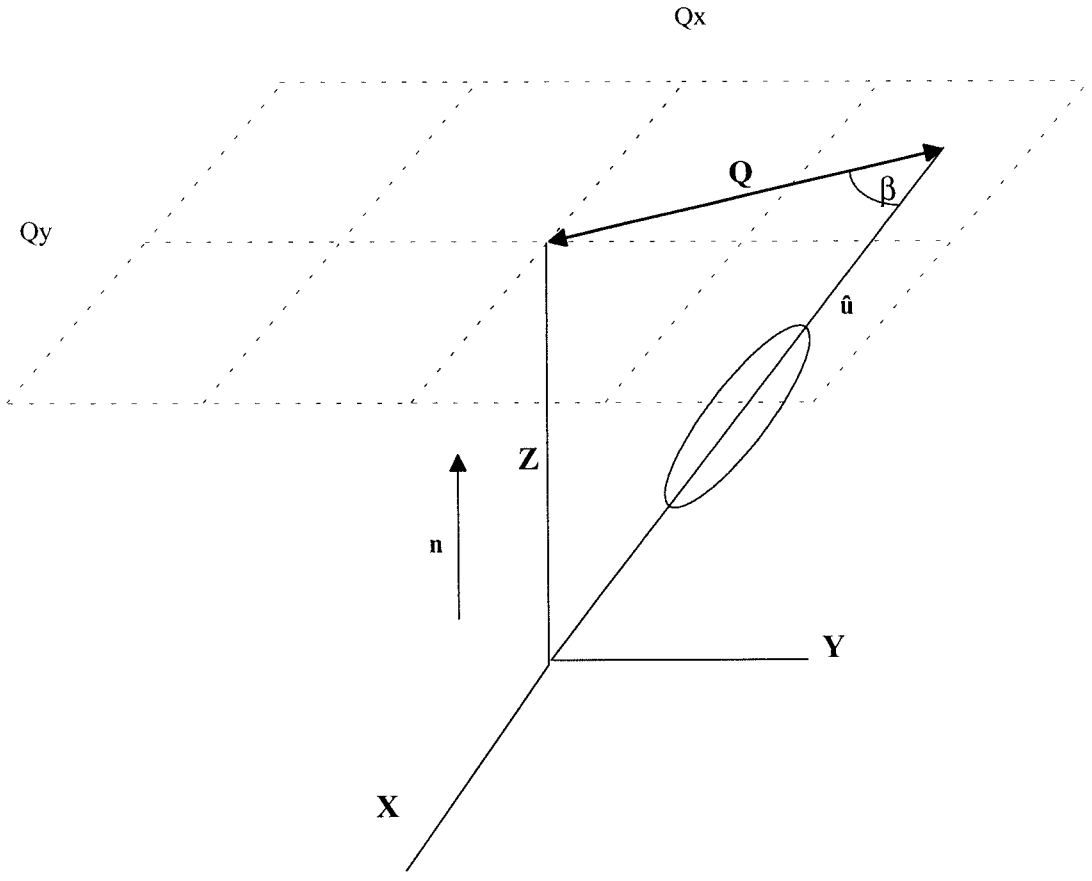

Figure 4.7: *Representation of the geometry of the model used to calculate the X-ray or neutron diffraction pattern from an ellipsoid at the position of each Gay-Berne particle in a configuration taken from the simulation.*

The form factors, in equation (4.25), for the total scattering thus become

$$F_{\mathrm{T}}(\mathbf{Q}) = \sum_{i=1}^{N} f(\mathbf{Q})\exp(\mathrm{i}\mathbf{Q}.\mathbf{r}_i) \quad \text{and} \quad F^{*}_{\mathrm{T}}(\mathbf{Q}) = \sum_{i=1}^{N} f(\mathbf{Q})\exp(-\mathrm{i}\mathbf{Q}.\mathbf{r}_i), \tag{4.28}$$

where $\mathbf{r}_i$ is the position vector for the i^{th} site in the laboratory frame, and the summation is over the N particles in the configuration. It was found that it was computationally less expensive to calculate the trigonometric forms of the form factors than the exponential version, thus the total coherent scattering is written as

$$\begin{aligned} I_{\mathrm{T}}(\mathbf{Q}) &= F_{\mathrm{T}}(\mathbf{Q})F^{*}_{\mathrm{T}}(\mathbf{Q}) \\ &= \sum_{i=1}^{N} f(\mathbf{Q})[\cos(\mathbf{Q}.\mathbf{r}_i)+\mathrm{i}\sin(\mathbf{Q}.\mathbf{r}_i)]\sum_{j=1}^{N} f(\mathbf{Q})[\cos(\mathbf{Q}.\mathbf{r}_j)-\mathrm{i}\sin(\mathbf{Q}.\mathbf{r}_j)]. \end{aligned} \tag{4.29}$$

It should be noted that in our program, we calculate $F_{\mathrm{T}}(\mathbf{Q})$ and $F^{*}_{\mathrm{T}}(\mathbf{Q})$ by summing over all particles and thus we do not need to look at all pairs which is far more computationally expensive. As well as calculating the total intensity, we can also calculate the intramolecular or single particle scattering in the same way so that

$$\begin{aligned} I_{\mathrm{S}}(\mathbf{Q}) &= F^{K}_{\mathrm{S}}(\mathbf{Q})F^{K*}_{\mathrm{S}}(\mathbf{Q}) \\ &= \sum_{i=1}^{N} f(\mathbf{Q})[\cos(\mathbf{Q}.\mathbf{r}^{k}_i)+\mathrm{i}\sin(\mathbf{Q}.\mathbf{r}^{k}_i)]\sum_{i=1}^{N} f(\mathbf{Q})[\cos(\mathbf{Q}.\mathbf{r}^{k}_i)-\mathrm{i}\sin(\mathbf{Q}.\mathbf{r}^{k}_i)], \end{aligned} \tag{4.30}$$

where $\mathbf{r}^{k}_i$ is the position vector in of the i^{th} molecule in the k^{th} director frame. From a real X-ray diffraction pattern we only obtain the total scattering, $I_{\mathrm{T}}(\mathbf{Q})$, from the sample; this highlights another advantage of a computer simulation in that we can separate out the interference or intermolecular scattering, which is given by the difference between the total and intramolecular scattering,

$$I_{\mathrm{I}}(\mathbf{Q}) = I_{\mathrm{T}}(\mathbf{Q}) - I_{\mathrm{S}}(\mathbf{Q}). \tag{4.31}$$

4.3.4 Computational procedure

We start from the results of our simulations, having stored on magnetic tape the positions, orientations and director orientation of a series of configurations, each separated by 50 time steps. The maximum number of configurations stored was a thousand with any number from 10 to a 1000 configurations being used for the calculation of the diffraction pattern for the 256 particle system. Having generated these coordinates in the simulation box frame, we need to transform them into the director frame. This is necessary, as on average

the director does not lie parallel to a side of the simulation box and will change orientation throughout the simulation. So by transforming into a director frame, we can put the director along a fixed box edge, namely the Z axis, so making the calculations easier as we can always locate the director and thus maintain a constant relationship to the scattering vector. The coordinates from the simulation frame (X_o, Y_o, Z_o) are transformed into the director frame (X_n, Y_n, Z_n) by the relationship

$$\begin{pmatrix} X_n \\ Y_n \\ Z_n \end{pmatrix} = \begin{pmatrix} \iota_{X_nX_o} & \iota_{X_nY_o} & \iota_{X_nZ_o} \\ \iota_{Y_nX_o} & \iota_{Y_nY_o} & \iota_{Y_nZ_o} \\ \iota_{Z_nX_o} & \iota_{Z_nY_o} & \iota_{Z_nZ_o} \end{pmatrix} \begin{pmatrix} X_o \\ Y_o \\ Z_o \end{pmatrix}. \tag{4.32}$$

This rotation matrix of direction cosines ι_{ab} can be defined in terms of the Euler angles α, β and γ[12] (see figure 4.8), so that

$$D = \begin{pmatrix} c\alpha c\beta c\gamma - s\alpha s\gamma & -c\alpha c\beta s\gamma - s\alpha c\gamma & c\alpha s\beta \\ s\alpha c\beta c\gamma + c\alpha s\gamma & -s\alpha c\beta s\gamma + c\alpha c\gamma & s\alpha s\beta \\ -s\beta c\gamma & s\beta s\gamma & c\beta \end{pmatrix}, \tag{4.33}$$

where s denotes sine and c, cosine. This procedure simply rotates the whole configuration into a new axis frame, conserving the number of particles in the original simulation box.

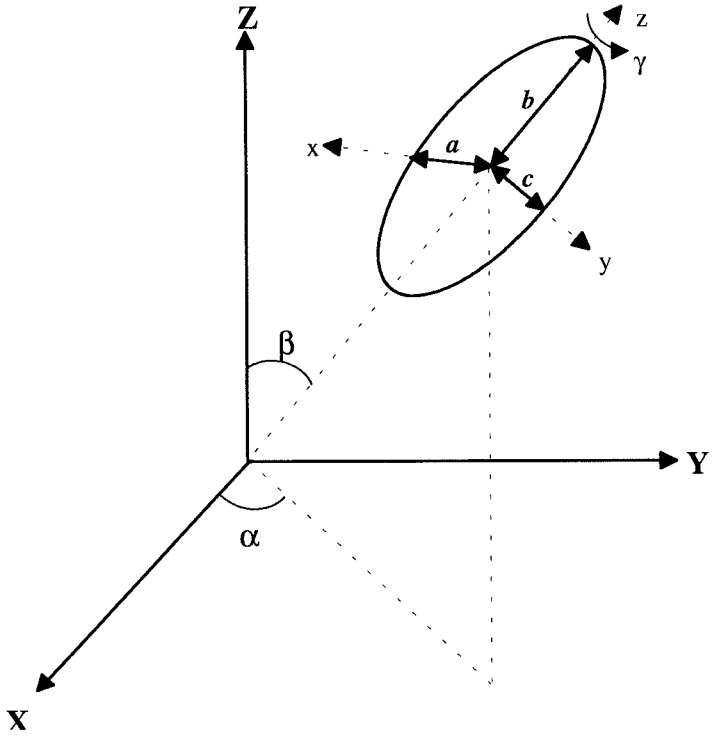

Figure 4.8: *An ellipsoid having semi-axes a, b and c with a representation of the Euler angles (α, β, γ) used to define the relationship between the particle fixed axes (x, y, z) and the axes of the director frame (X, Y, Z).*

Once we have transformed the coordinates into the director frame, we can now calculate the total, $I_T(\mathbf{Q})$, and intramolecular, $I_S(\mathbf{Q})$, scattering, (from equations (4.29) and (4.30) respectively), both parallel and perpendicular to the director. The patterns are calculated in reciprocal or **Q** space, but as we use a scaled separation of $r^* = r/\sigma_s$ in real space, we can similarly scale **Q** space such that $\mathbf{Q}^* = \mathbf{Q}/(2\pi/\sigma_s) = 1/r^*$. As the director now lies along the Z axis in the new coordinate system, the diffraction pattern parallel to the director is calculated in the (Qx*, Qy*) plane with Qz* set to zero, while for the perpendicular direction, the (Qx*, Qz*) and (Qy*, Qz*) planes are used to check on the symmetry of the phase. Once we have calculated the pattern for one frame, we perform the same calculation for consecutive frames, summing up as we go. The patterns are plotted using the Gnuplot program[13]. The optimum number of configurations used and the influence of the system size will be discussed in the following section. We shall now go on to discuss the simulated intramolecular and total scattering patterns obtained.

4.4 Results and discussion

4.4.1 Intramolecular diffraction patterns

As with previous studies[8], the main aim of calculating the intramolecular scattering was to check the procedure for the calculation of the total diffraction pattern. The system we have investigated is that from the previous chapter of this Thesis, a system of 256 Gay-Berne ellipsoids interacting with σ_f/σ_e of 0.345 and $\varepsilon_f/\varepsilon_e$ of 5.0, in which isotropic, discotic nematic and hexagonal columnar phases at ρ^* of 2.5, and a rectangular columnar phase at ρ^* of 2.7, were formed. First, we shall look at the scattering parallel to the director, in the (Qx*, Qy*) plane, then proceed onto the perpendicular direction, the (Qx*, Qz*) plane and since all of these patterns are generally well-averaged and smooth with a small signal-to-noise ratio, they are calculated from just 10 configurations. We will represent each diffraction pattern as a three dimensional graph with a corresponding contour plot, the axes being the plane in which the pattern was calculated.

First, however, it may be useful to look at the diffraction for just a single ellipsoidal particle, along its symmetry axis. From this direction, the ellipsoid will appear circular and hence should show a symmetrical diffraction pattern. As we can see from figure 4.9a, the pattern for a single ellipsoid does indeed appear to be isotropic, giving us some confidence

in our calculation of the structure factor. We can now move onto the intramolecular patterns for the liquid-crystalline mesophases under investigation. For the subsequent patterns of the isotropic phase, (figure 4.9b), the nematic phase at T^* of 9.09, (figure 4.9c), the nematic phase at T^* of 3.03, (figure 4.10a), the hexagonal columnar phase (figure 4.10b) and the rectangular columnar phase, (figure 4.10c), we can see that the diffraction pattern is also isotropic in this direction. Some of the diffraction patterns are not perfectly isotropic, as there is a slight difference in the Q_{xx} and Q_{yy} elements, (see §2.2.5), of the ordering **Q** tensor i.e. the phases are very slightly biaxial. It is also interesting to note that the peaks become sharper as the temperature is decreased, this reflecting the increased orientational order the particles are under in the mesophase.

We obtain a different diffraction pattern for **Q*** perpendicular to the director, in the (Qx*, Qz*) plane. For the single ellipsoid, (see figure 4.11a), there is a band of scattering concentrated along the X axis. This reflects the anisotropic shape of the ellipsoid in this plane. But in the isotropic phase, (see figure 4.11b), we can see that this pattern is again essentially isotropic, then as the orientational order increases, the pattern becomes less isotropic (see figure 4.12) reflecting the increased anisotropic environment the particles find themselves in. As the orientational order increases, the band of diffraction narrows. We obtain similar patterns in the (Qy*, Qz*) plane.

One further check on the appearance of these diffraction patterns is in the intensity of the diffraction pattern. For an ideal crystal, the intramolecular scattering is simply, N, the number of particles in the simulation multiplied by the scattering intensity from one molecule, multiplied by the number of configurations used. Thus, as the scattering intensity, $I(\mathbf{Q}^*)$, from one, oblate ellipsoid has a value of 1, the maximum total intensity for each of the different phases should be 1 x 256 x 10 = 2560, which as we can see from the various patterns is observed. Having satisfied ourselves about the intramolecular diffraction we shall now move onto the total diffraction patterns.

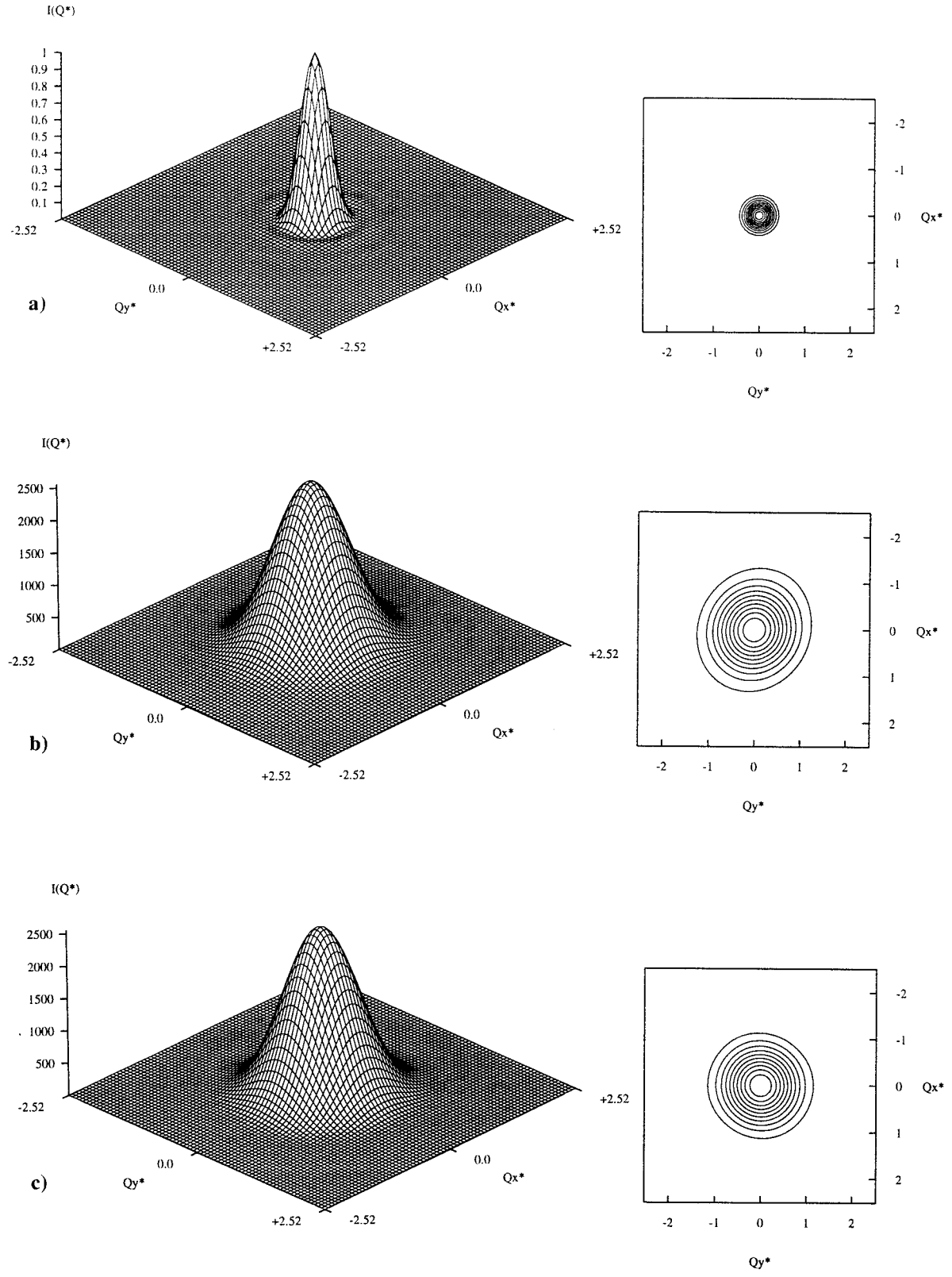

Figure 4.9: *The intramolecular X-ray diffraction patterns for* ***Q**** *parallel to the director, in the (Qx*, Qy*) plane, for a) a single, oblate ellipsoid from 1 configuration, b) the isotropic phase at T* of 10.77 from 10 configurations and c) the discotic nematic phase at T* of 9.09 from 10 configurations. The director is orthogonal to this plane.*

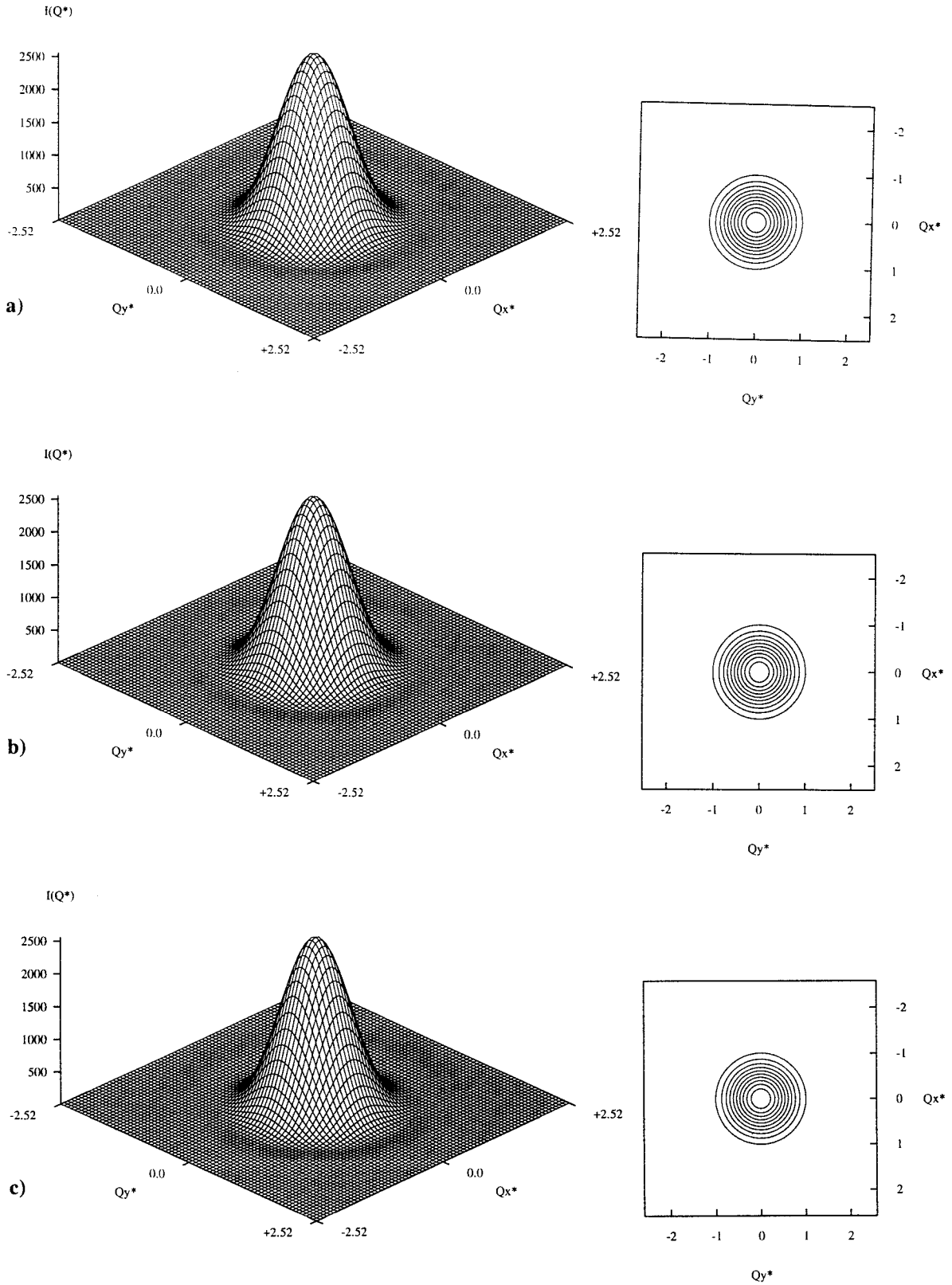

Figure 4.10: *The intramolecular X-ray diffraction patterns for* ***Q**** *parallel to the director, in the (Qx*, Qy*) plane, for a) the discotic nematic phase at T* of 3.03 from 10 configurations, b) the hexagonal columnar phase at T* of 2.01 from 10 configurations and c) the rectangular columnar phase at T* of 2.04 from 10 configurations. The director is orthogonal to this plane.*

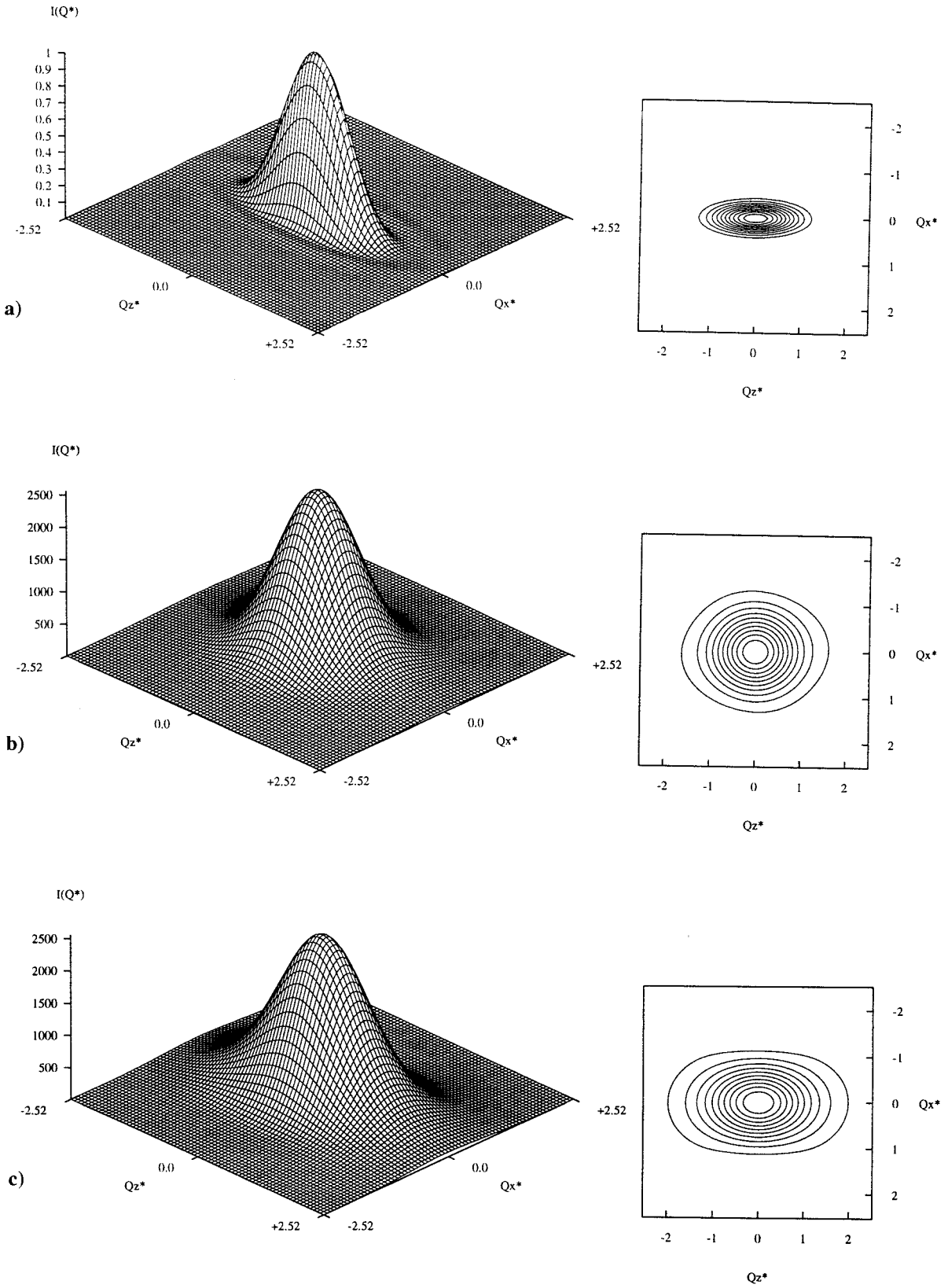

Figure 4.11: *The intramolecular X-ray diffraction patterns for* ***Q**** *perpendicular to the director, in the (Qx*, Qz*) plane, for a) a single, oblate ellipsoid from 1 configuration, b) the isotropic phase at T* of 10.77 from 10 configurations and c) the discotic nematic phase at T* of 9.09 from 10 configurations. The director is parallel to the Qz* axis.*

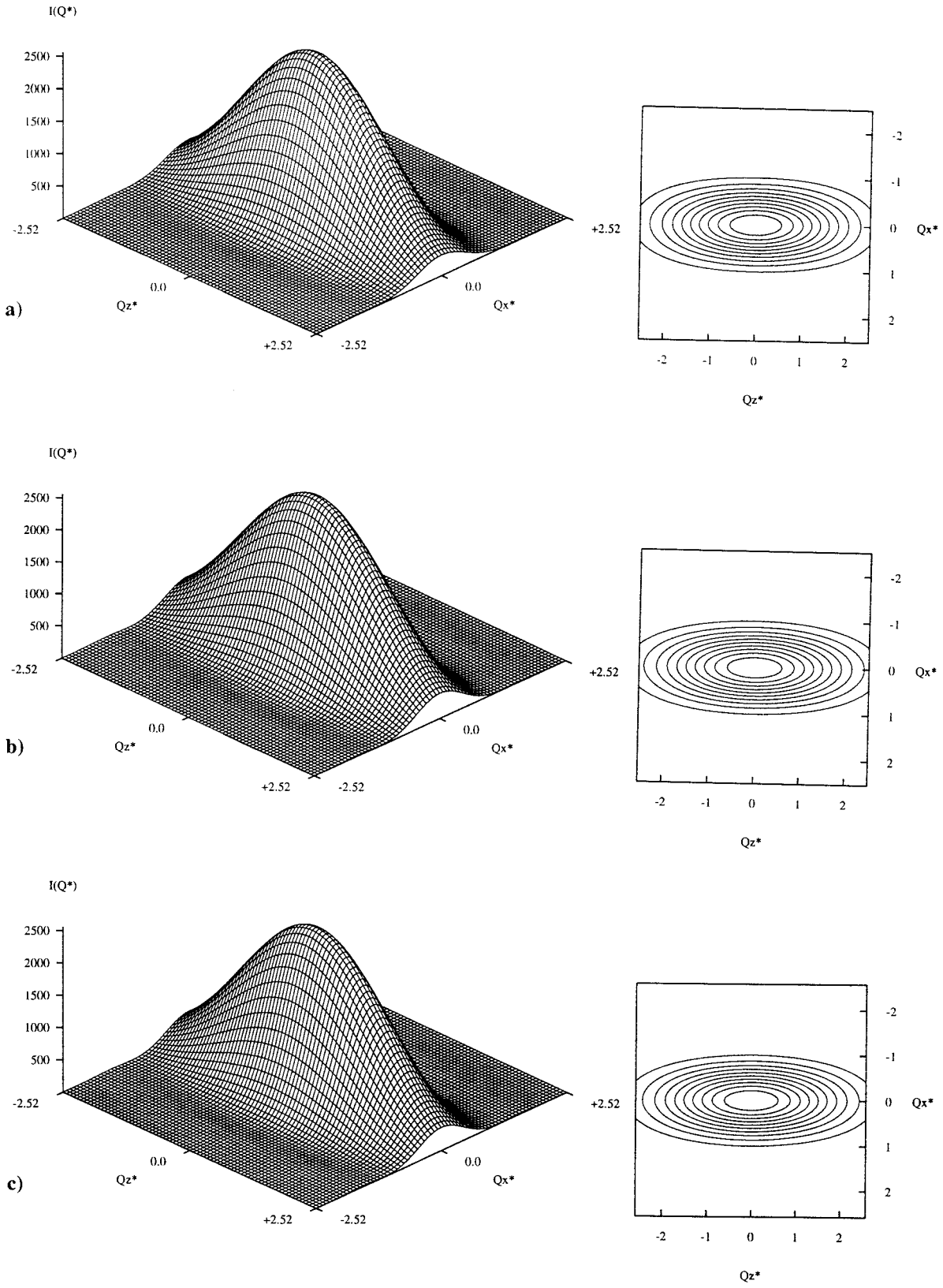

Figure 4.12: *The intramolecular X-ray diffraction patterns for* ***Q**** *perpendicular to the director, in the (Qx*, Qz*) plane, for a) the discotic nematic phase at T* of 3.03 from 10 configurations, b) the hexagonal columnar phase at T* of 2.01 from 10 configurations and c) the rectangular columnar phase at T* of 2.04 from 10 configurations. The director is parallel to the Qz* axis.*

4.4.2 Total diffraction patterns

We have calculated the total diffraction patterns both parallel and perpendicular to the director, by transforming from the simulation axes frame to that of the director, which is now aligned along the Z axis of the new coordinate system. The diffraction patterns are again visualised via a three dimensional surface representation and a corresponding contour plot. For these total diffraction patterns we need to remove the central area, as a peak at $\mathbf{Q}^*$ of 0 dominates; this arises from the term exp(i$\mathbf{Q}.\mathbf{r}$) in equation (4.28), this procedure being similar to using a beam stop in a real experiment. Initially, the size of the beam stop allowed just separations of the order of the box length to remain. Again, the systems we have investigated are the phases produced in the previous chapter, namely, isotropic, discotic nematic, hexagonal columnar and rectangular columnar phases produced from a system of Gay-Berne ellipsoids interacting with σ_f/σ_e of 0.345 and $\varepsilon_f/\varepsilon_e$ of 5.0. The system consists of 256 particles and in general 10 configurations were used to generate the diffraction patterns. We could quite easily extend the number of configurations used, as this would improve the signal-to-noise ratio, but as we shall see, the improvement of the pattern is small compared to the extra computer resources needed to calculate the scattering. On average, it requires about 10s of c.p.u. time to calculate a diffraction pattern from one configuration. In the contour plots, there are 10 contours evenly spaced at a distance automatically set by the plotting software. We can add more contours but this generally complicates the contour plot. Thus the contour plot only reveals the more intense structural features and in some cases, can appear much different from that of the three dimensional surface plot.

Isotropic phase T^* of 10.77: Figure 4.13a shows the diffraction patterns for the isotropic phase parallel to the director. For this first pattern, the radius of the beam stop is 0.43$\mathbf{Q}^*$, but even with this, we can see that two spurious peaks at the centre, dominate the pattern. We shall discuss these later. The remainder of the pattern is generally isotropic as expected in the diffraction plane with a very weak diffuse ring at $\approx 1.1\mathbf{Q}^*$ corresponding to $r^* \approx 0.9$. This is in reasonable agreement with the position of the peak in the radial distribution function obtained from the simulation, but as this peak in the $g(r^*)$ is very weak we would also expect the resultant X-ray diffraction feature to be very weak i.e. there are very few particles at this separation.

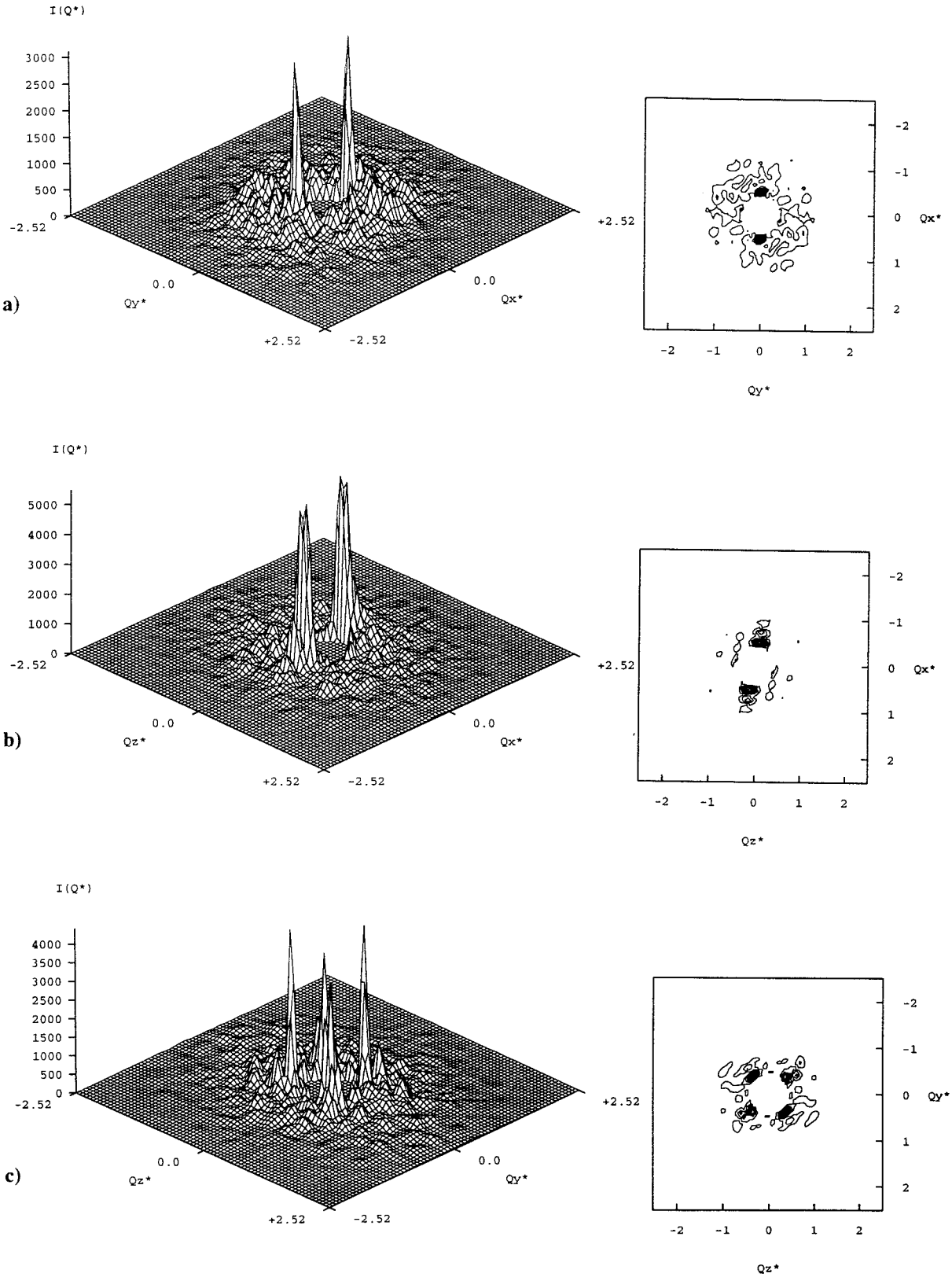

Figure 4.13: *The total scattering for the isotropic phase at T* of 10.77 from 10 configurations, a) parallel to the director in the (Qx*, Qy*) plane, b) perpendicular to the director in the (Qx*, Qz*) plane and c) perpendicular to the director in the (Qy*, Qz*) plane for N of 256.*

An isotropic phase has no orientational order, but due to our method of calculating the order parameter, (see §2.4.2), we observe $\langle P_2 \rangle$ to be 0.15, and thus we can define a director. So we can calculate the diffraction patterns perpendicular to the director, (see figure 4.13b and 4.13c). We can see a weak circular area of scattering which correlates with the isotropic phase even though there is a small degree of orientational order. We could calculate the diffraction patterns without having to transform into a director frame, by the use of a common laboratory frame, giving the advantage of providing more isotropic averaging but we found that this method did not improve the patterns significantly. We now return to the issue of the origin of the central peaks which are present in the total diffraction patterns. They are at $\mathbf{Q}^*$ of 0.5, which equates to a distance of r^* of 2.0. This does correspond to a real separation in the simulation box as the maximum length of the simulation box is $2.34\sigma_0$, but inspection of the corresponding $g(r^*)$, (see figure 3.10 in §3.4.3), reveals that at this separation, there appears to be no correlation between particles, so we speculate that they might come from the small, finite size of the simulation box, an idea we shall explore in §4.4.3.

Discotic nematic phase T^* of 9.09: The next set of diffraction patterns we shall look at, are for the discotic nematic phase, just below the discotic nematic - isotropic phase transition. Parallel to the director in the (Qx*, Qy*) plane, we do not expect the pattern to be significantly different from that of the isotropic phase, with just a diffuse ring visible at $\approx 1.1\mathbf{Q}^*$, representing the edge-to-edge correlations within the phase as seen in the $g(r^*)$. From figure 4.14a, we do indeed see a scattering feature at $\approx 1.0\mathbf{Q}^*$ with another less intense ring at $\approx 2.0\mathbf{Q}^*$, this probably being the second order reflection from the main ring. Again we see four dominant peaks, the presence of which we shall ignore for now as they do not interfere with the pattern. Perpendicular to the director in both the (Qx*, Qz*) plane, (see figure 4.14b), and the (Qy*, Qz*) plane, (see figure 4.14c), we expect two weak arcs of scattering located on the equatorial axis, Qz* ≈ 0.0 on our pattern. Unfortunately these patterns are dominated by both the spurious peaks and by a band of scattering in the meridional axis, Qx* ≈ 0.0. Though in the (Qy*, Qz*) plane, there seems to be an intense peak at Qy* ≈ 0.9. This corresponds to a distance of r^* of 1.1 and as they lay off the Qz* axis by about 10 - 15°, they could suggest a staggered edge-to-edge arrangement of particles.

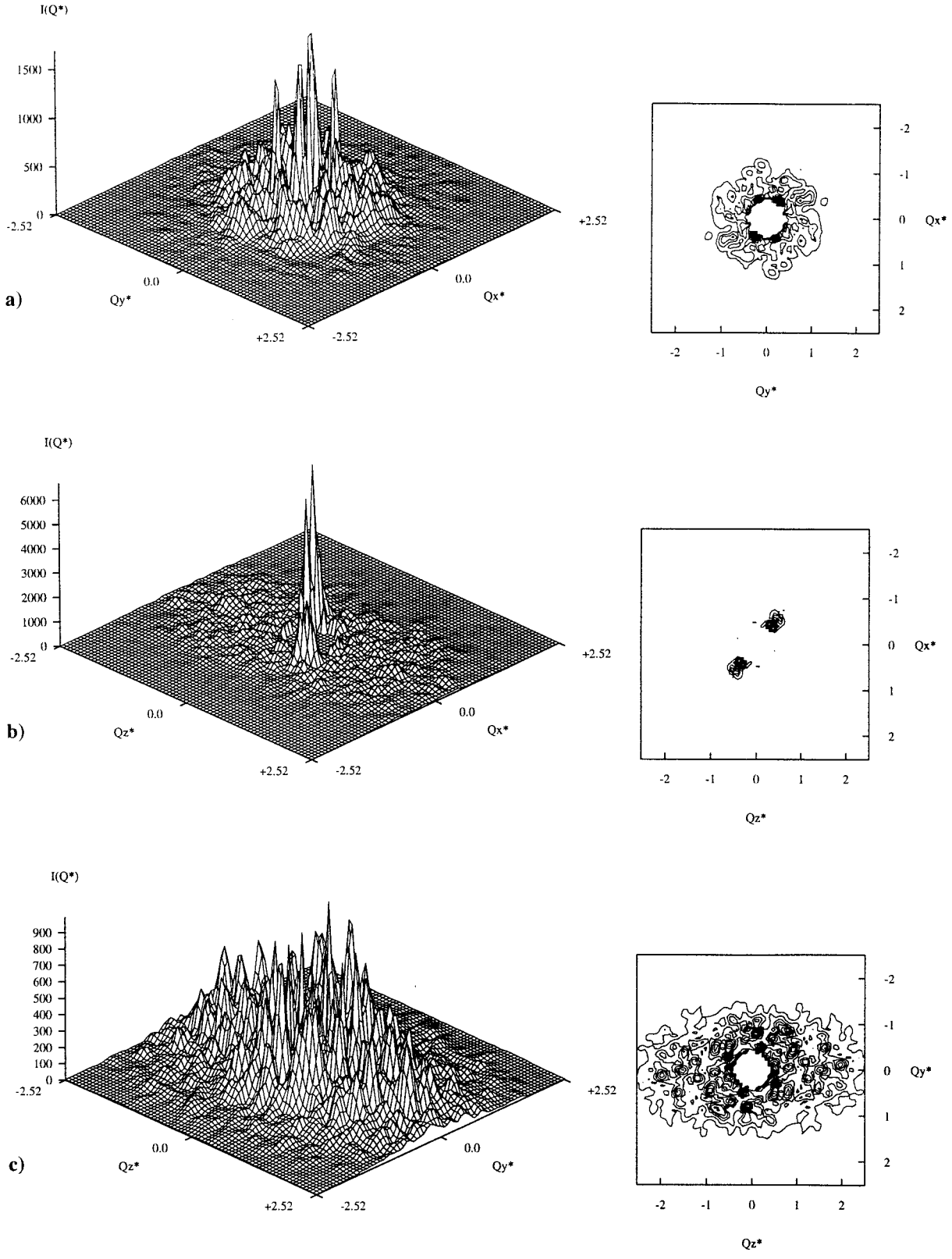

Figure 4.14: *The total scattering for the nematic phase at T* of 9.09 from 10 configurations, a) parallel to the director in the (Qx*, Qy*) plane, b) perpendicular to the director in the (Qx*, Qz*) plane and c) perpendicular to the director in the (Qy*, Qz*) plane for N of 256.*

Discotic nematic phase T^* of 3.03: As we lower the temperature during the simulation to just above the columnar - discotic nematic phase transition, there is increased long range orientational and short range translational order within the mesophase; this is reflected in the diffraction patterns, (see figure 4.15). With **Q*** parallel to the director, we can see that the diffraction pattern corresponds well with the data obtained from various distribution functions we have calculated such as the $g(r^*)$ and $g_\perp(r_\perp^*)$, (see §3.4.3). We can see an isotropic scattering feature, as the phase should be uniaxial in this plane, at $\approx 1.0\mathbf{Q}^*$ or r^* of 1.0, this corresponding to particles in an edge-to-edge arrangement without any interdigitation while there is the second order reflection at $\approx 2.0\mathbf{Q}^*$, this being very much weaker in intensity. This is due to the positional order being short range. We can also observe a structure within the diffraction circle and this could signal that only certain orientations are preferred within the phase.

The scattering pattern for **Q*** perpendicular to the director is again dominated by the spurious peaks and the intramolecular scattering in the meridional plane, but we do see two diffraction peaks, along the equatorial axis at $Qx^* \approx 1.0$, representing the increased edge-to-edge correlations and agreeing with both the distribution function $g_\perp(r_\perp^*)$ and the parallel diffraction pattern. There also appears to be the beginnings of a concentrated diffraction feature at $Qz^* \approx 2.0$, this corresponds to r^* of 0.5 i.e. face-to-face ordering.

Hexagonal columnar phase T^* of 2.01: The next two mesophases we shall investigate are the translationally ordered columnar phases. From the results of our simulations we have a hexagonal columnar phase, D_h, where the columns are arranged in a hexagonal net, and a rectangular columnar phase, D_r, with four fold symmetry. For both of these phases, the particles within each column are ordered and are correlated with those in neighbouring columns but with a periodicity of half the molecular thickness. For the hexagonal columnar phase, with **Q*** parallel to the director, (see figure 4.16a), we can indeed see the six peaks representing the hexagonal packing, while it is also possible to see the second order reflections resulting from these peaks, an indication of the long range nature of the translational order and its non-sinusoidal character.

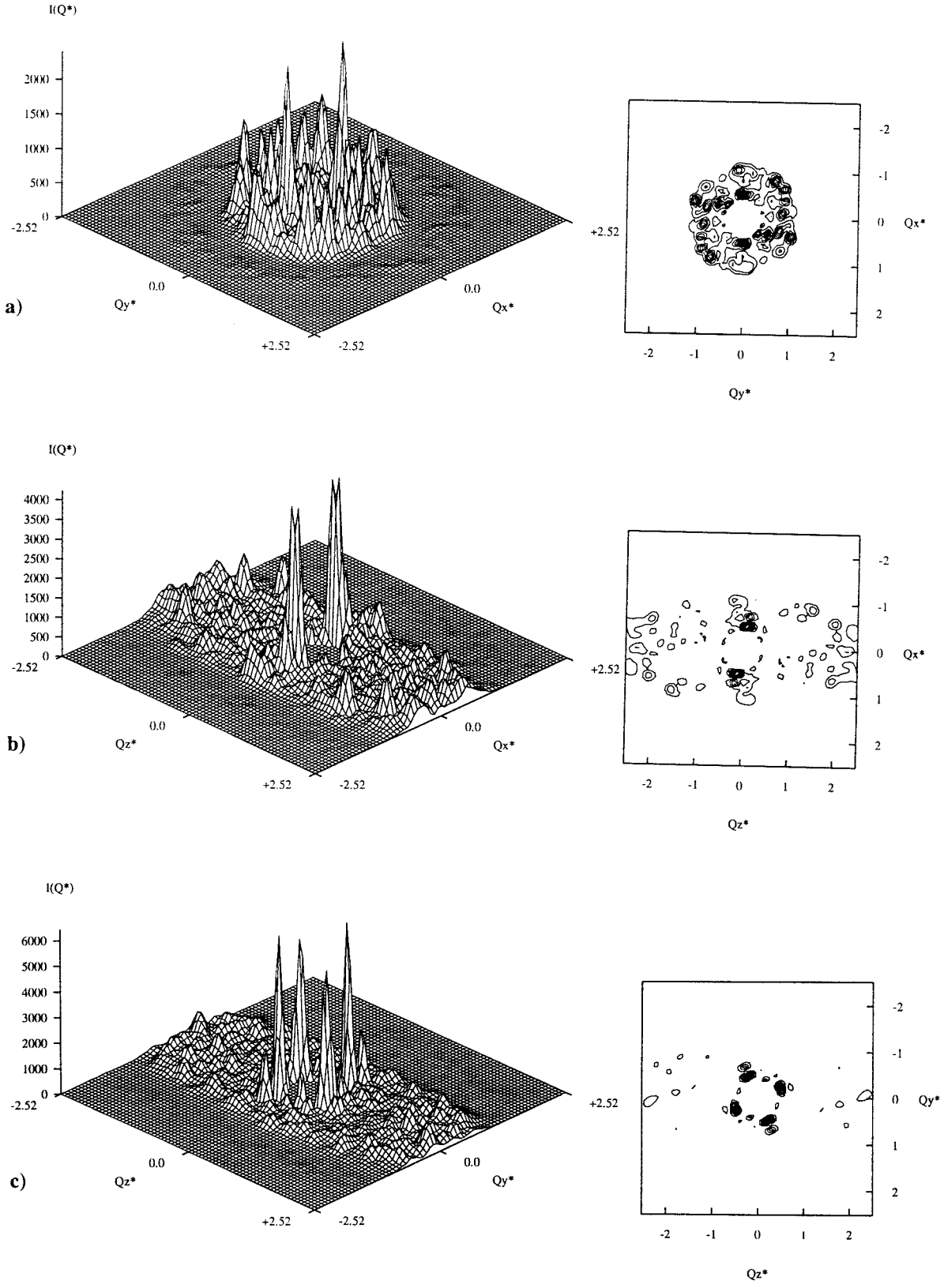

Figure 4.15: *The total scattering for the nematic phase at T* of 3.03 from 10 configurations, a) parallel to the director in the (Qx*, Qy*) plane, b) perpendicular to the director in the (Qx*, Qz*) plane and c) perpendicular to the director in the (Qy*, Qz*) plane for N of 256.*

The position of the main peaks are at $\approx 1.1\mathbf{Q}^*$ which gives a real distance for r^* of 0.9, and though it does not seem to correspond to the distances observed in the $g_\perp(r_\perp^*)$, it is consistent with the columns being close packed i.e. $1.0\sigma_0$, as observed in a graphic snapshot of a configuration, (see figure 3.14). This is because the diffraction pattern is actually picking up the closest distance between planes of columns as seen in figure 4.17. We should also mention the hexagonal packing of the columns is not perfect as is shown by the slightly distorted nature of the six peaks and the difference in the intensity. This illustrates the power of X-ray diffraction, as although we could tell this by looking at the graphic snapshots, no other distribution function could pick this up so effectively.

Perpendicular to the director, we should pick up both edge-to-edge and face-to-face correlations. Looking at the contour plot, (see figure 4.16b), we can see that along the Qz* axis, the director, there are peaks at $\approx 2.2\mathbf{Q}^*$ or r^* of 0.45, which corresponds well to the $g(r^*)$ value of 0.46 for particles in a face-to-face orientation. The edge-to-edge or intercolumn correlations are represented along the Qx* axis at $\approx 1.1\mathbf{Q}^*$ which gives r^* of 0.9. This is similar to the values obtained parallel to the director, and is the closest distance between planes of neighbouring columns.

We also see that the face-to-face peaks at Qz* $\approx$ 2.2 are off axis by about 10^o. This possibly indicates that the columns are slightly tilted with respect to the director. Again this illustrates the potential of X-ray diffraction, as from our results in Chapter 3, it was not obvious that the columns were tilted. If indeed, the columns are tilted what would cause this, as there is no term in the intermolecular potential which could explain this phenomenon, though a tilted phase was observed by Chalam *et al.*[114] in their studies of a rod-shaped Gay-Berne mesogen. Perhaps the fixed shape and volume of our constant *NVE* ensemble simulation box forces the columns to be tilted, in order to be commensurate with the periodic images.

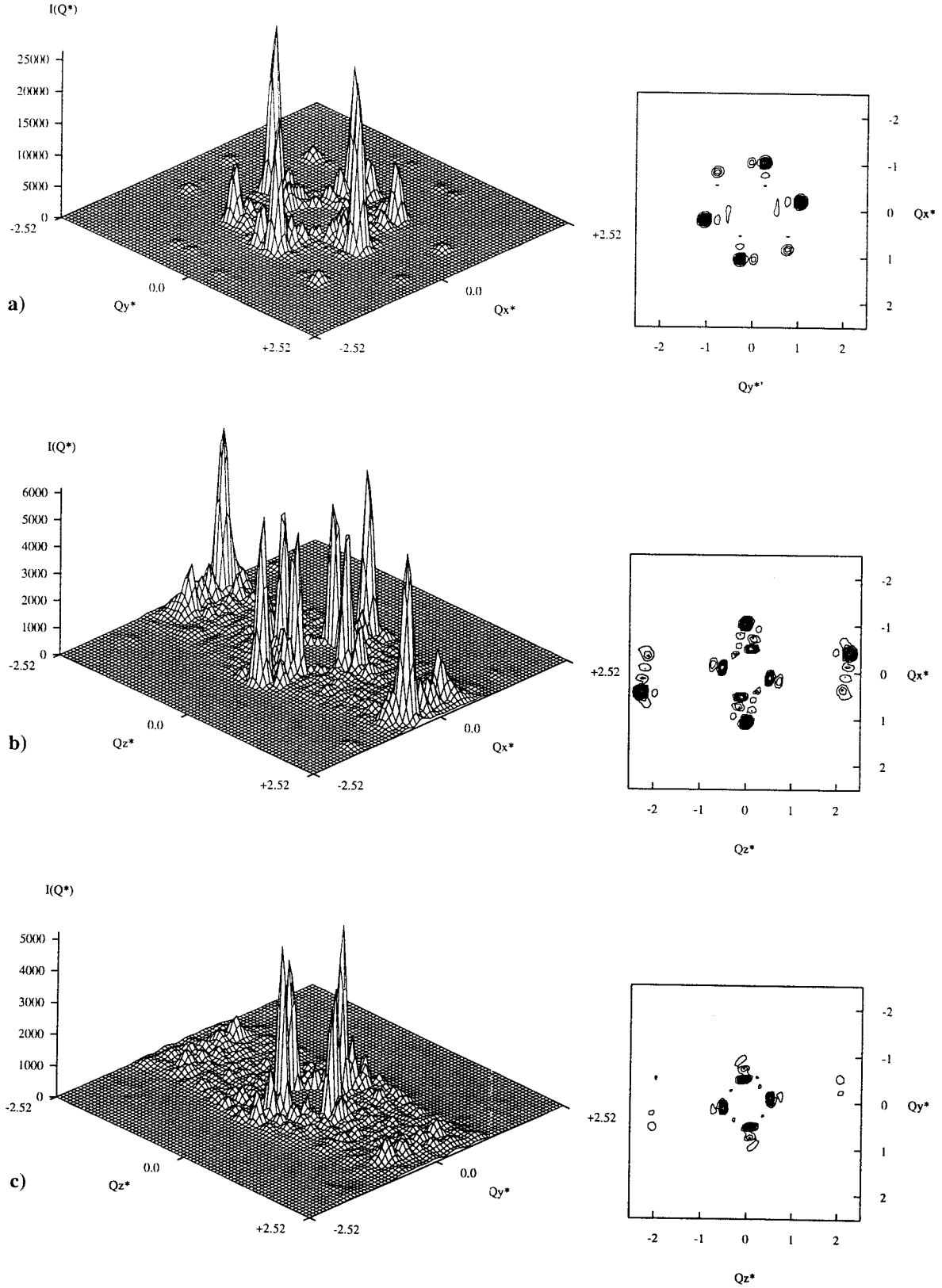

Figure 4.16: *The total scattering for the hexagonal columnar phase at T* of 2.01, from 10 configurations, a) parallel to the director in the (Qx*, Qy*) plane, b) perpendicular to the director in the (Qx*, Qz*) plane and c) perpendicular to the director in the (Qy*, Qz*) plane for N of 256.*

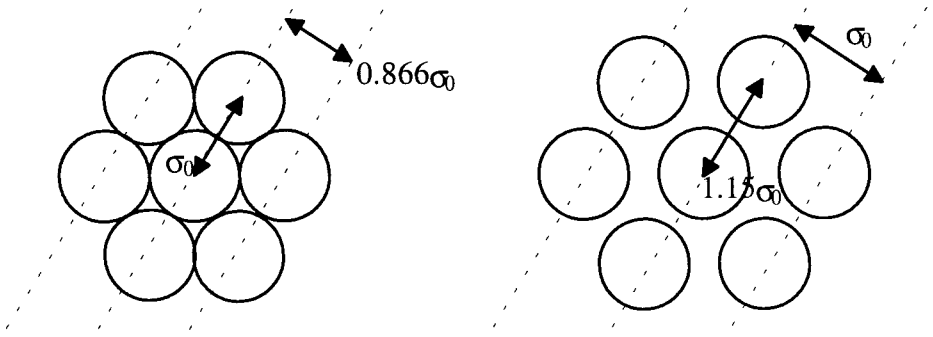

Figure 4.17: *A representation of the relationship between the g(r*) and X-ray diffraction values for the distance between neighbouring columns, that are a) close packed and b) with an expanded packing lattice.*

Rectangular columnar phase *T of 2.04:** For the rectangular columnar phase, at ρ^* of 2.7, the constituent columns actually penetrate each other, the distance being $0.9\sigma_0$ between the centres, and as with the hexagonal columnar phase, this is picked up by the diffraction pattern. Parallel to the director, (see figure 4.18a), the four peaks are at $\approx 1.0\mathbf{Q}^* \equiv 1.0\sigma_0$ and using the same arguments for the hexagonal packing, gives the columns at a distance less than $1.0\sigma_0$ apart. For $\mathbf{Q}^*$ perpendicular to the director, we can see the face-to-face peaks at $\approx 2.2\mathbf{Q}^*$ and the edge-to-edge features at $\approx 1.0\mathbf{Q}^*$. It is surprising that the edge-to-edge peaks are stronger and the face-to-face weaker than the hexagonal phase. Though still not perfect, it is interesting to see that the patterns for both the columnar phases are much better resolved and more realistic than those for the isotropic and discotic nematic phases. This is probably due to the scattering being concentrated in smaller regions of $\mathbf{Q}^*$ space, giving a more intense peak, thus allowing a good signal-to-noise ratio.

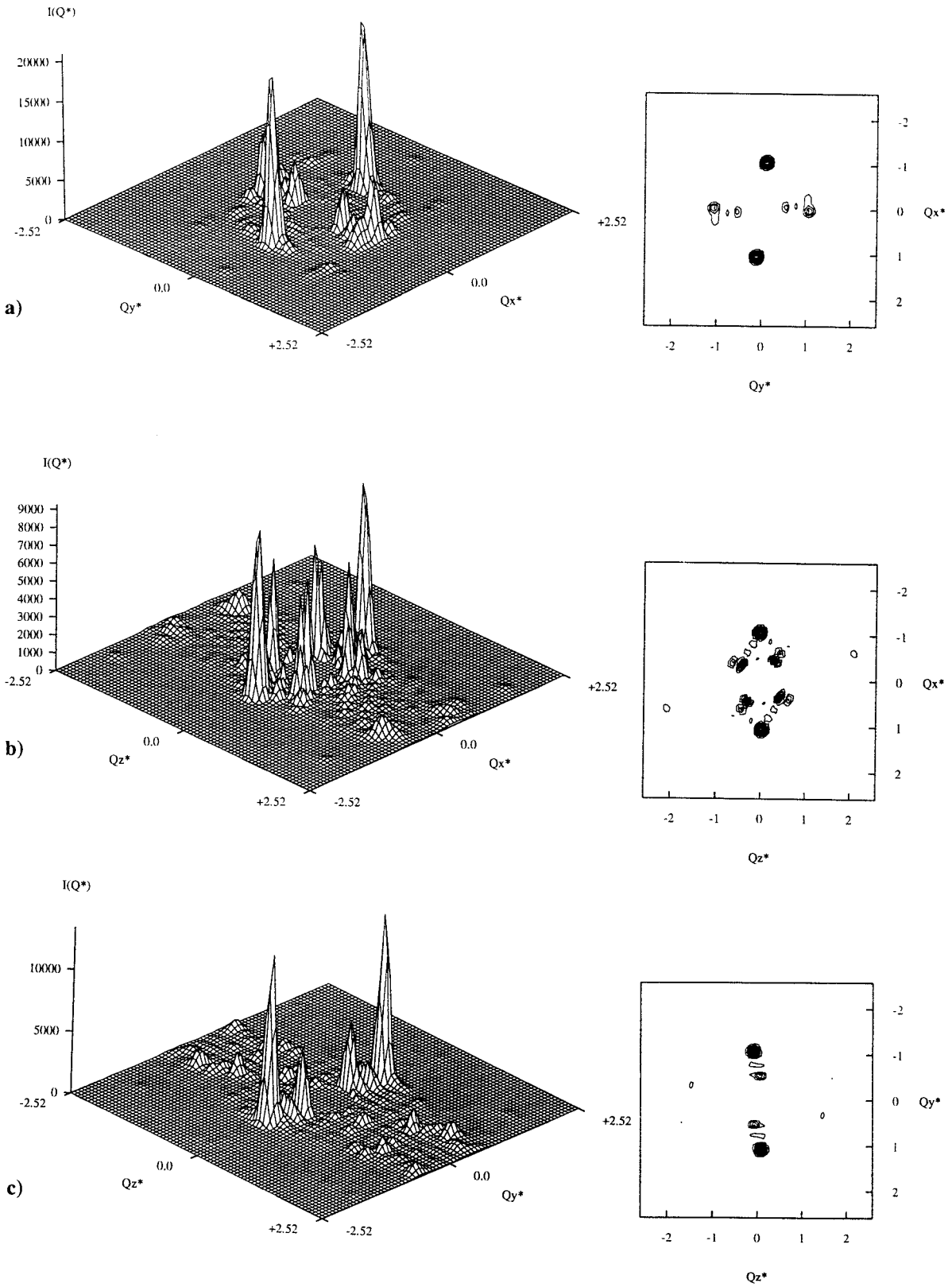

Figure 4.18: *The total scattering for the rectangular columnar phase at T* of 2.04 from 10 configurations, a) parallel to the director in the (Qx*, Qy*) plane, b) perpendicular to the director in the (Qx*, Qz*) plane and c) perpendicular to the director in the (Qy*, Qz*) plane for N of 256.*

Problems encountered

Though the intramolecular diffraction patterns obtained from the simulations produced the expected results, all is not perfect with the total diffraction patterns. As we have seen in various diffraction patterns, (most notably figures 4.15b and 4.17a) there is apparently a series of peaks with four fold symmetry at a distance of $0.5\mathbf{Q}^*$ or $2.0\sigma_0$, As we had previously discussed, we have speculated that these arise from the small, finite system size. But can we improve the patterns and find with a greater certainty the origin of the spurious peaks. These peaks can be observed more clearly in the scattering from one configuration of a discotic nematic phase with $\mathbf{Q}^*$ parallel to the director, (see figure 4.19).

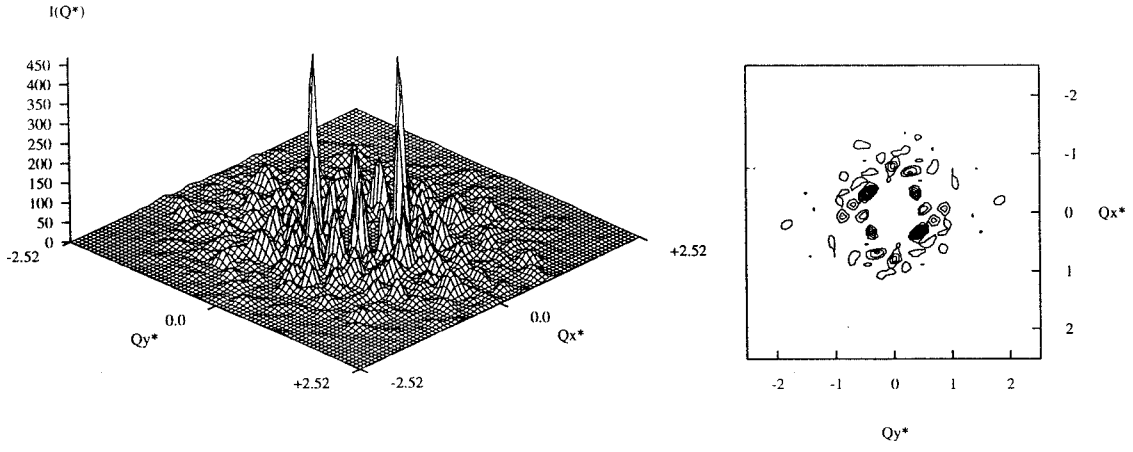

Figure 4.19: *The total diffraction pattern from one configuration of the discotic nematic phase at T* of 9.09 for 256 particles, with Q* parallel to the director, showing the presence of four spurious peaks.*

From the simulation, we expect on average to find particles in an overlapping edge-to-edge orientation with a distance of $r^* \approx 0.9$ between the centre of masses of each ellipsoid, this is indicated by the transverse pair correlation function $g_\perp(r_\perp^*)$, (see §4.4). This arrangement of the particles should give a diffuse ring at a distance $1/r^*$ i.e. 1.1Qx* in the diffraction pattern, with maybe a second, weaker ring at twice this distance $\approx$ 2.2Qx*. But as we can see from our pattern, there are a series of peaks, with fourfold symmetry and which correspond to physical distances in the real simulation box, i.e. they represent a distance of $\approx 2.0\sigma_0$, while the size of the simulation box is $2.34\sigma_0$. At first we thought they may have been part of the intramolecular scattering but subtraction of this quantity from the total pattern to give the intermolecular scattering, (see equation (4.32)), did not remove them.

This can be illustrated for the discotic nematic phase at T^* of 9.09, with $\mathbf{Q}^*$ perpendicular to the director as shown in figure 4.20. So it seems that the peaks arise from either the method used to calculate the diffraction patterns or from some artefact caused by the small size of the box.

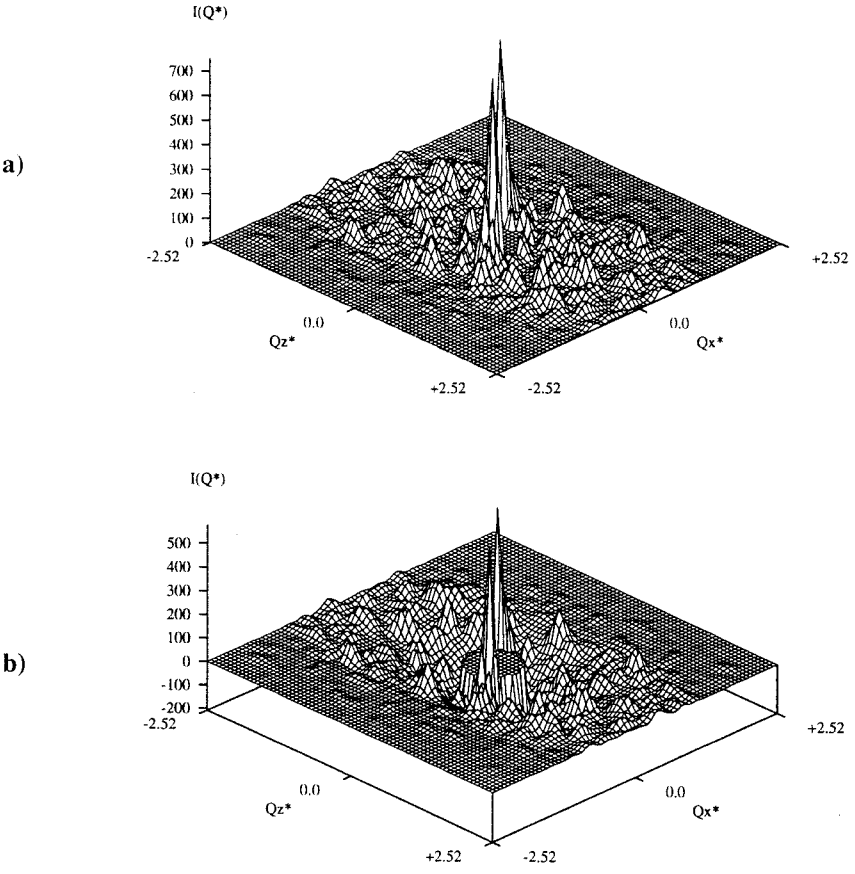

Figure 4.20: *The diffraction pattern from one configuration of the discotic nematic phase at T* of 9.09 for 256 particles, with Q* perpendicular to the director, showing a) the presence of the spurious peaks discussed previously in the total diffraction pattern and b) the effect of subtracting the intramolecular scattering from the total scattering to give the intermolecular scattering and how the peaks are still visible.*

Even excluding the unidentified peaks present, the form of the diffraction patterns is not consistent with those from real experiments. Again, this could be due to the small system size of the simulation. Another factor, could be that the simulation box contains an uneven density of particles along each axis. As is evident from the graphic snapshots of the mesophases generated from our simulations, (see §4.4), in some instances the director does not lie parallel to a side of the simulation box. However, when we transform into the director frame, by lining up the director with the Z axis, we can still be left with the director along a box diagonal, which for the columnar mesophase, results in an uneven

numbers of particles in each column. This can lead to some artificial weakening, and even the disappearance, of some diffraction features. So to ensure an even number of particles throughout each column we need to define a new box with the director along an edge. We do this by generating the next shell of periodic images and then starting from the centre of the original simulation box, form a cubic box with the same dimensions, which may or may not include particles from the periodic images. Thus we find that sometimes the number of particles within the new box may be larger or smaller than in the original simulation box, which is usually by < 10 particles. In theory, the uniform density of particles along the columns should improve the pattern, but as we can see from figure 4.21, it had the effect of smearing out the diffraction pattern while not succeeding in removing the spurious, central peaks.

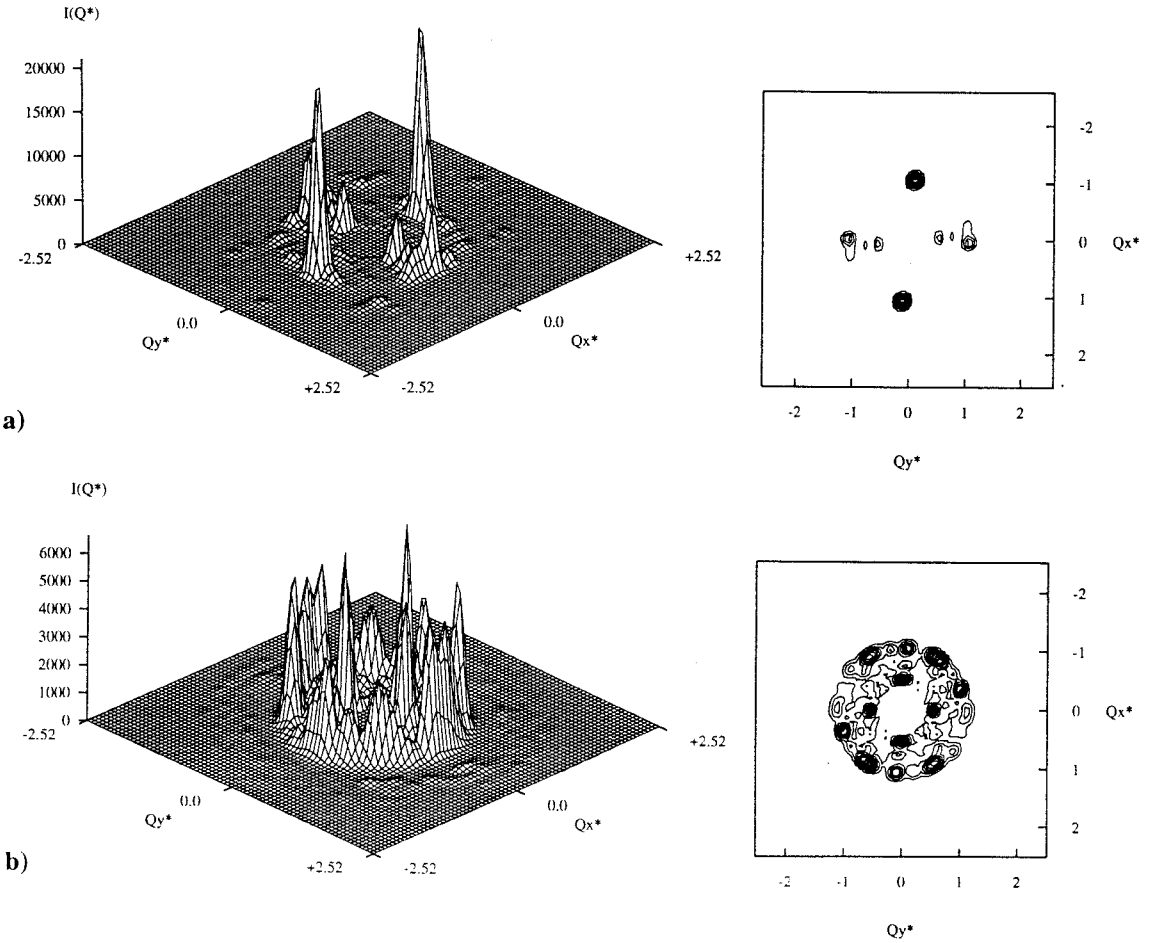

Figure 4.21: *The effect of constructing a new simulation box, with the same number of particles in each column, from a series of periodic images. Illustrated here is the total scattering parallel to the director for the rectangular columnar phase at T* of 2.04, in a) a box with an uneven particle density along the columns and b) a box with an even particle density along the columns.*

Even though we lined up the X and Y axes of the simulation frame from one configuration to another, it is impossible to line up the phase symmetry axes, thus if the phase rotates slightly from one configuration to another this will produce the smearing effect. It is interesting to see that in the box without the uniform density the spurious peaks are at an angle with respect to the X axis, while in the box with the uniform density of particles these peaks had now lined up with the axes. This lead us to the conclusion that they might be due to the small, finite size of the system. This same effect can be seen in the optical transforms of a series of model configurations i.e. masks with a series of spherical holes in[115].

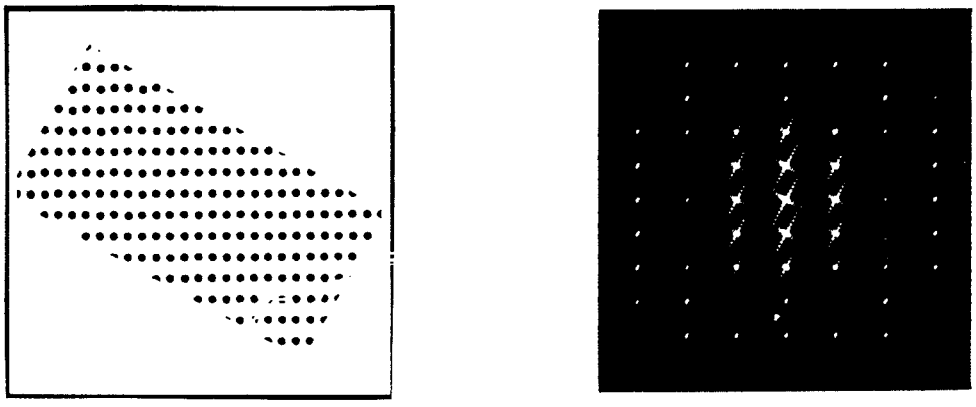

Figure 4.22: *An optical mask of a rectangular box with an uneven number of particles in each column and its diffracted transform.*

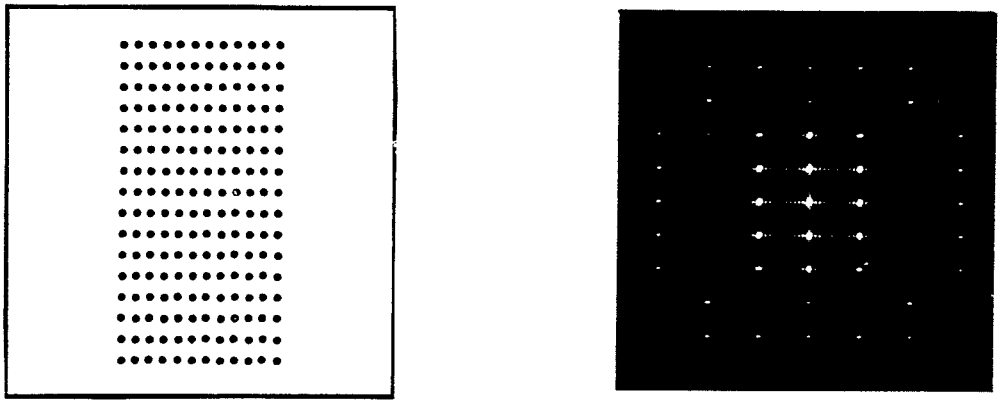

Figure 4.23: *An optical mask of a rectangular box with an even number of particles in each column and its diffracted transform.*

These transforms are masks containing an image of a geometric configuration projected onto a plane that will diffract a monochromatic beam of light. Figure 4.22 shows the optical mask and its corresponding transform of a oriented rectangular box containing a series of spherical diffraction centres. As expected we can see a regular scattering pattern. An important observation is the subsidiary features of the central peaks which lie at an angle to the central peaks but are orthogonal to the initial orientation of the initial scattering pattern. This is equivalent to a simulation box that has an uneven density of particles within each column. Figure 4.23 illustrates the effect of rotating the box so that each column now has the same number of particles in each column. This has a minimal effect on the overall pattern but it is interesting to note that the subsidiary scattering features of the central peaks have rotated, to remain orthogonal with respect to the optical mask. This same behaviour is observed with the spurious peaks, leading us to the conclusion that these peaks are somehow due to the small, finite size of the system.

4.5 Conclusions

In this Chapter we have investigated the possibility of calculating X-ray diffraction patterns of the model mesophases generated from computer simulations. Initial results for a system of prolate particles using a series of spherical scattering centres placed in line along the symmetry axis of each particle gave promising results. But to extend these ideas to oblate particles, such as the disc-shaped mesogens studied in this Thesis, it was decided to place a three dimensional ellipsoid at each site instead. This approach produced mixed results. The intramolecular X-ray scattering mainly provided a means to check the calculation procedure, and as such showed the expected results. All these diffraction patterns were smooth with a good signal-to-noise ratio and produced isotropic peaks parallel to the director but with an anisotropic peak perpendicular to the director, the anisotropy of this peak increasing with increasing orientational and translational order of the mesophase.

But of greatest interest to us, were the total X-ray diffraction patterns, which would hopefully give us detailed information on the molecular packing within each mesophase. In comparison to the intramolecular scattering, these patterns were considerably noisier and provided less clear cut information than we had hoped for.

The first thing we noticed was the presence of a large number of intense peaks between $\mathbf{Q}^*$ of 0.4 - 0.8, but these were attributed to the small, finite size of the system studied. Of all the mesophases investigated, the isotropic and discotic nematic phases produced the worst patterns. Though scattering with $\mathbf{Q}^*$ parallel to the director seemed to show the uniaxial nature of these phases, scattering perpendicular to the director yielded no real information. It did not help that any feature would be very weak, as the corresponding radial distribution functions $g(r^*)$ did not exhibit many intense peaks. The diffraction patterns for the hexagonal and square columnar phases were reasonably sharp and well-defined as expected for more ordered phases. Scattering with $\mathbf{Q}^*$ both parallel and perpendicular to the director produced information on the structure within the phase, with peaks corresponding to both edge-to-edge and face-to-face orientations. It seems that only good patterns are produced, at least for this system, when the scattering is concentrated into small regions of $\mathbf{Q}$ space thus giving intense diffraction peaks.

There are several ways of trying to improve the diffraction patterns, the most obvious being the inclusion of more configurations into the scattering calculation. This seemed to bring some improvement for the isotropic and nematic phases, but had little effect on the columnar phases as these were already well-resolved. Though not strictly an ideal method, increasing the size of the beam stop, to remove the spurious peaks created by the finite system size, also brought about some improvement in the patterns. Another method would be to recreate the simulation box with an even density particles throughout, but as we had no easy way of lining up the x and y axis or the phase symmetry axis, the procedure just smeared out the patterns.

A more drastic way to improve the patterns would be to increase the number particles in the system. Although in theory it is possible to calculate the singlet orientational distribution function $f(\cos\beta)$ from the intensity of the wide angle arcs, it was not attempted as we felt that the patterns did not produce the expected quality needed to make a reasonable estimate. We have shown that it is possible to calculate the X-ray diffraction patterns for a series of computer generated model liquid-crystalline mesophases. Overall, some meaningful information could be extracted especially from the more ordered columnar phases but the patterns for the nematic phase were disappointing. It seems that as

with the simulations themselves, the use of computer X-ray diffraction will only produce results similar to experimental patterns, as the size of system grows.

4.6 References

[1] P.W.Atkins. *Physical Chemistry. 2nd Ed.* Oxford (1992).

[2] J.S.V.D.Lingen. *Ber.dt.Chem.Ges.* (1913) **15** 913.

[3] D.W.L.Hukins. *X-Ray Diffraction by Disordered and Ordered Systems.* Pergamon Press (1981).

[4] A.Guinier and G.Fournet. *Small-angle Scattering of X-Rays.* Wiley (1955).

[5] A.J.Leadbetter *in The Molecular Physics of Liquid Crystals.* (G.R.Luckhurst and G.W.Gray. eds) Academic Press (1979).

[6] J.Falgeirettes and P.Delord. *Liquid Crystals and Plastic Crystals:Vol 2.* (P.A.Winsor and G.W.Gray. eds) Ellis Horwood (1974).

[7] G.R.Luckhurst, R.A.Stephens and R.W.Phippen. *Liq.Cryst.* (1990) **8** 451.

[8] I.W.Hamley. *Ph.D. Thesis*, University of Southampton (1991).

[9] J.G.Gay and B.J.Berne. *J.Chem.Phys.* (1981) **74** 3316.

[10] R.Hashim, G.R.Luckhurst and S.Romano. *J.Chem.Soc.Faraday.Trans.* (1995) **91** 2141.

[11] M.Kerker. *The Scattering of Light and other Electromagnetic Radiation.* Academic Press (1969).

[12] C.J.Gray and K.E.Gubbins. *Theory of Molecular Fluids. Vol 1.* Oxford University Press (1984).

[13] T.Williams and C.Kelley. *Gnuplot (version 3.2).* (1992).

[14] M.K.Chalam, K.E.Gubbins, E.de Miguel and L.F.Rull. *Molec.Sim.* (1991) **7** 357.

[15] G.Harburn, C.A.Taylor and T.R.Welberry. *Atlas of Optical Transforms.* G.Bell and Sons Ltd. (1975).

5. The Gay-Berne discogen II

5.1 Introduction

In §1.3.4, we briefly described the variety of smectic phases formed by disc-shaped metallomesogens[1] but in all cases, the symmetry axes of the constituent molecules lay parallel to the layers. But we can envisage another scenario in which the symmetry axis of each particle lays perpendicular to the layers. This would be analogous to the behaviour observed in several lyotropic systems[2,3] in which the micelles, ellipsoidal in shape, are claimed to remain intact on transition from the discotic nematic to form what is know as a discotic lamellar phase (L_D). It is this intriguing behaviour that we aim to look at in greater detail.

5.2 Parametrisation of the Gay-Berne potential

As with simulations of the discotic mesogen in Chapter 3, we need to use a much simplified model incorporating just the essential features which we feel are needed to model accurately the main characteristics of the mesophase in question. The potential we have chosen is the Gay-Berne potential, which as well as having an ellipsoidal repulsive core, incorporates the attractive forces that would be needed in order to induce and stabilise any translationally ordered mesophases.

We now move on to the problem of how to parametrise the Gay-Berne potential in order to represent the behaviour of a discotic smectic system. In order to model the columnar phase shown by the Gay-Berne discogen, we parametrised the potential so that the face-to-face arrangement of the ellipsoids was energetically favoured. This was achieved by setting the well depth anisotropy, $\varepsilon_f/\varepsilon_s$, to have a value of 5.0. But now we do not want the system to form columns, instead we want the particles to associate in horizontal sheets thus the edge-to-edge arrangement should be preferred to the face-to-face arrangement. To achieve this by the parametrisation of the well depth term means setting $\varepsilon_f/\varepsilon_e$ to a value less than 1 but having no prior knowledge of what this value should be, we simply invert the value used by Emerson *et al.*[4] in their system of disc-shaped thermotropic mesogens and choose $\varepsilon_f/\varepsilon_e$ to be 0.2. These simulations are of interest in their own right, as they allow us to explore further the phase behaviour of particles interacting via the Gay-Berne potential.

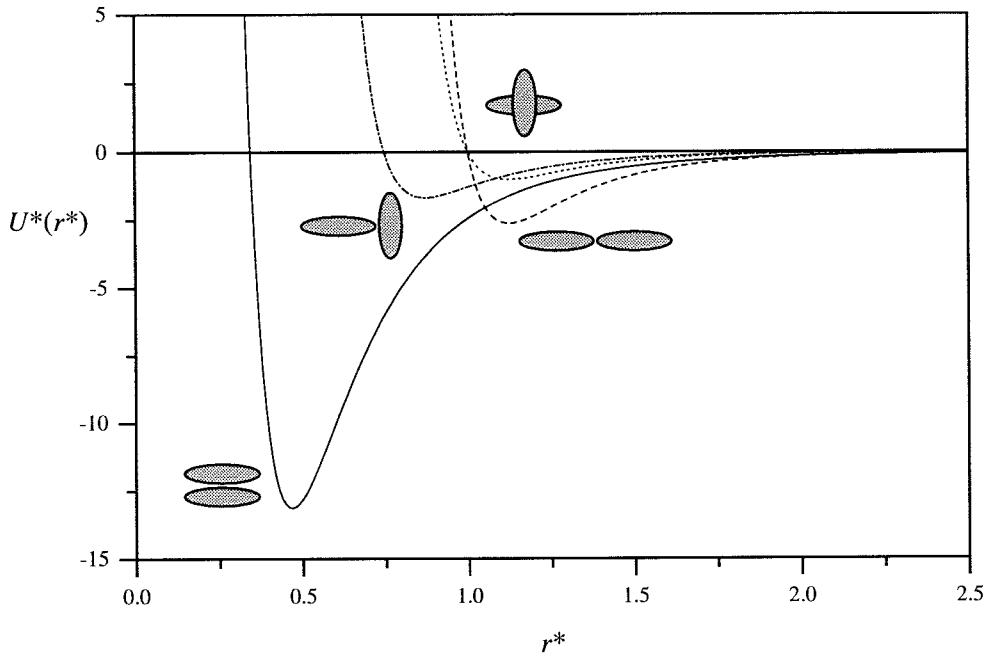

Figure 5.1: *The Gay-Berne potential parametrised to model a system of ellipsoidal particles, having the parameters,* σ_f/σ_e *of 0.345 and* $\varepsilon_f/\varepsilon_e$ *of 5.0.*

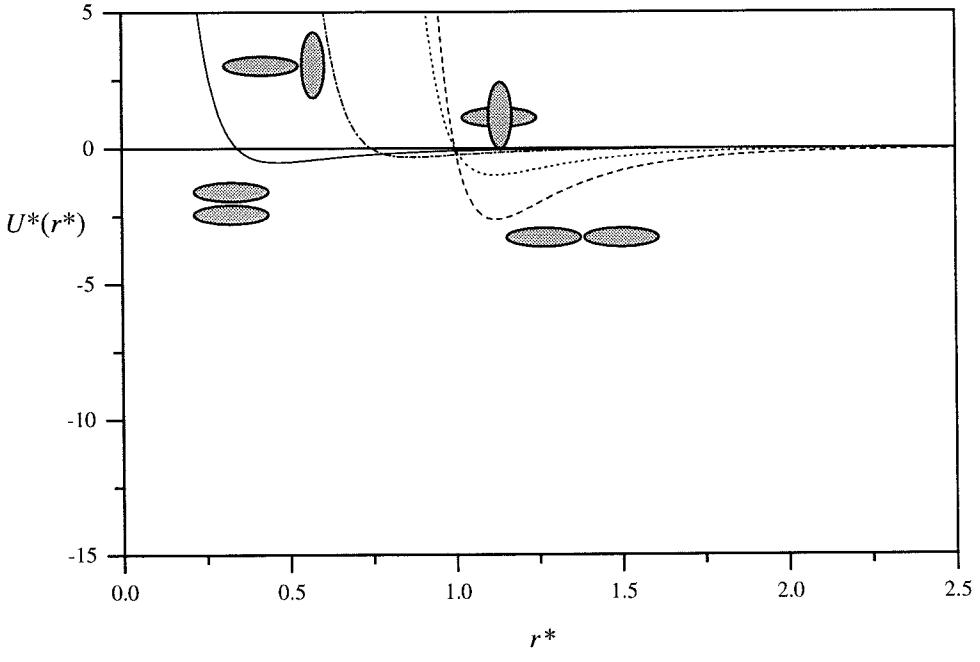

Figure 5.2: *The Gay-Berne potential parametrised to model a system of ellipsoidal particles, having the parameters,* σ_f/σ_e *of 0.345 and* $\varepsilon_f/\varepsilon_e$ *of 0.2.*

Thus to examine the effect of this parametrisation of the well depth term, we keep the exponent parameters μ and ν the same as those used by Emerson[4], namely μ of 1 and ν of 2. The potential energy diagram for the Gay-Berne potential parametrised in this way is shown in figure 5.2. We can see how the potential energy curve for the edge-to-edge arrangement is now favoured. But one effect is to allow the cross arrangement to be the next preferred arrangement. This happens as the well depth equation for both the face-to-face and tee arrangements contain terms relating to the strength parameters $\varepsilon_e/\varepsilon_s$. Comparing to the original Gay-Berne potential parametrised for disc-shaped particles, the cross and end-to-end arrangements remain the same but it is the tee and face-to-face that have reduced well depths.

5.3 The molecular dynamics simulation

The simulation was performed in the constant *NVE* (microcanonical) ensemble, with 256 particles in a cubic box with periodic boundary conditions. A minimum image summation and a spherical cut-off of $2.4\sigma_0$ were also employed. This cut-off is larger than previously used, (see §3.3), as the attractive tail of the potential is longer for the parametrisation used in this Chapter. The scaled density used was between 2.7 and 3.0, again larger than before, as the trial simulations at lower densities produced cavities within the box. The simulation was started from an α-*f.c.c.* lattice with all 256 particles parallel to the x axis. A scaled time step δt^* of 0.001 was used, the simulations being performed on a Silicon Graphics Iris Indigo R3000 workstation, with each time step taking about 1s of c.p.u. time. The phases were identified by graphic visualisation and various structural distribution functions.

The initial simulation was performed at the scaled density ρ^* of 2.7. The system was set up by starting with a crystal at the low density ρ^* of 1.8, $\varepsilon_f/\varepsilon_e$ of 0.2 and T^* of 10.0. After 30,000 time steps, $\langle P_2 \rangle$ had reached a value of 0.092, consistent with the isotropic phase. The system was then compressed in steps of 0.3 scaled density units until the desired density, ρ^* of 2.7 had been reached. After 50,000 time steps the value of $\langle P_2 \rangle$ was now 0.087, showing that the system had remained in the isotropic phase. From this state point the system was cooled until T^* of 0.1. By now $\langle P_2 \rangle$ had a value of 0.998, but looking at the graphic snapshot of the lowest temperature phase, (see figure 5.3), it can be seen that the

system had indeed crystallised and that the particles had come away from the sides of the box. This indicated that at least for this highly ordered phase with a well depth anisotropy $\varepsilon_f/\varepsilon_e$ of 0.2, the density ρ^* of 2.7 is too low. If we used a higher density, the system would be slightly compressed perhaps solving the problem of the particles coming away from the box sides. So we tried a simulation at the higher density ρ^* of 3.0 by compressing the system at a low temperature and then crystallising it to investigate the behaviour of the particles. It was observed that in the crystal phase at the higher density the particles remained well behaved in that they did not come away from the sides of the box. It was decided, therefore, to perform a fuller simulation at this density ρ^* of 3.0.

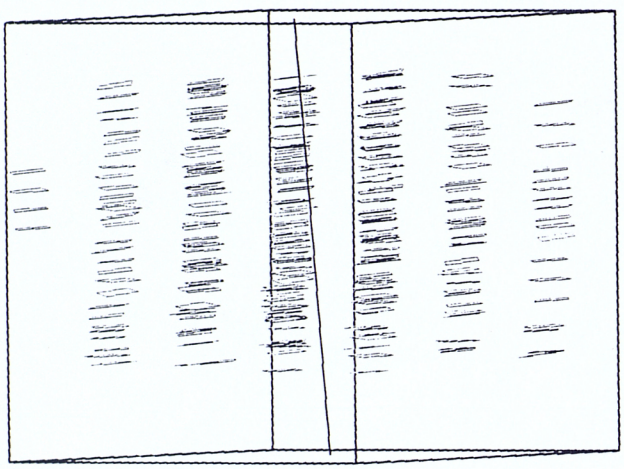

Figure 5.3: *Configurational snapshot for the crystal phase at ρ^* of 2.7, using the IBM WINGS vector graphics package where the particles are represented as squares; they are half the correct size in relation to the simulation box to aid visualisation. The director is represented as a line in the centre of the box, the length being proportional to $\langle P_2 \rangle$, thus when $\langle P_2 \rangle$ has a value of 1, the director is the same size as the length of one side of the box.*

For the more detailed simulation, the system was prepared by compressing the state point, T^* of 6.0 and ρ^* of 2.7, an isotropic configuration, straight to the higher density. By now the order parameter $\langle P_2 \rangle$ had a value of 0.102, which though somewhat high for an isotropic phase with 256 particles, (see §3.4.1), indicated a generally disordered phase, a conclusion that was backed up by the graphic snapshots. These illustrations also confirmed the absence of any cavities in the simulation box. The temperature was then lowered in steps of 0.25 scaled units until T^* of 0.1 was reached.

At each state point an equilibrium run of between 50,000 and 300,000 time steps was performed, the actual number dependent on how quickly an equilibrium state was reached. This was followed by a production run, in which the temperature scaling was turned off, of between 20,000 and 50,000 time steps, again the length of the simulation was dependent on how quickly the important properties had stabilised about a constant value. The various orientational and thermodynamic properties are shown in table 5.1.

Set T^*	Actual T^*	$N_E/10^3$	$N_P/10^3$	$\langle U^* \rangle$	$\langle P_2 \rangle$
6	5.97 ± 0.09	100	20	−1.35 ± 0.041	0.079 ± 0.015
5.5	5.45 ± 0.11	50	20	−1.96 ± 0.034	0.095 ± 0.032
5	4.83 ± 0.09	50	20	−2.88 ± 0.027	0.131 ± 0.056
4.75	4.74 ± 0.07	100	50	−2.87 ± 0.023	0.118 ± 0.047
4.5	4.43 ± 0.08	100	50	−3.53 ± 0.018	0.178 ± 0.045
4.25	4.14 ± 0.05	200	100	−7.14 ± 0.018	0.623 ± 0.031
4	4.02 ± 0.09	100	50	−7.83 ± 0.021	0.667 ± 0.030
3.75	3.75 ± 0.06	100	50	−9.72 ± 0.015	0.768 ± 0.024
3.5	3.57 ± 0.05	300	50	−10.94 ± 0.013	0.814 ± 0.027
3.25	3.27 ± 0.04	100	100	−12.59 ± 0.019	0.863 ± 0.013
3	3.01 ± 0.07	100	40	−13.61 ± 0.023	0.887 ± 0.014
2.75	2.87 ± 0.05	200	100	−14.21 ± 0.015	0.901 ± 0.011
2.5	2.48 ± 0.06	100	40	−15.47 ± 0.016	0.924 ± 0.014
2.25	2.29 ± 0.06	100	100	−16.03 ± 0.011	0.933 ± 0.012
2	2.03 ± 0.05	100	40	−16.77 ± 0.015	0.944 ± 0.015
1.75	1.77 ± 0.03	100	50	−17.54 ± 0.011	0.954 ± 0.011
1.5	1.51 ± 0.03	100	40	−18.24 ± 0.009	0.962 ± 0.012
1.25	1.25 ± 0.01	100	50	−19.02 ± 0.004	0.971 ± 0.009
1	1.06 ± 0.01	100	40	−19.82 ± 0.008	0.977 ± 0.008
0.75	0.76 ± 0.01	100	50	−20.66 ± 0.006	0.984 ± 0.005
0.5	0.51 ± 0.02	100	40	−21.33 ± 0.006	0.989 ± 0.006
0.25	0.23 ± 0.01	100	50	−2204 ± 0.003	0.994 ± 0.004
0.1	0.07 ± 0.01	50	40	−22.44 ± 0.002	0.997 ± 0.003

Table 5.1: *Values of T^*, $\langle U^* \rangle$ and $\langle P_2 \rangle$ from the cooling run at ρ^* of 3.0. N_E and N_P are the number of time steps performed during the equilibrium and production stages, respectively.*

5.4 Results and discussion

5.4.1 Orientational properties

Second and fourth rank order parameters: The variation of the order parameters $\langle P_2 \rangle$ and $\langle P_4 \rangle$ with temperature T^* for the cooling run are shown in figure 5.4. Between T^* of 5.97 and 4.43, $\langle P_2 \rangle$ remains between the values 0.1 to 0.2. This near but not total absence of orientational order is generally a characteristic of an isotropic phase in a molecular dynamics simulation. The main reason for the values not being zero is discussed in §2.4.2, but also at constant volume, the system goes through a biphasic region so that $\langle P_2 \rangle$ from the simulation is the weighted average of the order parameter for the isotropic and nematic phases. As the temperature is lowered, the system undergoes a phase transition with $\langle P_2 \rangle$ rising sharply to a value of 0.67, then as the system is cooled further, the order slowly increases with decreasing temperature until near perfect orientational order is reached. At this stage we can only speculate on the variety of phases formed. More than likely, the high temperature phase is isotropic while at temperatures of 1.06 and below, a crystal phase could exist. The sharp rise in the order parameter at the transition from the isotropic phase to an orientationally ordered phase probably indicates a first order transition.

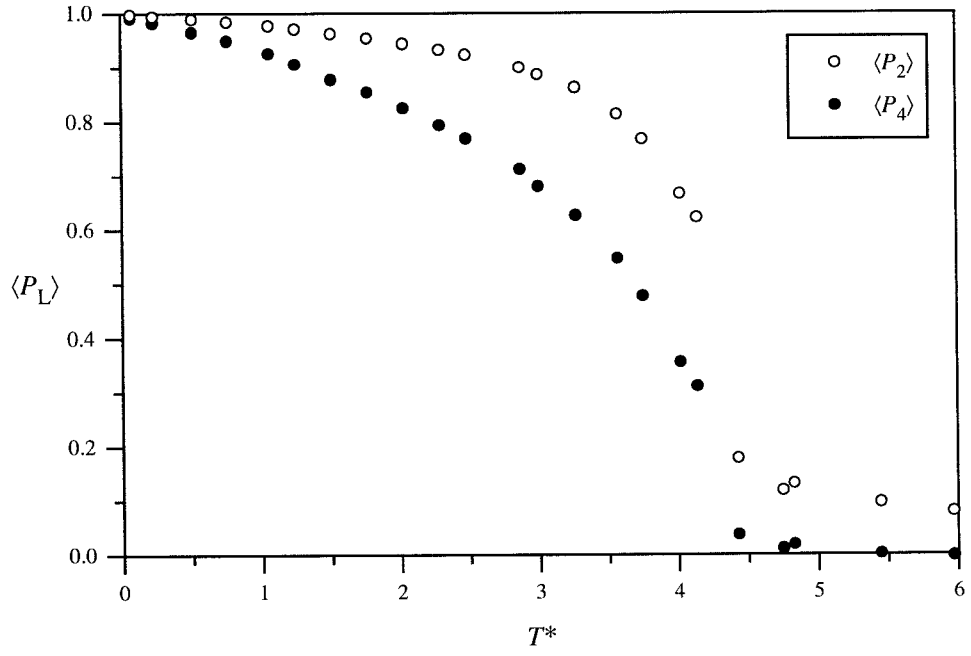

Figure 5.4: *Variation of $\langle P_2 \rangle$ and $\langle P_4 \rangle$ with the scaled temperature T^*.*

The variation of the fourth rank order parameter $\langle P_4 \rangle$ with temperature T^* is also shown in figure 5.4. The shape of the curve for $\langle P_4 \rangle$ is similar to that of $\langle P_2 \rangle$, though having lower values at all temperatures. In figure 5.5 we plot $\langle P_4 \rangle$ against $\langle P_2 \rangle$. This is useful as there are various predications as to what this curve should be[151]. Here, we have included the Maier-Saupe curve (see §3.4.6), and as in Chapter 3, the curve fits well to the simulation data.

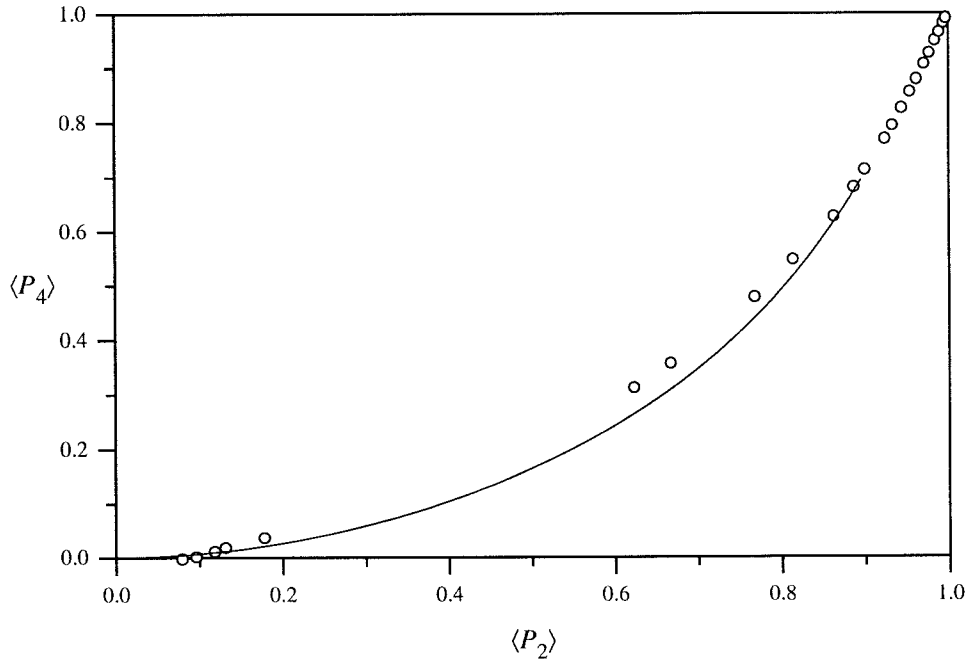

Figure 5.5: *Plot of the order parameters $\langle P_4 \rangle$ vs. $\langle P_2 \rangle$ from our simulations (circles) against that predicted by the Maier-Saupe theory (solid line).*

Singlet orientational distribution function: The behaviour of the singlet orientational distribution function $f(\cos\beta)$, follows that to be expected from a system exhibiting isotropic and nematic phases, (see figure 5.6). In the isotropic phase, T^* of 4.43, we can see that there is no preferred direction of orientation as $f(\cos\beta)$ takes the value ≈ 0.55, which is in good agreement with the expected value of 0.5. Once in the nematic phase, between the scaled temperatures of 4.14 and 3.57, the plot of $f(\cos\beta)$ shows a large peak at the value of $\beta = 0$ i.e. along the director. This peak increases in intensity with an associated decrease in width as the orientational order increases with decreasing temperature.

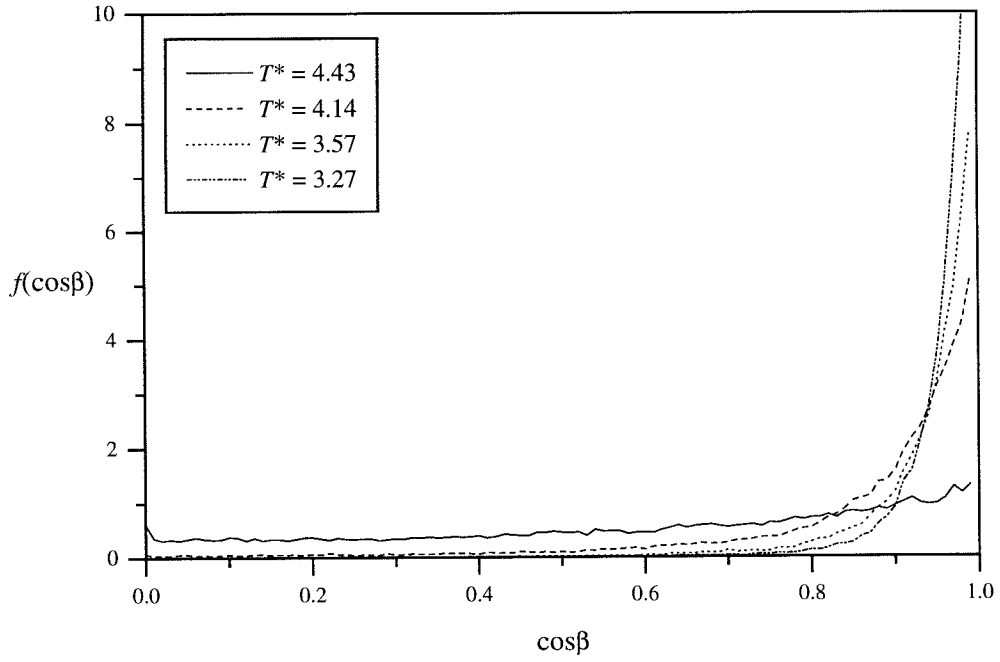

Figure 5.6: *Variation of f(cosβ) with cosβ at the scaled temperatures T* indicated.*

5.4.2 Thermodynamic properties

Internal energy: The plot of the scaled internal energy per particle $\langle U^* \rangle$ against scaled temperature is shown in figure 5.7. This is slightly more revealing than the plot of $\langle P_2 \rangle$, in that it shows two possible discontinuities, each indicative of a phase transition. The first transition visible is between the temperatures 4.43 and 4.14, mirroring that shown by the orientational behaviour of the system. The sharp drop in $\langle U^* \rangle$ backs up the view that this could be a first order transition, though to be precise we would have to calculate the free energy. The next transition is between 3.57 and 3.27 and the last possible sign of a phase transition is between T^* of 1.25 and 1.06 where there is a change, albeit slight, in the slope of the graph. The first drop could be attributed to a nematic - isotropic transition, the second could be between a smectic - nematic phase and the third between a smectic and another ordered phase, possibly crystal. Though, we really need a lot more data points to be able to say that we have a definite transition for these latter two. We must also tale into account that phase transitions also appear more continuous in the *NVE* ensemble.

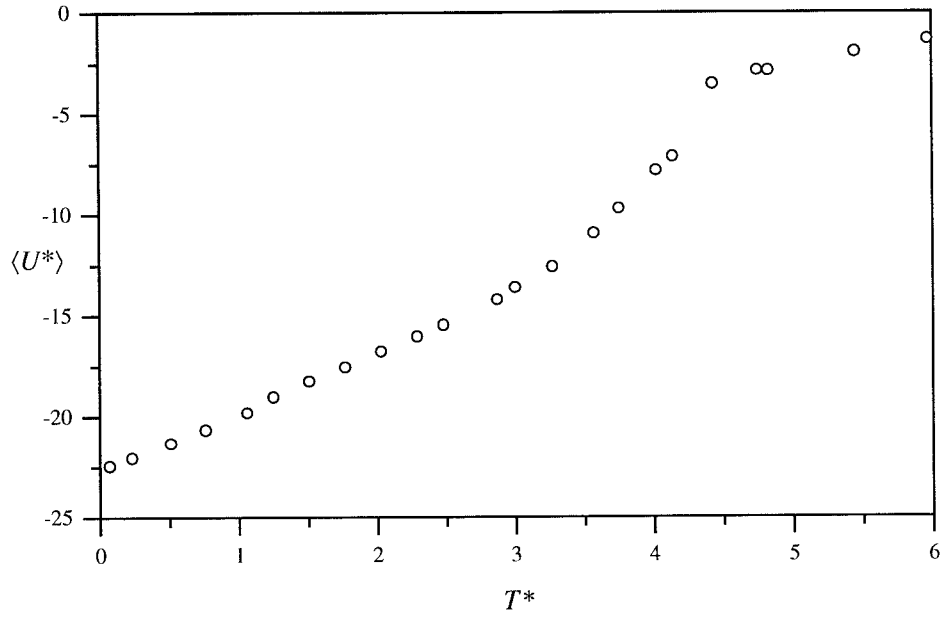

Figure 5.7: *Variation of* $\langle U^* \rangle$ *with the scaled temperature* T^*.

Heat capacity: The plot of the scaled heat capacity against temperature is shown in figure 5.8. The heat capacity calculated by the fluctuation method, (see §2.4.1), shows that the values are subject to large errors and as such the graph yields no real information about the system, though we do observe a large peak close to the discotic nematic - isotropic transition and another peak around the region of the scaled temperature 3.5. There also seems to be evidence of a transition at around T* of 1.25 and 1.06, though again there is not enough data points to conclusively prove the existence of a transition. We can also calculate the heat capacity from a plot of the internal energy $\langle U^* \rangle$. The derivative of a cubic spline fit to the internal energy gives the $\langle C_V^* \rangle$. This has essentially the same shape as the $\langle C_V^* \rangle$ calculated directly from the simulation, and it highlights the discontinuities in the plot of $\langle U^* \rangle$ already discussed. The origin of the difference between the values obtained from the two methods can be explained. One is the differentiation of a potential energy plot while the other is calculated from fluctuations in the kinetic energy

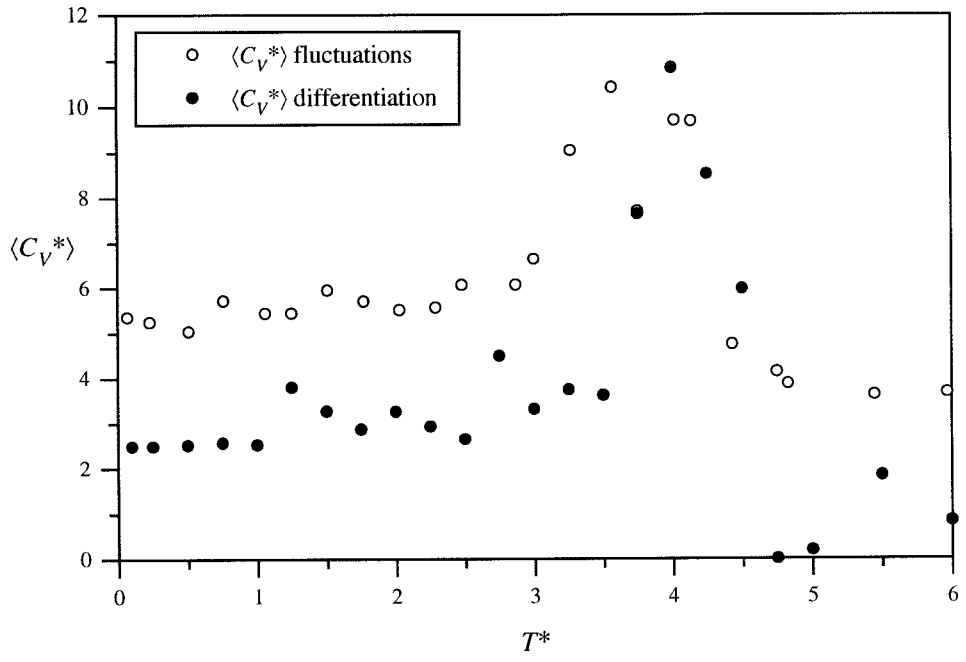

Figure 5.8: *Variation of* ⟨C_V*⟩ *with the scaled temperature* T*.

5.4.3 Structural properties

From the orientational and thermodynamic properties, we have identified several possible mesophases. At temperatures of 4.43 and above, we seem to observe an isotropic phase. On cooling, we see the presence of two orientationally ordered phases, one between T* of 4.14 and 3.57 and the other between 3.27 and 1.25. Then at temperatures of T* of 1.06 and below, the phase attains near perfect orientational order, possibly indicating a crystal phase. But to understand fully which mesophases are produced during the simulation, we need to calculate various structural properties, thus in the following section, we attempt to characterise, by means of these properties, each phase more accurately and for the sake of clarity, we shall only discuss the scaled temperatures bordering the phase boundaries.

Graphic visualisation and g(r):* The first two structural properties we have calculated are the radial distribution function $g(r^*)$, (see §2.4.3) and a graphic visualisation of the system, (see §3.4.3). Although we cannot describe fully the detailed structure of the phase from these techniques and in some cases, especially the graphics, they can be misleading,

they are a useful starting point from which to distinguish between the isotropic, nematic and possible smectic phases.

The first temperature we shall deal with is T^* of 4.43, at the boundary between a possible discotic nematic - isotropic transition as indicated by the graphs of $\langle P_2 \rangle$ and $\langle U^* \rangle$. The plot of the $g(r^*)$, (see figure 5.9), confirms our initial characterisation as it shows the typical shape for an isotropic phase[6,7] where the limiting value tends to the ideal fluid value of one. There are two peaks present, the one at r^* of 0.9 probably indicates particles in a slightly staggered edge-to-edge arrangement. There is also an additional peak at r^* of 0.35, which corresponds to particles in a face-to-face arrangement though as the height of this peak is below one it is not expected to be significant. We can also see from the graphic image, (see figure 5.11), that the particles are more or less random in their orientations as expected for an isotropic phase.

If we inspect $g(r^*)$ for T^* of 4.14, there is a small but significant change in shape, as the peaks at r^* of 0.3 and 1.0 have become sharper and more pronounced, indicating the increased tendency to find particles in the edge-to-edge arrangement i.e. the phase has increased short range translational order, though from the configurational snapshot, we can identify a nematic at this temperature (see figure 5.12). At the lower end of the range of this mesophase, at T^* of 3.57, the plot of $g(r^*)$ has a similar shape, though the peak at r^* of 0.3 has reached a value of just over one, indicating that there is now significant face-to-face ordering. Though if this is the case, it indicates that there seems to be some physical overlap between the particles as the thickness is $0.345\sigma_0$. The configurational snapshot reveals the presence of the more ordered nematic structure of the phase, but it does not show clearly, the suspected particle overlap. Looking down the director, (see figure 5.13a), shows that even though the orientational order is high, there is still a random distribution of the centres of mass of the particles. Taking a configurational snapshot perpendicular to the director, (see figure 5.13b), indicates some short range translational order in the form of face-to-face ordering, between several pairs of particles, as indicated by the $g(r^*)$, though the considerable degree of translational disorder confirms the presence of a discotic nematic phase.

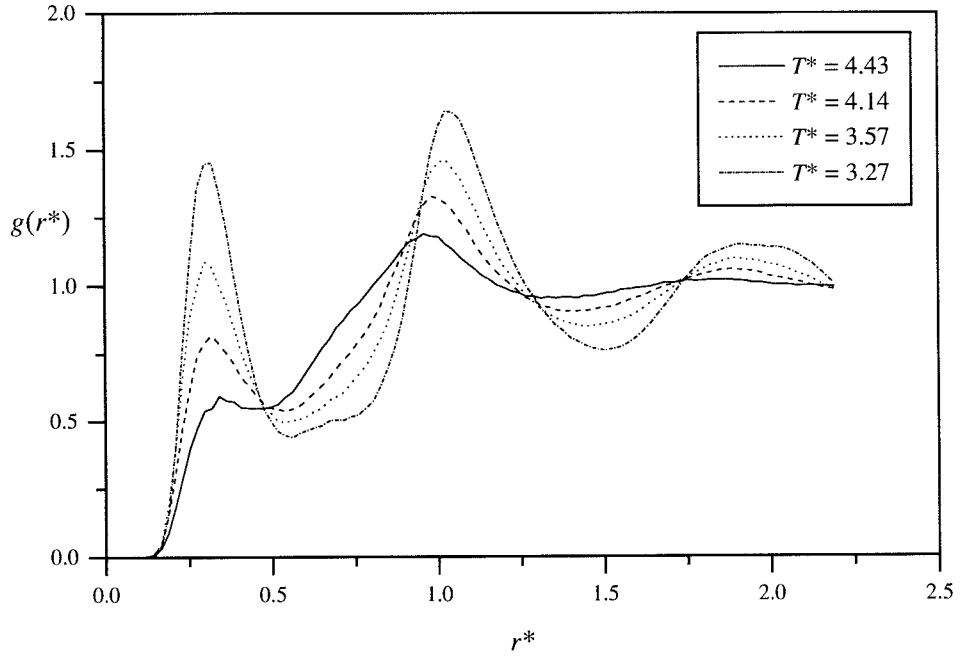

Figure 5.9: *The radial distribution function g(r*) for the scaled temperatures T* indicated.*

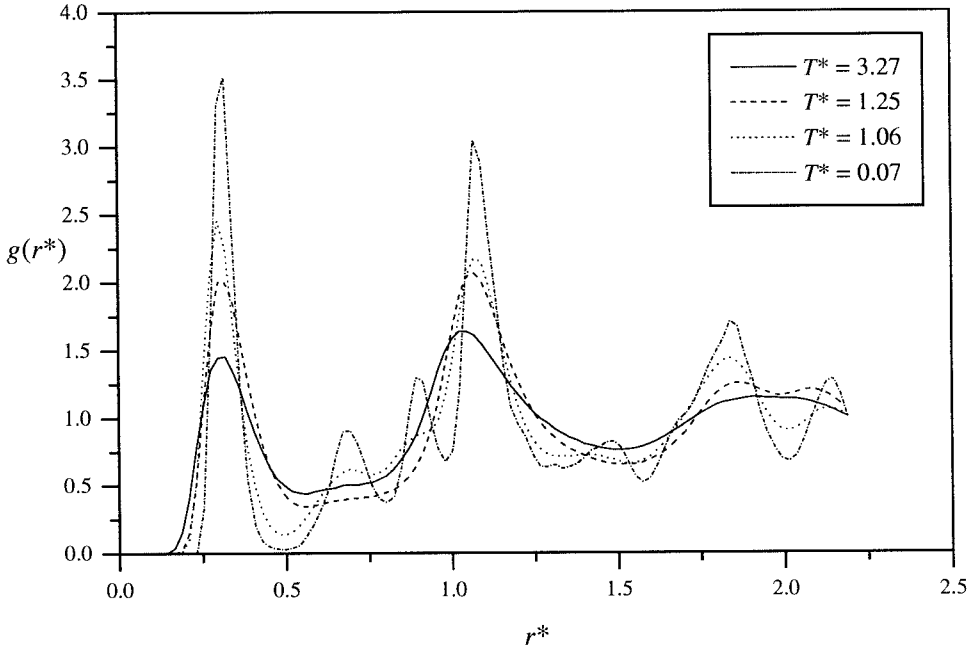

Figure 5.10: *The radial distribution function g(r*) for the scaled temperatures T* indicated.*

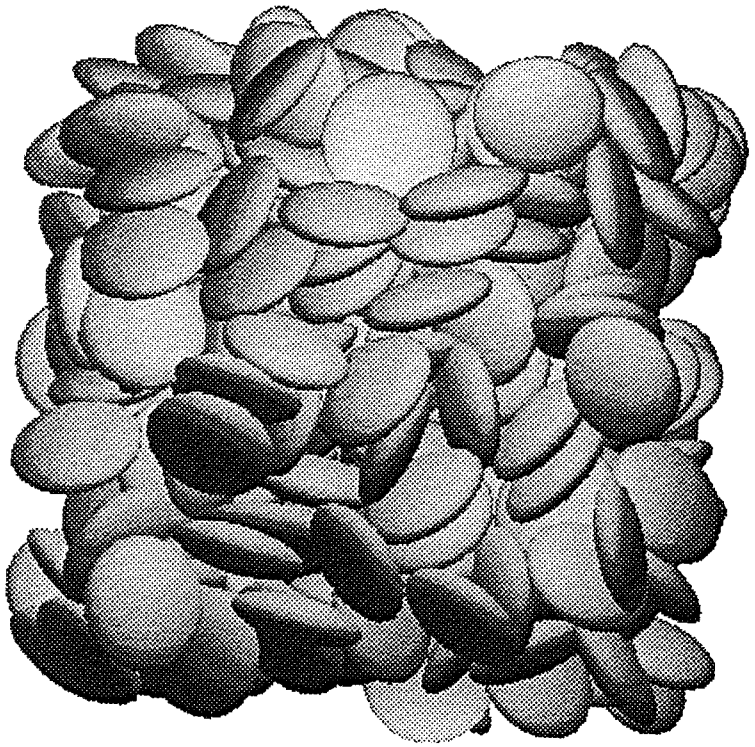

Figure 5.11: *The configurational snapshot of the isotropic phase at T* of 4.43.*

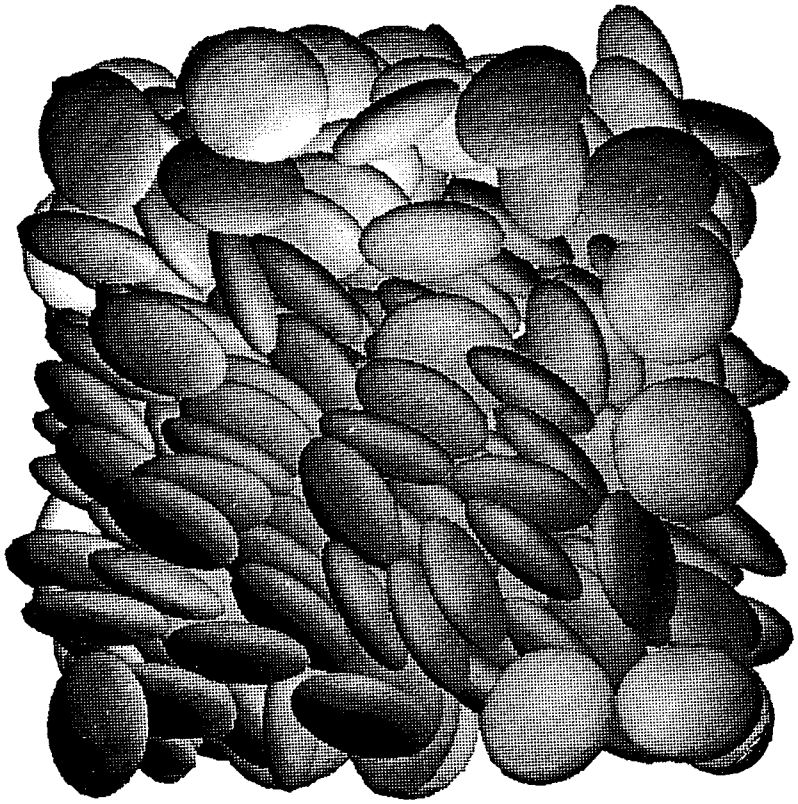

Figure 5.12: *The configurational snapshot of the nematic phase at T* of 4.14.*

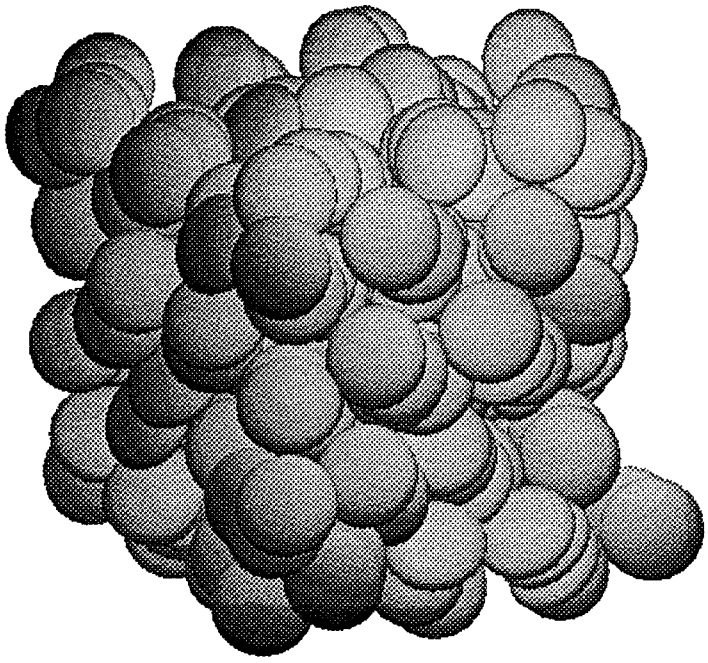

a)

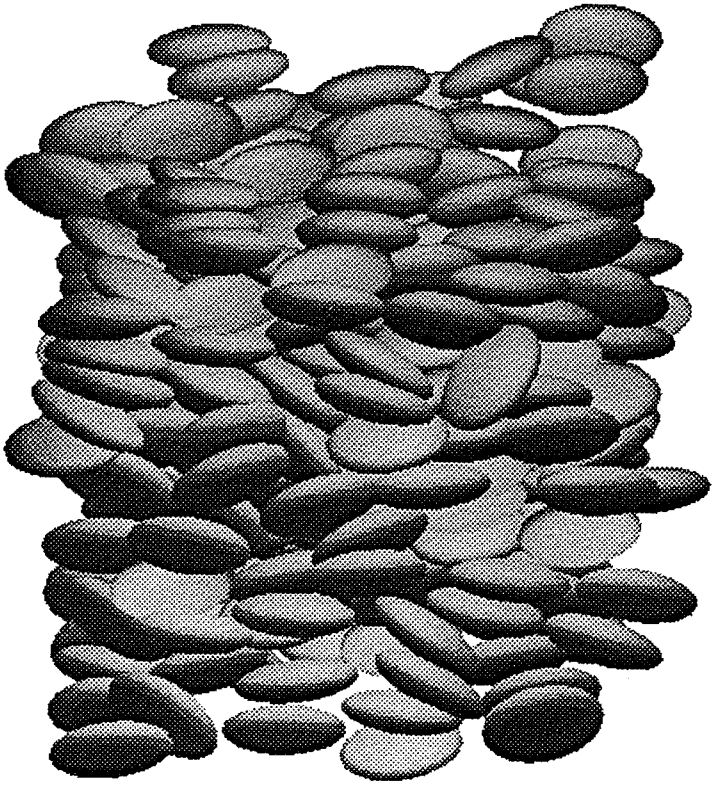

b)

Figure 5.13: *The configurational snapshots of the discotic nematic phase at T* of 3.57, a) parallel and b) perpendicular to the director.*

The next mesophase to characterise lies between the scaled temperatures of 3.27 and 1.25. At T^* of 3.27, the peak at r^* of 0.3 in the $g(r^*)$, (see figure 5.10), has increased in intensity, quite considerably, showing the onset of ordering with a face-to-face arrangement, possibly indicating a columnar phase. There is also a large peak developing at r^* of 2.0, the origin of which we shall discuss presently. At the scaled temperature of 1.25, the general shape of the $g(r^*)$ curve remains unchanged, with peaks at r^* of 0.3 and 1.0 increasing in intensity as the translational order increases. The large peak at r^* of 2.0 has become more clearly defined, resolving into two peaks at r^* of 1.8 and 2.1. This is a "fingerprint" for a phase possessing hexagonal ordering, and this fact is borne out by the configurational snapshots, parallel to the director (see figure 5.14a).

Looking at the configurational snapshot perpendicular to the director, should reveal the columnar ordering within the phase and as we can see from figure 5.14b, this is the case. Though there seems to be considerable disorder within the columns with some particles tilted with respect to the column axes. The view orthogonal to this snapshot, but still perpendicular to the director (see figure 5.15) is even more revealing. It shows the structure to consist of short columns of particles usually about three, arranged in layers. The columns in the adjoining layers, seem to be "shifted", lying in between the columns of the next layer. Though it is had to tell the precise structure from a graphic snapshot, by manipulating the image in three dimensions via computer of both this phase and the crystal, it seems to consist of columns of 2 to 3 particles arranged in a hexagonal net. The next layer of columns then lies in the holes of the adjoining layer, (see figure 5.16), in an ABAB packing.

For the scaled temperature of 1.06, the shape of the radial distribution function has changed, compared with T^* of 1.25, (see figure 5.10). The peak at r^* of 1.8 has increased greatly while the peaks at r^* of 1.0 has been resolved into additional peaks. This change in the $g(r^*)$ backs up the assumption that a phase transition occurs between these two temperatures. The configurational snapshots at T^* of 1.06, (see figure 5.17), reveals the almost perfect orientational and translational order. Taking this, and the evidence such as the value of the order parameter into account we can identify this phase as the crystal.

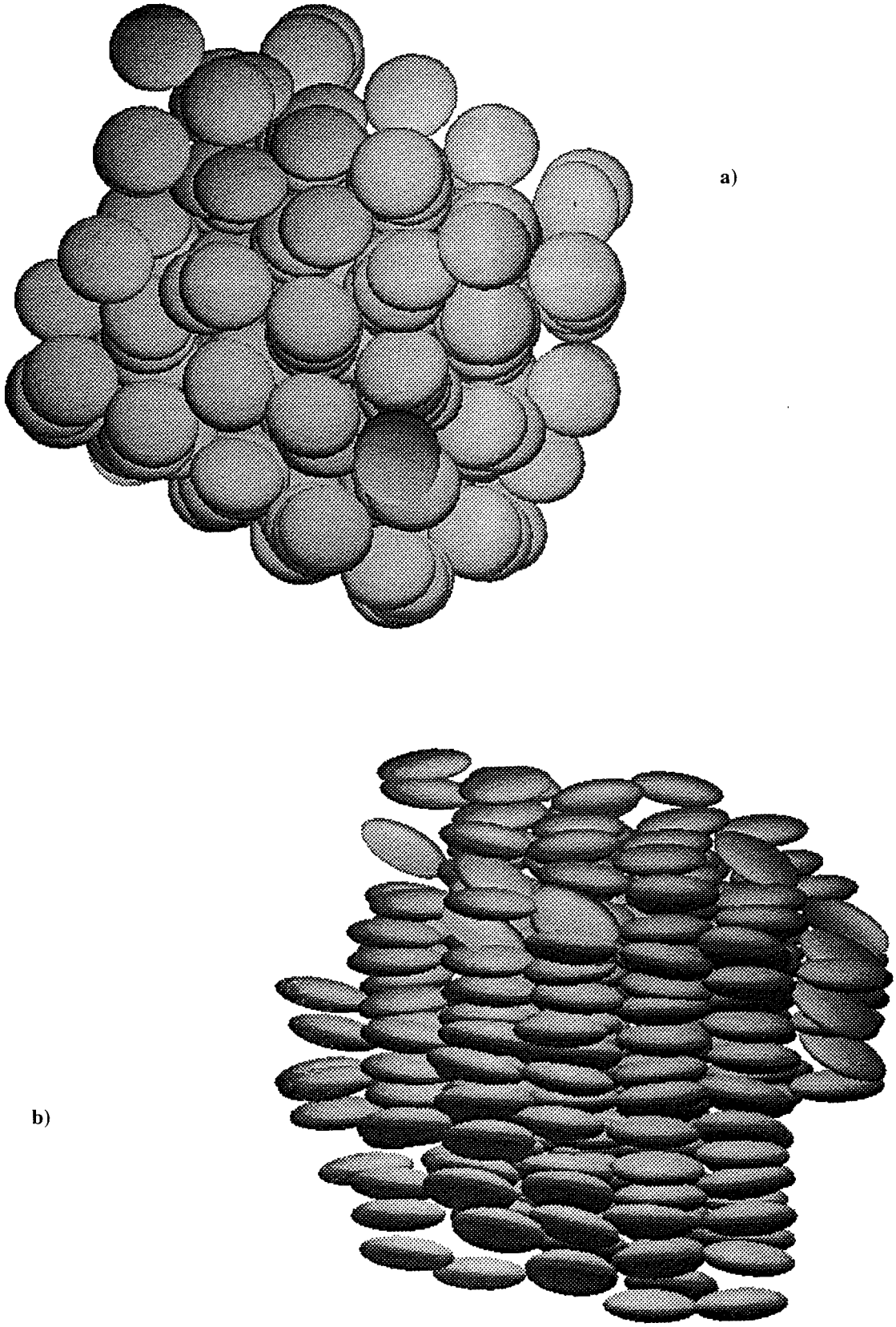

Figure 5.14: *The configurational snapshots of a columnar phase at T* of 1.25, a) parallel and b) perpendicular to the director.*

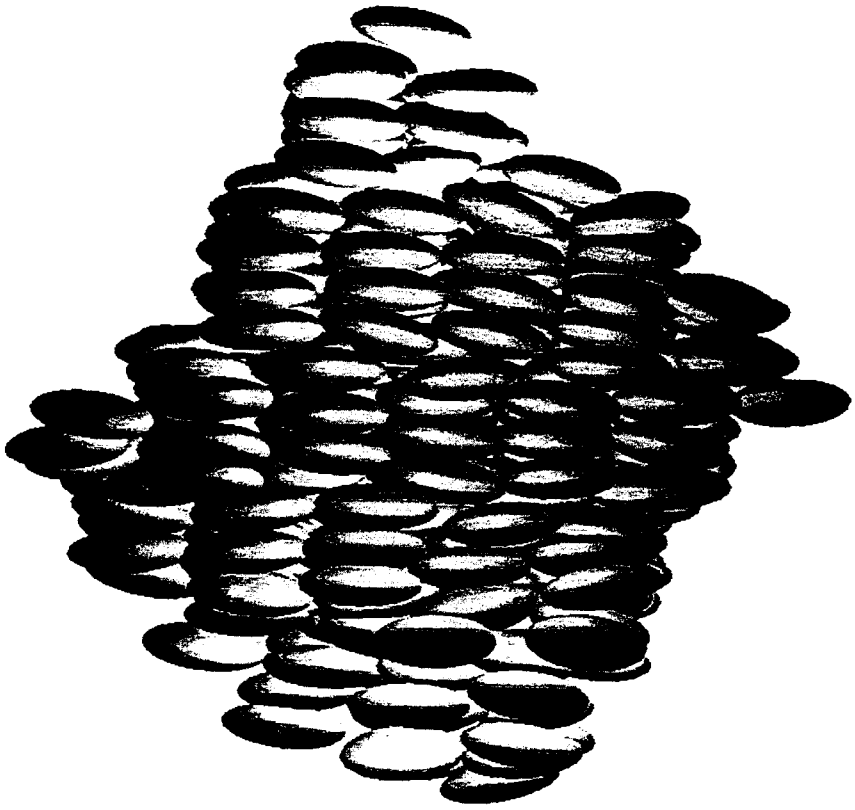

Figure 5.15: *The configurational snapshots of a columnar phase at T* of 1.25, perpendicular to the director, but in a direction orthogonal to that in figure 5.15b.*

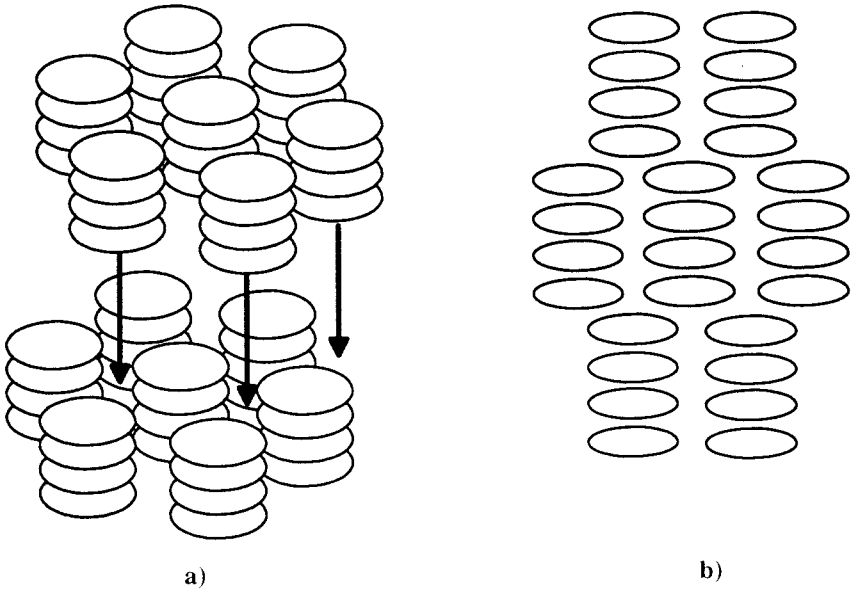

Figure 5.16: *Schematic of "shifted" columnar phase showing a) the ABAB packing of the columns and b) the view perpendicular to the director.*

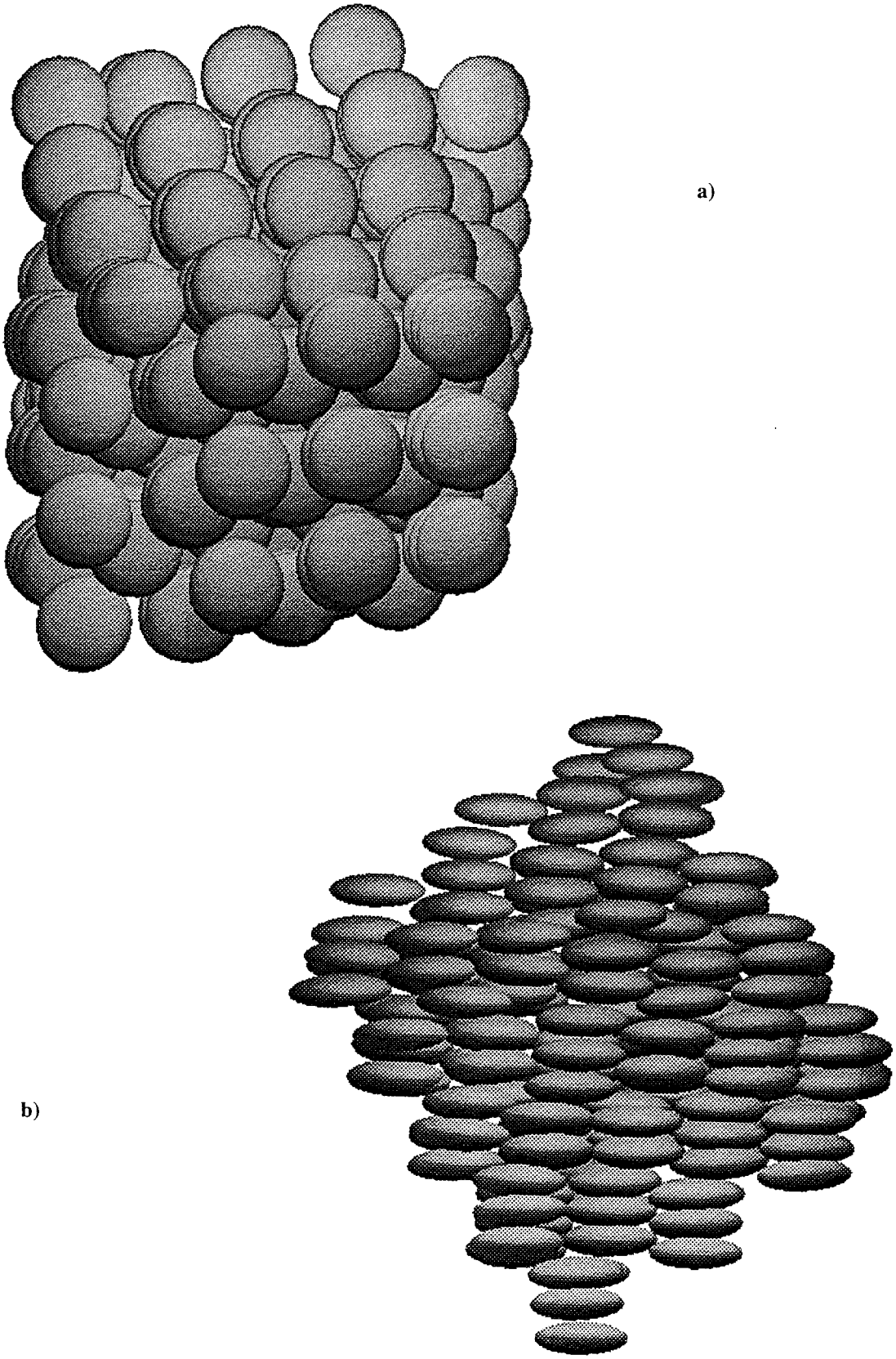

Figure 5.17: *The configurational snapshots of the crystal phase at T* of 1.06, a) parallel and b) perpendicular to the director.*

From an initial inspection of the radial distribution function and configurational snapshots, we have clearly identified three possible phase transitions. Between the scaled temperatures T^* of 4.43 and 4.14, we have the discotic nematic - isotropic transition, characterised by the onset of long range orientational order. There seems to be another phase transition between the temperatures of 3.57 and 3.27, and from the configurational snapshots, this transition is from the discotic nematic phase to a smectic columnar phase. We define the smectic columnar phase as essentially a phase having smectic layers which are composed of small columns of disc-shaped mesogens. Finally, from the form of $g(r^*)$, there is a transition from this columnar phase to a crystal, between the temperatures T^* of 1.25 and 1.06. In all of these phases, the particles seem to overlap when in a face-to-face orientation, the separation being $0.3\sigma_0$, smaller than the thickness of a particle which is defined as $0.345\sigma_0$ but we shall leave the discussion of this situation for a later section.

Why should this structure in the columnar phase result? If two particles, say 1 and 2, are in a face-to-face arrangement, (see figure 5.18), they can approach each other relatively closely even overlapping without a major loss in energy as the depth of the face-to-face energy well is small, (see figure 5.2). A third particle, 3, approaching particle 2 in a pure edge-to-edge arrangement will have a strong energy of interaction with this particle. But as particle 1 is overlapping with particle 2, its edge-to-edge arrangement with particle 3, though not "pure", has increased, helping to stabilise its own interaction with its overlapping neighbour, particle 2. Thus the propagation of the observed columns, are not by the face-to-face interaction but by a series of edge-to-edge interactions from particles within neighbouring columns. Thus the columnar phase in this system results from the interaction between columns while in our columnar phase in Chapter 3, the structure arises from the face-to-face interaction between particles within one column. But what causes the shifted structure? The most likely explanation is that after 2 to 3 particles have formed a column, the strong edge-to-edge interactions overcome the tendency to form columns. There would also be some effect from having a fixed shape and size simulation box thus to be commensurate with its periodic images, the system packs into this unusual structure.

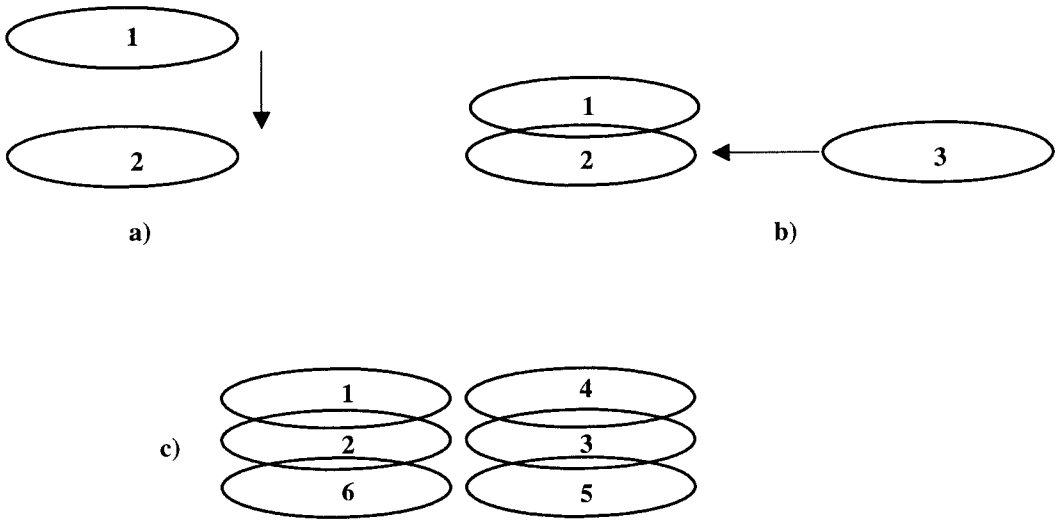

Figure 5.18: *The propagation of columns within a system parametrised to form a smectic phase.*

The orientational correlation function: Figure 5.19 shows the pair orientational correlation function $G_2(r^*)$ for various scaled temperatures. The difference in the limiting value between T^* of 4.43 and 4.14 is further evidence of the discotic nematic - isotropic phase transition. We can see from table 5.2, that the agreement of $\langle P_2 \rangle$ calculated from the limiting value of $G_2(r^*)$ with that obtained from the diagonalisation of the **Q** tensor is reasonably good.

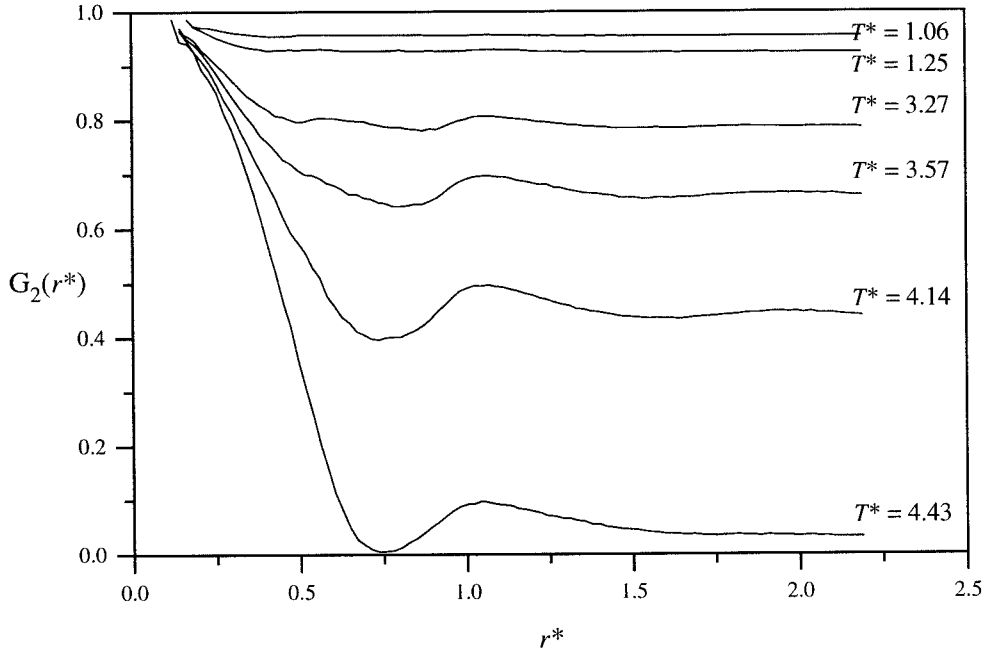

Figure 5.19: *The pair orientational correlation functions for the scaled temperatures indicated.*

T^*	$\langle P_2 \rangle$ *from* **Q** *tensor*	$\langle P_2 \rangle$ *from* $G_2(r^*)$
4.43 ± 0.08	0.178 ± 0.045	0.179
4.14 ± 0.05	0.623 ± 0.025	0.633
3.57 ± 0.05	0.814 ± 0.027	0.813
3.27 ± 0.04	0.863 ± 0.013	0.866
1.25 ± 0.01	0.962 ± 0.009	0.961
1.06 ± 0.01	0.977 ± 0.008	0.977

Table 5.2: *Values of* $\langle P_2 \rangle$ *calculated from the* **Q** *tensor and the limiting values of* $G_2(r^*)$.

Longitudinal and transverse pair correlation functions: The longitudinal pair correlation function $g_{||}(r_{||}^*)$, (see figures 5.20 and 5.21), will reveal the extent of any translational structure in the various phases, along the vector parallel to the director. As expected for the isotropic phase at T^* of 4.43, there is no translational structure present. For the discotic nematic phase at T^* of 4.14 and 3.57, there is also very little translational structure though there is a small peak emerging at r^* of 0.3 indicating a degree of face-to-face correlation at short range. Even in the smectic columnar phase, the plot of $g_{||}(r_{||}^*)$, shows little structure apart from this peak at r^* of 0.3, though there is some evidence of a peak at r^* of 0.6, this probably indicating a particle in the second shell of neighbours within a column. It is interesting to see that the plot of $g_{||}(r_{||}^*)$ cannot pick up the columnar ordering as it did for the columnar phase in Chapter 3. This is most probably because there is no long range correlation between particles in neighbouring columns, a feature, which to some extent, can be seen in the configurational snapshots, especially of the crystal phase, (see figure 5.17).

The plots of the transverse pair correlation function $g_{\perp}(r_{\perp}^*)$, (see figures 5.22 and 5.23), are more revealing. In the isotropic phase, T^* of 4.43, we see a broad peak at around r^* of 0.9 but it is very small. As we lower the temperature, the shape of the $g_{\perp}(r_{\perp}^*)$ changes quite dramatically. In the discotic nematic phase at T^* of 4.14 and 3.57, this peak at r^* of 0.9 now becomes quite visible, with an additional peak at the origin which represents particles lying above each other in a face-to-face arrangement, increasing in intensity. This indicates the presence of short range order in which the particles stack on top of each other. At T^* of 3.27, in the smectic columnar phase, $g_{\perp}(r_{\perp}^*)$ now shows pronounced structure perpendicular to the director. The peak at r^* of 1.0 are particles in neighbouring columns, but in a close packed edge-to-edge arrangement. The additional peak at r^* of 1.8 is the next nearest shell of hexagonal neighbours. We see further proof of the possible transition between the columnar and crystal phases, in the plots of $g_{\perp}(r_{\perp}^*)$ for the scaled temperatures of 1.25 and 1.06, in which at T^* of 1.06, the curve for the crystal shows a series of very well-defined peaks. The peak at r^* of about 0.5, represents the columns in adjoining lamellae.

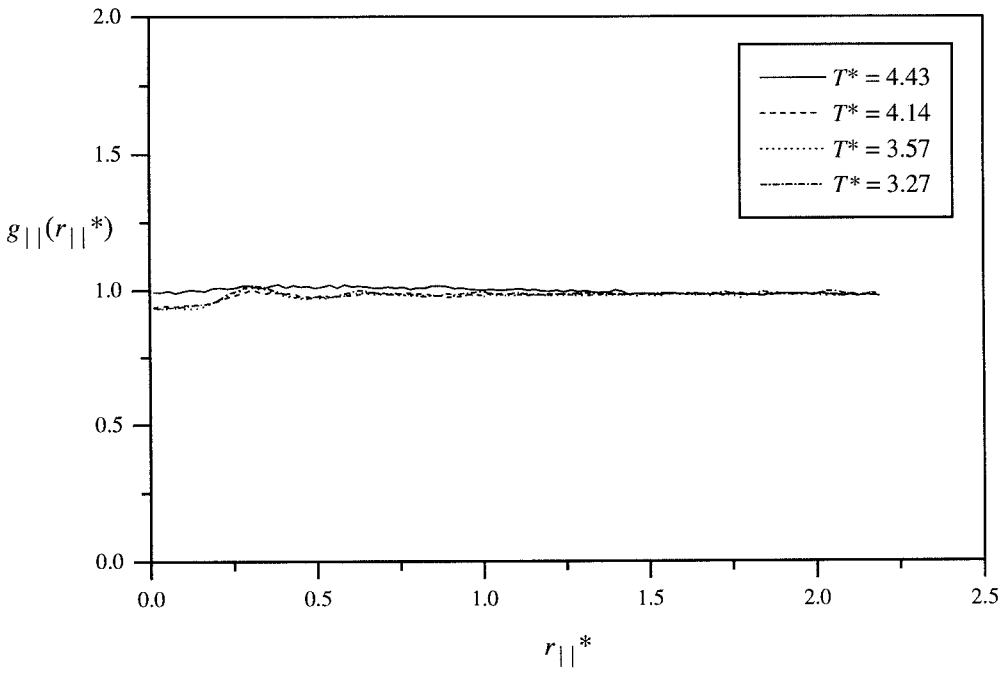

Figure 5.20: *The longitudinal pair correlation function $g_{||}(r_{||}^*)$ at the scaled temperatures T* indicated.*

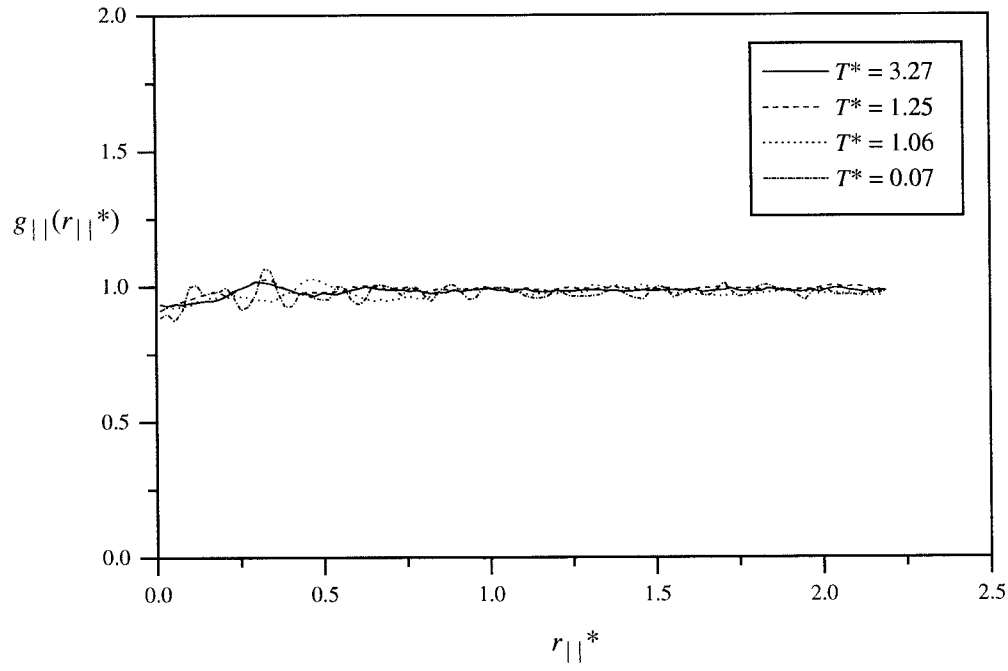

Figure 5.21: *The longitudinal pair correlation function $g_{||}(r_{||}^*)$ at the scaled temperatures T* indicated.*

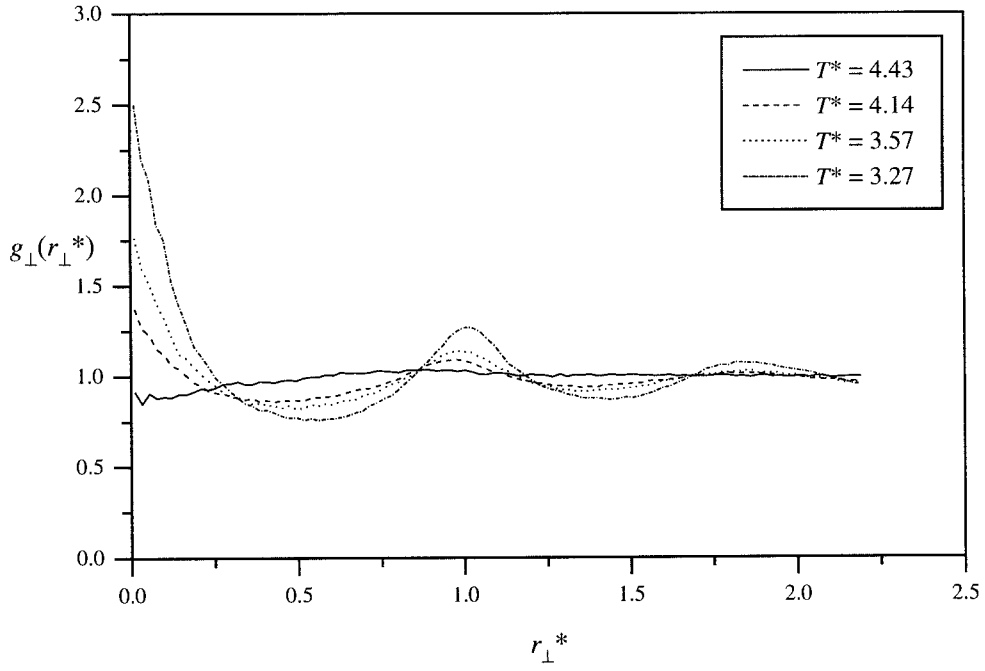

Figure 5.22: *The transverse pair correlation function $g_\perp(r_\perp^*)$ at the scaled temperatures T* indicated.*

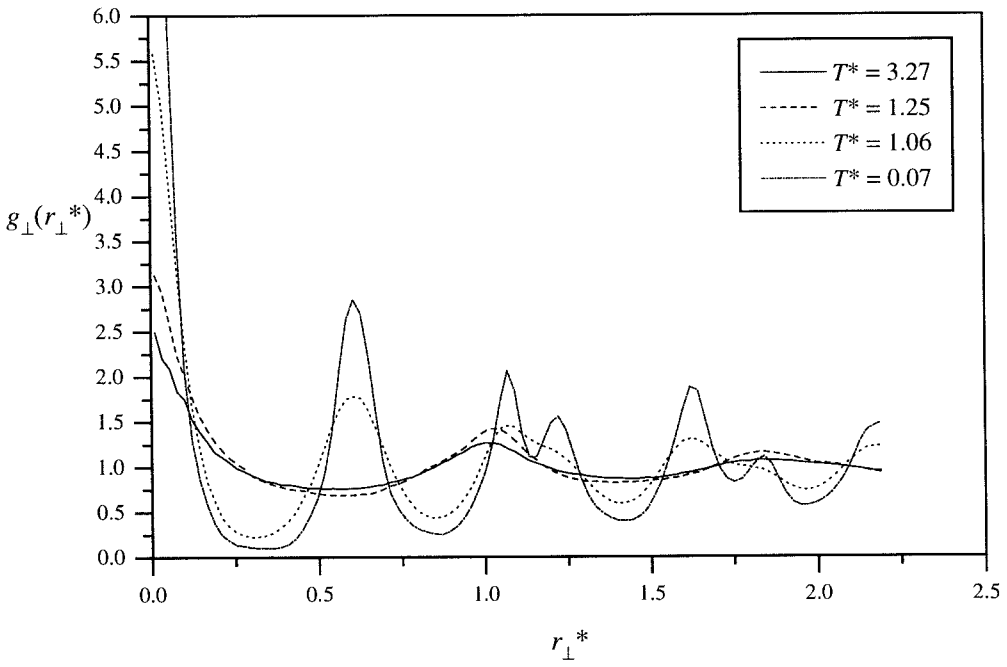

Figure 5.23: *The transverse pair correlation function $g_\perp(r_\perp^*)$ at the scaled temperatures T* indicated.*

5.4.4 Dynamic properties

The mean squared displacement: The mean squared displacements calculated as a function of scaled time for a variety of scaled temperatures are shown in figures 5.24 and 5.25. For most scaled temperatures, the plot is linear with time and we can see quite easily, that as the temperature is decreased, the particles' translational motion decreases and hence the phases becomes more solid-like, as the translational and orientational order increases. From the slope of the $m^*(t^*)$, we can calculate the diffusion coefficient D^*, (see table 5.3).

T^*	*Phase*	D^* *from* $m^*(t^*)$	$D_{\|\|}^*$	$D_{\perp}^*$	$D_{\|\|}^*/D_{\perp}^*$
4.43	I	0.566	0.405	0.299	1.35
4.14	N	0.505	0.098	0.201	0.49
3.57	N	0.345	0.064	0.146	0.44
3.27	D_L	0.171	0.032	0.078	0.41
1.25	D_L	0.024	0.01	0.009	1.11
1.06	C	0.015	0.003	0.004	0.75

Table 5.3: *The values of the scaled diffusion coefficient for the system at the scaled temperatures* T^* *indicated, where* D_L *represents the column phase..*

By looking at the mean squared displacement, parallel and perpendicular to the director, (see figure 5.26), we can get a more detailed idea of the nature/anisotropy of the motion within each phase. For the isotropic phase, T^* of 4.43, the particles are extremely mobile in both directions, though the plots are not linear with time and we must remember that we can only define a director due to an artefact from the calculation of the order parameter, (see §2.4.2). On cooling into the discotic nematic phase, the diffusion tensor has decreased by a factor of two, again indicating the increased translational and orientational order. It is also evident that the particles are more mobile in a direction perpendicular to the director, but this is to be expected as this fits in with the results, from Chapter 3, where in the discotic nematic phase composed of ellipsoidal particles, the ellipses are able to slide over each other without encountering steric hindrance.

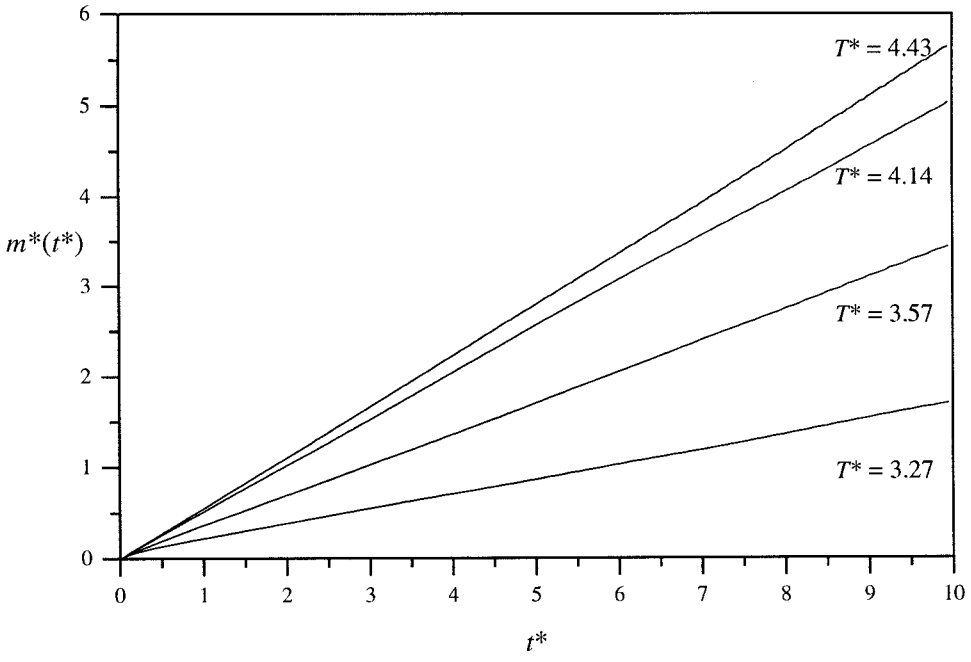

Figure 5.25: *The total mean squared displacement m*(t*) at the scaled temperatures T* indicated.*

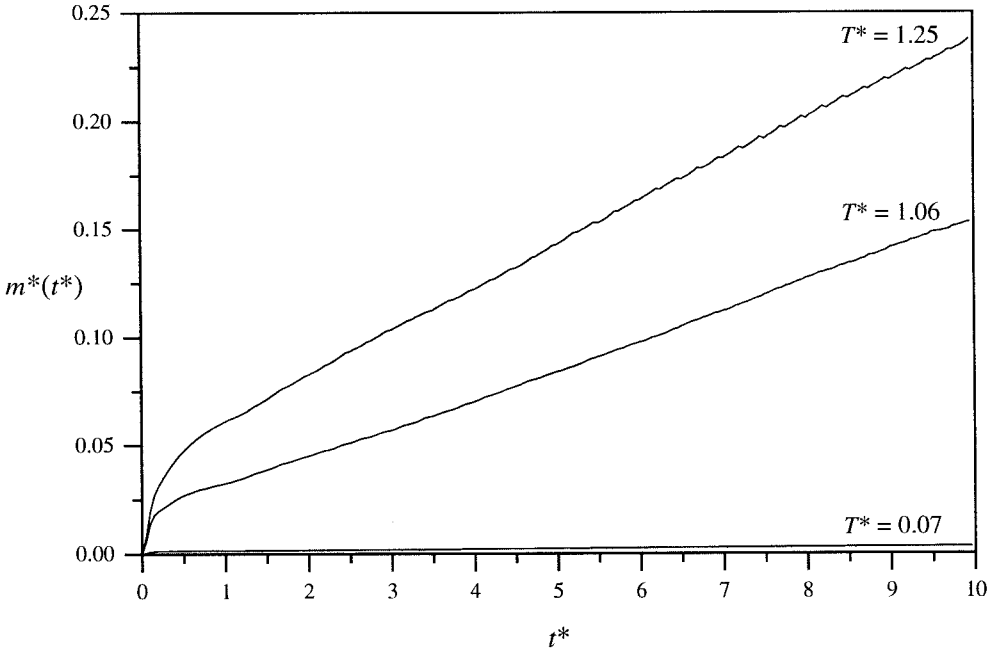

Figure 5.26: *The total mean squared displacement m*(t*) at the scaled temperatures T* indicated.*

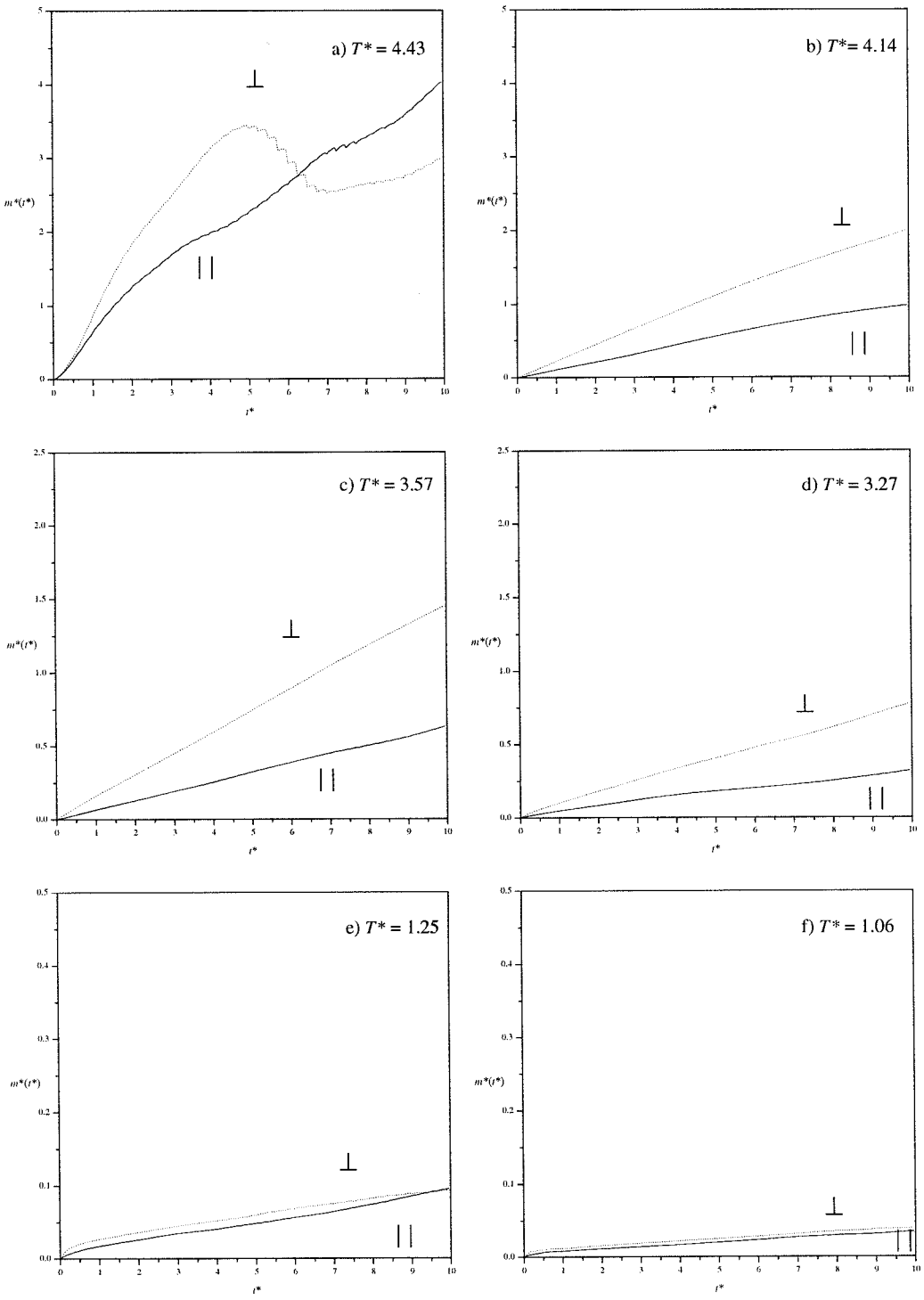

Figure 5.27: *The mean squared displacement resolved, parallel (solid line) and perpendicular (dotted line) to the director at the scaled temperatures T* indicated.*

It is also noticeable that for several of these plots there is some deviation from linearity, suggesting it would be useful to follow the calculation of the mean squared displacement over longer time scales though limited computer resources prevent us from performing such investigations. The transition between the discotic nematic, T^* of 3.57 and columnar phases, T^* of 3.27, is again highlighted, by a change of almost a factor of two in the anisotropy of the diffusion tensor, in the relative motions, parallel and perpendicular to the director.

As the columnar phase is cooled to the boundary of the crystal - columnar transition, the differences between the directions orthogonal to the director are slowly being frozen out, and the overall motion is very small. The lack of anisotropy in the diffusion tensors, parallel and perpendicular for the temperatures T^* of 1.25 and 1.06, is probably explained by the rattling motion of a cage effect in which each particle vibrates about a central position.

The velocity autocorrelation function: We can see from the shape of the total velocity autocorrelation function, (see figures 5.27 and 5.28), that it decays to zero relatively rapidly, indicating that correlations between the velocities of a particle are lost quickly.

The resolution of the velocity autocorrelation function into the components, parallel and perpendicular to the director, provides slightly more detailed information on the dynamic behaviour of the various mesophases, (see figure 5.29). Parallel to the director, the $C_{vv||}(t^*)$ decays to zero much quicker than the in orthogonal direction, showing that the motion is hindered in this direction. The change in sign, denotes a reversal in the direction of movement, and as such indicates a cage effect where the particles undergo collisions and rattle between nearest neighbours.

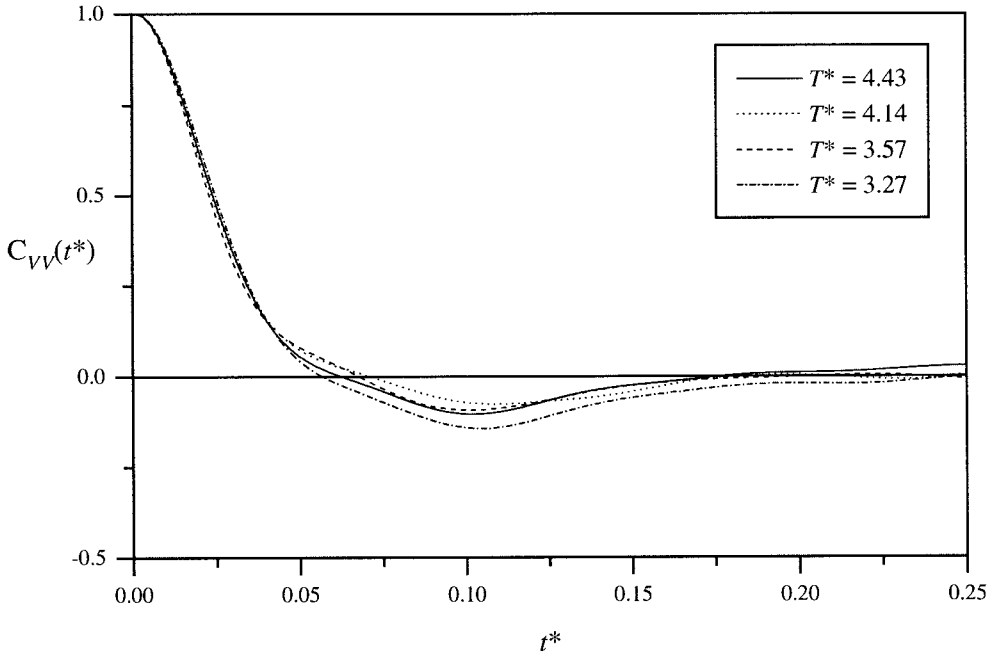

Figure 5.27: *The total velocity autocorrelation function $C_{VV}(t^*)$ at the scaled temperatures T^* indicated.*

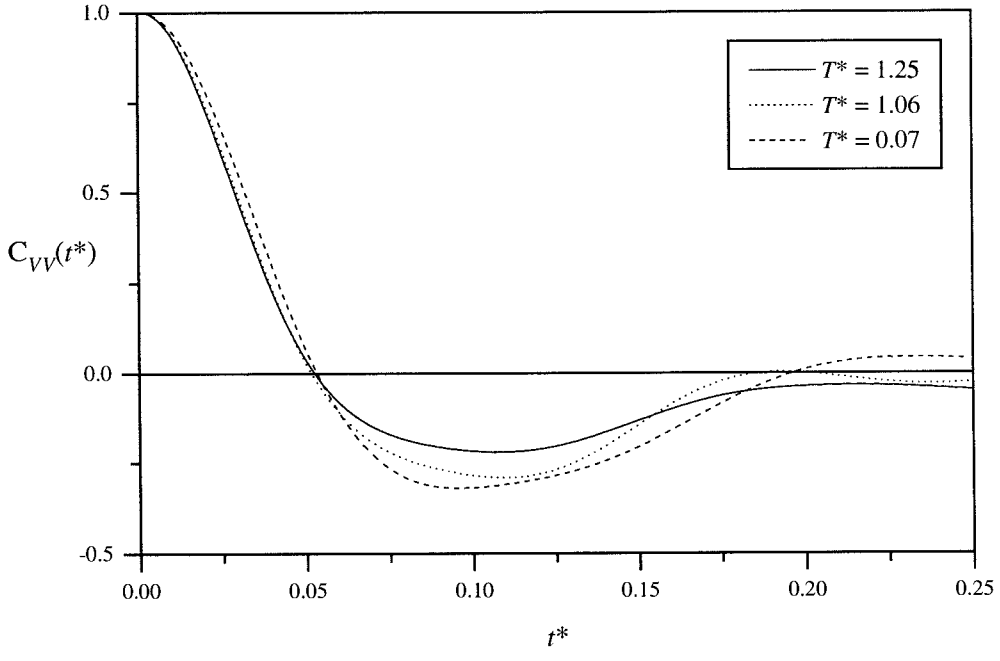

Figure 5.28: *The total velocity autocorrelation function $C_{VV}(t^*)$ at the scaled temperatures T^* indicated.*

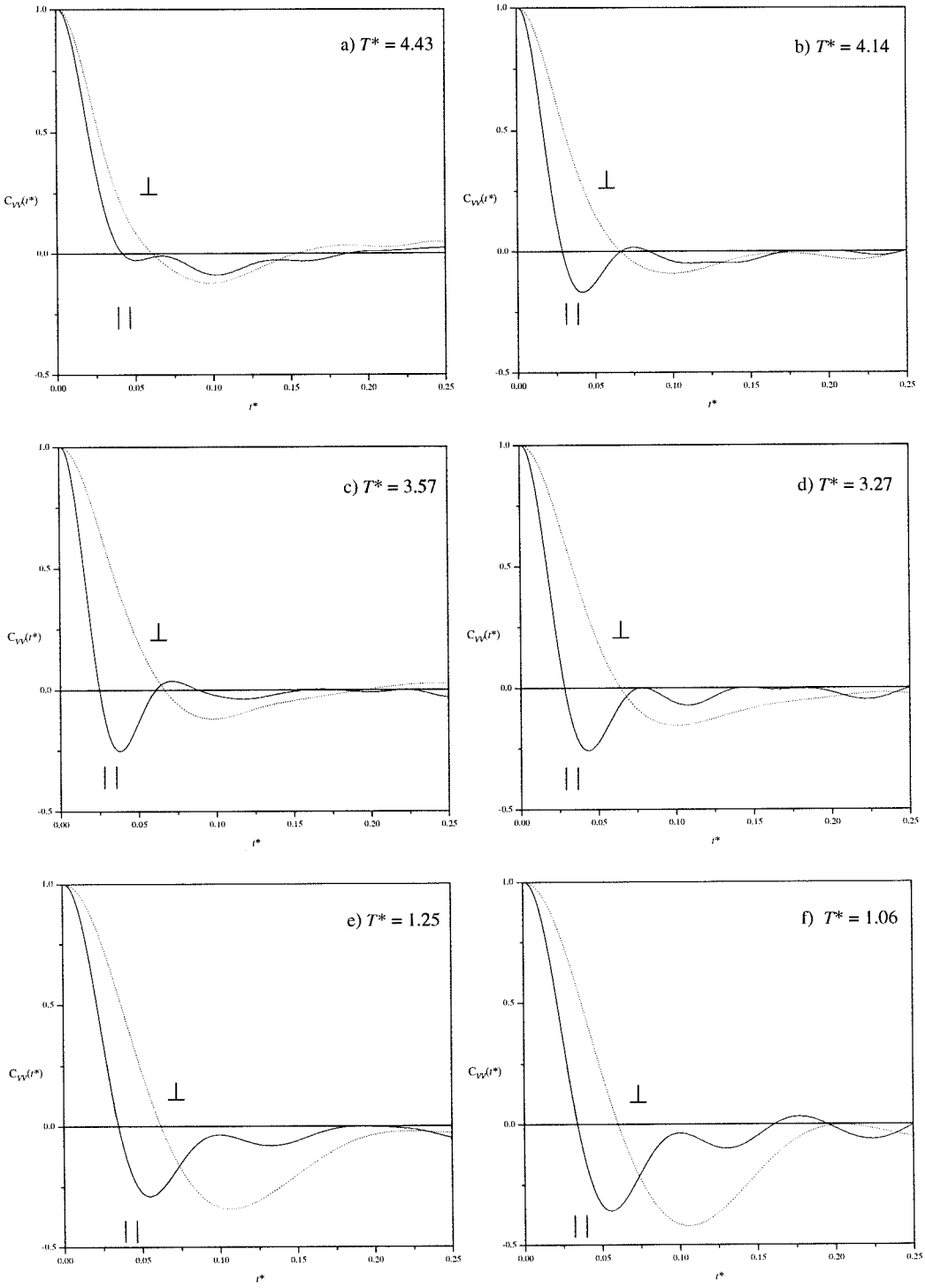

Figure 5.29: *The velocity autocorrelation functions resolved parallel, (solid line), and perpendicular, (dotted line), to the director, at the scaled temperatures T* indicated.*

The behaviour of the particles, perpendicular to the director remains quite similar for different temperatures. We can see from figure 5.29, that as the $C_{VV\perp}(t^*)$ decays quite slowly to zero, the molecular motion must be hindered as the particles find it hard to diffuse orthogonal to the director. We must assume that the strong edge-to-edge interactions tend to slow the particles down. But we must also take into account the respective time scales over which the mean squared displacement and the velocity autocorrelation function are calculated. We could obtain the diffusion coefficient D^* from the integration of the velocity autocorrelation function, but as with our results in Chapter 3, the calculations were not in agreement and shall not be repeated here.

5.4.5 Deficiencies in the Gay-Berne potential

We have used the Gay-Berne potential to represent an oblate mesogen, in the hope of forming a variety of discotic mesophases, and in this respect we have met with varying degrees of success. In Chapter 3, we observed the formation of an interdigitated hexagonal columnar phase while in this Chapter we have tried to form a discotic smectic phase, but only succeeded in forming a discotic nematic and "shifted" columnar phases. This lack of success was partly due to the oversimplification of the forces involved and partly due to a deficiency that has arisen in the potential used and it is this that we shall discuss first.

Though we encountered no problem in Chapter 3, in our study of a discogen, it became obvious, that when we parametrised the potential to represent a mesogen with strong edge-to-edge interactions, we observed significant particle overlap for the face-to-face arrangement. This is due to the relative softness of the potential for particles in this arrangement i.e. for a interparticle separation of $< 1.0\sigma_0$, the energy of interaction is positive but relatively small, (see figure 5.30). This means that if there are other energetically favoured interactions, they can compensate, in terms of energy, for this slight overlap, as we only expect the potential to be infinitely repulsive when the molecular centres themselves overlap. If two particles approach each other in an edge-to-edge arrangement, when the particles start to overlap, the separation between the molecular centres is non-zero, but they will only infinitely repel each other when the separation between these molecular centres, and not the actual discs, is zero, so the potential must reflect this.

If the diameter of the spherical force centre is the thickness of a disc, when two particles are in a face-to-face arrangement, they will infinitely repel when the separation is zero. We can rewrite the Gay-Berne potential as:

$$U(\hat{\mathbf{u}}_1, \hat{\mathbf{u}}_2, \mathbf{r}) = 4\varepsilon(\hat{\mathbf{u}}_1, \hat{\mathbf{u}}_2, \hat{\mathbf{r}})\left[\left\{\frac{\sigma_x}{r-\sigma(\hat{\mathbf{u}}_1, \hat{\mathbf{u}}_2, \hat{\mathbf{r}})+\sigma_x}\right\}^{12} - \left\{\frac{\sigma_x}{r-(\hat{\mathbf{u}}_1, \hat{\mathbf{u}}_2, \hat{\mathbf{r}})+\sigma_x}\right\}^{6}\right]. \quad (5.2)$$

For the potential used in this thesis, σ_x is equal to σ_e, that is the width of one Gay-Berne particle. This means that the potential energy of a pair of discs becomes infinite when,

$$r = \sigma(\hat{\mathbf{u}}_1, \hat{\mathbf{u}}_2, \hat{\mathbf{r}}) - \sigma_e. \quad (5.2)$$

For particles aligned in the face-to-face arrangement, they approach each other at a distance less than σ_e, so the potential is infinite at unphysical negative separations.

To make this more realistic, $U^*(r^*)$ should tend to infinity at $r^* \geq 0$, thus $\sigma(\hat{\mathbf{u}}_1, \hat{\mathbf{u}}_2, \hat{\mathbf{r}})$ should be larger than σ_x for all orientations. As the separation is smallest when in a face-to-face arrangement, σ_x should be equal to σ_f, the thickness of a disc and not σ_e. Thus the modified Gay-Berne potential, the GBII model, for discs is given in equation (5.3) with the distance r still scaled by σ_e, so that:

$$U(\hat{\mathbf{u}}_1, \hat{\mathbf{u}}_2, \mathbf{r}) = 4\varepsilon(\hat{\mathbf{u}}_1, \hat{\mathbf{u}}_2, \hat{\mathbf{r}})\left[\left\{\frac{\sigma_f}{r-\sigma(\hat{\mathbf{u}}_1, \hat{\mathbf{u}}_2, \hat{\mathbf{r}})+\sigma_f}\right\}^{12} - \left\{\frac{\sigma_f}{r-\sigma(\hat{\mathbf{u}}_1, \hat{\mathbf{u}}_2, \hat{\mathbf{r}})+\sigma_f}\right\}^{6}\right]. \quad (5.3)$$

The potential energy diagram for the modified potential is shown in figure 5.31. The potential now has the correct form for the repulsive core, and as we can see it now exhibits narrower well widths, so in effect the attractive part of the potential has reduced in range. There is also a slight change in the slope, thus the potential has become harder. The effect this has on the phase behaviour will need to investigated. One consequence is that the system should behave more like a system of hard ellipsoids, thus the tendency to form columnar phases will be reduced. This indeed has been shown to be the case, with a system of 512 particles interacting with $\varepsilon_e/\varepsilon_s$ of 0.2 showing just a discotic nematic phase[8] and a system of 2000 particles interacting with $\varepsilon_e/\varepsilon_s$ of 5.0, having a columnar phase range[9] over a reduced temperature range when compared with the system in Chapter 3.

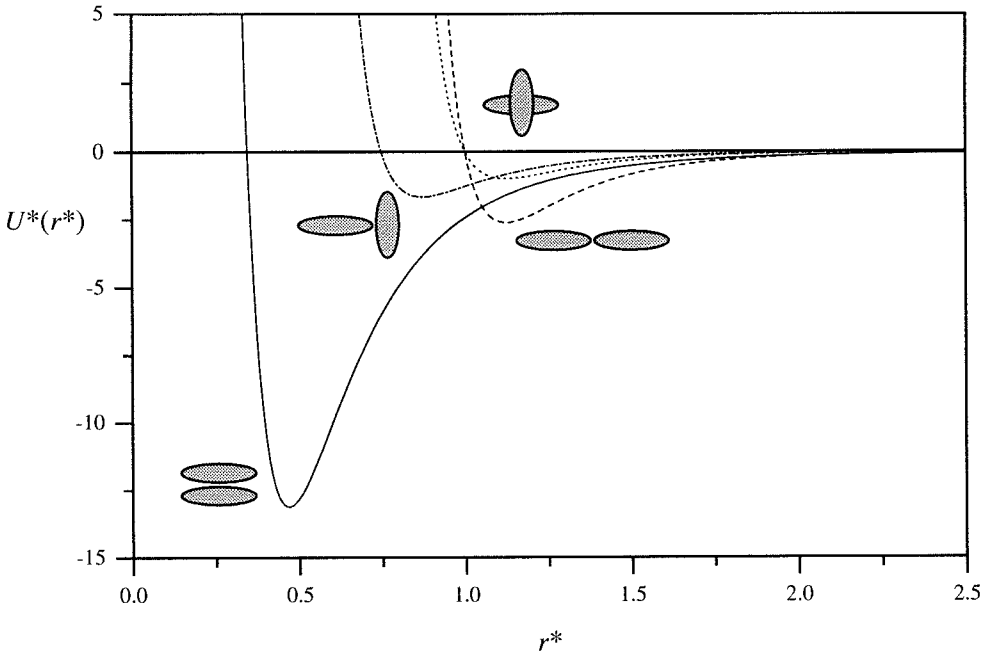

Figure 5.31: *The potential energy diagram for the original Gay-Berne potential GBI, with* σ_f/σ_e *of 0.345 and* $\varepsilon_f/\varepsilon_e$ *of 5.0.*

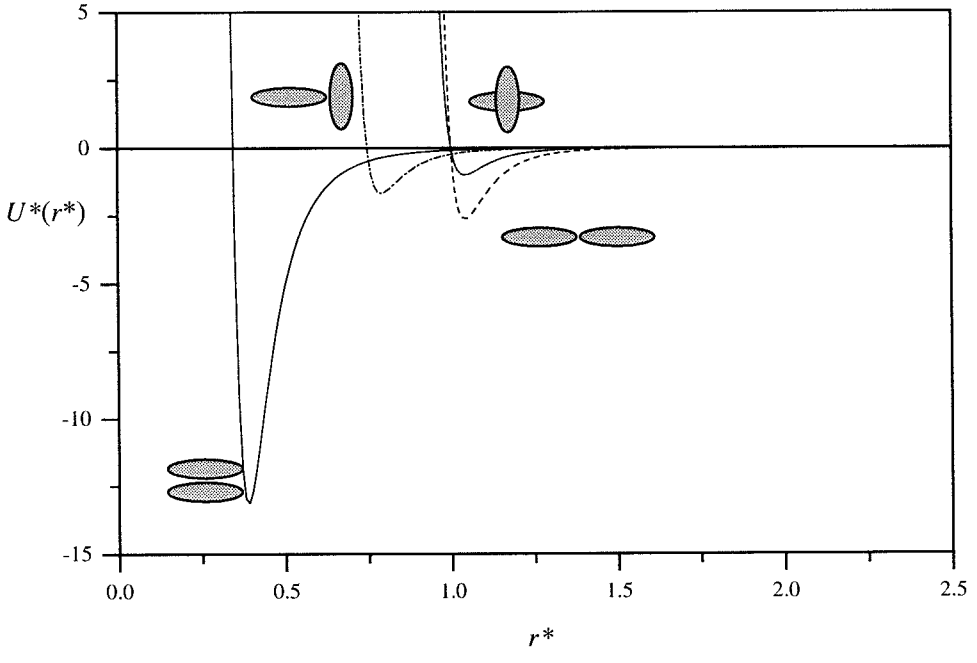

Figure 5.32: *The potential energy diagram for the modified Gay-Berne potential GBII, with* σ_f/σ_e *of 0.345 and* $\varepsilon_f/\varepsilon_e$ *of 5.0.*

There are quantitative way of measuring the difference between these two models, and one which is suited to computer simulation is the calculation of the thermodynamic parameter Γ, and it is that which we shall define and discuss in the next section.

The calculation of Γ

At constant pressure, the change in the order parameter is thought mainly to be due to the temperature while there is a part due to the density change associated with the thermal expansion. To test this idea further, McColl[10] studied the mesophase behaviour of 4, 4'-dimethoxyazoxybenzene (PAA) at various pressures. While noting no dramatic changes in the nature of the isotropic to nematic transition with pressure, it was impossible to investigate the density dependence of $\langle P_2 \rangle$ without the equation of state. So instead he introduced as a measure of the relative importance of density and temperature in establishing nematic order, the thermodynamic parameter Γ,

$$\Gamma = -(\partial \ln T / \partial \ln V)_{\bar{P}_2}. \tag{5.4}$$

The experimental value of 4.0 ± 0.1[11] obtained by McColl agreed well with the results for PAA made by Alben[12] which gave Γ of 4.3, from the analysis of thermodynamic data not related to the order parameter. Despite this, to discuss the real significance of Γ, a comparison of the experimental values with some theoretical models was needed. One of the main models at the time was that developed by Maier and Saupe[13], which took into account the anisotropic dispersion forces between molecules thus leading to the potential of mean torque, which for rigid, cylindrically symmetrical particles can be expressed as

$$U(\beta) = -\varepsilon V^{-\gamma} \langle P_2 \rangle P_2(\cos \beta), \tag{5.5}$$

where β is the angle between the director and the molecular symmetry axis, and ε is a constant related to the molecular anisotropy. It was originally thought that γ could be identified with Γ, but Cotter[14] noted that if equation (5.5) was to be statistical mechanically correct then γ had to take the value of 1. This was only for derivations of equation (5.5) based on the pair potential. For others, such as the variational approach, there is no such constraint on Γ. The exact dependence of the potential of mean torque on the density is not known but it is thought to be ρ^2, thus Γ was given the value of 2, which comes from the dispersion forces dependent on r^{-6}.

But compared to the experimental values for Γ of between 2 and 6, this model was not dependent enough on density. The other theoretical model that had been widely studied was the hard rod model[15]. By its very nature, transitions between the different mesophases are completely driven by a change in density so that means that $\Gamma = \infty$, clearly the hard rod model is too dependent on density. Thus from this, it can be implied that further theoretical models will have to blend both of these extremes, i.e. include both attractive and repulsive interactions. So from this, by calculating Γ for a potential model, we can deduce the role of the various forces within the model in determining Γ and hence how realistic it is when compared to experimental values.

The only study done to date on model systems by computer simulation has been by Emsley *et al.*[16]. They chose to use the Gay-Berne potential parametrised to represent a system of rod-shaped mesogens with the length-to-breadth ratio of 3 and $\varepsilon_s/\varepsilon_e$ of 5, this being a well studied system[17,18]. We shall discuss the two methods used to determine Γ later, but from these they found Γ to be 8.0 ± 1.0. They then modified the potential, increasing the steepness of the repulsive part, being careful to retain the key features of the original potential, finding that Γ increased to 10.5 ± 1.0. This confirmed the ability of Γ to measure the balance of the attractive and repulsive forces in a potential model. The two methods of calculating Γ we shall discuss are, (i) the *direct* method, similar to the experimental technique used previously and (ii), from the density dependence of T_{NI}*.

For the direct method of finding Γ, we calculate the variation of the order parameter $\langle P_2 \rangle$ with temperature T* at more than one constant density. For our purposes, we concentrate on the parametrisation of the Gay-Berne potential used in Chapter 3, i.e. $\varepsilon_f/\varepsilon_e$ of 5.0. From this work, we have a plot of $\langle P_2 \rangle$ at ρ* of 2.5 and from previous simulations[19] we can also obtain data at ρ* of 2.7 and 3.0, (see figure 5.33). From this we then extract the values of temperature and volume at a constant value of $\langle P_2 \rangle$ for each density. It has been suggested[16] that a value of $\langle P_2 \rangle$ should be chosen where it is changing most rapidly with temperature thus a value of $\langle P_2 \rangle$ of 0.4 should be used, as this would allow us to make a direct comparison with the previous determination of Emsley *et al.*[16]

But as we can see, the value of $\langle P_2 \rangle$ of 0.4 lies in the middle of the transition and not clearly in the nematic phase, so to be rigorous we will extend the calculation to values of $\langle P_2 \rangle$ up to 0.9. From this data, a graph of $\ln T^*$ versus $\ln V^*$ was then constructed, (see figure 5.34), the slope of which being $-\Gamma$. The values of Γ obtained from this procedure are shown in table 5.4.

Value of constant $\langle P_2 \rangle$	Γ *from direct method.*
0.4	1.12
0.5	1.12
0.6	1.45
0.7	1.87
0.8	1.51

Table 5.4: *Values of* Γ*, obtained from the plot of* $\ln T^*$ *versus* $\ln V^*$ *in figure 5.35*

Pairs of densities used	Γ
2.5, 2.7	1.3
2.5, 3.0	0.99
2.7, 3.0	0.77

Table 5.5: Γ *calculated from the density dependence of* T_{NI}^* *with the pairs of densities used in brackets.*

As we can see, the value obtained for Γ was between 1.0 and 2.0. This did not change significantly depending on the value of $\langle P_2 \rangle$ used. Using the potential model and its parametrisation from this Chapter, σ_f/σ_e of 0.345 and $\varepsilon_f/\varepsilon_e$ of 0.2, we have also obtained a value Γ of 1.0. This illustrates that a different parametrisation, for a given potential model, makes little difference to the density dependence of the order parameter which is an unexpected result suggesting it is the overall potential model which has the main effect on the dependence rather than a subtle effect from the parametrisation.

We can also calculate Γ from the density dependence of T_{NI}* from equation (5.5) with γ = Γ, leading to

$$\Gamma = -\ln\left(\frac{T^*_{NI}}{V^*}\right). \tag{5.6}$$

The values of Γ obtained are shown in table 5.5, and confirm, within experimental error, the results from the direct method. Simulations have been performed with the modified potential GBII[9] and though we shall not discuss the results in depth here, we have made a preliminary attempt to calculate Γ. From our knowledge of how the new potential looks, (see figure 5.32), it should act more like a system of hard ellipsoids than the GBI model, thus from the inference that Γ measures the balance between attractive and repulsive forces, Γ should have a value greater than 1 found for GBI.

There was a problem that data from the GBII model simulations were performed at constant pressure, and that an accurate value for the volume had not been recorded from the simulation. To calculate Γ from the constant pressure simulations we first plotted the order parameter $\langle P_2 \rangle$ against the scaled temperature T^* at the scaled pressures P^* of 25 and 50. Then, taking a constant value of $\langle P_2 \rangle$ we found the corresponding T^* value. Then for this value of T^* on a plot of the scaled density ρ* against T*, we found the scaled density which corresponds to the constant value of $\langle P_2 \rangle$ first chosen. From the following relationship,

$$\rho^* = \frac{N}{V^*}, \tag{5.7}$$

we can find the volume V^* and then by plotting the graph of $\ln V^*$ against $\ln T^*$, as in the direct method, and making the assumption that the volume at the end of the simulation is not that much larger than during the simulation[22], we obtain a value of $\Gamma \approx 8$. This agrees with our thinking that the GBII potential is harder than the GBI potential.

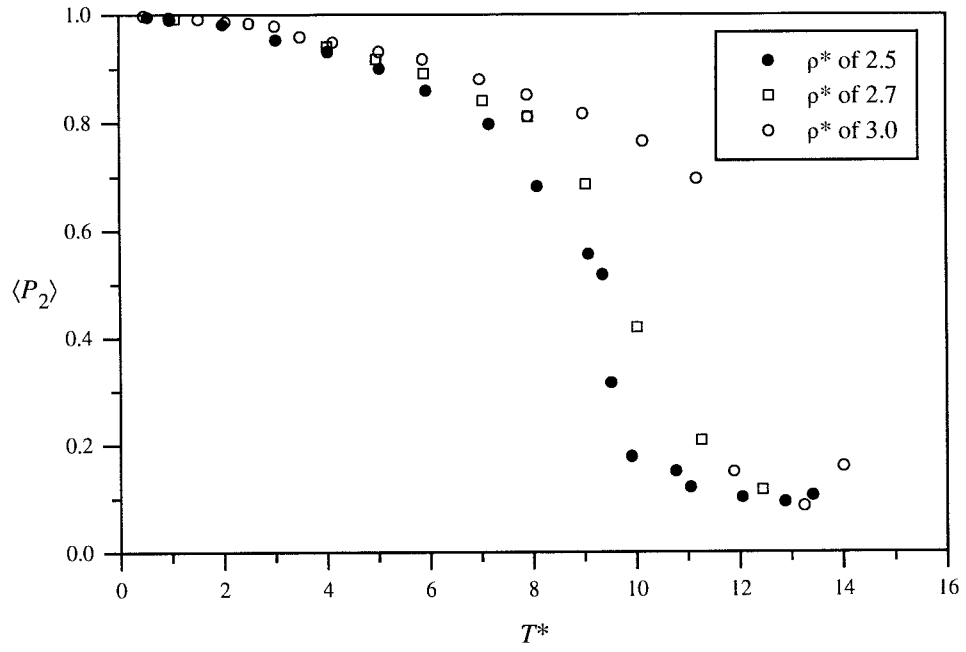

Figure 5.33: *The variation of* $\langle P_2 \rangle$ *with scaled temperature T* at the scaled densities indicated, for the Gay-Berne potential with the parameters* σ_f/σ_e *of* 0.345 *and* $\varepsilon_f/\varepsilon_e$ *of* 5.0.

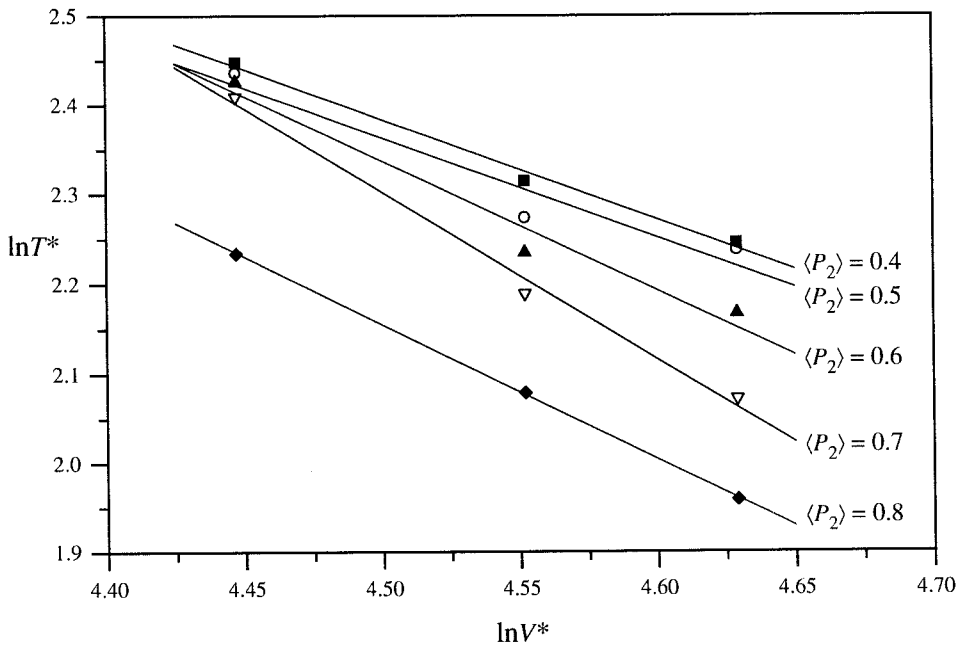

Figure 5.34: *A plot of lnT* versus lnV* at the constant order parameter* $\langle P_2 \rangle$*, the slope of which is* $-\Gamma$*, obtained using a best fit line to the data points.*

5.5 Conclusions

In this Chapter we have used the Gay-Berne potential in which the edge-to-edge arrangement is favoured over the face-to-face, in an attempt to model a discotic smectic phase, in which the particles lie with their faces parallel to the layer. We succeeded in forming discotic nematic and columnar phases in which the columns seem to consist of only three or four particles before a plane of columns gets shifted. This unusual columnar phase could have resulted from either the parametrisation used or the influence of the fixed shape and size of the simulation box.

The next step would be to simulate the system using constant *NPT* ensemble in which the simulation box is allowed to vary in size. An increase in the number of particles used would also be desirable. The structure of both the nematic and columnar phases revealed a deficiency in the potential which allowed the constituent particles to physically overlap. We have highlighted how this could be rectified and the findings of the resultant simulations.

To measure any quantitative differences between the original GBI and the modified GBII, potentials, we have calculated the parameter Γ with which to give us information on the role of attractive and repulsive forces within our model potentials in the stabilisation of liquid crystal phases. It has been suggested that this quantity be used to test the realism of the model by comparing values of Γ from the simulations with those from experiments.

5.6 References

[1] A.M.Giroud-Godquin and P.M.Maitlis. *Angew.Chem.Int.Ed.Engl.* (1991) **30** 375.

[2] N.Boden, S.A.Corne and K.W.Jolley. *J.Phys.Chem.* (1987) **91** 4092.

[3] N.Boden, J.Clements, K.W.Jolley, D.Parker and M.H.Smith. *J.Chem.Phys.* (1990) **93** 9096.

[4] A.P.J.Emerson, G.R.Luckhurst and S.G.Whatling. *Molec.Phys.* (1994) **82** 113.

[5] U.Fabbri and C.Zannoni. *Molec.Phys.* (1986) **58** 763.

[6] A.Perera and G.N.Patey. *J.Chem.Phys.* (1989) **91** 3045.

[7] J.Talbot, A.Perera and G.N.Patey. *Molec.Phys.* (1990) **70** 285.

[8] M.Bates, G.R.Luckhurst and S.G.Whatling. *Unpublished results*. (1995).

[9] M.Bates and G.R.Luckhurst. *J.Chem.Phys.* (1996) **104** 6696.

[10] J.R.McColl. *Phys.Lett.A*. (1972) **A38** 55.

[11] J.R.McColl and C.S.Shih. *Phys.Rev.Lett.* (1972) **29** 85.

[12] R.Alben. *Mol.Cryst.Liq.Cryst.* (1971) **13** 193.

[13] W.Maier and A.Saupe. *a) Z.Naturforsch.* (1958) **13a** 564. *b) Z.Naturforsch.* (1959) **14a** 882.

[14] M.A.Cotter. *Molec.Cryst.Liq.Cryst.* (1977) **39** 173.

[15] L.Onsager. *Ann.N.Y.Acad.Sci.* (1949) **51** 627.

[16] J.W.Emsley, G.R.Luckhurst, W.E.Palke and D.J.Tildesley. *Liq.Cryst.* (1992) **11** 519.

[17] G.R.Luckhurst, R.A.Stephens and R.W.Phippen. *Liq.Cryst.* (1990) **8** 451.

[18] E.de Miguel, L.F.Rull, M.K.Chalam and K.E.Gubbins. *Molec.Phys.* (1991) **74** 405.

[19] A.P.J.Emerson. *Ph.D. Thesis*, University of Southampton (1991).

[20] M.A.Bates. *Personnal communication.* (1995)

6. The Gay-Berne mesogen

6.1 Introduction

The essential characteristic of a mesogenic molecule is that it deviates from spherical symmetry, but as we can see from figure 6.1, the molecule also needs to exceed a certain length-to-breadth ratio before it can exhibit any enantiotropic liquid-crystalline mesophases. We have deliberately chosen the polyphenyls as examples of this important behaviour as they come closest to an experimental analogue of the simple geometric shapes used in computer simulations. This dependence on the length-to-breadth ratio has been investigated in previous simulations using the spherocylinder[1] and ellipsoid[2] hard core models to represent the mesogenic molecule.

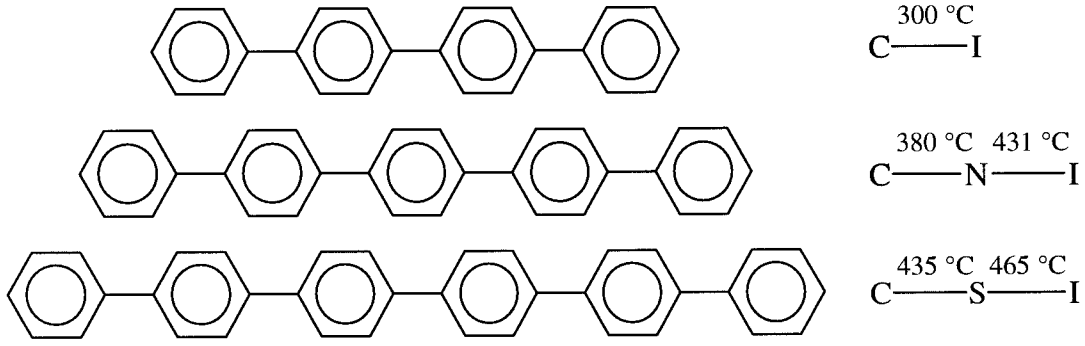

Figure 6.1: *Illustration of how a molecule needs to have a certain length-to-breadth ratio before it can exhibit enantiotropic liquid-crystalline mesophases*[3].

For a system of hard spherocylinders[1] of length L and diameter D, (see §2.5.2), we have seen that for length-to-breadth ratios $L/D < 3$, no mesophases are formed. At L/D of 3.0, a stable smectic phase appears while at values greater than 3, both nematic and smectic phases are formed. For a system of hard ellipsoids of revolution[2], we can also observe a dependence on the length-to-breadth ratio, as to whether the system exhibits a mesophase. For prolate or rod-shaped ellipsoids the aspect ratio a/b must be greater than 3 for the system to form exhibit a nematic phase, otherwise the system crystallises on cooling from the isotropic fluid. The next stage in developing computer models of liquid crystals is to build attractive forces into the system. Taking the example of ellipsoids of revolution, the purely repulsive system only exhibits a nematic phase, predicted by Onsager[4] for infinitely thin rods, but the addition of attractive forces might be the difference that allows the

system to form the translationally ordered smectic phases. The first simulations of such attractive ellipsoids, though the precise shape of real molecules deviates from a true ellipsoid of revolution[5], (also see §2.5.2), were those interacting via the Gay-Berne potential as performed by Luckhurst *et al.*[6], and indeed, the addition of attractive forces stabilised the system enough for smectic A and smectic B phases to be formed. These simulations were for ellipsoids with σ_e/σ_s of 3.0, where σ_e is the distance between the centre-of-mass of two particles in an end-to-end arrangement and σ_s when in a side-by-side arrangement. From the phase diagram of hard ellipsoids, we know that systems with σ_e/σ_s ratios greater than 3 will form a liquid-crystalline mesophase, and indeed systems with σ_e/σ_s of 4.4 are being investigated[7], and so to see what happens for smaller aspect ratios is of special interest.

For σ_e/σ_s ratios less than 3, we speculate that a liquid-crystalline mesophase might be stabilised by the addition of attractive forces. This should be possible as shown by the use of the Luckhurst-Romano[8] and Gay-Berne-Luckhurst-Romano[9] potentials, (see §2.5.3), which do exhibit liquid-crystalline phases. These are of interest because these potentials have a spherical force centre which can be thought to be analogous to an ellipsoid in the limit of zero shape anisotropy. The Luckhurst-Romano potential model is defined as

$$U_{LR} = U_o + U_a, \tag{6.1}$$

where

$$U_o = 4\varepsilon\left[\left(\frac{\sigma}{r_{12}}\right)^{12} - \left(\frac{\sigma}{r_{12}}\right)^{6}\right], \tag{6.2}$$

and

$$U_a = -4\lambda\varepsilon\left(\frac{\sigma}{r_{12}}\right)^{6} P_2(\cos\beta_{12}), \tag{6.3}$$

where λ is an adjustable parameter and r_{12} is the intermolecular separation. The formation of the mesophases is possible through the addition of an anisotropic, attractive part, dependent on the $P_2(\cos\beta_{12})$ term of the potential. So for this work, we shall look at the σ_e/σ_s ratios which are smaller than the commonly used value of 3, thus we shall concentrate on the values 2.5 and 2.0, for a system of prolate ellipsoids interacting via the Gay-Berne potential.

6.2 Parametrisation of the Gay-Berne potential

For this study we examine the effect of changing the length-to-breadth ratio of the constituent particles on the phase behaviour, but it makes sense to remain as consistent as possible in all other ways with previous simulations. Thus we chose the parameters μ of 1, ν of 2 and the well depth anisotropy parameter $\varepsilon_e/\varepsilon_s$ of 0.2. It should be noted that the values of μ and ν are reversed from those used originally by Gay and Berne[10] as our choice favours the side-by-side arrangement over the cross and tee arrangements. We have plotted the scaled potential energy $U^*(r^*)$ as a function of the scaled distance r^*, (see figure 6.2), for particles with length-to-breadth ratios of *a*) σ_e/σ_s of 2.5 and *b*) σ_e/σ_s of 2.0. We can see that compared to the potential energy diagram for particles with σ_e/σ_s of 3.0, (see figure 2.15), the well depth for side-by-side arrangement is less, thus the main driving force for nematic mesophase formation, the ratio between the side-by-side and tee arrangements, is reduced. This occurs because the well depth anisotropy term is dependent not on just the parameter $\varepsilon_e/\varepsilon_s$ but on the shape anisotropy parameter σ_e/σ_s via χ. This can be seen by looking at the general expression for the well depth term for a Gay-Berne particle in a side-by-side arrangement; this is given as

$$\varepsilon(\hat{\mathbf{u}}_1,\hat{\mathbf{u}}_2,\hat{\mathbf{r}}) = \varepsilon_0\varepsilon^{\nu}(\hat{\mathbf{u}}_1,\hat{\mathbf{u}}_2)\varepsilon_1^{\mu}(\hat{\mathbf{u}}_1,\hat{\mathbf{u}}_2,\hat{\mathbf{r}}), \tag{6.5}$$

$$= \varepsilon_0\left[1-\chi^2(\hat{\mathbf{u}}_1.\hat{\mathbf{u}}_2)^2\right]^{\frac{-\nu}{2}}\left[1-\frac{\chi'}{2}\left\{\frac{(\hat{\mathbf{u}}_1.\hat{\mathbf{r}}+\hat{\mathbf{u}}_2.\hat{\mathbf{r}})^2}{1+\chi'(\hat{\mathbf{u}}_1.\hat{\mathbf{u}}_2)}+\frac{(\hat{\mathbf{u}}_1.\hat{\mathbf{r}}-\hat{\mathbf{u}}_2.\hat{\mathbf{r}})^2}{1-\chi'(\hat{\mathbf{u}}_1.\hat{\mathbf{u}}_2)}\right\}\right]^{\mu}, \tag{6.6}$$

where

$$\chi = \frac{(\sigma_e/\sigma_s)^2-1}{(\sigma_e/\sigma_s)^2+1}, \tag{6.7}$$

and

$$\chi' = \frac{1-(\varepsilon_e/\varepsilon_s)^{\frac{1}{\mu}}}{1+(\varepsilon_e/\varepsilon_s)^{\frac{1}{\mu}}}. \tag{6.8}$$

Thus as σ_e/σ_s is reduced, the corresponding well depth term is reduced. We justify keeping the actual well depth term $\varepsilon_e/\varepsilon_s$ the same as used in previous simulations in order to isolate the effect of changing the shape anisotropy. The other effect of changing the shape anisotropy can be observed in the plots of the scaled potential energy, (see figure 6.2), where the cross over points between the different potential energy wells decreases i.e. the difference in total shape anisotropy for the model is reduced.

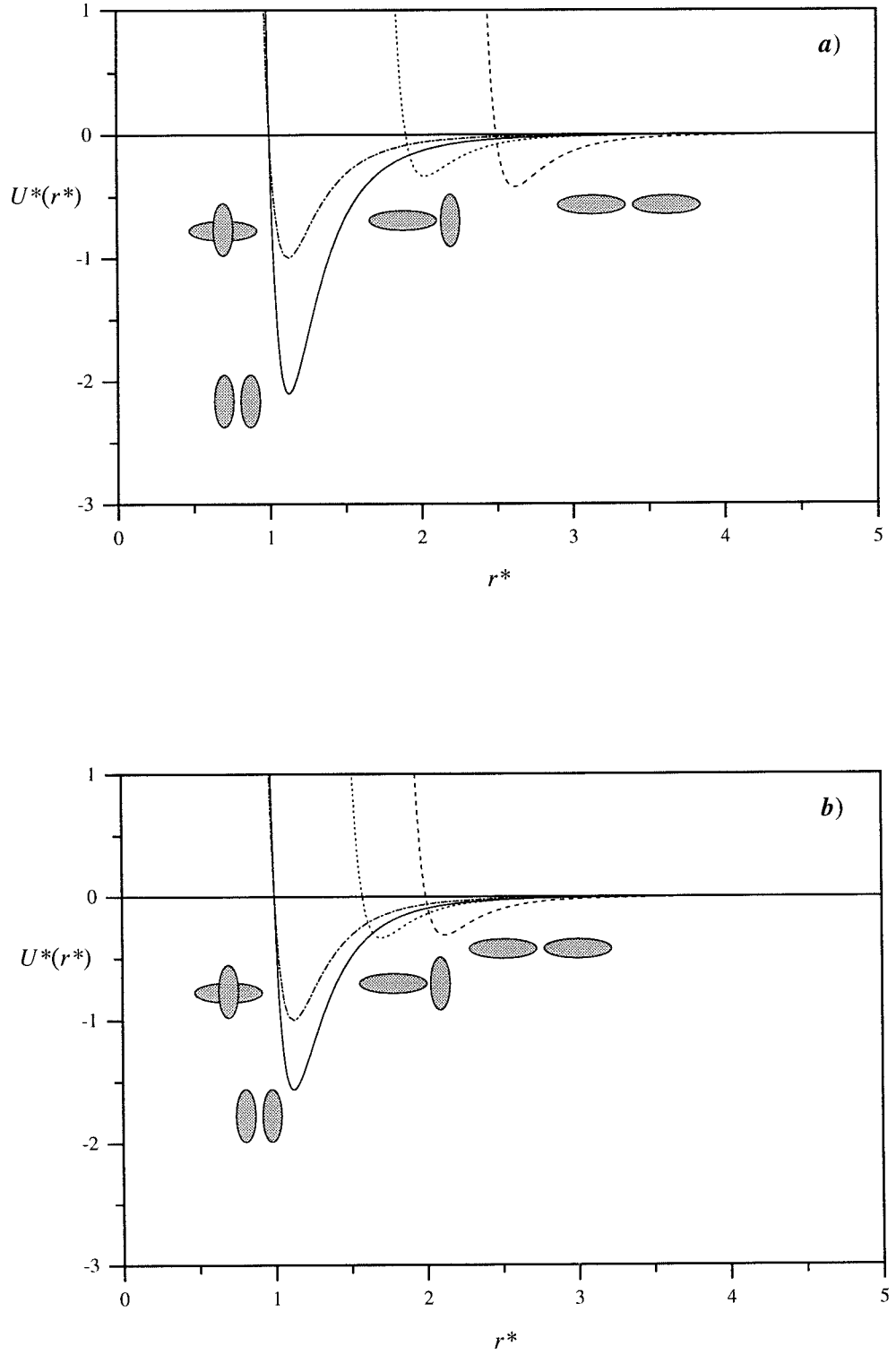

Figure 6.2: *The scaled potential energy U*(r*) as a function of the scaled distance r*, for a system of prolate ellipsoids interacting via the Gay-Berne potential with length-to-breadth ratios of a) 2.5 and b) 2.0.*

Having decided on the parameters we shall use for the Gay-Berne potential, we must now decide on the state variables at which to study the system i.e. the scaled temperature T^* and the scaled number density ρ^*. To assist in the selection of the density, we use the phase diagram for the corresponding system of hard ellipsoids of revolution, (see figure 2.5). As in Chapter 3, we can re-draw this phase diagram using the scaled number density used in our simulations rather than the more usual packing fraction, (see figure 6.3). We must state that this diagram is only used as a guide for locating the desired density when we consider that there is not a nematic - isotropic transition at ratios of 2.5 and 2.0.

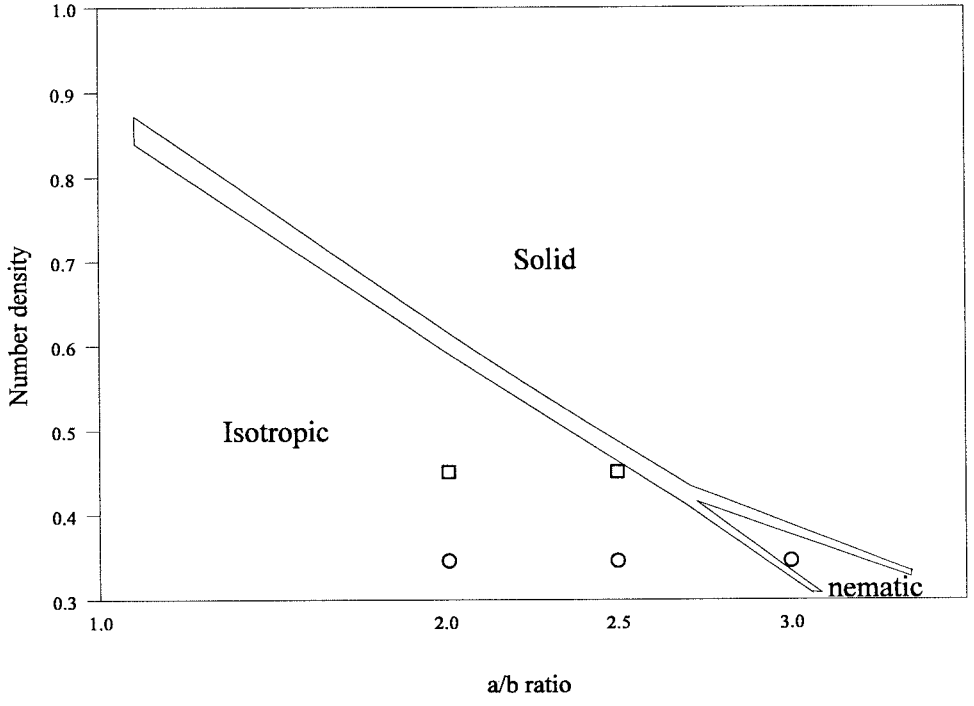

Figure 6.3: *The phase diagram for hard ellipsoids as a function of the scaled number density, as used in this Thesis, with the densities used in this study,* ρ^* *of* 0.35 (○) *and* ρ^* *of* 0.45 (□).

It has been shown that this phase diagram is a good guide as to what density to use to stabilise the liquid-crystalline phases. Generally the density chosen is on or near the boundary between the nematic and isotropic phases. However as well as extending the search for different state points which show liquid-crystalline behaviour, we would like to retain some contact with previous simulations. So following this we have chosen to use the densities ρ^* of 0.35 and 0.45 for ellipsoids with σ_e/σ_s of 2.5 and 2.0. These are marked on the phase diagram together with that of 0.35 used for σ_e/σ_s of 3.0.

6.3 The molecular dynamics simulation

The procedure was very similar to that undertaken in Chapters 3 and 5 for a system of Gay-Berne discs. For both length-to-breadth ratios at each density, an initial α-*f.c.c.* lattice of 500 particles was set up with the particles pointing along the box diagonal. This was then heated to a temperature sufficiently high for the system to exhibit an isotropic phase and once this had been achieved, the system was cooled. Each simulation was performed in the constant *NVE* ensemble, with cubic periodic boundary conditions and a spherical potential cut-off of $3.8\sigma_0$, which from the potential energy diagrams, (see figure 6.2), was sufficient to ensure that the interaction between particles had just ceased. The equilibrium stages consisted of between 10,000 and 250,000 time steps, and each production stage being between 10,000 and 20,000 time steps, the scaled time step δt^* of 0.005, which conserves the energy to a few parts in 10^4. The results of the important properties, $\langle P_2 \rangle$ and $\langle U^* \rangle$, determined during the simulation are shown in tables 6.1-6.5.

Set T^*	Actual T^*	$N_c/10^3$	$N_p/10_3$	$\langle U^* \rangle$	$\langle P_2 \rangle$
4	3.90 ± 0.02	100	20	0.83 ± 0.12	0.136 ± 0.022
3.75	3.82 ± 0.03	50	20	0.33 ± 0.11	0.349 ± 0.025
3.5	3.51 ± 0.02	100	20	−0.92 ± 0.09	0.586 ± 0.013
3.25	3.20 ± 0.04	50	20	−1.85 ± 0.09	0.682 ± 0.011
3	3.01 ± 0.05	50	20	−2.35 ± 0.11	0.723 ± 0.009
2.5	2.52 ± 0.03	50	20	−3.53 ± 0.15	0.801 ± 0.011
2.25	2.21 ± 0.04	50	20	−4.66 ± 0.08	0.829 ± 0.012
2	1.99 ± 0.01	50	20	−4.71 ± 0.09	0.853 ± 0.008
1.75	1.73 ± 0.03	50	20	−5.33 ± 0.08	0.877 ± 0.007
1.5	1.53 ± 0.03	50	20	−7.61 ± 0.06	0.946 ± 0.003
1	1.00 ± 0.02	50	20	−9.01 ± 0.11	0.972 ± 0.002
0.5	0.49 ± 0.01	50	20	−10.14 ± 0.05	0.986 ± 0.002
0.1	0.08 ± 0.01	25	20	−11.07 ± 0.01	0.996 ± 0.001

Table 6.1: *The thermodynamic averages at* ρ^* *of* 0.35 *for Gay-Berne particles with* σ_e/σ_s *of* 3.0.

Set T^*	Actual T^*	$N_e/10^3$	$N_p/10^3$	$\langle U^* \rangle$	$\langle P_2 \rangle$
1.3	1.32 ± 0.03	25	20	−3.05 ± 0.12	0.126 ± 0.019
1.2	1.19 ± 0.02	100	50	−3.31 ± 0.05	0.227 ± 0.012
1.1	1.10 ± 0.03	300	20	−3.92 ± 0.06	0.603 ± 0.013
1	0.97 ± 0.01	150	20	−4.31 ± 0.09	0.705 ± 0.011
0.9	0.89 ± 0.02	50	20	−4.58 ± 0.09	0.767 ± 0.008
0.8	0.81 ± 0.02	125	20	−4.86 ± 0.03	0.812 ± 0.008
0.7	0.72 ± 0.03	100	20	−5.80 ± 0.03	0.902 ± 0.008
0.6	0.61 ± 0.01	100	20	−6.30 ± 0.01	0.931 ± 0.006
0.5	0.50 ± 0.02	250	20	−6.65 ± 0.02	0.950 ± 0.003
0.4	0.41 ± 0.01	20	10	−6.89 ± 0.02	0.961 ± 0.002
0.3	0.29 ± 0.01	20	10	−7.22 ± 0.02	0.972 ± 0.002
0.2	0.22 ± 0.02	20	10	−7.69 ± 0.01	0.980 ± 0.001
0.1	0.09 ± 0.02	10	10	−8.01 ± 0.01	0.990 ± 0.001

Table 6.2: *The thermodynamic averages at* ρ^* *of* 0.35 *for Gay-Berne particles with* σ_e/σ_s *of* 2.5.

Set T^*	Actual T^*	$N_e/10^3$	$N_p/10^3$	$\langle U^* \rangle$	$\langle P_2 \rangle$
3	3.03 ± 0.09	40	20	0.96 ± 0.19	0.064 ± 0.019
2.5	2.49 ± 0.05	25	20	0.02 ± 0.09	0.097 ± 0.022
2.2	2.18 ± 0.06	50	20	−0.68 ± 0.07	0.128 ± 0.016
2	1.97 ± 0.02	125	20	−2.33 ± 0.08	0.680 ± 0.011
1.8	1.81 ± 0.04	50	20	−2.85 ± 0.07	0.739 ± 0.010
1.6	1.59 ± 0.03	50	20	−3.56 ± 0.05	0.798 ± 0.009
1.4	1.39 ± 0.03	50	20	−4.19 ± 0.06	0.838 ± 0.005
1.2	1.18 ± 0.04	50	20	−4.80 ± 0.05	0.867 ± 0.006
1	1.01 ± 0.02	125	20	−6.56 ± 0.05	0.950 ± 0.004
0.5	0.50 ± 0.01	40	20	−7.64 ± 0.03	0.965 ± 0.003
0.1	0.09 ± 0.01	10	20	−8.67 ± 0.01	0.985 ± 0.002

Table 6.3: *The thermodynamic averages at* ρ^* *of* 0.45 *for Gay-Berne particles with* σ_e/σ_s *of* 2.5.

Set T^*	Actual T^*	$N_e/10^3$	$N_p/10^3$	$\langle U^* \rangle$	$\langle P_2 \rangle$
2	1.99 ± 0.04	50	10	−1.90 ± 0.11	0.046 ± 0.004
1.5	1.52 ± 0.03	25	10	−2.16 ± 0.06	0.046 ± 0.007
1	0.99 ± 0.01	25	10	−2.48 ± 0.02	0.053 ± 0.009
0.5	0.51 ± 0.01	25	10	−2.92 ± 0.01	0.120 ± 0.012
0.4	0.42 ± 0.02	100	20	−4.01 ± 0.03	0.757 ± 0.005
0.3	0.30 ± 0.01	100	20	−5.52 ± 0.02	0.946 ± 0.010
0.2	0.19 ± 0.02	50	20	−5.87 ± 0.01	0.968 ± 0.008
0.1	0.09 ± 0.01	25	20	−6.20 ± 0.02	0.984 ± 0.002

Table 6.4: *The thermodynamic averages at* ρ^* *of* 0.35 *for Gay-Berne particles with* σ_e/σ_s *of* 2.0.

Set T^*	Actual T^*	$N_e/10^3$	$N_p/10^3$	$\langle U^* \rangle$	$\langle P_2 \rangle$
1	0.99 ± 0.08	25	20	−3.04 ± 0.05	0.105 ± 0.012
0.9	0.90 ± 0.07	10	20	−3.14 ± 0.04	0.072 ± 0.011
0.8	0.81 ± 0.11	25	20	−3.27 ± 0.03	0.093 ± 0.009
0.7	0.69 ± 0.09	25	20	−3.49 ± 0.02	0.156 ± 0.008
0.6	0.62 ± 0.05	150	20	−4.01 ± 0.03	0.626 ± 0.009
0.5	0.50 ± 0.03	150	20	−4.46 ± 0.03	0.784 ± 0.005
0.4	0.42 ± 0.02	50	20	−5.21 ± 0.03	0.900 ± 0.003
0.3	0.29 ± 0.02	50	20	−5.75 ± 0.01	0.951 ± 0.003
0.2	0.19 ± 0.01	10	10	−6.01 ± 0.02	0.969 ± 0.002
0.1	0.09 ± 0.01	10	10	−6.30 ± 0.01	0.978 ± 0.002

Table 6.5: *The thermodynamic averages at* ρ^* *of* 0.45 *for Gay-Berne particles with* σ_e/σ_s *of* 2.0.

6.4 Results and discussion

We shall now discuss the results obtained using various orientational, thermodynamic and structural properties calculated from the molecular dynamics simulation. First we shall look at the plots of the second rank order parameter $\langle P_2 \rangle$ and the internal energy $\langle U^* \rangle$, which can be used to provide initial evidence of a phase transition, then we shall concentrate on the various structural distribution functions and configurational snapshots.

6.4.1. Length-to-breadth ratio σ_e/σ_s of 3.0

The first system we shall look at is a set of Gay-Berne rods with σ_e/σ_s of 3.0 which is one of the most widely investigated. Adams *et al.*[11] first simulated this system at a scaled density of 0.32 with μ of 2 and ν of 1. They observed a nematic - isotropic transition at T^* of between 1.8 and 1.7. Phippen[12] used μ of 2 and ν of 1, and on heating 256 particles at ρ^* of 0.35, could not form a isotropic phase. Reducing the density to 0.32 allowed a nematic - isotropic transition to be observed at T^* of 1.8. Emerson[13] then repeated the simulation of Phippen but with N of 500 in order to investigate the system size effect. He observed hysteresis in the values of the order parameters and that the transition was lowered to a value of 1.5. Chalam *et al.*[14] have also produced numerous simulations at both constant temperature and constant volume. Using the same parameters as the original Gay-Berne paper, they observed a nematic - isotropic transition at T^* of 1.21 and a smectic B - nematic at T^* of 0.8. Luckhurst *et al.*[6] reversed the values of μ and ν, taking the values of 1 and 2 respectively, forming isotropic, nematic, smectic A and smectic B phases. This procedure favoured the face-to-face and side-by-side over the tee and cross configurations, so enhancing the probability of mesophase formation. Thus it is these parameters that we have decided to use in this study. A brief summary of these simulations can be found in table 6.6. We have also decided to perform a simulation with parameters σ_e/σ_s of 3.0, $\varepsilon_e/\varepsilon_s$ of 0.2, μ of 1 and ν of 2 at a scaled density of 0.35, not only to act as a point of contact for the other length-to-breadth ratios but as a simulation in its own right.

Reference	σ_e/σ_s	$\varepsilon_e/\varepsilon_s$	μ	ν	ρ^*	N
Adams[11]	3	0.2	2	1	0.32	256
Chalam[14]	3	0.2	2	1	0.32	256
Phippen[12]	3	0.2	2	1	0.35	256
Phippen[12]	3	0.2	2	1	0.32	256
Emerson[13]	3	0.2	2	1	0.32	500
Luckhurst[6]	3	0.2	1	2	0.3	256

Table 6.6: *A summary of the parameters used in previous simulations of Gay-Berne rods with* σ_e/σ_s *of 3.0.*

From the plot of the second rank orientational order parameter $\langle P_2 \rangle$ for the density ρ^* of 0.35, we can observe a nematic - isotropic transition between T^* of 3.90 and 3.82, (see figure 6.4), though the value of $\langle P_2 \rangle$ of 0.136 for the isotropic phase does seem high, compared with the theoretical value of $1/\sqrt{N} \equiv 0.045$. Evidence of long range orientational order, necessary to identify a nematic phase, is given by the order parameter $\langle P_2 \rangle$ of 0.349 and by the pair orientational correlation function $G_2(r^*)$, (see figure 6.5). From this we can clearly observe the nematic - isotropic transition to be between T^* of 3.90 and 3.82, as at long interparticle distances, there still remains some orientational correlation.

From the scaled internal energy $\langle U^* \rangle$, we do not observe any indication of the nematic - isotropic transition but we can see a change in the slope between T^* of 1.73 and 1.53, indicating a possible phase transition. And though we really need more state points to be able to more readily identify the phase transition, it is accompanied by a corresponding increase in $\langle P_2 \rangle$. From the radial distribution function $g(r^*)$, (see figure 6.6), we can gather some information on the various phases present. At T^* of 3.90, the $g(r^*)$ shows some short range translation correlations but as the order parameter $\langle P_2 \rangle$ has a value of only 0.14, we can identify this as the isotropic phase. As we decrease the temperature to 3.82, the shape of $g(r^*)$ changes very little. Again, we observe some short range, side-by-side ordering, the peaks at r^* of 1.1 and 2.2 and end-to-end ordering, the peak at r^* of 3.0. It is interesting to note that the peak representing the side-by-side arrangement is at the position of the potential energy minima, r^* of 1.1, (see figure 6.2), rather than the particle diameter, r^* of 1.0.

As we lower the temperature, the system remains in a nematic phase until T^* of 1.73. At temperatures below this, the $g(r^*)$, (see figure 6.7), reveals the presence of considerable short range and long range translational order. This is probably the onset of a more ordered smectic phase such as the crystal or smectic B. The split peak in the $g(r^*)$ at r^* of 2 is consistent with the smectic B phase obtained from other simulations[15], though from the values of these peaks, the system is not close packed. For this system, we observe two important features, namely, the increased nematic - isotropic transition temperature, at T^* of 3.82, and the absence of the smectic A phase when compared to the system at the lower density ρ^* of 0.3[6]. At this density, the phase sequence is C-S_B-S_A-N-I, with the nematic -

isotropic transition temperature being between T^* of 3.0 and 2.0. The first difference between the two densities is easily explainable, as at the higher density, the particles are compressed closer together, hence the attractive interaction that each particle experiences, increases. The loss of the smectic A phase is harder to quantify, but could result from the use of a constant volume simulation box. This is not an entirely unreasonable suggestion, as a similar phase sequence was observed in a similar system of Gay-Berne rods, σ_e/σ_s of 3.0, where a nematic to smectic B transition was seen, the simulation performed using constant *NVT* molecular dynamics[15].

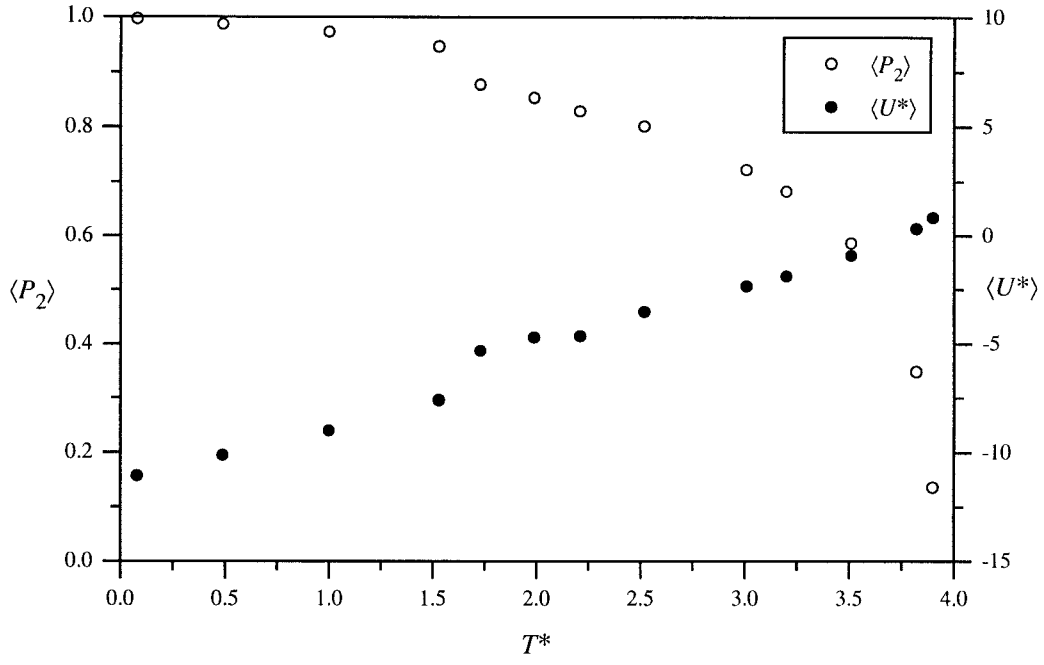

Figure 6.4 *The variation of the second rank orientational order parameter* $\langle P_2 \rangle$ *and the scaled internal energy per particle* $\langle U^* \rangle$ *with scaled temperature* T^* *at* ρ^* *of* 0.35.

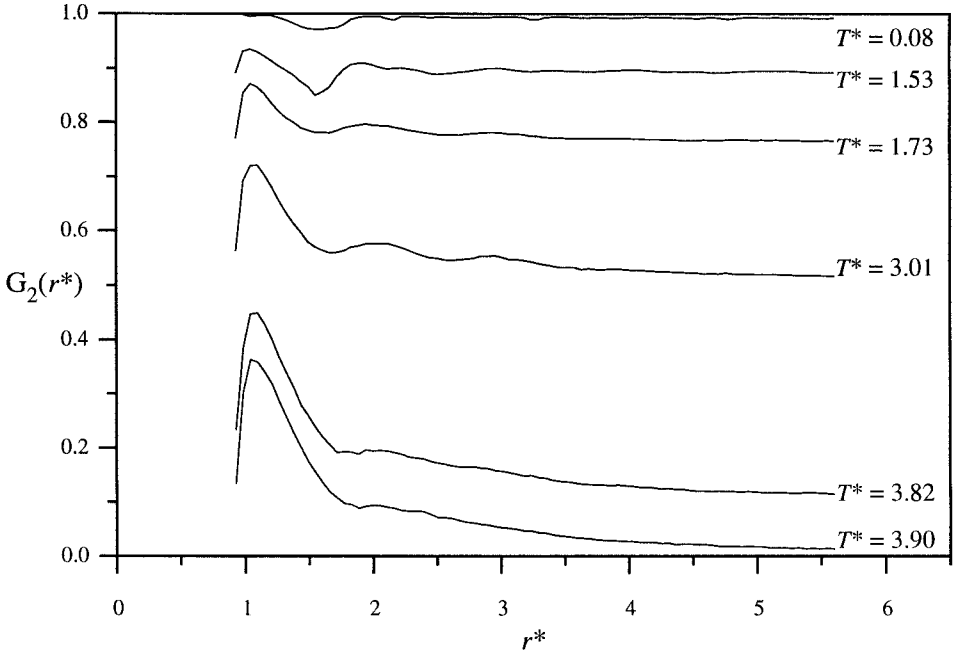

Figure 6.5: *The pair orientational correlation function* $G_2(r^*)$ *at the scaled temperatures* T^* *indicated.*

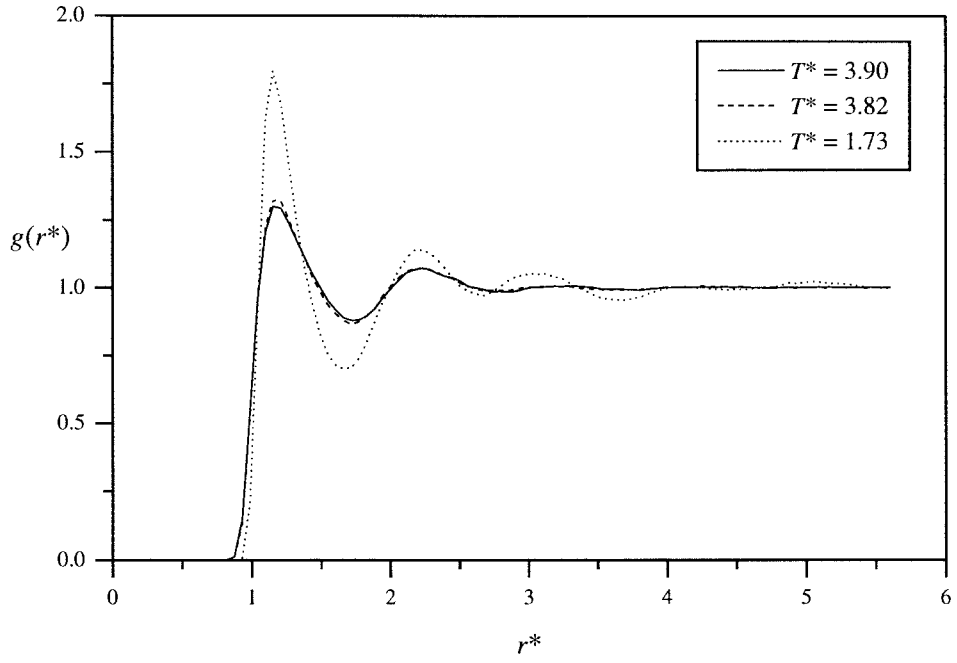

Figure 6.6: *The radial distribution function g(r*) at the scaled temperatures T* indicated.*

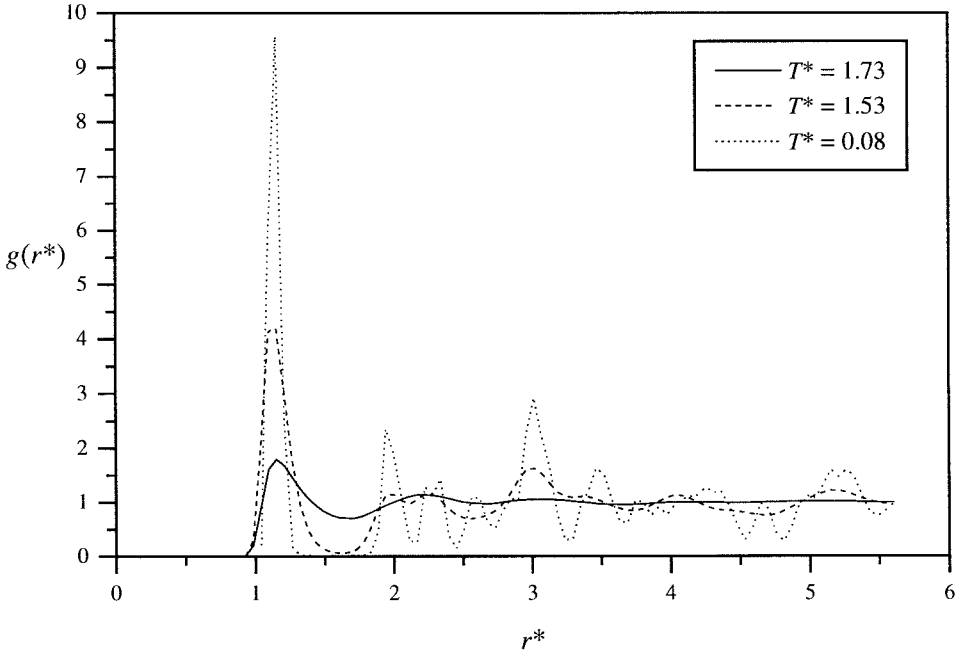

Figure 6.7: *The radial distribution function g(r*) at the scaled temperatures T* indicated.*

6.4.2. Length-to-breadth ratio σ_e/σ_s of 2.5

We shall now investigate the behaviour of a system of Gay-Berne particles with a smaller than usual length-to-breadth ratio, σ_e/σ_s of 2.5 at the scaled densities of 0.35 and 0.45. For the system at ρ^* of 0.35, from the radial distribution function $g(r^*)$, (see figure 6.11), we can see that there seems to be a variety of mesophases present. Due to a lack of transitional order and a small value of $\langle P_2 \rangle \approx 0.1$, there is an isotropic phase present at T^* of 1.19. Evidence of a phase transition from the isotropic phase at T^* of 1.19 to a nematic phase at T^* of 1.10, comes from a number of sources. The most obvious is the increase in orientational order shown by the plot of the order parameter $\langle P_2 \rangle$, (see figure 6.9), and the pair orientational correlation function $G_2(r^*)$, (see figure 6.10). There is also a corresponding increase in translational order of the phase. Peaks at r^* of 1.1 and 2.2 in the $g(r^*)$ indicating shells of particles in side-by-side orientations.

The phases at the other temperatures need further investigation before any firm conclusions can be drawn. Initially there seems to be a smectic A phase at T^* of 0.81 and smectic B phase at T^* of 0.72. These can be deduced by inspection of the $g_{||}(r_{||}^*)$, (see figure 6.13). This shows that there is no translational order along the director for the nematic phase at T^* of 0.89. The broad peaks at T^* of 0.81, reveal the slightly ordered layers of the smectic A phase, while for the smectic B phase, the intensity of the peaks is much greater. But to confirm our identification of the smectic A phase at T^* of 0.81, we have performed an additional 50,000 time step simulation, then checked the form of the $g_{||}(r_{||}^*)$ to see if it had changed to that for a smectic B phase, (see figure 6.13). This problem was identified by de Miguel *et al.*[13], who following this same routine, subsequently reclassified their phase as a smectic B. After our simulation, the plot of the $g_{||}(r_{||}^*)$ remained with this broad modulation and so was classified as a smectic A phase. Graphic snapshots from just one configuration from each of the smectic phases, illustrates nicely the difference in the translational order of the layers, (see figure 6.14).

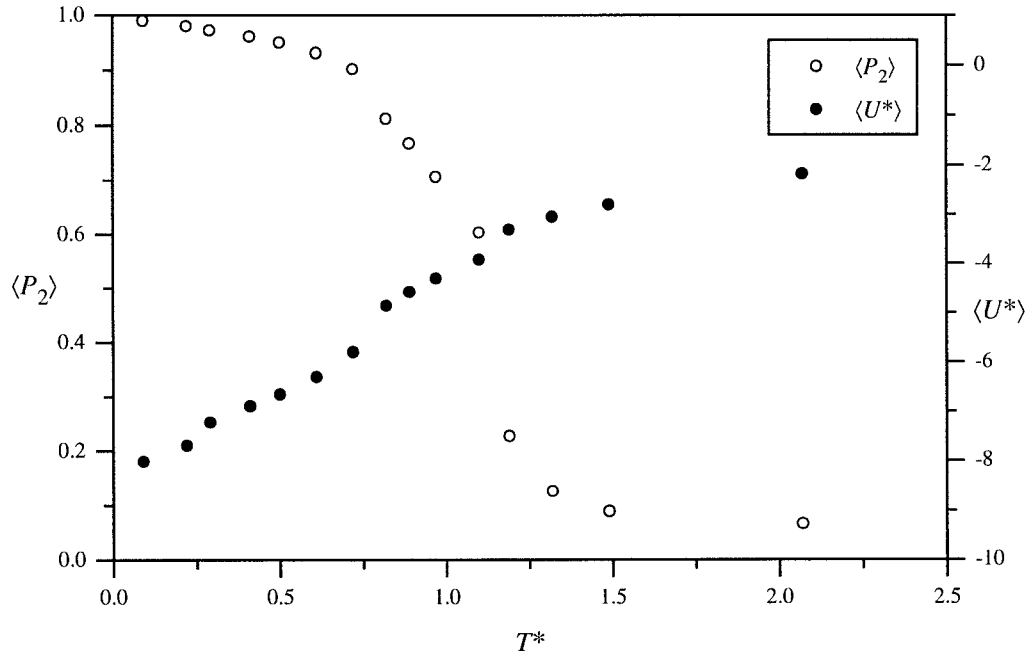

Figure 6.9: *The variation of the second rank orientational order parameter* $\langle P_2 \rangle$ *and the scaled internal energy per particle* $\langle U^* \rangle$ *with scaled temperature* T^* *at* ρ^* *of* 0.35.

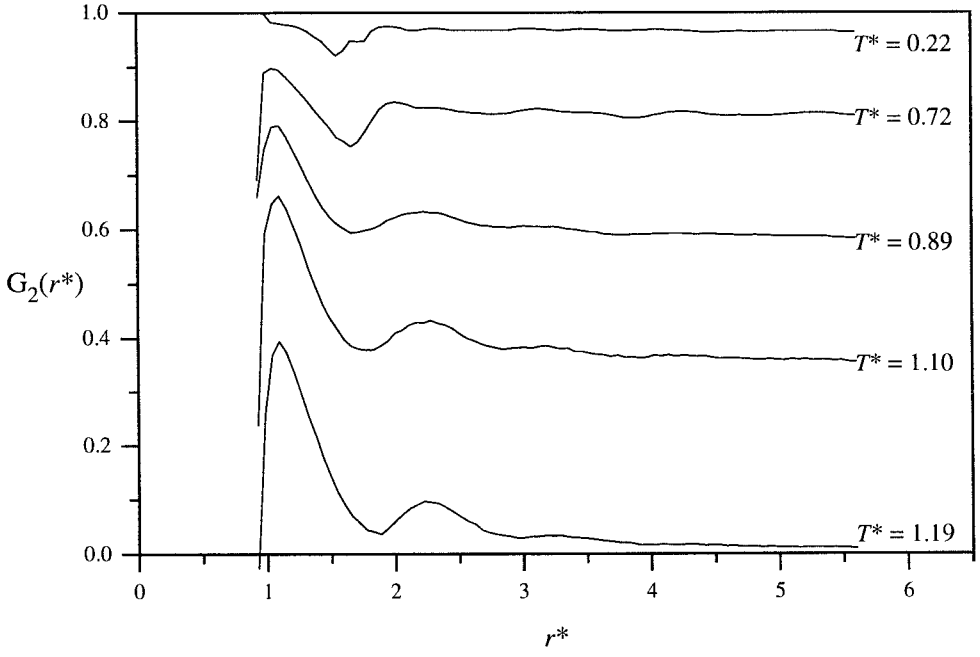

Figure 6.10: *The pair orientational correlation function* $G_2(r^*)$ *at the scaled temperatures* T^* *indicated.*

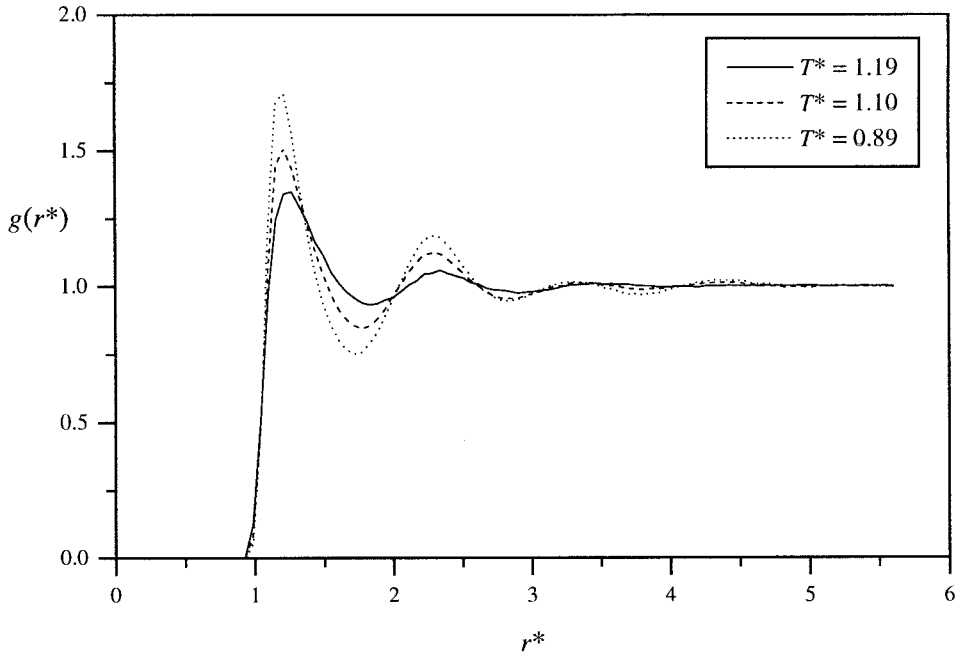

Figure 6.11: *The radial distribution function g(r*) at the scaled temperatures T* indicated.*

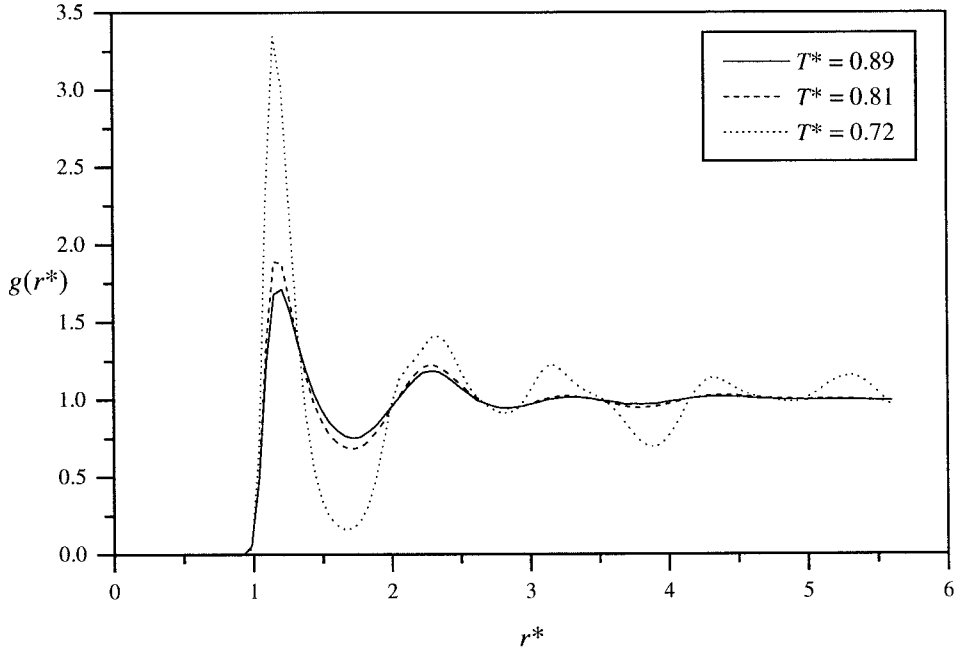

Figure 6.12: *The radial distribution function g(r*) at the scaled temperatures T* indicated.*

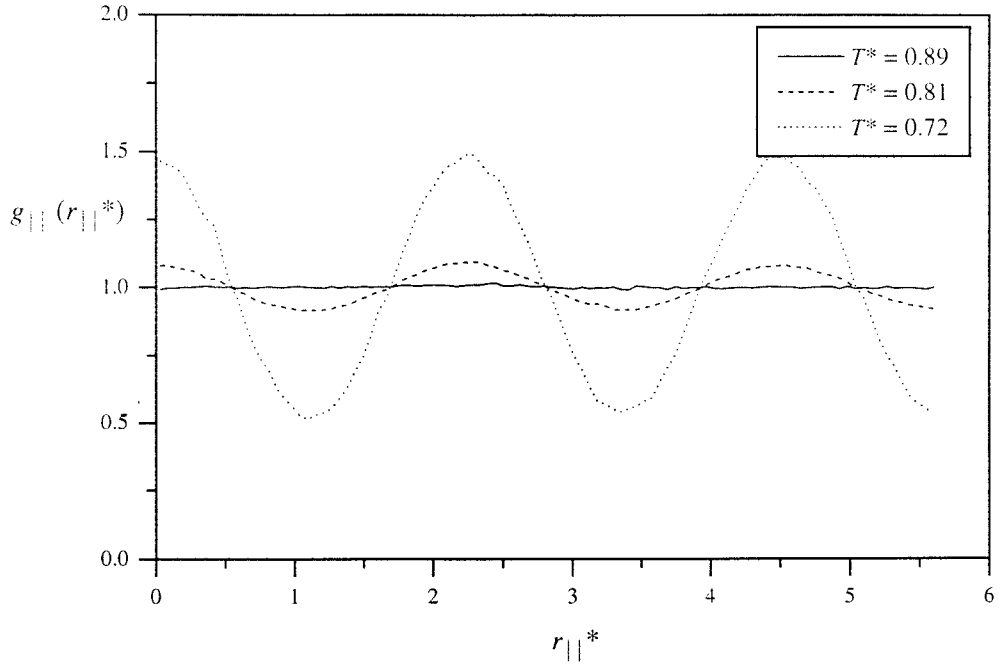

Figure 6.13: *The longitudinal pair distribution function* $g_{||}(r_{||}^*)$ *at the scaled temperatures T* indicated.*

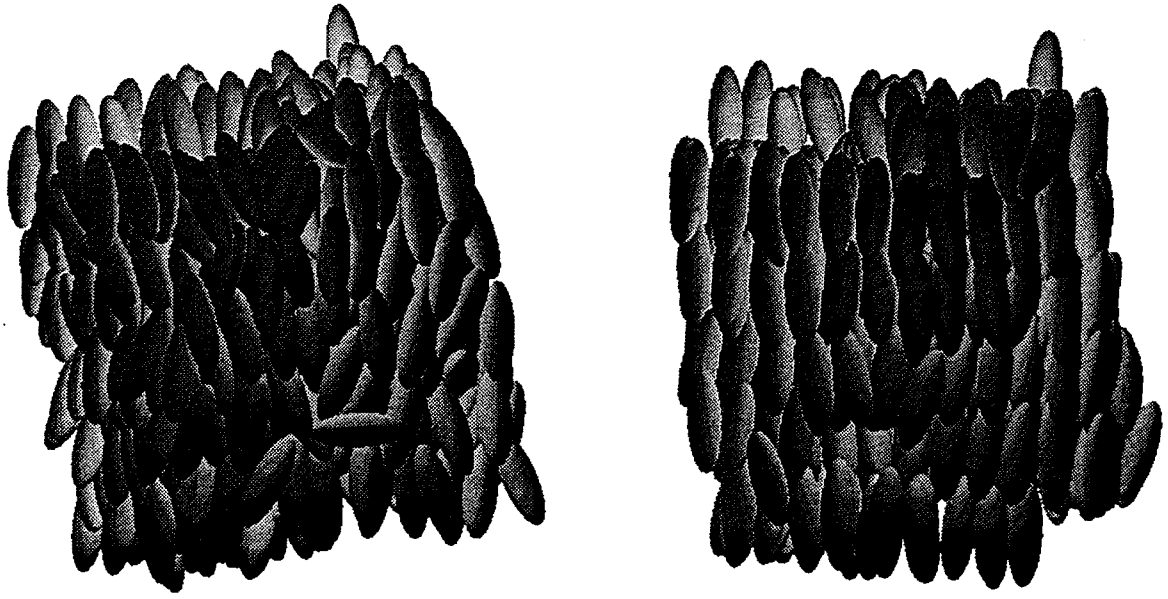

a) **b)**

Figure 6.14: *Graphic snapshots of a configuration taken from a) the smectic A phase at T* of* 0.81 *and b) the smectic B phase at T* of* 0.72.

If we increase the scaled density to 0.45, we can see that the nematic - isotropic transition temperature has increased to be between T^* of 2.18 and 1.97. From previous arguments in this Chapter, this is to be expected, though the rise is reasonably large. From the plots of the $\langle U^* \rangle$, (see figure 6.15), there is another observable transition between T^* of 1.18 and 1.01. Figure 6.16 shows the $g(r^*)$ for the two phases. At T^* of 1.18 we have a form similar to the nematic, while at T^* of 1.01, a highly ordered smectic B phase has been formed, with considerable in-plane hexagonal packing. The layer spacing of the smectic phase is $2.0\sigma_0$, reduced from $2.25\sigma_0$, probably due to the increased density, (see figure 6.17).

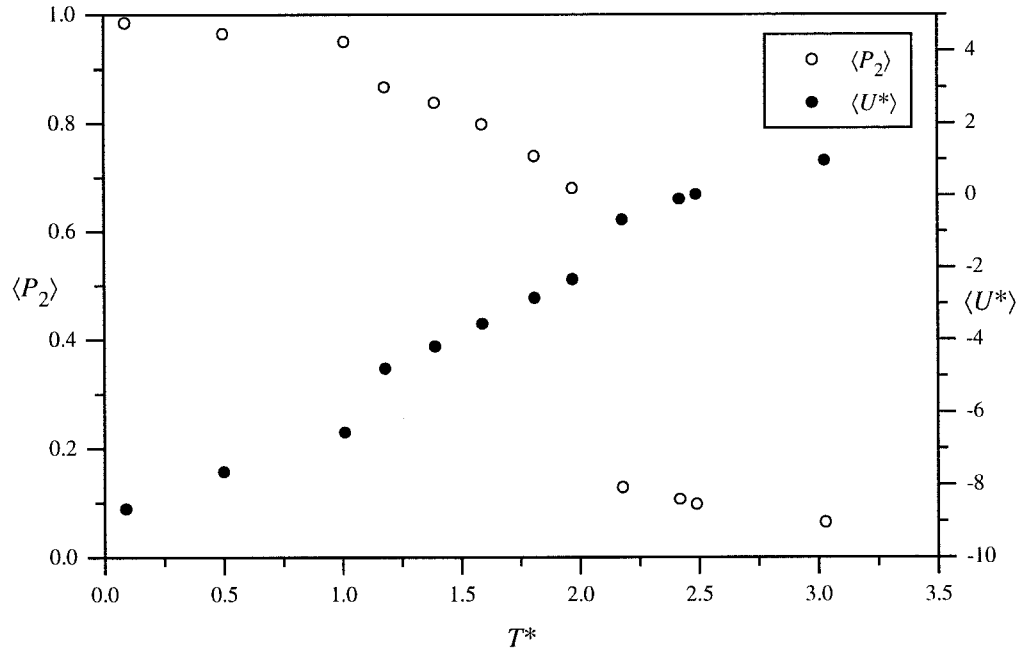

Figure 6.15: *The variation of the second rank orientational order parameter $\langle P_2 \rangle$ and the scaled internal energy per particle $\langle U^* \rangle$ with scaled temperature T^*.*

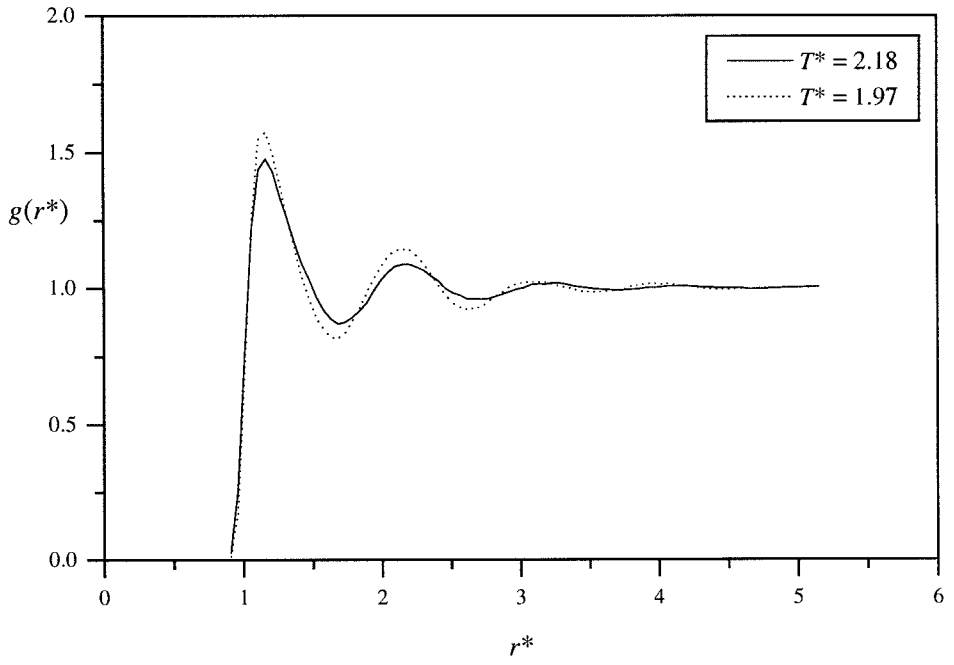

Figure 6.16: *The radial distribution function g(r*) at the scaled temperatures T* indicated.*

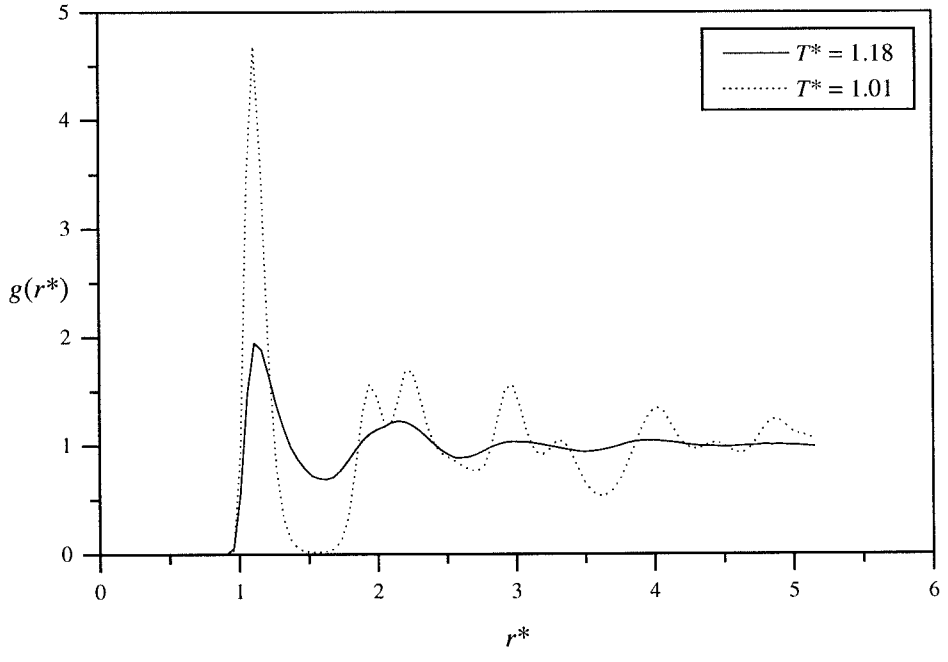

Figure 6.17: *The radial distribution function g(r*) at the scaled temperatures T* indicated.*

6.4.3 Length-to-breadth ratio σ_e/σ_s of 2.0.

For the system at ρ^* of 0.35, a phase transition occurs between T^* of 0.51 and 0.42, as shown by the plot of $\langle P_2 \rangle$ and $\langle U^* \rangle$, (see figure 6.18). Inspection of the $g(r^*)$, (see figure 6.19) and the graphic snapshot, (see figure 6.20), reveal the phases to be the isotropic and nematic respectively. The graphic snapshot also reveals the formation of a cavity in the simulation box, indicating this particular system to be unstable, at least at this density.

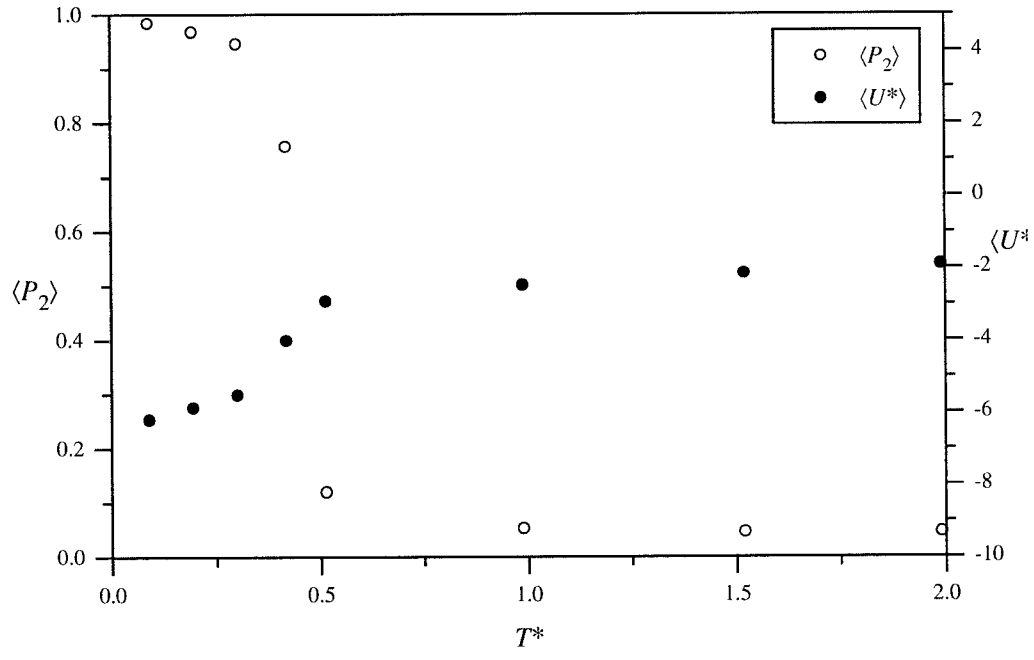

Figure 6.18: *The variation of the second rank orientational order parameter* $\langle P_2 \rangle$ *and the scaled internal energy per particle* $\langle U^* \rangle$ *with scaled temperature* T^*.

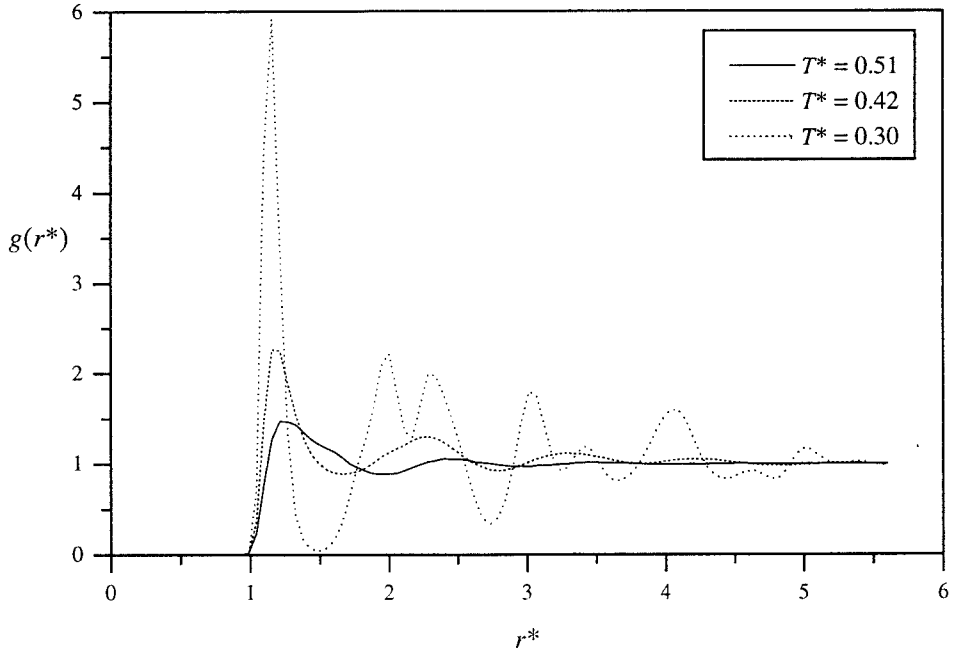

Figure 6.19: *The radial distribution function g(r*) at the scaled temperatures T* indicated.*

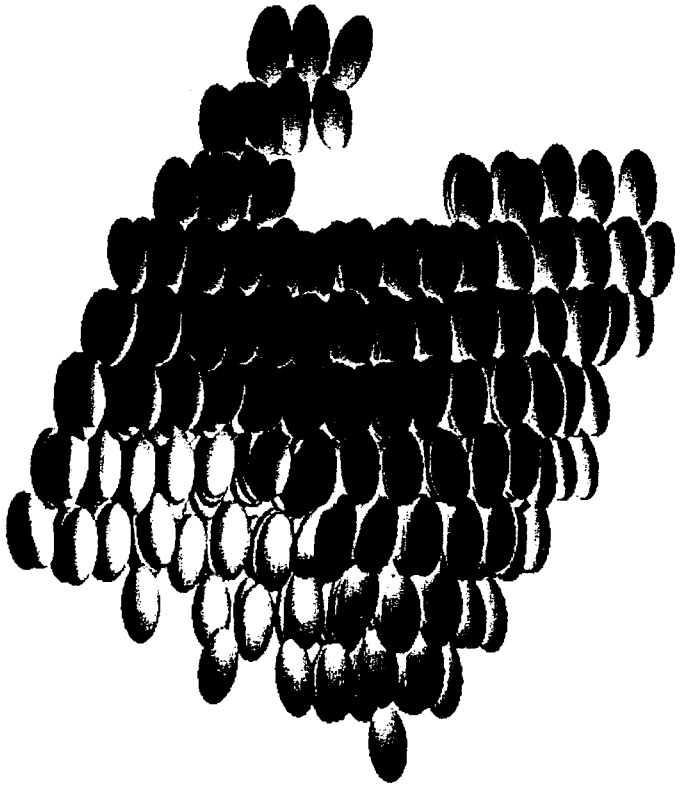

Figure 6.20: *The graphic snapshot at T* of 0.42, showing the formation of a cavity in the simulation box.*

From the plot of $\langle P_2 \rangle$ at the scaled density ρ* of 0.45, (see figure 6.21), we can see the orientational order-disorder phase transition between T^* of 0.69 and 0.62. This backed up by the $G_2(r^*)$, (see figure 6.23), in which the plot at T^* of 0.62 does not decay to zero, indicating residual long range orientational order. From the $g(r^*)$, we can see that the system remains in the nematic phase until T^* of 0.42, where we observe a smectic B phase, with the hexagonal order revealed by the characteristic feature of a split peak at r^* of 2, (see figures 6.23 and 6.24). Inspection of the $g_{||}(r_{||}^*)$ reveals the layers within the smectic B phase to be interdigitated with a layer spacing of $1.7\sigma_0$, (see figure 6.25). It is also interesting to see that the interdigitation causes the layer structure in the $g_{||}(r_{||}^*)$ to be weak, similar to the smectic A structure observed for σ_e/σ_s of 3.0, (see figure 6.13). Overall it seems that at the higher density, the system is stable enough to exhibit liquid crystalline mesophases.

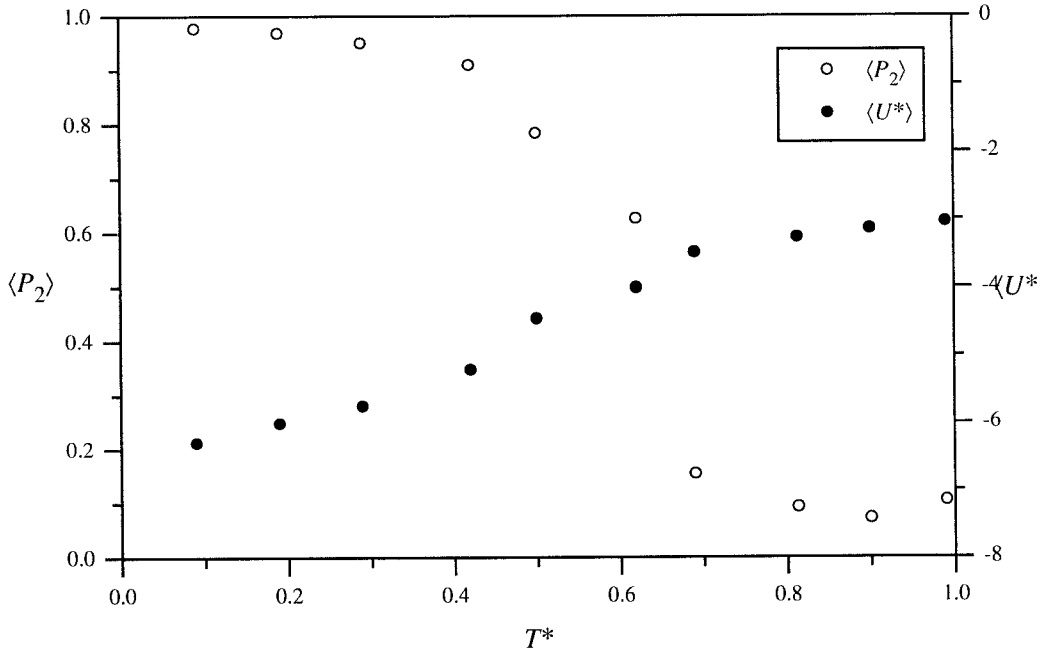

Figure 6.21: *The variation of the second rank orientational order parameter* $\langle P_2 \rangle$ *and the scaled internal energy per particle* $\langle U^* \rangle$ *with scaled temperature* T^*.

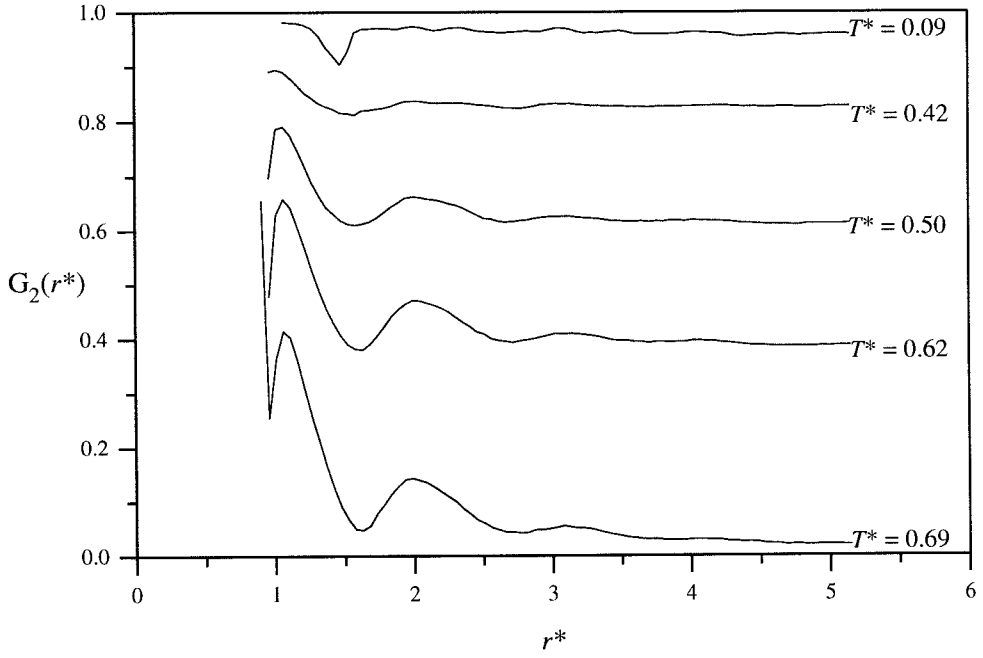

Figure 6.22: *The pair correlation function $G_2(r^*)$ at the scaled temperatures T^* indicated.*

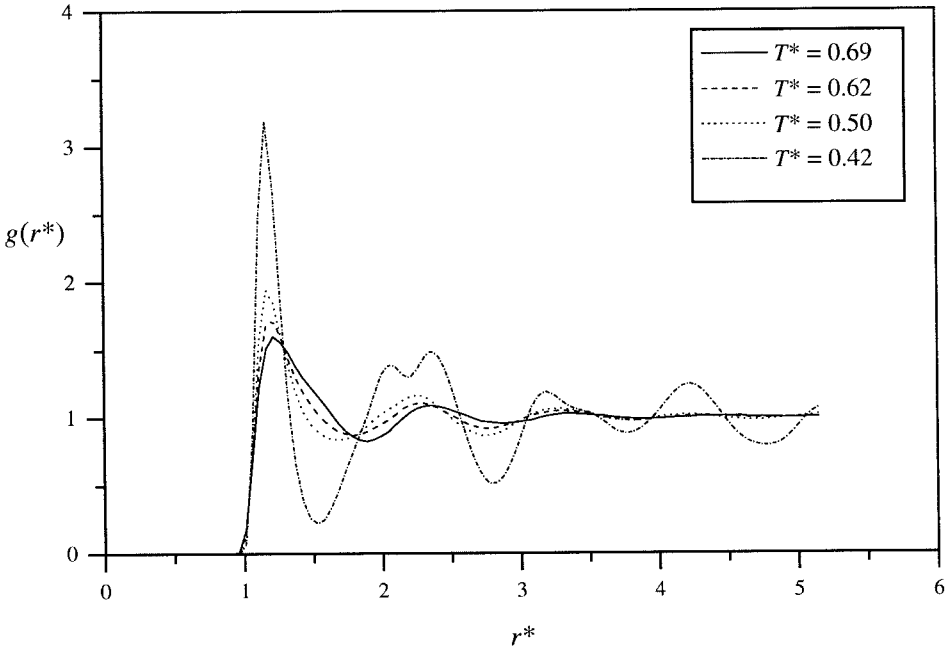

Figure 6.23: *The radial distribution function $g(r^*)$ at the scaled temperatures T^* indicated.*

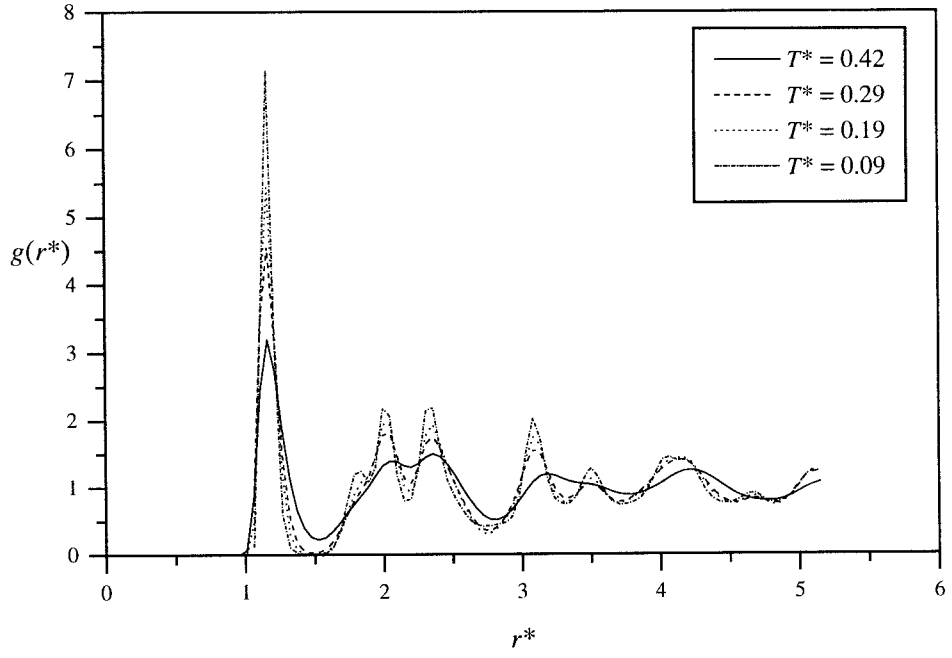

Figure 6.24: *The radial distribution function g(r*) at the scaled temperatures T* indicated.*

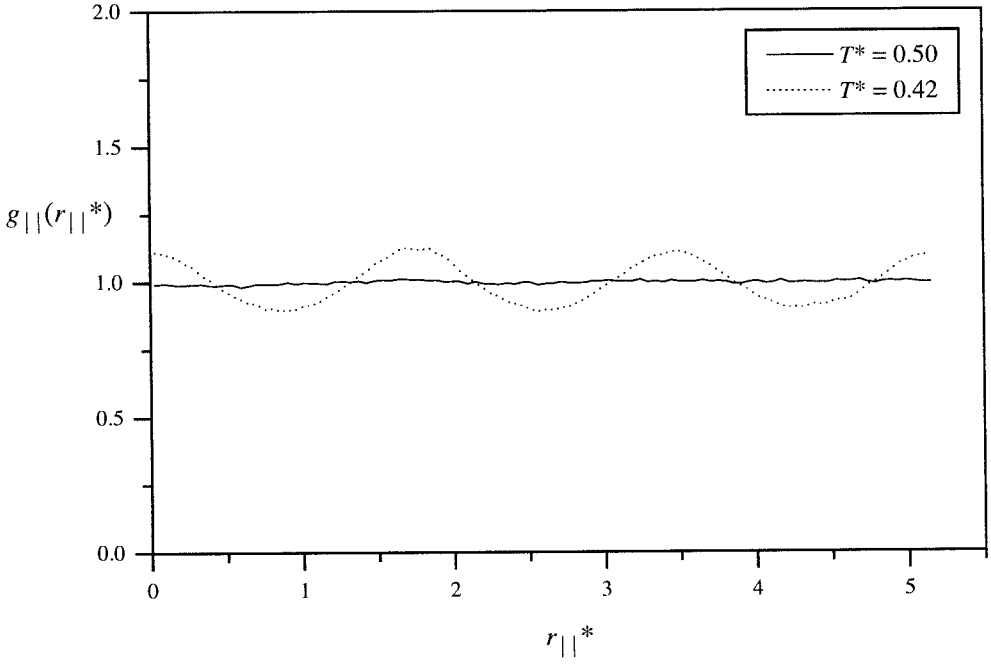

Figure 6.25: *The longitudinal pair distribution function $g_{||}(r_{||}^*)$ at the scaled temperatures T* indicated.*

6.5 Conclusions

In this Chapter we have investigated the phase behaviour of a series of Gay-Berne rods with differing length-to-breadth ratios. The idea was to see if the attractive forces present in the potential model could induce the less anisotropic ellipsoidal particles to form liquid-crystalline mesophases. This has proved a great success in that liquid-crystalline phases have been observed in systems of Gay-Berne ellipsoids with length-to-breadth ratios of 2.5 and 2.0, though their appearance is greatly dependent on the simulation density.

If we produce a table of the transition temperatures and layer spacing for all of our simulations, (see table 6.7), there seems to be several trends observable in the phase behaviour. First, as the scaled density is increased for a particular system, the nematic - isotropic transition temperature increases, and at σ_e/σ_s of 3.0, the smectic A phase present at lower densities, disappears as the density increases. Similar trends can be seen for a fixed density, that as the anisotropy of the particles is reduced, the nematic - isotropic transition temperature is reduced, presumably because the smaller the particle, the less attractive forces it experiences, thus a lower temperature is needed to overcome these forces. The reduced shape anisotropy would also contribute to the reduced transition temperature.

There also appears to be a trend in the layer spacing of the smectic B phases. For σ_e/σ_s of 3.0, the layer spacing is approximately $3.0\sigma_0$, the length of the constituent Gay-Berne mesogen. But for σ_e/σ_s of 2.5, the layer spacing of 2.25 and 2.0, for the densities of 0.35 and 0.45 respectively, is less than the length of the constituent particles. This aspect is also present for σ_e/σ_s of 2.0, where the layer spacing is $1.7\sigma_0$. This leads to smectic layers which are interdigitated. It would be sensible to perform a constant *NpT* simulation in order to investigate the effect of fixed boundary conditions on the layer spacing. By looking at the value of the second rank order parameter $\langle P_2 \rangle$ at the nematic - isotropic transition, we can see that apart from the simulation at σ_e/σ_s of 3.0, the value of $\langle P_2 \rangle$ is approximately the same at 0.4. This value is obtained by taking the value of $\langle P_2 \rangle$ at the middle of the nematic - isotropic transition as identified by the simulation points which are in the nematic and isotropic phases.

σ_e/σ_s	N	ρ^*	I	N	S_A	S_B	d /(σ_0)	$\langle P_2 \rangle$ at T^*_{NI}
3	500	0.35	3.86	-	1.63		3	0.28
2.5	500	0.35	1.15	0.8	0.72		2.25	0.4
2.5	500	0.45	2.08	-	1.01		2	0.4
2	500	0.35	-	-	-		-	-
2	500	0.45	0.65	-	0.42		1.7	0.4

Table 6.7: *A summary of the phase transition temperatures for the simulations at σ_e/σ_s of 2.0, 2.5 and 3.0.*

In conclusion, it seems that the attractive part of the Gay-Berne potential allows less elongated particles than usual (in terms of previous simulations) to form liquid-crystalline mesophases, though the repulsive forces seem to dominate in the nematic phase, in that, the system must still be sufficiently dense for the orientational ordered phases to be observed.

6.6 References

[1] D.Frenkel, H.N.W.Lekkerkerker and A.Stroobants. *Nature.* (1988) **332** 822.

[2] D.Frenkel. *Molec.Phys.* (1987) **60** 1.

[3] D.Demus, H.Demus and H.Zaschke. *Flüssige Kristallen in Tabellen.* VEB (1972).

[4] L.Onsager. *Ann.N.Y.Acad.Sci.* (1949) **51** 627.

[5] G.R.Luckhurst and P.S.J.Simmonds. *Molec.Phys.* (1993) **80** 233.

[6] G.R.Luckhurst, R.A.Stephens and R.W.Phippen. *Liq.Cryst.* (1990) **8** 451.

[7] M.A.Bates and G.R.Luckhurst. *To be submitted* (1995).

[8] G.R.Luckhurst and S.Romano. *Proc.R.Soc.Lond.* (1980) **A373** 111.

[9] M.D.De Luca, M.P.Neal and C.M.Care. *Liq.Cryst.* (1994) **16** 257.

[10] J.G.Gay and B.J.Berne. *J.Chem.Phys.* (1981) **74** 3316.

[11] D.J.Adams, G.R.Luckhurst and R.W.Phippen. *Molec.Phys.* (1987) **61** 1575.

[12] R.W.Phippen. *Ph.D. Thesis*, University of Southampton. (1988).

[13] A.P.J.Emerson. *Ph.D. Thesis*, University of Southampton (1991).

[14] M.K.Chalam, K.E.Gubbins, E. de Miguel and L.F.Rull. *Molec.Sim.* (1991) **7** 357.

[15] E.de Miguel, L.F.Rull, M.K.Chalam and K.E.Gubbins. *Molec.Phys.* (1991) **74** 405.